Magnetic and optical properties of correlated rare-earth compounds from first principles

James Boust

INSTITUT POLYTECHNIQUE DE PARIS

NNT : 2022IPPAX114

Thèse de doctorat

Magnetic and optical properties of correlated rare-earth compounds from first principles

Thèse de doctorat de l'Institut Polytechnique de Paris
préparée à l'École polytechnique

École doctorale n°626 École doctorale de l'Institut Polytechnique de Paris (EDIPP)
Spécialité de doctorat: Physique

Thèse présentée et soutenue à Palaiseau, le 18 novembre 2022, par

James BOUST

Composition du Jury :

Silke Biermann Professeur, Ecole polytechnique (CPHT)	Présidente
Alexander Lichtenstein Professeur, Universität Hamburg (Institut für Theoretische Physik)	Rapporteur
Markus Aichhorn Professeur associé, Graz University of Technology (Institute of Theoretical and Computational Physics)	Rapporteur
Nora Dempsey Directrice de recherche, Institut Néel CNRS	Examinatrice
Olle Eriksson Professeur, Uppsala University (Department of Physics and Astronomy)	Examinateur
Cesare Franchini Professeur, University of Vienna (Faculty of Physics and Center for Computational Materials Science) and University of Bologna (Department of Physics and Astronomy)	Examinateur
Leonid Pourovskii Ingénieur de recherche, Ecole polytechnique (CPHT) et Collège de France	Directeur de thèse

Acknowledgments

I would first like to warmly thank my supervisor Leonid. You have taught me a lot, thanks to your counselling and constant constructive feedback. Your patience, your availability and your benevolence have meant a lot to me!

I wish to thank Alexander Lichtenstein and Markus Aichhorn for taking time to review this manuscript and together with Silke Biermann, Nora Dempsey, Cesare Franchini and Olle Eriksson for accepting to be in the committee of this thesis.

I am grateful to all the wonderful people I have met at Ecole polytechnique, without whom these three years would simply not have been the same. Thank you for the fruitful discussions, the lectures we gave together, the help with administrative requests, the help with computer issues and thank you all for your kindness: Anna Galler, Benjamin Bacq-Labreuil, Erik Linnér, Steffen Backes, Edmond Baratte, Yannis Laplace, Alain Louis-Joseph, Jean-Charles Vanel, Jakob Steinbauer, Michel Ferrero, Florence Auger, Malika Lang, Fadila Guimonet Debbou, Yannick Fitamant, Danh Pham Kim, Evgeny Stepanov, Alaska Subedi, Renaud Garioud, Jan Schneider, Maria Chatzieleftheriou. I especially thank Silke Biermann for her guidance and counselling since my years as a graduate student.

I would also like to thank all the people I have had the chance to meet and work with during the MagHEM collaboration, especially Nora Dempsey, Yuan Hong, Thibault Devillers, Gabriel Gomez Eslava, Konstantin Skokov, Alex Aubert and Oliver Gutfleisch.

I am grateful to the doctoral school Institut Polytechnique de Paris, to the Ecole polytechnique and to the CPHT for making this thesis possible.

I would like to thank all my friends for their heartwarming presence throughout these three years, especially Lucas, Jacques-Antoine, Anne-Isabelle, Robin and Maxence.

I wish to thank my family for their support throughout my studies. Maman, Jean-Claude, Tomi, Sarah, Mélissa, Lucie: I know I can always count on you, thank you!

Finally, I would like to thank Léa, the love of my life. Thank you for your never ending support, your comforting smile and, more generally, the happiness you bring me; everything is so much easier when we are together. Now that this project of mine is over, I can't wait to focus on our mutual projects!

Abstract for the general public

In so-called "strongly correlated" materials, the strong Coulomb interaction which correlates the movement of electrons at the atomic scale can give rise to outstanding properties at the macroscopic scale. The materials studied in this thesis contain rare-earth elements (like neodymium) which usually exhibit these strong correlation effects.

Due to their remarkable properties, rare-earth compounds have numerous technological applications; they are for instance used as high-performance magnets in electric motors. The demand for rare earths is therefore increasing; on the other hand, mining them is difficult, expensive and polluting. Hence, optimizing the properties and composition of rare-earth-based materials can be of great technological, economical and environmental interest.

From the point of view of theoretical physics, describing these materials constitutes a real challenge, precisely due to their strongly correlated nature. In this thesis, we develop theoretical approaches to study the magnetic and optical properties of rare-earth compounds, notably the industrially relevant neodymium magnet. These theoretical methods are said to be from "first principles" as they are based on the fundamental laws governing the physics at the atomic level.

Résumé grand public

Dans les matériaux dits "fortement corrélés", la forte interaction de Coulomb qui corrèle le mouvement des électrons à l'échelle atomique peut donner lieu à des propriétés exceptionnelles à l'échelle macroscopique. Les matériaux étudiés dans cette thèse contiennent des atomes de terres rares (comme le néodyme) qui présentent généralement ces effets de fortes corrélations.

Du fait de leurs propriétés remarquables, les composés de terres rares ont de nombreuses applications technologiques; ils sont par exemple utilisés comme aimants très performants dans les moteurs électriques. La demande en terres rares est donc en plein essor; mais les miner s'avère difficile, coûteux et polluant. Optimiser les propriétés et la composition des matériaux à base de terres rares est ainsi intéressant pour des raisons à la fois technologiques, économiques et écologiques.

Du point de vue de la physique théorique, décrire ces matériaux constitue un véritable défi, précisément de par leur nature fortement corrélée. Dans cette thèse, nous développons des approches théoriques pour étudier les propriétés magnétiques et optiques de composés de terres rares, notamment l'aimant au néodyme employé dans l'industrie. Ces méthodes théoriques sont dites "depuis les premiers principes" car elles reposent sur les lois fondamentales gouvernant la physique à l'échelle atomique.

Abstract

This thesis focuses on magnetic and optical properties of various rare-earth-based materials from an *ab initio* perspective. Rare-earth ($\mathcal{R}$) elements usually exhibit a partially filled $4f$ shell which is very localized around the nucleus; the resulting strong Coulomb interaction between $4f$ electrons gives rise to electronic correlation effects. These compounds hence fall into the category of so-called "strongly correlated" materials.

In the first part of this thesis, we describe the quantum many-body problem which governs the physics of materials. Well established since the 1920s, it remains in general insoluble. However, a remarkable progress in the treatment of this problem has since been achieved by approximate approaches.
The first chapter deals with one of them, developed in the 1960s: the exact Density Functional Theory (DFT) combined with the Local Density Approximation (LDA) for exchange and correlation effects. While DFT has now become the standard method for electronic structure calculation of real materials, it fails at treating strong electronic correlations such as those at play in the rare-earth compounds.
In the second chapter, we describe the Dynamical Mean-Field Theory (DMFT) which was designed in the 1990s to study correlation effects in the Hubbard model – a simplified version of the full quantum many-body problem in a solid. DMFT is based on a mapping of this model onto a quantum impurity problem of an atom exchanging electrons with a bath, easier to solve.
The third chapter reviews the DFT+DMFT method which combines the applicability to real materials of DFT and the proper treatment of strong correlations by DMFT. It is now widely applied to correlated materials, in particular rare-earth compounds. The present thesis is based on this DFT+DMFT scheme in conjunction with a quasi-atomic approximation for the quantum impurity problem involved in DMFT. This so-called Hubbard-I (HI) approximation is relevant for the rare-earth $4f$ shell which is in the strong (Coulomb) coupling regime.

In the second part of this thesis, we focus on magnetic properties of rare-earth transition metal intermetallics.
The fourth chapter details our treatment of these systems, which is based on DFT+HI. We focus in particular on the crystal field effects which, combined with the strong $4f$ spin-orbit coupling, are at the origin of significant magnetic anisotropy in many of them.
In the fifth chapter, we apply our DFT+HI-based approach to the $\mathcal{R}Co_5$ family. We notably show that a large value of a rank-6 crystal field parameter in $\mathcal{R}Co_5$ predicted by our calculations explains a puzzling reduction of the zero-temperature Nd moment in $NdCo_5$.
In the sixth chapter, we use the same technique to study partial substitution of Nd by Ce or Dy in $Nd_2Fe_{14}B$, the most widely used high-performance permanent magnet in the industry. We predict that optimizing the Ce (Dy) occupancy on one precise crystallographic site yields enhanced magnetic anisotropy.

In the third part (seventh chapter), we focus on spectral and optical properties of rare-earth semiconductors. In order to address the systematic DFT underestimation of non-correlated gaps, we combine the DMFT approach to strongly-correlated $4f$ electrons with the modified Becke-Johnson exchange potential. We then apply this method to study optical properties of rare-earth sesquioxides $\mathcal{R}_2O_3$ and fluorosulfides $\mathcal{R}SF$. We notably explain the characteristic onset of the measured optical conductivity in $\mathcal{R}_2O_3$ compounds and determine the nature of the optical gap in the light $\mathcal{R}SF$ series.

In the fourth part (eighth chapter), to go beyond the Hubbard-I approximation, we explore a new approach to solve the DMFT quantum impurity problem in the strong coupling limit. This method is based on an equation of motion formalism preserving the analytical properties of the impurity Green's function.

Résumé

Dans cette thèse, nous étudions les propriétés magnétiques et optiques de divers composés de terres rares dans une perspective *ab initio*. Les terres rares ($\mathcal{R}$) présentent généralement une couche $4f$ partiellement pleine, très localisée autour du noyau. Il en résulte une forte interaction de Coulomb entre les électrons $4f$ et donc des effets de corrélations électroniques. Ces composés appartiennent ainsi à la catégorie des matériaux "fortement corrélés".

Dans la première partie de cette thèse, nous décrivons le problème quantique à N-corps qui gouverne la physique des matériaux. Bien établi depuis les années 20, il s'avère généralement insoluble ; mais il peut être traité de façon approximative grâce à des approches de plus en plus sophistiquées.
Le premier chapitre traite de l'une d'entre elles, développée dans les années 60 : la Théorie de la Fonctionnelle de la Densité (DFT), combinée à l'Approximation de Densité Locale (LDA) pour les effets d'échange et de corrélation. Bien que la DFT soit devenue la méthode standard de calcul électronique des matériaux, elle ne peut traiter les effets de fortes corrélations comme ceux en jeu dans les composés de terres rares.
Dans le chapitre deux, nous décrivons la Théorie du Champ Moyen Dynamique (DMFT) conçue dans les années 90 pour étudier les effets de corrélation dans le modèle de Hubbard – version simplifiée du problème quantique à N-corps dans un solide. La DMFT représente le modèle de Hubbard par un problème d'impureté quantique échangeant des électrons avec un réservoir, plus facile à résoudre.
Le chapitre trois décrit la méthode DFT+DMFT qui combine l'applicabilité aux matériaux de la DFT et le traitement des fortes corrélations par la DMFT. Elle est de nos jours largement appliquée aux matériaux corrélés, en particulier aux composés de terres rares. Cette thèse est fondée sur cette méthode en conjonction avec une approximation quasi-atomique pour le problème d'impureté quantique de la DMFT. Cette approximation, appelée Hubbard-I (HI), est pertinente pour la couche $4f$ des terres rares qui est dans le régime de couplage fort.

Dans la deuxième partie, nous étudions les propriétés magnétiques des composés intermétalliques de terres rares et de métaux de transition.
Le chapitre quatre décrit notre traitement, fondé sur la DFT+HI, de ces systèmes. Nous mettons l'accent sur les effets de champ cristallin qui, combinés au fort couplage spin-orbite de la couche $4f$, sont à l'origine d'une importante anisotropie magnétique dans la plupart d'entre eux.
Dans le chapitre cinq, nous appliquons notre approche DFT+HI à la famille $\mathcal{R}Co_5$. Nous montrons qu'une valeur élevée d'un paramètre de champ cristallin de rang 6, prédite par nos calculs, permet d'expliquer une réduction du moment Nd à température nulle dans $NdCo_5$.
Dans le chapitre six, nous étudions la substitution partielle de Nd par Ce ou Dy dans $Nd_2Fe_{14}B$, l'aimant performant le plus employé dans l'industrie. Nous prédisons qu'optimiser l'occupation d'un site cristallographique par Ce (Dy) augmente l'anisotropie magnétique.

La troisième partie (chapitre sept) traite des propriétés spectrales et optiques des semiconducteurs à base de terres rares. Pour pallier la sous-estimation systèmatique des *gaps* non corrélés par la DFT, nous combinons l'approche DMFT pour les électrons $4f$ avec le potentiel d'échange de Becke et Johnson modifié. Nous appliquons cette méthode à l'étude des sesquioxydes $\mathcal{R}_2O_3$ et fluorosulfides $\mathcal{R}SF$ de terres rares. Nous expliquons l'amorce caractéristique de la conductivité optique mesurée expérimentalement dans $\mathcal{R}_2O_3$ et déterminons la nature du *gap* optique dans $\mathcal{R}SF$.

Dans la quatrième partie (chapitre huit), afin de dépasser l'approximation HI, nous explorons une nouvelle approche pour résoudre le problème d'impureté quantique de la DMFT dans le régime de couplage fort. Cette méthode est fondée sur une équation du mouvement qui préserve les propriétés analytiques de la fonction de Green de l'impureté.

List of publications

1. Higher-order crystal field and rare-earth magnetism in rare-earth–Co_5 intermetallics
   L. V. Pourovskii, J. Boust, R. Ballou, G. Gomez Eslava, and D. Givord
   Phys. Rev. B 101, 214433 (2020)

2. Correlated electronic structure and optical response of rare-earth based semiconductors
   A. Galler, J. Boust, A. Demourgues, S. Biermann, and L. V. Pourovskii
   Phys. Rev. B 103, L241105 (2021)

3. Combining semilocal exchange with dynamical mean-field theory: Electronic structure and optical response of rare-earth sesquioxides
   J. Boust, A. Galler, S. Biermann, and L. V. Pourovskii
   Phys. Rev. B 105, 085133 (2022)

4. Ce and Dy substitutions in $Nd_2Fe_{14}B$: Site-specific magnetic anisotropy from first principles
   J. Boust, A. Aubert, B. Fayyazi, K. P. Skokov, Y. Skourski, O. Gutfleisch, and L. V. Pourovskii
   Phys. Rev. Materials 6, 084410 (2022)

Contents

Part I

Introduction

Chapter 1

Real material electronic band structure and density functional theory

In this first chapter, we introduce the general quantum many-body problem that needs to be solved to understand the different (magnetic and optical) properties of real materials that are the focus of this thesis. We then describe one theoretical approach to tackle this problem: the density functional theory. For a general review of this method, the reader can refer to [Jones and Gunnarsson, 1989, Jones, 2015]. The different conventions and acronyms used in this thesis are summarized in appendices A and B respectively.

1.1 The quantum many-body problem in crystals

Real materials are condensed matter, in which the relevant particles are nuclei and electrons; in this context, almost all the physics (one can add relativistic corrections) can be explained by the interplay between the kinetic energy and the Coulomb interaction of these particles. More formally, the many-body wave function Ψ describing the stationary state of a system of nuclei ν (masses M_ν, atomic numbers Z_ν) and N electrons i is governed by the Schrödinger equation $\hat{H}\Psi = \epsilon\Psi$ where the Hamiltonian $\hat{H}$ is given by:

$$\hat{H} = -\sum_{\nu} \frac{\nabla_\nu^2}{2M_\nu} - \sum_{i} \frac{\nabla_i^2}{2} + \frac{1}{2}\sum_{\nu\neq\nu'} \frac{Z_\nu Z_{\nu'}}{|\boldsymbol{R}_\nu - \boldsymbol{R}_{\nu'}|} + \frac{1}{2}\sum_{i\neq j} \frac{1}{|\boldsymbol{r}_i - \boldsymbol{r}_j|} - \sum_{i\nu} \frac{Z_\nu}{|\boldsymbol{r}_i - \boldsymbol{R}_\nu|}. \tag{1.1}$$

The first two terms are the kinetic energy of nuclei and electrons, the last three terms the nuclei-nuclei, electron-electron and electron-nuclei Coulomb interactions, respectively. The laws governing condensed matter are hence well-known.

The number of involved particles is, however, colossal. Indeed, for instance, 12 g of ^{12}C contains $N_A = 6,02 \times 10^{23}$ nuclei and six times more electrons; storing the many-body wave function Ψ for a macroscopical piece of matter is therefore impossible. It follows that the

well-established quantum many-body problem 1.1, without further approximations, is generally insoluble, as stated by [Dirac, 1929]:

> *The underlying laws necessary for the mathematical theory of a large part of physics and the whole of chemistry are thus completely known, and the difficulty is only that exact applications of these laws lead to equations which are too complicated to be soluble. It therefore becomes desirable that approximate practical methods of applying quantum mechanics should be developed, which can lead to an explanation of the main features of complex atomic systems without too much computation.*

One first step to simplify equation 1.1 is the Born-Oppenheimer approximation: because nuclei are much heavier, and hence much slower, than electrons, one can consider them to be immobile on the typical electronic timescale. This leads to the electronic Hamiltonian $\hat{H}_{\mathrm{e}}$:

$$\hat{H}_{\mathrm{e}} = \hat{K} + \hat{V}_{ext} + \hat{U} \tag{1.2}$$

$$= \sum_i \left(-\frac{\nabla_i^2}{2} + v_{\mathrm{ext}}(\boldsymbol{r}_i) \right) + \frac{1}{2} \sum_{i \neq j} \frac{1}{|\boldsymbol{r}_i - \boldsymbol{r}_j|} \tag{1.3}$$

where $\hat{K}$ is the electronic kinetic energy, $\hat{U}$ is the electronic Coulomb interaction and $\hat{V}_{ext}$ is the electron-nuclei Coulomb interaction with

$$v_{\mathrm{ext}}(\boldsymbol{r}) = -\sum_\nu \frac{Z_\nu}{|\boldsymbol{r} - \boldsymbol{R}_\nu|} \tag{1.4}$$

the external potential acting on electrons and created by the nuclei whose positions $\boldsymbol{R}_\nu$ depend on the compound. In particular, as we will model real materials by perfect and infinite crystals, v_{ext} will be periodic from now on. Despite this simplification, equation 1.3 still faces the same issue as equation 1.1 and further approximations are required. In sections 1.2 to 1.5, we describe one such approximate scheme: the Density Functional Theory (DFT) combined with the Local Density Approximation (LDA).

1.2 Hohenberg-Kohn theorems

The crucial quantity involved in DFT is the density $n(\boldsymbol{r})$ (proportional to the probability density of finding an electron at $\boldsymbol{r}$) associated to an electronic N-body wave function Ψ. With the notations $\boldsymbol{x} = (\boldsymbol{r}, \sigma)$ and $\int d^4\boldsymbol{x} = \sum_\sigma \int d^3\boldsymbol{r}$, where $\sigma \in (\uparrow, \downarrow)$ denotes the spin degree of freedom, it is given by:

$$n(\boldsymbol{r}) = N \sum_\sigma \int d^4\boldsymbol{x}_2 ... \int d^4\boldsymbol{x}_N |\Psi(\boldsymbol{x}, \boldsymbol{x}_2, ..., \boldsymbol{x}_N)|^2. \tag{1.5}$$

At heart of DFT are indeed the two Hohenberg-Kohn (HK) theorems which state the following [Hohenberg and Kohn, 1964]:

1. The external potential v_{ext} (Eq. 1.4) is a unique functional (up to an additive constant) of the Ground State (GS) electron density n (Eq. 1.5) which therefore uniquely determines all the properties of the system. The many-body GS wave function Ψ is hence a functional of n, denoted by $\Psi[n]$. Furthermore, $F[n] = K[n] + U[n] = \langle \Psi[n] | \hat{K} + \hat{U} | \Psi[n] \rangle$ is a universal functional called the HK functional.

2. For a given external potential v_{ext}, the GS electron energy E_0 and density n_0 can be obtained variationally by minimizing the total energy functional $E[n]$, i.e:

$$E_0 = E[n_0] = \min_n E[n] \tag{1.6}$$

$$E[n] = F[n] + V_{\text{ext}}[n] \tag{1.7}$$

$$V_{\text{ext}}[n] = \langle \Psi[n] | \hat{V}_{ext} | \Psi[n] \rangle \, . \tag{1.8}$$

Hence, according to the first theorem, the GS electron density n_0 is enough to characterize the GS of such an electronic system; there is no need for the complicated many-body wave function Ψ discussed above, which is an enormous simplification. The second theorem provides a theoretical framework to find n_0. The idea behind DFT is therefore to minimize $E[n]$. However, while $V_{\text{ext}}[n]$ can be explicitly evaluated, as

$$V_{\text{ext}}[n] = \int v_{\text{ext}}(\boldsymbol{r}) n(\boldsymbol{r}) d^3\boldsymbol{r}, \tag{1.9}$$

it is not the case of the universal HK functional $F[n]$. Hence, in practice, $E[n]$ is not known and the minimization is not feasible. The next two sections explain how DFT deals with this difficulty.

1.3 Kohn-Sham equations

To simplify equation 1.6, we follow [Kohn and Sham, 1965] and consider an auxiliary system of non-interacting electrons. The GS density of this so-called Kohn-Sham (KS) system is assumed to be n (representability assumption). Its GS wave function is a Slater determinant $\Phi[n]$ of N KS spin-orbitals $\{\phi_i\}$ and its GS kinetic energy is $K_{\text{s}} = \langle \Phi[n] | \, \hat{K} \, | \Phi[n] \rangle$. We write for the interacting system:

$$F[n] = K_s[n] + E_{\text{Hxc}}[n] \tag{1.10}$$

$$E_{\text{Hxc}}[n] = U[n] + K[n] - K_{\text{s}}[n] \tag{1.11}$$

where E_{Hxc} is the Hartree-exchange-correlation energy functional which is discussed in the next section. The second HK theorem 1.6 then becomes

$$E[n_0] = \min_{\Phi} \left(\langle \Phi | \, \hat{K} + \hat{V}_{\text{ext}} \, | \Phi \rangle + E_{\text{Hxc}}[n] \right) \tag{1.12}$$

$$= \min_{\phi_i} \left(\sum_i \int \phi_i^*(\boldsymbol{x}) \Big(-\frac{\nabla^2}{2} + v_{\text{ext}}(\boldsymbol{r}) \Big) \phi_i(\boldsymbol{x}) d^4\boldsymbol{x} + E_{\text{Hxc}}[n] - \sum_{ij} \Lambda_{ij} \Big(\langle \phi_i | \phi_j \rangle - \delta_{ij} \Big) \right) \tag{1.13}$$

where Λ_{ij} is a Lagrangian multiplier which ensures orthonormality of the spin-orbitals ϕ_i and, according to the representability assumption, the density $n(\boldsymbol{r})$ is evaluated as

$$n(\boldsymbol{r}) = \sum_{\sigma} n_\sigma(\boldsymbol{r}) = \sum_{\sigma i} |\phi_i(\boldsymbol{x})|^2. \tag{1.14}$$

One can show that the stationary conditions related to equation 1.13 are

$$\Big(-\frac{\nabla^2}{2} + v_{\text{KS}}(\boldsymbol{r}) \Big) \phi_i(\boldsymbol{x}) = \epsilon_i \phi_i(\boldsymbol{x}) \tag{1.15}$$

where $\epsilon_i = \Lambda_{ii}$[1] and the KS potential $v_{\text{KS}}(\boldsymbol{r})$ is given by

$$v_{\text{KS}}(\boldsymbol{r}) = v_{\text{ext}}(\boldsymbol{r}) + v_{\text{Hxc}}(\boldsymbol{r}) \tag{1.16}$$

$$v_{\text{Hxc}}(\boldsymbol{r}) = \frac{\partial E_{\text{Hxc}}[n]}{\partial n(\boldsymbol{r})}. \tag{1.17}$$

As the KS potential 1.16 depends itself on the density 1.14, the KS equations 1.15 and 1.14 must be solved iteratively. DFT hence consists in the following self-consistent algorithm:

1. Initialize the density, typically by the superposition of atomic ones.
2. From the density, compute the Hartree-exchange-correlation potential 1.17 and corresponding KS potential 1.16.
3. Solve the KS equation 1.15 to get the infinite set of KS spin-orbitals and corresponding KS energies.
4. Compute the new density 1.14 from the N KS spin-orbitals with lowest energies.
5. Repeat the sequence 2-4 until self-consistency of the density has been reached.

DFT is hence in principle exact. However, evaluating the Hartree-exchange-correlation potential in step 2 requires an approximation, such as the local density approximation detailed in the following section.

[1] Λ is forced to be diagonal.

1.4 The Hartree-exchange-correlation potential and the local density approximation

Let us first consider the GS Coulomb energy $U_\mathrm{s}[n]$ of the KS system. It can be decomposed as

$$U_\mathrm{s}[n] = \langle\Phi[n]|\hat{U}|\Phi[n]\rangle \tag{1.18}$$

$$= \frac{1}{2}\int d^3\boldsymbol{r}\int d^3\boldsymbol{r}'\frac{1}{|\boldsymbol{r}-\boldsymbol{r}'|}\sum_{\sigma\sigma'}\sum_{ij}\Big(\phi_i^*(\boldsymbol{x})\phi_j^*(\boldsymbol{x}')\phi_i(\boldsymbol{x})\phi_j(\boldsymbol{x}') - \phi_i^*(\boldsymbol{x})\phi_j^*(\boldsymbol{x}')\phi_i(\boldsymbol{x}')\phi_j(\boldsymbol{x})\Big) \tag{1.19}$$

$$= \frac{1}{2}\int d^3\boldsymbol{r}\int d^3\boldsymbol{r}'\frac{n(\boldsymbol{r})n(\boldsymbol{r}')}{|\boldsymbol{r}-\boldsymbol{r}'|} + \frac{1}{2}\int d^3\boldsymbol{r}\int d^3\boldsymbol{r}'\frac{n(\boldsymbol{r})h_\mathrm{x}(\boldsymbol{r},\boldsymbol{r}')}{|\boldsymbol{r}-\boldsymbol{r}'|} \tag{1.20}$$

$$= E_\mathrm{H}[n] + E_\mathrm{x}[n], \tag{1.21}$$

where E_H is the Hartree energy, E_x the exchange energy and $h_\mathrm{x}(\boldsymbol{r},\boldsymbol{r}')$ the exchange hole. The physical meaning of the latter becomes apparent when noting that

$$n(\boldsymbol{r})\Big(n(\boldsymbol{r}') + h_\mathrm{x}(\boldsymbol{r},\boldsymbol{r}')\Big) \tag{1.22}$$

amounts to the joint probability of finding two electrons at $(\boldsymbol{r},\boldsymbol{r}')$. Then, $n(\boldsymbol{r}') + h_x(\boldsymbol{r},\boldsymbol{r}')$ amounts to the probability of finding one electron at $\boldsymbol{r}'$ knowing that one is at $\boldsymbol{r}$, which is not simply the probability of finding an electron at $\boldsymbol{r}'$: the correction is accounted by the exchange hole $h_\mathrm{x}(\boldsymbol{r},\boldsymbol{r}')$. Ignoring (or approximating) the latter leads to a self-interaction error as an electron unphysically interacts with itself via Coulomb interaction. The exchange arises from the Pauli exclusion principle which requires a Slater determinant for the KS GS wave function.

We can now write for the interacting system:

$$E_\mathrm{Hxc}[n] = U[n] + K[n] - K_\mathrm{s}[n] \tag{1.23}$$

$$= U_\mathrm{s}[n] + \Big((U[n] - U_\mathrm{s}[n]) + (K[n] - K_\mathrm{s}[n])\Big) \tag{1.24}$$

$$= E_\mathrm{H}[n] + E_\mathrm{x}[n] + E_\mathrm{c}[n] \tag{1.25}$$

$$= E_\mathrm{H}[n] + E_\mathrm{xc}[n]. \tag{1.26}$$

$E_\mathrm{c}[n]$ is the correlation energy functional: it takes into account correlation contributions to the kinetic and Coulomb energies, i.e. effects arising from the fact that interacting electrons are not independent and that the GS wave function is not a single Slater determinant as in the KS system. $E_\mathrm{xc}[n]$ is the exchange-correlation energy functional.

As described in the previous section, DFT requires the Hartree-exchange-correlation poten-

tial. While the Hartree contribution can be evaluated as

$$v_{\mathrm{H}}(\boldsymbol{r}) = \frac{\delta E_{\mathrm{H}}[n]}{\delta n(\boldsymbol{r})} \tag{1.27}$$

$$= \int \frac{n(\boldsymbol{r}')}{|\boldsymbol{r} - \boldsymbol{r}'|} d^3\boldsymbol{r}', \tag{1.28}$$

the exchange-correlation part $v_{\mathrm{xc}}(\boldsymbol{r})$ cannot be computed. DFT hence comes with different flavors depending on the approximation used to evaluate the latter. The simplest one is the Local Density Approximation (LDA) [Kohn and Sham, 1965], used in this thesis. It writes the exchange-correlation energy in the following form

$$E_{\mathrm{xc}}[n] = \int n(\boldsymbol{r}) \epsilon_{\mathrm{xc}}[n](\boldsymbol{r}) d^3\boldsymbol{r} \tag{1.29}$$

and approximates the exchange-correlation energy density $\epsilon_{\mathrm{xc}}[n]$ at each point $\boldsymbol{r}$ by the corresponding (i.e. exchange-correlation) energy density of a Uniform Electron Gas (UEG) of density $n_{\mathrm{UEG}} = n(\boldsymbol{r})$. Namely,

$$E_{\mathrm{xc}}^{\mathrm{LDA}}[n] = \int n(\boldsymbol{r}) \epsilon_{\mathrm{xc}}^{\mathrm{UEG}}\big(n(\boldsymbol{r})\big) d^3\boldsymbol{r} \tag{1.30}$$

with $\epsilon_{\mathrm{xc}}^{\mathrm{UEG}} = \epsilon_{\mathrm{x}}^{\mathrm{UEG}} + \epsilon_{\mathrm{c}}^{\mathrm{UEG}}$. It can be shown that

$$\epsilon_{\mathrm{x}}^{\mathrm{UEG}}(n_{\mathrm{UEG}}) = -\frac{3}{4}\left(\frac{3}{\pi} n_{\mathrm{UEG}}\right)^{\frac{1}{3}} \tag{1.31}$$

$$v_x^{\mathrm{LDA}}(\boldsymbol{r}) = \frac{\delta E_{\mathrm{x}}^{\mathrm{LDA}}[n]}{\delta n(\boldsymbol{r})} = -\left(\frac{3}{\pi}\right)^{\frac{1}{3}} n(\boldsymbol{r})^{\frac{1}{3}}. \tag{1.32}$$

The correlation counterparts $\epsilon_{\mathrm{c}}^{\mathrm{UEG}}(n_{\mathrm{UEG}})$ and $v_{\mathrm{c}}^{\mathrm{LDA}}(\boldsymbol{r})$ have been computed thanks to Monte-Carlo simulations [Ceperley and Alder, 1980].

Within this approximation the KS potential 1.16 is hence fully known as

$$v_{\mathrm{KS}}^{\mathrm{LDA}} = v_{\mathrm{ext}} + v_{\mathrm{H}} + v_{\mathrm{x}}^{\mathrm{LDA}} + v_{\mathrm{c}}^{\mathrm{LDA}} \tag{1.33}$$

and one can use the DFT self-consistent cycle described in the previous section to compute a LDA-approximate GS electronic density of an interacting system.

1.5 Merits and limits of density functional theory

Compared to the original problem of interacting electrons 1.3, the KS equation 1.15 is much easier to solve as the KS system is made of independent particles. In the case of the perfect infinite crystals studied in this thesis, the KS potential is periodic and the well-known Bloch's

theorem gives the form of the solutions:

$$\phi_{n\boldsymbol{k}}(\boldsymbol{r}) = e^{i\boldsymbol{k}\cdot\boldsymbol{r}} u_{n\boldsymbol{k}}(\boldsymbol{r}) = \sum_{\boldsymbol{K}} c_{n\boldsymbol{K}}^{\boldsymbol{k}} e^{i(\boldsymbol{k}-\boldsymbol{K})\cdot\boldsymbol{r}} \tag{1.34}$$

associated with energies $\epsilon_{n\boldsymbol{k}}$, where $u_{n\boldsymbol{k}}$ has the periodicity of the Bravais lattice of the crystal, n is a band index, $\boldsymbol{k}$ is a reciprocal space vector within the first Brillouin zone and $\boldsymbol{K}$ is a reciprocal lattice vector. This leads to tractable computations on modern computers, even for quite large unit cells such as the one of $Nd_2Fe_{14}B$ (68 atoms) studied in chapter 6 for example.

Furthermore, the framework can be extended to account for spin polarization [von Barth and Hedin, 1972, Rajagopal and Callaway, 1973]. The energy becomes a functional of the spin densities $n_\sigma(\boldsymbol{r})$ and the KS potential becomes spin dependent, e.g.

$$v_{\mathrm{x}\uparrow}(\boldsymbol{r}) = \frac{\partial E_{\mathrm{x}}[n_\uparrow, n_\downarrow]}{\partial n_\uparrow(\boldsymbol{r})}. \tag{1.35}$$

Correspondingly, LDA is extended to LSDA (for Local Spin Density Approximation). In the following, we will use the spin-polarized formalism but keep the notation "LDA" for simplicity. Spin-orbit coupling can also be included, within the second-variational procedure [Koelling and Harmon, 1977] as implemented in WIEN2k [Blaha et al., 2018, Blaha et al., 2020] for instance (see also [Martins, 2010]).

Perhaps the greatest success of DFT (and LDA) is its ability to reproduce GS properties (such as volume or bulk moduli) and relative structural stability of numerous compounds [Jones, 2015], giving this method a significant predictive power. Furthermore, although it is a GS theory and the band structure of the KS auxiliary system given by Bloch's theorem 1.34 has no formal meaning, these KS band energies were proven to reliably reproduce experimental results for numerous compounds. Therefore, one usually speaks of DFT band structure although, technically, there is no such thing. This amounts to the following approximation

$$\hat{H}_{\mathrm{e}} \approx \hat{H}_{\mathrm{KS}} = \sum_{nn'\boldsymbol{k}\sigma} \left[H_{\mathrm{KS}}^{\boldsymbol{k}\sigma}\right]_{nn'} \hat{c}_{n\boldsymbol{k}\sigma}^\dagger \hat{c}_{n'\boldsymbol{k}\sigma} = \sum_{n\boldsymbol{k}\sigma} \epsilon_{n\boldsymbol{k}}^\sigma \hat{c}_{n\boldsymbol{k}\sigma}^\dagger \hat{c}_{n\boldsymbol{k}\sigma} \tag{1.36}$$

where $\hat{c}_{n\boldsymbol{k}\sigma}$ annihilates an electron in the KS orbital $\phi_{n\boldsymbol{k}}^\sigma$. We will also use the notation $\hat{H}_{\mathrm{LDA}} = \hat{H}_{\mathrm{KS}}$ to sometimes emphasize the fact that the local density approximation is used. DFT has now become the standard electronic structure approach for real materials.

However, the KS electronic structure within LDA also has limitations. First, it cannot properly describe many-body effects and electronic correlations as it treat the electron-electron Coulomb interaction by an effective potential in the KS equations. The LDA band structure can for instance wrongly predict a metallic behavior in strongly-correlated systems. These strong correlations can be more properly taken into account by combining LDA with the dynamical mean-field theory presented in the next chapter.

Second, the LDA band structure systematically underestimates the fundamental gap E_{g} of insulators. Indeed, it can be shown that [Perdew and Levy, 1983, Sham and Schlüter, 1983]:

$$E_{\mathrm{g}} = E_{\mathrm{g}}^{\mathrm{KS}} + \Delta_{\mathrm{xc}} \tag{1.37}$$

where $E_{\mathrm{g}}^{\mathrm{KS}}$ is the band gap given by the KS band structure. Δ_{xc} is the derivative discontinuity[2]:

$$\Delta_{\mathrm{xc}} = \lim_{\delta \to 0} \left(\frac{\partial E_{\mathrm{xc}}[n]}{\partial n(\boldsymbol{r})}\Big|_{N+\delta} - \frac{\partial E_{\mathrm{xc}}[n]}{\partial n(\boldsymbol{r})}\Big|_{N-\delta} \right) \tag{1.38}$$

where N is the number of electrons. To evaluate the fundamental gap, even if one had access to the true exchange-correlation functional, one would therefore still need to add the derivative discontinuity to the KS gap to evaluate E_{g}. Δ_{xc} can be of the same order of magnitude as $E_{\mathrm{g}}^{\mathrm{KS}}$. However, for simple local potentials like LDA, the derivative discontinuity is equal to zero so that the gap is simply evaluated as $E_{\mathrm{g}}^{\mathrm{KS}}$ and usually substantially underestimated. One way to circumvent this issue is to use the modified Becke-Johnson exchange potential described in the next section.

1.6 The modified Becke-Johnson exchange potential

Several approaches have been proposed to improve the LDA description such as the Generalized Gradient Approximation (GGA) [Perdew et al., 1996] and hybrid functionals [Becke, 1993b, Becke, 1993a]. In this section, we deal with one such approach: the modified Becke-Johnson exchange (mBJ) potential [Becke and Johnson, 2006, Tran and Blaha, 2009]. This mBJ potential will be used in chapter 7 in the framework of DFT+dynamical mean-field theory. The idea behind mBJ is that the Optimized Effective Potential (OEP) [Sharp and Horton, 1953, Talman and Shadwick, 1976] method can compute the exact exchange potential v_{x} and enhance the accuracy of the fundamental gap estimation compared to LDA (see previous section), without needing the derivative discontinuity 1.38 (the exact correlation potential must hence partially cancel out this discontinuity). However, OEP is numerically expensive. The mBJ exchange potential is by design a semi-local potential which approximates well this OEP exact exchange potential; it should hence give better gap estimation while maintaining an interesting computational cost.

More precisely, to derive mBJ, one starts with the following natural decomposition of the exchange potential by functional derivative within spin-polarized DFT (see Eq. 1.35):

$$v_{\mathrm{x}\sigma}(\boldsymbol{r}) = v_{\mathrm{x}\sigma}^{\mathrm{S}}(\boldsymbol{r}) + v_{\mathrm{x}\sigma}^{\mathrm{r}}(\boldsymbol{r}) \tag{1.39}$$

$$v_{\mathrm{x}\sigma}^{\mathrm{S}}(\boldsymbol{r}) = \int \frac{h_{\mathrm{x}\sigma}(\boldsymbol{r}, \boldsymbol{r}')}{|\boldsymbol{r} - \boldsymbol{r}'|} d^3\boldsymbol{r}' \tag{1.40}$$

[2] It is independent on $\boldsymbol{r}$.

with

$$h_{\mathrm{x}\sigma}(\boldsymbol{r},\boldsymbol{r}') = -\sum_{ij}\frac{\phi_i^*(\boldsymbol{r},\sigma)\phi_j^*(\boldsymbol{r}',\sigma)\phi_i(\boldsymbol{r}',\sigma)\phi_j(\boldsymbol{r},\sigma)}{n_\sigma(\boldsymbol{r})}. \tag{1.41}$$

$v_{\mathrm{x}\sigma}^{\mathrm{S}}$ is the Slater potential [Slater, 1951] and $v_{\mathrm{x}\sigma}^{\mathrm{r}}$ is the response potential (see for instance [Gritsenko et al., 1995]). Neglecting the latter would result in an exchange potential which wouldn't have the correct UEG limit as $v_{\mathrm{x}\sigma}^{\mathrm{S}} = \frac{3}{2}v_{\mathrm{x}\sigma}^{\mathrm{LDA}}$ in this case. [Becke and Johnson, 2006] (BJ) hence proposed the following approximation for the exchange potential:

$$v_{\mathrm{x}\sigma}^{\mathrm{BJ}} = v_{\mathrm{x}\sigma}^{\mathrm{S}} + \frac{1}{\pi}\sqrt{\frac{5}{12}}\sqrt{\frac{t_\sigma}{n_\sigma}} \tag{1.42}$$

where t_σ is the KS kinetic energy density given by

$$t_\sigma = \sum_i |\nabla\phi_{i\sigma}|^2. \tag{1.43}$$

This potential was shown to approximate well the OEP exchange potential in atoms and to give the correct UEG limit. Yet, it only gave a slightly better estimation of fundamental gaps when applied to different semiconductors [Tran et al., 2007].

[Tran and Blaha, 2009] therefore proposed to modify this BJ exchange potential in the following way:

$$v_{\mathrm{x}\sigma}^{\mathrm{mBJ}} = cv_{\mathrm{x}\sigma}^{\mathrm{BR}} + (3c-2)\frac{1}{\pi}\sqrt{\frac{5}{12}}\sqrt{\frac{t_\sigma}{n_\sigma}} \tag{1.44}$$

$$c = \alpha + \beta\left(\frac{1}{V_{\mathrm{cell}}}\int_{V_{\mathrm{cell}}}\frac{|\nabla n(\boldsymbol{r})|}{n(\boldsymbol{r})}d^3\boldsymbol{r}\right)^{1/2} \tag{1.45}$$

where $v_{\mathrm{x}\sigma}^{\mathrm{BR}}$ is the Becke-Roussel (BR) potential [Becke and Roussel, 1989]. The BR potential is, by design, a numerically cheap approximation to the Slater potential in atoms and turned out to also work well in solids. The parameters α and β in the mBJ potential were set empirically by [Tran and Blaha, 2009] by minimizing the mean absolute relative error on the band gap estimation of different semiconductors: $\alpha = -0.012$, $\beta = 1.023$ Bohr$^{\frac{1}{2}}$. In the case $c = 1$, one recovers the original BJ potential and for all values of c, the correct UEG limit is achieved. This modified Becke-Johnson (mBJ) exchange potential is usually used in conjunction with LDA for the correlation potential and has been shown to substantially increase the accuracy of fundamental gap estimations of insulators [Tran and Blaha, 2009]. However, it is a semi-empirical potential. Furthermore, it is not the derivative of an energy functional [Gaiduk and Staroverov, 2009], i.e. there is no $E_{\mathrm{x}}^{\mathrm{mBJ}}[n_\uparrow, n_\downarrow]$ such that

$$v_{\mathrm{x}\sigma}^{\mathrm{mBJ}}(\boldsymbol{r}) = \frac{\partial E_{\mathrm{x}}^{\mathrm{mBJ}}[n_\uparrow, n_\downarrow]}{\partial n_\sigma(\boldsymbol{r})}. \tag{1.46}$$

This implies that mBJ is not suitable for total energy calculation and that there is no guaranteed existence of a self-consistent solution to the KS equations with this potential.

Chapter 2

The Hubbard model and dynamical mean-field theory

In this chapter, we describe another theoretical approach to condensed matter problems: the Dynamical Mean-Field Theory (DMFT) which, contrary to DFT, can explicitly treat electronic correlations. For a general review of DMFT, the reader can refer to [Georges et al., 1996, Kotliar and Vollhardt, 2004].

2.1 The Hubbard model

While DFT was designed to tackle the general many-body problem in a solid 1.3, DMFT was made to solve a simplified version of it, called the Hubbard model (HM) [Hubbard, 1963]. It can be derived from the second quantization form of the general Hamiltonian 1.3:

$$\hat{H}_{\mathrm{e}} = -\sum_{ij\eta\beta\sigma} t^{ij}_{\eta\beta} \hat{f}^{\dagger}_{i\eta\sigma} \hat{f}_{j\beta\sigma} + \frac{1}{2} \sum_{\substack{ijj'i' \\ \eta\beta\gamma\delta\sigma\sigma'}} U^{iji'j'}_{\eta\beta\gamma\delta} \hat{f}^{\dagger}_{i\eta\sigma} \hat{f}^{\dagger}_{j\beta\sigma'} \hat{f}_{i'\delta\sigma'} \hat{f}_{j'\gamma\sigma} \tag{2.1}$$

$$t^{ij}_{\eta\beta} = -\int w^{*}_{i\eta}(\boldsymbol{r}) \Big(-\frac{\nabla^2}{2} + v_{\mathrm{ext}}(\boldsymbol{r}) \Big) w_{j\beta}(\boldsymbol{r}) d^3\boldsymbol{r} \tag{2.2}$$

$$U^{iji'j'}_{\eta\beta\gamma\delta} = \int\int w^{*}_{i\eta}(\boldsymbol{r}) w^{*}_{j\beta}(\boldsymbol{r'}) \frac{1}{|\boldsymbol{r} - \boldsymbol{r'}|} w_{j'\delta}(\boldsymbol{r'}) w_{i'\gamma}(\boldsymbol{r}) d^3\boldsymbol{r} d^3\boldsymbol{r'} \tag{2.3}$$

where the annihilation (creation) operators $\hat{f}^{(\dagger)}$ are represented in a localized orbital basis $\{w_{i\eta}\}$ indexed by the lattice site i (located at $\boldsymbol{R}_i$) and orbital character η. This localized basis can be a Wannier basis for example, as described in the following chapter. We now restrict ourselves to the site-independent, nearest-neighbor hopping, on-site Coulomb repulsion, single-orbital case.

Within the grand canonical ensemble, this Hamiltonian then becomes

$$\hat{H}_{\mathrm{HM}} = -t \sum_{\langle ij\rangle\sigma} (\hat{f}^\dagger_{i\sigma}\hat{f}_{j\sigma} + \hat{f}^\dagger_{j\sigma}\hat{f}_{i\sigma}) - \mu \sum_{i\sigma} n_{i\sigma} + U \sum_i \hat{n}_{i\uparrow}\hat{n}_{i\downarrow} \tag{2.4}$$

$$= \sum_{\boldsymbol{k}\sigma} \epsilon_{\boldsymbol{k}} \hat{f}^\dagger_{\boldsymbol{k}\sigma}\hat{f}_{\boldsymbol{k}\sigma} + \sum_i \hat{H}^{(i)}_{\mathrm{at}}, \tag{2.5}$$

where $\langle ij\rangle$ denotes a nearest-neighbor pair of sites, $t = t^{ij}$ for nearest-neighbors[1], $\hat{n}_{i\sigma} = \hat{f}^\dagger_{i\sigma}\hat{f}_{i\sigma}$ and μ is the chemical potential. The first (non-interacting) part of the Hamiltonian can be diagonalized in the Fourier space by Bloch states, as seen in section 1.5. We have hence introduced the eigenenergies indexed by the pseudo-momentum $\boldsymbol{k}$: $\epsilon_{\boldsymbol{k}} = -t\sum_{j\in N_i} e^{i\boldsymbol{k}\cdot(\boldsymbol{R}_i - \boldsymbol{R}_j)}$, where N_i is the ensemble of sites neighbor to i. We have also introduced the local atomic Hamiltonian at site i, $\hat{H}^{(i)}_{\mathrm{at}} = -\mu\sum_\sigma n_{i\sigma} + U\hat{n}_{i\uparrow}\hat{n}_{i\downarrow}$. This is the one-orbital Hubbard model Hamiltonian which describes single-orbital atoms arranged in a lattice: the electrons can hop from one site to another with amplitude t (delocalization tendency), the energy cost for double occupation of a site is U, impeding this hopping (localization tendency). The number of electrons is governed by the chemical potential μ. It hence exhibits all essential ingredients of the many-body problem on a lattice. Though simple looking, solving this Hubbard model is a theoretical challenge.

2.2 Dynamical mean-field theory

In this section, we derive the DMFT self-consistent equations [Georges and Kotliar, 1992] that can approximately solve the single-orbital Hubbard model 2.4 – more general versions will be studied in the next chapter. Inspired by [Georges, 2004], this derivation is made in analogy with DFT (described in the previous chapter) as both theories exhibit many similarities which are summarized in table 2.1.

Theory	DFT	DMFT
Observable	Local density $n(\boldsymbol{r})$	Local Green's function $G^\sigma_{ii}(z)$
Auxiliary system	Independent electrons in a potential	Quantum impurity model
Weiss field	$v_{\mathrm{KS}}(\boldsymbol{r})$	$\mathcal{G}^\sigma_0(z) = \left(G^\sigma_{\mathrm{imp}}(z)^{-1} + \Sigma^\sigma_{imp}(z)\right)^{-1}$
Representation	$n(\boldsymbol{r}) = \sum_{\sigma i} \lvert\phi_i(\boldsymbol{x})\rvert^2$	$G^\sigma_{ii}(z) = G^\sigma_{\mathrm{imp}}(z)$
Self-consistency	$v_{\mathrm{KS}}(\boldsymbol{r}) = v_{\mathrm{ext}}(\boldsymbol{r}) + \frac{\partial E_{\mathrm{Hxc}}[n]}{\partial n(\boldsymbol{r})}$	$G^\sigma_{ii}(z) = \sum_{\boldsymbol{k}} \left(z + \mu - \epsilon_{\boldsymbol{k}} - \Sigma^\sigma_{\mathrm{imp}}(z)\right)^{-1}$

Table 2.1: Comparison of DFT and DMFT. Adapted from [Georges, 2004].

Both DFT and DMFT are based on the representation of a local observable by a simpler auxiliary system. In the case of DFT, this quantity is the local density $n(\boldsymbol{r})$ (Eq. 1.5) – this choice is motivated by the HK theorems. Within DMFT, this quantity is the local Green's

[1] t^{ii} has been absorbed in the chemical potential.

function[2]

$$G^{\sigma}_{\mathrm{loc}}(z) = G^{\sigma}_{ii}(z) = \langle\langle \hat{f}_{i\sigma}, \hat{f}^{\dagger}_{i\sigma}\rangle\rangle_z \tag{2.6}$$

where i is a lattice site, z is a frequency in the complex plane. This propagator describes the local electronic dynamics, as $G^{\sigma}_{\mathrm{loc}}(\tau - \tau') = -\langle \mathcal{T} \hat{f}_{i\sigma}(\tau)\hat{f}^{\dagger}_{i\sigma}(\tau')\rangle$ in the imaginary time domain, where $\mathcal{T}$ is the time-ordered product. The motivation behind the choice of this observable in DMFT comes from the results of [Metzner and Vollhardt, 1989, Georges and Kotliar, 1992] in the infinite coordination limit which are described in section 2.6.

Within DFT, [Kohn and Sham, 1965] then suggested to represent the density $n(\boldsymbol{r})$ by a system of non-interacting electrons (Eq. 1.14) in an effective KS potential 1.16 which can be viewed as a generalized Weiss field. Within DMFT, a lattice site is represented by a quantum impurity with the same local atomic Hamiltonian $\hat{H}^{(i)}_{\mathrm{at}}$ but embedded in an effective uncorrelated bath with which it can exchange electrons. The dynamics of the electronic exchange between the impurity and the bath are encoded in the hybridization function $\Delta^{\sigma}(z)$. The latter is related to the generalized Weiss field $\mathcal{G}^{\sigma}_0(z)$, which is the bare propagator of the impurity, through

$$\mathcal{G}^{\sigma}_0(z) = \Big(z + \mu - \Delta^{\sigma}(z)\Big)^{-1}. \tag{2.7}$$

The impurity Green's function $G^{\sigma}_{\mathrm{imp}}(z)$ and self-energy $\Sigma^{\sigma}_{\mathrm{imp}}(z)$ are related via the Dyson equation

$$G^{\sigma}_{\mathrm{imp}}(z) = \Big(\mathcal{G}^{\sigma}_0(z)^{-1} - \Sigma^{\sigma}_{\mathrm{imp}}(z)\Big)^{-1}. \tag{2.8}$$

The DMFT representability assumption is then that the local Green's function of the true system is equal to the impurity Green's function

$$G^{\sigma}_{\mathrm{loc}}(z) = G^{\sigma}_{\mathrm{imp}}(z). \tag{2.9}$$

This effective quantum impurity problem can be modeled by an Anderson Impurity Model (AIM). DMFT requires to solve this impurity problem, i.e. to compute $G^{\sigma}_{\mathrm{imp}}(z)$ from $(\mathcal{G}^{\sigma}_0, U)$ or equivalently $(\Delta^{\sigma}, \hat{H}_{\mathrm{at}})$. An algorithm performing this task is called an "impurity solver". One of them is reviewed in section 2.4. We just point out here that the main gain in using this auxiliary system is that the impurity is coupled to uncorrelated bath degrees of freedom while in the original lattice problem each site is coupled to correlated orbitals. As this uncorrelated bath acts as an effective representation of the coupling of a given site with its environment (made of equivalent correlated sites), the Weiss field must be computed self-consistently.

Within DFT, the self-consistency condition, which closes the set of equation, is made of

[2]See appendix A for the Green's functions notations used in this thesis.

equations 1.16 and 1.17. Within DMFT, it is given by the following set of equations:

$$G^{\sigma}_{\mathrm{loc}}(z) = \sum_{\boldsymbol{k}} G^{\sigma}_{\boldsymbol{k}}(z) = \sum_{\boldsymbol{k}} \Big(z + \mu - \epsilon_{\boldsymbol{k}} - \Sigma^{\sigma}_{\boldsymbol{k}}(z) \Big)^{-1} \tag{2.10}$$

$$\Sigma^{\sigma}_{\boldsymbol{k}}(z) \approx \Sigma^{\sigma}_{\mathrm{imp}}(z). \tag{2.11}$$

In the first equation, we have introduced the space Fourier transform of the lattice Green's function $G^{\sigma}_{\boldsymbol{k}}(z)$ and of the lattice self-energy $\Sigma^{\sigma}_{\boldsymbol{k}}(z)$. The second equation, called the DMFT approximation, neglects all spatial dependency of the lattice self-energy and approximate the latter by the impurity self-energy. In real space, it is written $\Sigma^{\sigma}_{ij} = \Sigma^{\sigma}_{\mathrm{imp}} \delta_{ij}$. DMFT is then indeed a (spatial) mean-field theory. However, it keeps the full temporal structure (i.e. z dependency) of the observable, hence the adjective "dynamical". It allows DMFT to keep track of quantum fluctuations due to local correlations.

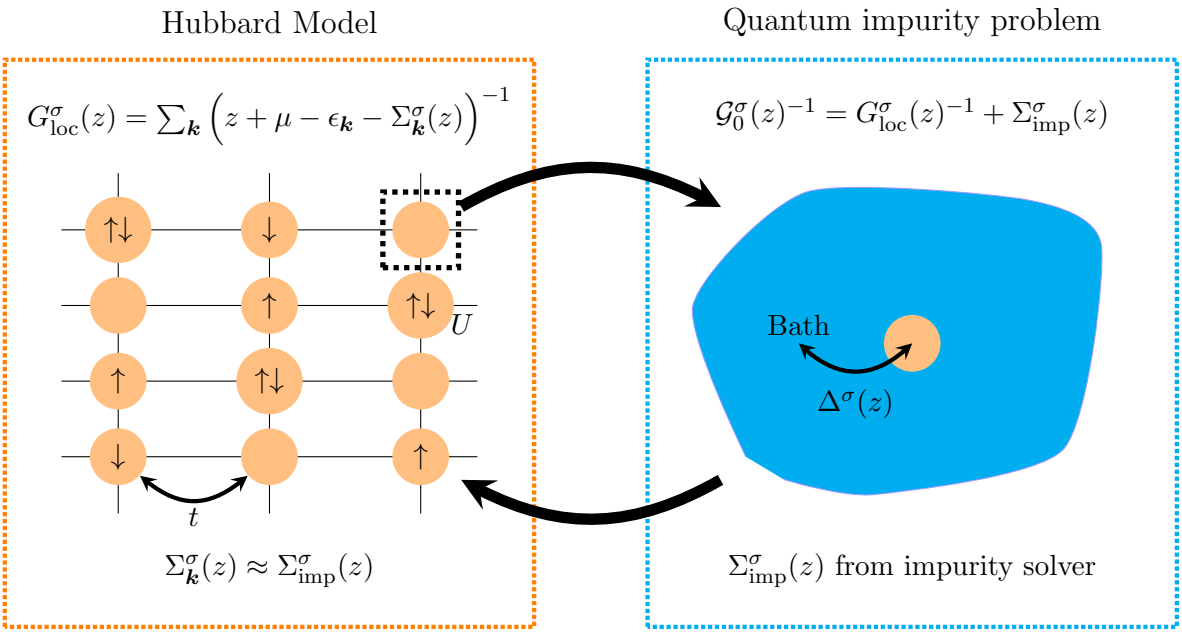

Figure 2.1: DMFT cycle.

Similary to DFT, the DMFT self-consistent algorithm as illustrated in figure 2.1 is:

1. **Initialize the observable.** The impurity self-energy is typically initialized as $\Sigma^{\sigma}_{\mathrm{imp}}(z) = 0$ and accordingly the local Green's function as $G^{\sigma}_{\mathrm{loc}}(z) = \sum_{\boldsymbol{k}} \Big(z + \mu - \epsilon_{\boldsymbol{k}} \Big)^{-1}$.

2. **From the observable, compute the Weiss field.** With the representability assumption 2.9, extract $\mathcal{G}^{\sigma}_{0}(z)$ from $\Sigma^{\sigma}_{\mathrm{imp}}(z)$ and $G^{\sigma}_{\mathrm{loc}}(z)$ thanks to the Dyson equation 2.8.

3. **Solve the auxiliary problem defined by the Weiss field.** Solve the impurity problem defined by the Weiss field and the local Coulomb interaction to get $G^{\sigma}_{\mathrm{imp}}(z)$.

4. **Using the representability assumption, compute the observable.** Extract $\Sigma^{\sigma}_{\mathrm{imp}}(z)$

by using the Dyson equation 2.8, then make the DMFT approximation 2.11 and compute $G^{\sigma}_{\mathrm{loc}}(z)$ thanks to equation 2.10.

5. **Iterate until steps 2-4 until self-consistency of the observable is reached.** The self-consistency is checked on $G^{\sigma}_{\mathrm{loc}}(z)$ and $\Sigma^{\sigma}_{\mathrm{imp}}(z)$. The converged $\Sigma^{\sigma}_{\mathrm{imp}}(z)$ can then be injected in the lattice Green's function thanks to the DMFT approximation 2.11 to extract lattice quantities.

While the DFT and DMFT algorithm are similar formally, their approach to the quantum many-body problem is opposite: the DFT auxiliary system is a Fermi gas while the DMFT one is a correlated atomic problem in a non-interacting gas. This allows the latter to capture strong correlation effects and new physics that are briefly explored in the last section of this chapter. Before this, we give in the next three sections some details on the auxiliary quantum impurity problem and how to solve it.

2.3 The Anderson impurity model

The impurity model which serves as an auxiliary system for DMFT can be modeled by an Anderson Impurity Model (AIM) [Anderson, 1961], presented here in its general multiorbital form for the sake of generality:

$$\hat{H}_{\mathrm{AIM}} = \hat{H}_f + \hat{H}_c + \hat{H}_{fc} \tag{2.12}$$

$$\hat{H}_f = \hat{H}_{1\mathrm{el}} + \hat{H}_U = \sum_{uv} \epsilon_{uv} \hat{f}^{\dagger}_u \hat{f}_v + \frac{1}{2} \sum_{uvu'v'} U_{uvu'v'} \hat{f}^{\dagger}_u \hat{f}^{\dagger}_v \hat{f}_{v'} \hat{f}_{u'} \tag{2.13}$$

$$\hat{H}_c = \sum_a e_a \hat{c}^{\dagger}_a \hat{c}_a \tag{2.14}$$

$$\hat{H}_{fc} = \sum_{ua} (V^*_{au} \hat{f}^{\dagger}_u \hat{c}_a + V_{au} \hat{c}^{\dagger}_a \hat{f}_u). \tag{2.15}$$

where $\hat{c}_a$ is the annihilation operator of an electron in the bath state a of energy e_a and V_{au} is the hopping between impurity (orbital, spin) state u and bath state a. $\hat{H}_f$ is the local impurity Hamiltonian which, in the context of DMFT, is taken as the local Hamiltonian of a given site $\hat{H}_f = \hat{H}^{(i)}_{\mathrm{at}}$. $\hat{H}_c$ is the Hamiltonian describing the degrees of freedom of the effective bath, coupled to the impurity via $\hat{H}_{fc}$. One can show that the bare propagator of the AIM is given by

$$\mathcal{G}_0^{-1}(z) = z\mathbb{I} - \epsilon - \Delta(z). \tag{2.16}$$

The matrix ϵ of impurity non-interacting level positions is defined in equation 2.13, $\mathbb{I}$ is the identity matrix and

$$\Delta_{uv}(z) = \sum_a \frac{V^*_{au} V_{av}}{z - e_a}. \tag{2.17}$$

The hybridization function Δ contains all the relevant information about the bath: the precise values of V_{ua} and e_a are theoretically not needed, but some approaches to solve the AIM (i.e.

compute G_{imp}) still need to actually fit in practice the input hybridization in the form 2.17. The strength of DMFT is that, like DFT, the auxiliary problem is simpler than the original one. This AIM can indeed be solved exactly, for instance with a continuous-time quantum Monte-Carlo algorithm which we briefly describe in the next section.

2.4 Solving the impurity problem: continuous-time quantum Monte-Carlo

Continuous-Time Quantum Monte-Carlo (CTQMC) is one of so-called "impurity solvers" of the Anderson impurity problem. The general idea behind it is to separate the impurity Hamiltonian in two parts, consider the interaction picture with respect to the first part and expand with respect to the second thanks to standard perturbation theory techniques in the Matsubara formalism:

$$\hat{H}_{\text{AIM}} = \hat{H}_0 + \hat{H}_1 \tag{2.18}$$

$$\text{Tr}\Big\{e^{-\beta\hat{H}_{\text{AIM}}}\mathcal{T}\hat{A}(\tau)\hat{B}(\tau')\Big\} = \text{Tr}\Big\{e^{-\beta\hat{H}_0}\mathcal{T}e^{-\int_0^\beta \hat{H}_1^I(\tau'')d\tau''}\hat{A}^I(\tau)\hat{B}^I(\tau')\Big\} \tag{2.19}$$

$$= \sum_n \frac{(-1)^n}{n!}\int_0^\beta d\tau_1 ... \int_0^\beta d\tau_n \,\text{Tr}\Big\{e^{-\beta\hat{H}_0}\mathcal{T}\hat{H}_1^I(\tau_1)...\hat{H}_1^I(\tau_n)\hat{A}^I(\tau)\hat{B}^I(\tau')\Big\} \tag{2.20}$$

where we have introduced imaginary times τ, the time-ordered product $\mathcal{T}$, two arbitrary operators in the Heisenberg representation $\hat{A}(\tau)$ and $\hat{B}(\tau')$ and the interaction picture with respect to $\hat{H}_1$ symbolized by the superscript I. Using this perturbation, the impurity Green's function

$$\big[G_{\text{imp}}(\tau)\big]_{uv} = -\frac{\text{Tr}\Big\{e^{-\beta\hat{H}_{\text{AIM}}}\mathcal{T}\hat{f}_u(\tau)\hat{f}_v^\dagger(0)\Big\}}{\text{Tr}\Big\{e^{-\beta\hat{H}_{\text{AIM}}}\Big\}} \tag{2.21}$$

is then usually expressed as

$$\big[G_{\text{imp}}(\tau)\big]_{uv} = \frac{\sum_{\mathcal{C}} w(\mathcal{C})g_{uv}(\mathcal{C},\tau)}{\sum_{\mathcal{C}} w(\mathcal{C})} \tag{2.22}$$

where C are some configurations. CTQMC comes in different flavors depending on the choice of this perturbation expansion: the auxiliary-field formulation [Gull et al., 2008], the interaction expansion [Rubtsov et al., 2005] and the hybridization expansion [Werner et al., 2006]. In this

thesis, we will use the latter in which:

$$\hat{H}_0 = \hat{H}_f + \hat{H}_c \tag{2.23}$$

$$\mathcal{C} = (n, \{u_i, v_i, \tau_i, \tau_i'\}_{i\in[\![1,n]\!]}) \tag{2.24}$$

$$w(\mathcal{C}) = \det_{1\leq i,j\leq n}[M^{-1}]_{ij}\,\mathrm{Tr}\left\{\mathcal{T}e^{-\beta\hat{H}_f}\prod_{i=1}^{n}(f_{u_i}^I)^\dagger(\tau_i)f_{v_i}^I(\tau_i')\right\} \tag{2.25}$$

$$g_{uv}(\mathcal{C},\tau) = \frac{-1}{\beta}\sum_{1\leq i,j\leq n} M_{ij}\delta(\tau_i - \tau_j' + \tau)\delta_{u_i,u}\delta_{v_i,v} \tag{2.26}$$

$$[M^{-1}]_{ij} = \Delta_{u_i v_j}(\tau_i - \tau_j'). \tag{2.27}$$

One would naturally like to consider $\{w(\mathcal{C})\}$ as Monte-Carlo weights but they can be negative because of the fermionic nature of the problem. Hence, one must take their absolute values and include the oscillating part into the observable, leading to:

$$G_{\mathrm{imp}}(\tau) = \frac{\sum_{\mathcal{C}}|w(\mathcal{C})|s_{\mathcal{C}}g(\mathcal{C},\tau)}{\sum_{\mathcal{C}}|w(\mathcal{C})|s_{\mathcal{C}}} \tag{2.28}$$

where $s_{\mathcal{C}}$ is the sign of $w(\mathcal{C})$. Now that $|w(\mathcal{C})|$ are positive, one can sample the configuration $\mathcal{C}$ with a probability density function $|w(\mathcal{C})|$ (thanks to a Metropolis-Hastings algorithm [Metropolis et al., 1953, Hastings, 1970]) and approximate, thanks to the central limit theorem for a large enough sample size N:

$$G_{\mathrm{imp}}(\tau) \approx \frac{\sum_{i=1}^{N} s_{\mathcal{C}_i}g(\mathcal{C}_i,\tau)}{\sum_{i=1}^{N} s_{\mathcal{C}_i}}. \tag{2.29}$$

One can then Fourier transform this equation to get the impurity Green's function on the imaginary frequency axis. Although the results are in principle numerically exact, if the average sign $\sum_i^N s_{\mathcal{C}_i}$ deviates significantly from 1 and becomes close to 0, the algorithm faces the so-called fermionic sign problem: $G_{\mathrm{imp}}(\tau)$ will be computed as a sum of large components with different signs leading to a small value due to mutual cancellation. Without sufficient sampling, the noise will hence be larger than the actual value of $G_{\mathrm{imp}}(\tau)$. In the cases where the needed sampling is unattainable (typically at low temperature and for large systems), the CTQMC algorithm becomes unusable. For a general review of CTQMC, the reader can refer to [Gull et al., 2011].

2.5 Analytic Continuation

As the CTQMC formalism works only on the imaginary axis, one needs to perform some post-processing to extract real frequency quantities of interest like the local spectral function

$$A_\sigma(\omega) = -\frac{1}{\pi} \operatorname{Im} G^\sigma_{\mathrm{loc}}(\omega + i0^+). \tag{2.30}$$

This extraction is possible because Green's functions are analytic on the complex plane except the real axis and one can write:

$$G^\sigma_{\mathrm{loc}}(z) = \int_{-\infty}^{+\infty} \frac{A_\sigma(\omega)}{z - \omega} d\omega \quad \forall z \in \mathbb{C}\backslash\mathbb{R}. \tag{2.31}$$

For the special cases $z = i\omega_n$, on a discretized real-frequency grid $\{\omega_m\}$ for computer implementation, we get the following matrix equation:

$$\boldsymbol{G} = K\boldsymbol{A} \tag{2.32}$$

$$\boldsymbol{G}_n = G^\sigma_{\mathrm{loc}}(i\omega_n) \tag{2.33}$$

$$\boldsymbol{A}_m = A_\sigma(\omega_m) \tag{2.34}$$

$$K_{nm} = \frac{\omega_{m+1} - \omega_m}{i\omega_n - \omega_m}. \tag{2.35}$$

Hence, formally, because of analytic properties, knowing the value of the Green's function on the imaginary axis allows the calculation of the spectral function (defined on the real axis) by inverting equation 2.32. This procedure is therefore called analytic continuation. The issue however is that the pseudo-inverse K^{-1} is ill-defined as the matrix elements of K decay quickly with n and m. Hence, a small numerical noise in $\boldsymbol{G}$ will lead to an uncontrollable error on the computed spectral function. Because noise is inherent to the CTQMC approach (which is stochastic in nature), this straightforward inversion is numerically impossible in this case. Several analytic continuation schemes have been developed such as the Padé approximation [Padé, 1892], the stochastic analytic continuation [Sandvik, 1998], the Nevanlinna/Carathéodory formalism [Fei et al., 2021a, Fei et al., 2021b] or the Maximum Entropy (MaxEnt) method [Jarrell and Gubernatis, 1996]. The latter will be used in this thesis [Kraberger et al., 2017]. While it is especially adapted for noisy CTQMC data, MaxEnt can however wash away some complicated spectral structure and sometimes it can be hard to distinguish real physical features from numerical artefacts, as we will see in chapter 7.

2.6 Merits of dynamical mean-field theory

Although DMFT is, in general, an approximated method, it is exact in a number of limits:

- **Infinite coordination limit.** It has been shown that, in this limit, with proper scaling of the parameters with the dimensionality, the lattice self-energy is indeed local and that the DMFT scheme is exact [Metzner and Vollhardt, 1989, Georges and Kotliar, 1992].

- $U = 0$**, i.e. itinerant limit.** In this case, one recovers the traditional band theory evoked in the previous chapter and since $\Sigma = \Sigma_{\text{imp}} = 0$, the DMFT approximation 2.11 is trivially exact. The Hamiltonian is diagonal in the Fourier space and electrons are completely delocalized. At zero temperature and half-filling $\mu = 0$, the local spectral function is given by $A_\sigma(\omega) = \sum_{\boldsymbol{k}} \delta(\omega - \epsilon_{\boldsymbol{k}})$, i.e. a band centered at the Fermi level which can contain 2 electrons (spin degeneracy included), and the system is metallic.

- $t = 0$**, i.e. atomic limit.** In this case, the system is a collection of independent atomic problems, $\Delta^\sigma(z) = 0$ and $\Sigma^\sigma_{ij} = \Sigma^\sigma_{\text{imp}}\delta_{ij}$ by construction. The Hamiltonian is diagonal in the real space and the electrons are completely localized. At zero temperature and half-filling $\mu = U/2$, the spectral function is given by $A_\sigma(\omega) = \frac{1}{2}\delta(\omega + U/2) + \frac{1}{2}\delta(\omega - U/2)$, i.e. two Hubbard bands, separated by a gap of size U, which can each contain 1 electron (spin degeneracy included), and the system is insulating.

It is hence reasonable to assume that DMFT interpolates well between the $t = 0$ and $U = 0$ limits, especially in high dimensions. For a finite U/t ratio, there is a competition between the itinerant and localized tendencies which DMFT was shown to capture (see Fig. 8.2 for instance). Indeed, in the half-filled case ($\mu = U/2$), increasing gradually U from the Fermi gas limit $U = 0$, the quasiparticle peak at the Fermi energy narrows, because hopping is impeded due to the double occupancy energy cost U, while the Hubbard bands appears. Quasiparticles now have a finite lifetime (when they are not exactly at the Fermi energy or if the system is at finite temperature) encoded by the imaginary part of the self-energy on the real axis. At higher values of the ratio U/t, the system undergoes a Mott-insulating transition: the quasiparticle peak disappears and only the lower and upper Hubbard bands remain, there is no spectral weight at the Fermi level. The system is insulating. This Mott insulating state is driven by the strong electronic correlations and is hence different from a usual band insulator.

Chapter 3

The LDA+DMFT approach to strongly correlated materials

As seen in the first chapter of this thesis, LDA is applicable to real materials but fails to capture the physics of strong correlations. On the other hand, in the second chapter, DMFT was shown to properly treat local correlations but was only applied to the Hubbard model. In this chapter, we explain how both aforementioned methods can be combined together to treat strong local correlations in real materials. For general reviews on this combined LDA+DMFT approach, the reader can refer to [Georges, 2004, Kotliar et al., 2006, Biermann, 2014, Pavarini, 2014].

3.1 Combining LDA and explicit local Coulomb interactions

The starting point of LDA+DMFT is the addition of the local Coulomb interaction to the LDA KS Hamiltonian $\hat{H}_{\text{KS}}$ defined in equation 1.36 with the following approximation for the general Hamiltonian $\hat{H}_{\text{e}}$ (Eq. 1.2):

$$\begin{aligned} \hat{H}_{\text{e}} &= \hat{K} + \hat{V}_{\text{ext}} + \hat{U} && (3.1)\\ &= \hat{H}_{\text{KS}} + \hat{U} - (\hat{H}^{\text{KS}} - \hat{K} - \hat{V}_{\text{ext}}) && (3.2)\\ &\approx \hat{H}_{\text{KS}} + (\hat{U} - \hat{H}_{\text{DC}}) && (3.3) \end{aligned}$$

where $\hat{H}_{\text{DC}}$ is the double counting correction substracting from $\hat{U}$ the Coulomb interaction effects already described by LDA (Hartree-exchange-correlation) and $(\hat{U} - \hat{H}_{\text{DC}})$ is assumed to be local. The construction of the localized orbitals and the double-counting correction $\hat{H}_{\text{DC}}$ are described in sections 3.2 and 3.4 respectively.

As seen in the first chapter, LDA is a good approximation in various systems for which $(\hat{U} - \hat{H}_{\text{DC}})$ can simply be neglected – i.e. plain DFT can be used. In so-called strongly correlates compounds however, neglecting $(\hat{U} - \hat{H}_{\text{DC}})$ usually leads to qualitatively wrong results – computed metallic phase instead of experimental insulating state for instance. Yet, even in these cases, only a few shells exhibit strong correlations, the (partially filled) localized ones, like

the $3ds$ and $4fs$. The Coulomb interaction between electrons in these shells is indeed at least comparable to the hybridization with neighboring atoms.

Hence, in strongly correlated materials, orbitals are separated into two categories: correlated and uncorrelated; $(\hat{U} - \hat{H}_{\mathrm{DC}})$ being neglected in the latter. The LDA+DMFT Hamiltonian 3.3 is then further approximated as:

$$\hat{H}_{\mathrm{e}} \approx \hat{H}_{\mathrm{KS}} + (\hat{U}^{\mathrm{c}} - \hat{H}^{\mathrm{c}}_{\mathrm{DC}}) \tag{3.4}$$

$$\approx \hat{H}_{\mathrm{KS}} + \sum_{\alpha l}^{\mathrm{corr.}} \left(\hat{H}^{\alpha l}_{U} - \hat{H}^{\alpha l}_{\mathrm{DC}} \right) \tag{3.5}$$

$$\approx \sum_{n\boldsymbol{k}\sigma} \epsilon^{\sigma}_{n\boldsymbol{k}} \hat{c}^{\dagger}_{n\boldsymbol{k}\sigma} \hat{c}_{n\boldsymbol{k}\sigma} + \sum_{\alpha l}^{\mathrm{corr.}} \left(\frac{1}{2} \sum_{\substack{\sigma\sigma' \\ mm'm''m'''}} U^{\alpha l}_{mm'm''m'''} \hat{f}^{\dagger}_{\alpha lm\sigma} \hat{f}^{\dagger}_{\alpha lm'\sigma'} \hat{f}_{\alpha lm'''\sigma'} \hat{f}_{\alpha lm''\sigma} \right.$$
$$\left. - \sum_{mm'\sigma\sigma'} \left[\Sigma^{\alpha l}_{\mathrm{DC}}\right]^{\sigma\sigma'}_{mm'} \hat{f}^{\dagger}_{\alpha lm\sigma} \hat{f}_{\alpha lm'\sigma'} \right) \tag{3.6}$$

where $\hat{U}^{\mathrm{c}} - \hat{H}^{\mathrm{c}}_{\mathrm{DC}}$ is the truncation of $\hat{U} - \hat{H}^{\mathrm{DC}}$ to the correlated subspace, α denotes a correlated site and $\hat{f}_{\alpha lm\sigma}$ destroys an electron in the correlated localized (orbital, spin) state (l, m, σ). This truncation procedure assumes that the effect of the other orbitals can be described by a simple screening of the local Coulomb interaction in the correlated subspace. Generally, the screened Coulomb interaction will acquire frequency dependence approaching to the bare unscreened value at high frequencies (see [Casula et al., 2012] for example); in practical applications of the LDA+DMFT approach one almost always employs the static limit of screened U. Hence, $U^{\alpha l}$ denotes here the screened Coulomb interaction (as opposed to the bare Coulomb tensor defined in Eq. 2.3). It is discussed in section 3.3.

3.2 Wannier functions

As seen in the previous section, LDA+DMFT requires the definition of local bases in real materials. Many different methods to construct these have been proposed, based for instance on Linear Muffin-tin Orbitals (LMTOs) [Andersen, 1975, Anisimov et al., 1997b, Lichtenstein and Katsnelson, 1998], Nth-Order Muffin-Tin Orbitals NMTOs [Andersen and Saha-Dasgupta, 2000, Pavarini et al., 2004] or maximally localized Wannier functions [Marzari and Vanderbilt, 1997, Lechermann et al., 2006]. In this thesis, we will use the method of [Anisimov et al., 2005, Amadon et al., 2008, Aichhorn et al., 2009] to generate Wannier functions, in particular the implementation of [Aichhorn et al., 2009] in the context of Full-potential Linearized Augmented Plane Wave (FLAPW) DFT which is derived below. FLAPW is based on the decomposition of the real space in spheres around nuclei, called muffin-tin spheres, and an interstitial region. For a general introduction to FLAPW DFT, the reader can refer to [Cottenier, 2013].

Let us consider the correlated shell l of the correlated atom α and the local atomic orbital

which is typically used within the FLAPW framework:

$$|\psi_{lm}^{\alpha\sigma}\rangle = |R_l^{\alpha\sigma}(E_{1l}^{\alpha})Y_l^m\rangle \tag{3.7}$$

where m is the orbital index, $R_l^{\alpha\sigma}(E_{1l}^{\alpha})$ and Y_l^m are the radial and spherical parts respectively of the solution of the Schrödinger equation in the muffin-tin sphere for the free atom α, at linearization energy E_{1l}^{α} (see [Cottenier, 2013]). These localized functions defined only in the atomic spheres do not form a complete basis set (the interstitial region is missing) but they can be expanded in the KS basis $\{\phi_{n\boldsymbol{k}}^{\sigma}\}$:

$$|\psi_{lm}^{\alpha\sigma}\rangle = \sum_{n\boldsymbol{k}} \langle\phi_{n\boldsymbol{k}}^{\sigma}|\psi_{lm}^{\alpha\sigma}\rangle\,|\phi_{n\boldsymbol{k}}^{\sigma}\rangle\,. \tag{3.8}$$

This infinite sum is usually truncated to a window of bands $\mathcal{W}$:

$$|\tilde{w}_{lm}^{\alpha\sigma}\rangle = \sum_{n\in\mathcal{W},\boldsymbol{k}} \left\langle\phi_{n\boldsymbol{k}}^{\sigma}\middle|\psi_{lm}^{\alpha,\sigma}\right\rangle|\phi_{n\boldsymbol{k}}^{\sigma}\rangle \tag{3.9}$$

$$= \sum_{n\in\mathcal{W},\boldsymbol{k}} \left[\widetilde{P}_{\boldsymbol{k}}^{\alpha l\sigma}\right]_{mn}|\phi_{n\boldsymbol{k}}^{\sigma}\rangle \tag{3.10}$$

where we have defined temporary projectors $\left[\widetilde{P}_{\boldsymbol{k}}^{\alpha l\sigma}\right]_{mn}$. Due to the truncation, the temporary correlated local orbitals $\{\tilde{w}_{lm}^{\alpha\sigma}\}$ are not orthonormal. After an orthonomalization procedure, the final Wannier functions and projectors are given by:

$$|w_{lm}^{\alpha\sigma}\rangle = \sum_{\boldsymbol{k}}|w_{lm\boldsymbol{k}}^{\alpha\sigma}\rangle = \sum_{n\in\mathcal{W},\boldsymbol{k}}\left[P_{\boldsymbol{k}}^{\alpha l\sigma}\right]_{mn}|\phi_{n\boldsymbol{k}}^{\sigma}\rangle \tag{3.11}$$

$$\left[P_{\boldsymbol{k}}^{\alpha l\sigma}\right]_{mn} = \sum_{\alpha' m'}\left[O(\boldsymbol{k},\sigma)^{-\frac{1}{2}}\right]_{mm'}^{\alpha\alpha'}\left[\widetilde{P}_{\boldsymbol{k}}^{\alpha l\sigma}\right]_{m'n} \tag{3.12}$$

$$\left[O(\boldsymbol{k},\sigma)\right]_{mm'}^{\alpha\alpha'} = \sum_{n\in\mathcal{W}}\left[\widetilde{P}_{\boldsymbol{k}}^{\alpha l\sigma}\right]_{mn}\left[\widetilde{P}_{\boldsymbol{k}}^{\alpha' l\sigma}\right]_{m'n}^{*} \tag{3.13}$$

where we have introduced the overlap matrix $O(\boldsymbol{k},\sigma)$. The projectors $P_{\boldsymbol{k}}^{\alpha l\sigma}$, which decompose the Wannier functions in the Bloch space, are matrices of the form $(2l+1)\times N_{\mathcal{W}}(\boldsymbol{k})$ where $N_{\mathcal{W}}(\boldsymbol{k})$ is the number of bands in the energy window $\mathcal{W}$ at $\boldsymbol{k}$. The window should at least enclose the $2(2l+1)$ KS bands (in the case of spin-polarized DFT) which exhibit the highest correlated orbital character. The projectors are unitary if ones chooses $N_{\mathcal{W}}(\boldsymbol{k}) = 2(2l+1)$, typically for well isolated correlated bands in insulators; they are only semi-unitary otherwise, typically in metals. The precise choice of the window remains, however, a parameter of the calculation.

To understand the physical meaning of $\mathcal{W}$, let us rewrite equation 3.9 as

$$|\tilde{w}_{lm}^{\alpha\sigma}\rangle = |\psi_{lm}^{\alpha\sigma}\rangle - \sum_{n\notin\mathcal{W},\boldsymbol{k}}\langle\phi_{n\boldsymbol{k}}^{\sigma}|\psi_{lm}^{\alpha\sigma}\rangle\,|\phi_{n\boldsymbol{k}}^{\sigma}\rangle\,. \tag{3.14}$$

A large window gives Wannier functions which are very close to the initial localized functions 3.7 as the second term in the right-hand side of equation 3.14 becomes negligible. A small window gives Wannier functions which are less localized and can exhibit some leakage to the neighboring sites due to hybridization, if $\langle \phi^{\sigma}_{n\boldsymbol{k}} | \psi^{\alpha\sigma}_{lm} \rangle$ is not negligible for some $n \notin \mathcal{W}$ (see for instance Fig. 5.6).

In this thesis, the above-introduced Wannier functions define the basis in which the local Coulomb interaction for correlated shells is written in equation 3.6 and the projectors $\left[P^{\alpha l\sigma}_{\boldsymbol{k}}\right]_{mn}$ allow to go from the local correlated subspace to the lattice space and back by the following operations:

- **Downfolding.** A quantity $Q^{\boldsymbol{k}}_{\mathrm{KS}}$ defined in the Bloch space can be projected onto the local correlated space (atom α, shell l, spin σ) by the operation $P^{\alpha l\sigma}_{\boldsymbol{k}} Q^{\boldsymbol{k}}_{\mathrm{KS}} \left[P^{\alpha l\sigma}_{\boldsymbol{k}}\right]^{\dagger}$ which is called downfolding.
- **Upfolding.** A quantity $Q^{\sigma}_{\alpha l}$ defined in the correlated subspace can be brought back to the Bloch space by the operation $\left[P^{\alpha l\sigma}_{\boldsymbol{k}}\right]^{\dagger} Q^{\sigma}_{\alpha l} P^{\alpha l\sigma}_{\boldsymbol{k}}$ which is called upfolding.

Notice that since the projection is not unitary in general, upfolding a downfolded quantity does not retrieve the original quantity – some information is lost in the process. Spin-orbit coupling can also naturally be included in this framework, as done in [Martins, 2010].

3.3 Slater parametrization of the Coulomb interaction

Let us consider a correlated shell l of an atom α – we will drop the indices α and l in this section for clarity. The screened Coulomb tensor U defining $\hat{H}_U$ in the LDA+DMFT Hamiltonian 3.6 is assumed to have the same shape as the bare local Coulomb tensor (see Eq. 2.3). Furthermore, we assume that the Wannier orbitals defining the correlated subspace, which are well localized, are close to the atomic ones and can be decomposed as $R_l(r)Y_l^m(\boldsymbol{\Omega})$ where $(r, \boldsymbol{\Omega}) = (r, \theta, \phi)$ are the spherical coordinates of $\boldsymbol{r}$, R_l is the radial part and $\{Y_l^m\}$ are the spherical harmonics. Then, the screened Coulomb tensor can be written as

$$U_{mm'm''m'''} = \int\int |R_l(r)|^2 |R_l(r')|^2 Y_l^{m*}(\boldsymbol{\Omega}) Y_l^{m'*}(\boldsymbol{\Omega}') \frac{1}{|\boldsymbol{r} - \boldsymbol{r}'|} Y_l^{m'''}(\boldsymbol{\Omega}') Y_l^{m''}(\boldsymbol{\Omega}) d^3\boldsymbol{r} d^3\boldsymbol{r}'. \quad (3.15)$$

Using the decomposition

$$\frac{1}{|\boldsymbol{r} - \boldsymbol{r}'|} = \sum_{k=0}^{\infty} \frac{r_<^k}{r_>^{k+1}} \frac{4\pi}{2k+1} \sum_{q=-k}^{k} Y_k^q(\boldsymbol{\Omega}') Y_k^{q*}(\boldsymbol{\Omega}) \quad (3.16)$$

where $r_< = \min(r, r')$, $r_> = \max(r, r')$, one can show that:

$$U_{mm'm''m'''} = \sum_{k=0}^{2l} \alpha_k(m, m'', m', m''') F^k \quad (3.17)$$

where $\alpha_k(m, m'', m', m''')$ are the Racah-Wigner parameters containing the integrals over the angular part and F^k are effective Slater integrals [Slater, 1960]. Only even k contribute and the ratios between the Slater integrals are usually approximated by the atomic ones [Anisimov et al., 1993]:

$$F^4/F^2 \approx 0.625 \text{ in } 3d \text{ shells} \tag{3.18}$$

$$F^4/F^2 \approx 0.67 \text{ and } F^6/F^4 \approx 0.49 \text{ in } 4f \text{ shells.} \tag{3.19}$$

The Coulomb interaction can then be entirely parametrized by the Hubbard interaction U and Hund's coupling J defined by (see [Anisimov et al., 1993, Vaugier, 2011])

$$U = F_0 \tag{3.20}$$

$$J = \begin{cases} \frac{F^2+F^4}{14} & \text{in } 3d \text{ shells} \\ \frac{286F^2+195F^4+250F^6}{6435} & \text{in } 4f \text{ shells} \end{cases} \tag{3.21}$$

The defining parameters U and J are reduced due to screening compared to the bare local Coulomb interaction. The estimation of these screened parameters is a theoretical challenge, but some approximate approaches exist such as the constrained Local Density Approximation (cLDA) [Gunnarsson et al., 1989, Anisimov et al., 1991, Cococcioni and de Gironcoli, 2005, Belozerov and Anisimov, 2014], the constrained Random Phase Approximation (cRPA) [Aryasetiawan et al., 2004, Aryasetiawan et al., 2006, Miyake et al., 2009, Miyake et al.,] and the constrained LDA+HI (cLDA+HI) approach [Galler and Pourovskii, 2022, Galler et al., 2021a, Boust et al., 2022a]. The latter is discussed in section 3.7.

To reduce the computational cost (in a CTQMC solver of the Anderson impurity model for instance), the screened Coulomb tensor is sometimes restricted to its density-density form, which conserves all orbital occupancies $n_{m\sigma} = \langle \hat{n}_{m\sigma} \rangle = \left\langle \hat{f}^\dagger_{m\sigma} \hat{f}_{m\sigma} \right\rangle$:

$$\hat{H}_U^{\text{dd}} = \frac{1}{2} \sum_{mm'\sigma} U_{mm'} \hat{n}_{m\sigma} \hat{n}_{m'\bar{\sigma}} + \frac{1}{2} \sum_{m \neq m'\sigma} (U_{mm'} - J_{mm'}) \hat{n}_{m\sigma} \hat{n}_{m'\sigma} \tag{3.22}$$

where

$$U_{mm'} = U_{mm'mm'} \tag{3.23}$$

$$J_{mm'} = U_{mm'm'm}. \tag{3.24}$$

Unlike the full Coulomb interaction defined in equation 3.6, this form breaks rotationnal symmetry. Here, we have introduced the notation $\bar{\sigma} = -\sigma$.

3.4 The double counting correction

The role of the correction $\hat{H}^{\text{c}}_{\text{DC}}$ is to avoid the double counting (DC) of the screened local Coulomb interaction in equation 3.4 as it is explicitly treated by $\hat{U}^{\text{c}}$ and also partially contained

in $\hat{H}_{\mathrm{KS}}$. However, the contribution of this interaction to the latter is not known so that one cannot derive an exact expression for the DC. Different approximate expressions have hence been proposed which we briefly review below. We focus on one site and one shell; we hence drop the atom index α and the shell index l.

Let us assume that the screened local Coulomb interaction has an Hartree-Fock like density-density contribution to the total energy functional, i.e.

$$E_{\mathrm{DC}} = \frac{1}{2}\sum_{mm'\sigma} U_{mm'} n_{m\sigma} n_{m'\bar{\sigma}} + \frac{1}{2}\sum_{m\neq m'\sigma} (U_{mm'} - J_{mm'}) n_{m\sigma} n_{m'\sigma}. \tag{3.25}$$

With the spherical average approximations $U_{mm'} \approx U$ and $J_{mm'} \approx J$, it yields

$$E_{DC} = \frac{1}{2}U \sum_{mm'\sigma} n_{m\sigma} n_{m'\bar{\sigma}} + \frac{1}{2}(U-J) \sum_{m\neq m'\sigma} n_{m\sigma} n_{m'\sigma} \tag{3.26}$$

$$= \frac{1}{2}U \sum_{\sigma} N_\sigma N_{\bar{\sigma}} + \frac{1}{2}(U-J) \sum_{\sigma} (N_\sigma^2 - \sum_m n_{m\sigma}^2). \tag{3.27}$$

At this point, one can define two different DC schemes:

- **The Fully Localized Limit (FLL).** In this approximation [Anisimov et al., 1993], LDA is assumed to give an atomic like contribution, i.e. the occupation numbers $n_{m\sigma}$ are 0 or 1 and hence $n_{m\sigma}^2 = n_{m\sigma}$. This gives, with $N = \sum_\sigma N_\sigma = \sum_\sigma \sum_m n_{m\sigma}$,

  $$E_{\mathrm{DC}}^{\mathrm{FLL}} = \frac{1}{2}UN(N-1) - \frac{1}{2}J\sum_\sigma N_\sigma(N_\sigma - 1) \tag{3.28}$$

  and correspondingly the DC potential (with the notation introduced in Eq. 3.6)

  $$[\Sigma_{\mathrm{DC}}^{\mathrm{FLL}}]_{mm'}^{\sigma\sigma'} = \big(U(N-\frac{1}{2}) - J(N_\sigma - \frac{1}{2})\big)\delta_{mm'}\delta_{\sigma\sigma'}. \tag{3.29}$$

- **The Around Mean-Field (AMF).** In this approximation [Czyżyk and Sawatzky, 1994], LDA is assumed to give an orbitally-averaged result, i.e. $n_{m\sigma} = \bar{n}_\sigma = \frac{1}{2l+1}\sum_m n_{m\sigma}$. This gives:

  $$E_{DC}^{\mathrm{AMF}} = \frac{1}{2}U\sum_\sigma N_\sigma(N-\bar{n}_\sigma) - \frac{1}{2}J\sum_\sigma N_\sigma(N_\sigma - \bar{n}_\sigma) \tag{3.30}$$

  and correspondingly the DC potential

  $$[\Sigma_{\mathrm{DC}}^{\mathrm{AMF}}]_{mm'}^{\sigma\sigma'} = \big(U(N-\bar{n}_\sigma) - J(N_\sigma - \bar{n}_\sigma)\big)\delta_{mm'}\delta_{\sigma\sigma'}. \tag{3.31}$$

Even within these two schemes, variations exist: the occupancies $n_{m\sigma}$ are either obtained from LDA or from the full Hamiltonian 3.6 (hence self-consistently within the LDA+DMFT cycle described in the next section). In the FLL case, the ionic occupancy is also often used (e.g. $N = N_{\mathrm{at}} = 3$ for the $4f$ shell of Nd^{3+}), an approximation called nominal occupancy FLL [Pourovskii et al., 2007].

These two DC terms are the most common, FLL (AMF) for strong (weaker) correlations usually, but other forms have been explored by [Anisimov et al., 1991, Lichtenstein et al., 2001, Karolak et al., 2010, Haule, 2015] for instance. In general, these two schemes are not equivalent and give different energetic positions of the correlated bands with respect to the others. However, it has been shown [Aichhorn et al., 2011] that this inequivalency was reduced within the charged self-consistent LDA+DMFT procedure described in the next section.

3.5 The LDA+DMFT scheme

Once the non-interacting LDA Hamiltonian $\hat{H}_{\mathrm{KS}}$ has been derived (by a plain LDA calculation), the projectors $P_{\boldsymbol{k}}$ extracted and the screened Coulomb matrices computed (with chosen U and J for each correlated orbitals), the interacting problem 3.6 can be approximately solved with DMFT. The DMFT approximation is especially relevant in real materials as the coordination number Z is usually high (e.g. $Z = 12$ for a face-centered cubic lattice). There are two major differences with respect to the simple Hubbard model 2.4 of the previous chapter. First, some orbitals are not correlated and LDA+DMFT hence requires to go in and out of the correlated space through the use of the downfolding and upfolding procedures defined in section 3.2. Second, several correlated shells might be considered. We use the grand canonical ensemble, call $i = (\alpha, l)$ and drop the spin index σ for clarity (by defining larger matrices). The DMFT cycle then becomes, with the nominal occupancy DC (see Sec. 3.4) used in this thesis (which doesn't require to be updated):

1. For each correlated shell in the unit cell, initialize the impurity self-energy and the local Green's function, typically as

$$\Sigma^i_{\mathrm{imp}}(z) = \Sigma^i_{\mathrm{DC}} \tag{3.32}$$

$$G^i_{\mathrm{loc}}(z) = \sum_{\boldsymbol{k}} P^i_{\boldsymbol{k}} \Big((z+\mu)\mathbb{I} - H^{\boldsymbol{k}}_{\mathrm{KS}} \Big)^{-1} P^{i\dagger}_{\boldsymbol{k}}. \tag{3.33}$$

2. For each correlated shell, compute the Weiss field from the Dyson equation $\mathcal{G}^i_0(z) = \left(G^i_{\mathrm{loc}}(z)^{-1} + \Sigma^i_{\mathrm{imp}}(z)\right)^{-1}$;

3. For each correlated shell, solve the Anderson impurity problem defined by the Weiss field $\mathcal{G}^i_0$ and the screened local Coulomb interaction $\hat{H}^i_U$; compute the impurity Green's function G^i_{imp}.

4. For each correlated shell, update the local self-energy from the Dyson equation $\Sigma^i_{\mathrm{imp}}(z) = \mathcal{G}^i_0(z)^{-1} - G^i_{\mathrm{imp}}(z)^{-1}$ and apply the DMFT approximation by upfolding the DC corrected impurity self-energies

$$\Sigma_{\boldsymbol{k}}(z) = \sum_i \left[P^i_{\boldsymbol{k}}\right]^\dagger \Big(\Sigma^i_{\mathrm{imp}}(z) - \Sigma^i_{\mathrm{DC}} \Big) P^i_{\boldsymbol{k}}. \tag{3.34}$$

Note that in this case the lattice self energy does have some $\boldsymbol{k}$ dependency due to the upfolding procedure and that a larger Wannier projection window $\mathcal{W}$ allows to include the effect of local correlations on more KS bands. The lattice Greens' function is then given by

$$G_{\boldsymbol{k}}(z)^{-1} = (z+\mu)\mathbb{I} - H^{\boldsymbol{k}}_{\mathrm{KS}} - \Sigma_{\boldsymbol{k}}(z). \tag{3.35}$$

Set the chemical potential μ so that the number of electrons is preserved and update the local Green's function for each correlated shell by

$$G^i_{\mathrm{loc}}(z) = \sum_{\boldsymbol{k}} P^i_{\boldsymbol{k}} G_{\boldsymbol{k}}(z) P^{i\dagger}_{\boldsymbol{k}} \tag{3.36}$$

5. Iterate until self-consistency over the self-energies and local Green's functions is reached.

This scheme is called "one-shot" LDA+DMFT. The correlations introduced by this DMFT cycle usually lead to a sgnificant redistribution of the charge density [Bhandary et al., 2016]. It is hence more consistent (but numerically more costly) to update the KS potential with the correlation-corrected charge density and perform a charged self-consistent LDA+DMFT scheme given by [Savrasov and Kotliar, 2004, Pourovskii et al., 2007, Haule et al., 2010, Aichhorn et al., 2011]:

1. Diagonalize the KS Hamiltonian and construct the correlated-space basis sets (Wannier projectors $P^i_{\boldsymbol{k}}$).
2. Perform the DMFT cycle described above.
3. Update the charge density and correspondingly the KS Hamiltonian.
4. Iterate until self-consistency over the charge density, self-energies and local Green's functions.

These two LDA+DMFT schemes ("one-shot" and "self-consistent") are summarized in figure 3.1. As noted in section 3.4, self-consistency largely removes the arbitrariness in the choice of double-counting [Aichhorn et al., 2011]. It is usually performed on the Matsubara axis as it requires less frequency points – and some solvers, like CTQMC, are defined only on this axis (applicable only for finite temperatures). In this case, the density matrix $\rho_{\boldsymbol{k}}$ inside the window can be computed as

$$\rho_{\boldsymbol{k}} = \frac{1}{\beta} \sum_{i\omega_n} G_{\boldsymbol{k}}(i\omega_n) e^{i\omega_n 0^+}. \tag{3.37}$$

and the correlation-corrected total charge density in real space as

$$n(\boldsymbol{r}) = n_{\mathrm{OW}}(\boldsymbol{r}) + \sum_{\boldsymbol{k}\sigma, nn' \in \mathcal{W}} \langle \boldsymbol{r} | \phi^\sigma_{n\boldsymbol{k}} \rangle \, [\rho^\sigma_{\boldsymbol{k}}]_{nn'} \, \langle \phi^\sigma_{n'\boldsymbol{k}} | \boldsymbol{r} \rangle \tag{3.38}$$

where n_{OW} is the (DFT) charge density outside the projection window.

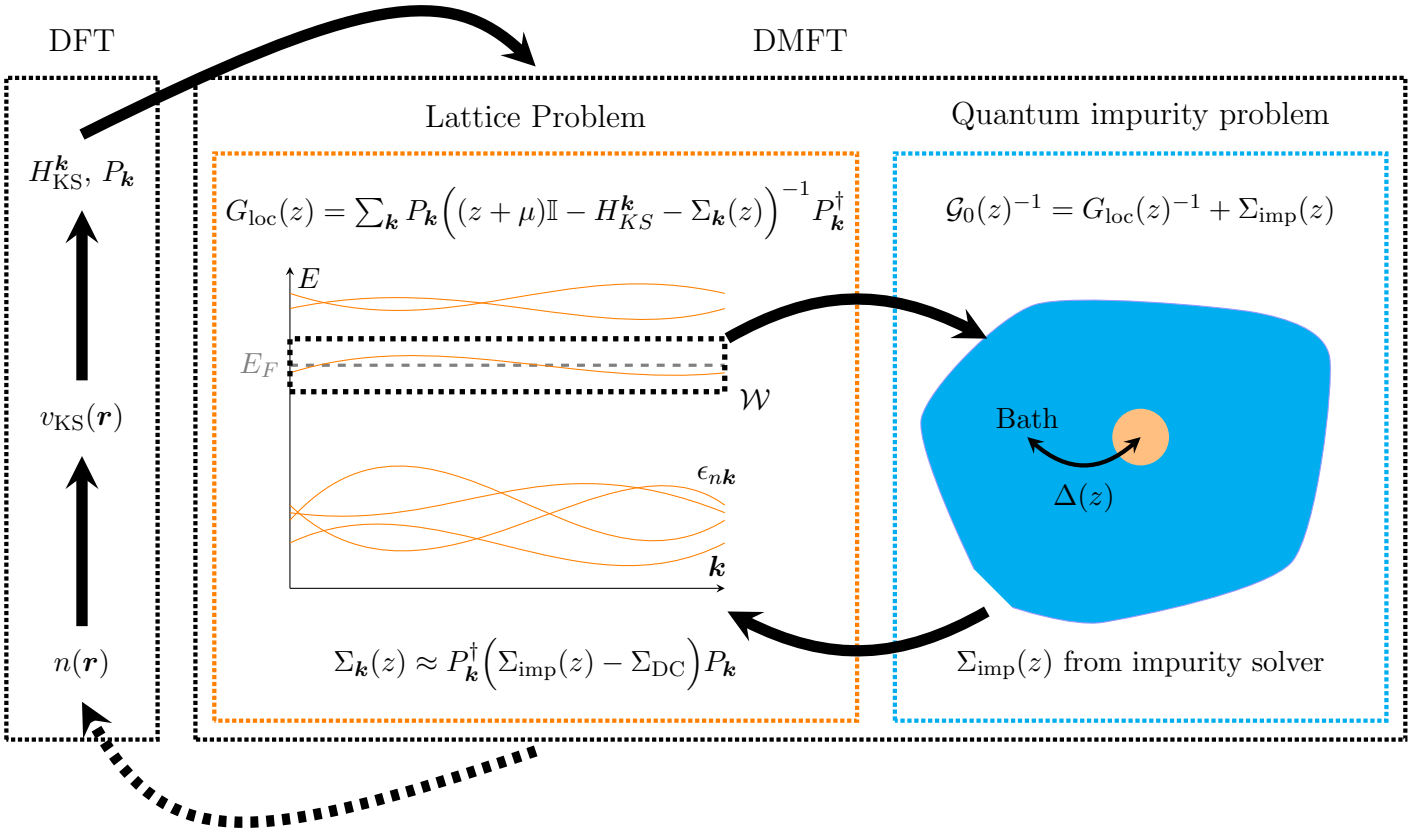

Figure 3.1: LDA+DMFT charge self-consistent cycle if the electronic density is updated by the modification induced by the correlations in the DMFT cycle (dashed arrow). Otherwise, the scheme is called "one-shot" LDA+DMFT. The figure displays the case of a single correlated shell (no atomic α and shell l indices) forming a well isolated band. $\mathcal{W}$ is the Wannier projection window and E_F the DFT Fermi level.

In this thesis, LDA+DMFT is implemented within the FLAPW band structure code WIEN2k [Blaha et al., 2018, Blaha et al., 2020] in conjunction with the TRIQS library [Parcollet et al., 2015, Aichhorn et al., 2016].

3.6 Achievements and shortcomings

The LDA+DMFT has been a very successful approach for numerous compounds. As examples, one may cite some works on systems such as transition metal oxides [Lechermann et al., 2006, Lichtenstein and Katsnelson, 1998, Pavarini et al., 2004, Biermann et al., 2005, Amadon et al., 2008, Thunström et al., 2012, Leonov et al., 2016], pure metals [Lichtenstein et al., 2001, Leonov et al., 2011, Pourovskii et al., 2014, Delange et al., 2016], rare-earths [Pourovskii et al., 2007, Locht et al., 2016], actinides [Savrasov et al., 2001, Shim et al., 2007, Pourovskii et al., 2005, Kolorenč et al., 2015], heavy fermion compounds [Shim et al.,], iron pnictides [Haule and Kotliar, 2009] and Hund's metals [Mravlje et al., 2011, Georges et al., 2013].

It proved to be a flexible method able to study spectral properties [Aichhorn et al., 2009], lattice parameters [Pourovskii et al., 2007] (one can construct a LDA+DMFT total energy functional [Savrasov and Kotliar, 2004]), optical gap and conductivity [Tomczak, 2007]. It can also evaluate crystal field parameters [Delange et al., 2017], which will be the starting point of the next part of this thesis.

LDA+DMFT however faces some limitations. Although it can give a finite gap between correlated states in Mott insulators, it still shares the same issue as the standard LDA regarding the estimation of non-correlated gaps. This issue will be at heart of the third part of this thesis. Furthermore, it is as good as the impurity solver used within it. Generally speaking, the standard solver CTQMC struggle with the 14 orbitals of the rare-earth $4f$ shell. This issue will be further discussed in the last part of this thesis. In the last two sections, we describe some computationally cheaper approaches to the LDA+DMFT Hamiltonian 3.6.

3.7 The rare-earth $4f$ shell and the Hubbard-I approximation

In this thesis, we will deal with rare-earth ($\mathcal{R}$) based compounds. These ions usually are in the $\mathcal{R}^{3+}$ valence state and exhibit a partially filled $4f$ shell (except La and Lu) which is very localized. Due to this strong local character, the $4f$ shell is usually treated within DMFT in an atomic like manner, called the Hubbard-I (HI) approximation, based on the work of [Hubbard, 1963]. Within this approximation, the hybridization function is neglected and the DMFT impurity problem is reduced to the diagonalization of the following quasi-atomic Hamiltonian [Lichtenstein and Katsnelson, 1998]:

$$\hat{H}_{\text{at}} = \hat{H}_{\text{1el}} + \hat{H}_U = \sum_{uv} \epsilon_{uv} \hat{f}_u^\dagger \hat{f}_v + \hat{H}_U. \tag{3.39}$$

Here, $\hat{H}_{\text{1el}}$ is the one-electron part, $\hat{f}_u$ is the annihilation operator for the correlated $4f$ (orbital, spin) state u, $\hat{H}_U$ is the Coulomb repulsion Hamiltonian (see Sec. 3.3) and ϵ_{uv} is the one-electron level-position matrix:

$$\epsilon = -\mu\mathbb{I} - \Sigma_{\text{DC}} + \sum_{\mathbf{k}} P_{\mathbf{k}} H_{\text{KS}}^{\mathbf{k}} P_{\mathbf{k}}^\dagger. \tag{3.40}$$

This expression for the one-electron level positions is obtained by high-frequency expansion of the local Green's function [Pourovskii et al., 2007]. Diagonalizing Hamiltonian 3.39 permits the

computation of the local Green's function thanks to the Lehmann representation

$$[G_{\text{at}}(z)]_{uv} = \frac{1}{Z}\sum_{AB}\frac{\langle A|\,\hat{f}_u\,|B\rangle\,\langle B|\,\hat{f}_v^\dagger\,|A\rangle}{z+E_B-E_A}(e^{-\beta E_A}+e^{-\beta E_B}), \quad Z=\sum_A e^{-\beta E_A} \tag{3.41}$$

where $|A\rangle$ are the eigenstates of the quasi-atomic Hamiltonian 3.39 with eigenenergies E_A. Then, the atomic-like impurity self-energy can be extracted from the Dyson equation

$$\Sigma_{\text{at}}(z) = z\mathbb{I} - \epsilon - G_{\text{at}}(z)^{-1}. \tag{3.42}$$

This solver allows for fast calculations, even in the cases of the $4f$ 14 orbitals, and calculation on both the imaginary and real axis. It hence does not require analytic continuation like the CTQMC solver. However, as detailed in section 8.1, the HI approximation cannot account for finite-lifetime effects, nor for mixed-valence states and the Kondo effect, nor for superexchange.

The use of this solver within LDA+DMFT is at the heart of this thesis as the DMFT correction is solely applied to $\mathcal{R}$ $4f$ shells. We used our own implementation of the HI approach in conjunction with the FLL with nominal occupancy (as it was proven to work well with very localized shells, like the rare-earth $4f$, within HI [Pourovskii et al., 2007]). Similar DFT+HI schemes were successfully applied to $\mathcal{R}$ systems by several authors [Locht et al., 2016, Lebègue et al., 2006, Shick et al., 2009].

In order to evaluate the screened Coulomb interaction U, a constrained approach has been formulated on the basis of LDA+HI [Galler and Pourovskii, 2022]. It will be employed in chapter 7. The general idea is to create a supercell, treat $4f$ shells within HI and constrain the occupancy of two sites to $N_{\text{at}}+1$ and $N_{\text{at}}-1$, where N_{at} is the atomic occupancy. Then, assuming a FLL local Coulomb contribution to the LDA[1] energy (see Sec. 3.4), the average $4f$ KS Hamiltonian matrix

$$\langle H_{\text{KS}}\rangle = \frac{1}{14}\,\text{Tr}\left\{\sum_{\boldsymbol{k}} P_{\mathbf{k}} H_{\text{KS}}^{\mathbf{k}} P_{\mathbf{k}}^\dagger\right\} \tag{3.43}$$

for an occupancy N can be written as

$$\langle H_{\text{KS}}\rangle_N = \langle H_{\text{KS}}^{(0)}\rangle + U\left(N-\frac{1}{2}\right) - J\left(\frac{N}{2}-\frac{1}{2}\right) \tag{3.44}$$

where $\langle H_{\text{KS}}^{(0)}\rangle$ is the average excluding the local Coulomb interaction contribution. As $\langle H_{\text{KS}}^{(0)}\rangle$ does not depend on the occupancy, taking the difference for the two constrained sites, one finds

$$U = \frac{1}{2}\Big(\langle H_{\text{KS}}\rangle_{N_{\text{at}}+1} - \langle H_{\text{KS}}\rangle_{N_{\text{at}}-1} + J\Big). \tag{3.45}$$

We can then assume that LDA reproduces J which is an intra-atomic parameter independent of

[1] Here non-spin polarized.

the crystalline environment for rare earths and can be measured by optical spectroscopy [Carnall et al., 1989]. In any case, some uncertainties in the J value can have only relatively small effect on U. Hence, this cLDA+HI scheme allows the estimation of the screened Coulomb U.

3.8 LDA+U

Another, and historically prior, approach which added explicitly the local Coulomb interaction to DFT is the LDA+U method [Anisimov et al., 1991, Anisimov et al., 1993, Solovyev et al., 1994, Liechtenstein et al., 1995]. It can be viewed as a Hartree-Fock approximation for the Hamiltonian 3.4. It hence loses all true many-body effects (real and static self-energy). We here give a short overview of the method, the reader can refer to [Anisimov et al., 1997a, Himmetoglu et al., 2014] for more details. Let us illustrate it on a single-site, single-orbital example

$$\hat{H}_{\mathrm{e}} \approx \hat{H}_{\mathrm{KS}} + \frac{1}{2}U\sum_{\sigma}\hat{n}_{\sigma}\hat{n}_{\bar{\sigma}} - \hat{H}_{\mathrm{DC}} \tag{3.46}$$

$$\approx \hat{H}_{\mathrm{KS}} - \hat{H}_{\mathrm{DC}} + \frac{1}{2}U\sum_{\sigma}(\hat{n}_{\sigma}n_{\bar{\sigma}} + n_{\sigma}\hat{n}_{\bar{\sigma}} - n_{\sigma}n_{\bar{\sigma}}) \tag{3.47}$$

$$\approx \hat{H}_{\mathrm{KS}} - \hat{H}_{\mathrm{DC}} + U\sum_{\sigma}\hat{n}_{\sigma}n_{\bar{\sigma}} \tag{3.48}$$

where we have dropped the last constant term. With, for instance, a FLL DC term, it gives

$$\hat{H}_{\mathrm{e}} \approx \hat{H}_{\mathrm{KS}} - \sum_{\sigma}U(N-\frac{1}{2})\hat{n}_{\sigma} + U\sum_{\sigma}\hat{n}_{\sigma}n_{\bar{\sigma}} \tag{3.49}$$

$$\approx \hat{H}_{\mathrm{KS}} + \sum_{\sigma}U(\frac{1}{2}-n_{\sigma})\hat{n}_{\sigma}. \tag{3.50}$$

Therefore, LDA+U shifts the energy levels of the correlated orbitals by $U/2$ if they are empty and $-U/2$ if they are full. If spin degeneracy is lifted (long range magnetic ordering), LDA+U hence opens a gap of size U between the two correlated spin species. This gap is however of different nature than the Mott gap which doesn't require magnetic ordering.

More generally, LDA+U with arbitrary double counting and in a multi-site, multi-orbital case can be expressed by the following Hamiltonian [Liechtenstein et al., 1995]:

$$\hat{H}_{\mathrm{LDA+U}} = \hat{H}_{\mathrm{LDA}} - \hat{H}^{c}_{\mathrm{DC}} + \sum_{imm'} t^{i\sigma}_{mm'}\hat{d}^{\dagger}_{im\sigma}\hat{d}_{im'\sigma} \tag{3.51}$$

$$t^{i\sigma}_{mm'} = \sum_{m''m'''} U^{i}_{mm''m'm'''}\left(n^{\bar{\sigma}}_{im''m'''} + [U^{i}_{mm''m'm'''} - U^{i}_{mm''m'''m'}]n^{\sigma}_{im''m'''}\right) \tag{3.52}$$

where i is a (site α, shell l) index and $n^{\sigma}_{imm'} = \left\langle \hat{d}^{\dagger}_{im\sigma}\hat{d}_{im'\sigma}\right\rangle$ are the density matrices of the

correlated shells[2]. It is associated with the following energy functional:

$$E_{\mathrm{LDA+U}}[n(\boldsymbol{r}), \{n^{\sigma}_{imm'}\}] = E_{\mathrm{LDA}}[n(\boldsymbol{r})] - E_{\mathrm{DC}} + \frac{1}{2} \sum_{imm'm''m'''} \Big(U^{i}_{mm''m'm'''} n^{\bar{\sigma}}_{im''m'''} n^{\sigma}_{imm'} \tag{3.53}$$

$$+ [U^{i}_{mm''m'm'''} - U^{i}_{mm''m'''m'}] n^{\sigma}_{im''m'''} n^{\sigma}_{imm'} \Big). \tag{3.54}$$

The LDA+U scheme is then similar to the LDA scheme, only the occupation matrices of the correlated shells must be computed at each iteration to create Hamiltonian 3.51 in the next iteration.

The main success of this approach is that it can reproduce the magnetic GS of Mott insulators and open a gap in cases where LDA would wrongly predict a metallic state. Yet, as discussed above, the opening of the gap within LDA+U is due to long range (magnetic, orbital) ordering. It hence cannot describe Mott insulating states in paramagnetic (symmetry unbroken) phases. In addition, LDA+U can significantly improve the description of magnetic properties compared to LDA even in metals [Solovyev et al., 1998, Nguyen et al., 2018], which is the reason why it will be applied to ferromagnetically ordered transition metals in the next part of this thesis.

[2]Compared to equation 3.6, we substituted $\hat{f} \to \hat{d}$ to highlight the fact that LDA+U will be used for d shells in this thesis.

Part II

Magnetic properties of rare-earth transition metal intermetallics

Chapter 4

Hard magnetism, crystal field and the two sublattice model

In this chapter, we introduce different notions and theories at heart of the study of rare-earth ($\mathcal{R}$) transition metal ($\mathcal{M}$) intermetallics presented in the next two chapters. We start with an introductory section (Sec. 4.1). We then build a theoretical model that can describe the magnetic properties of such systems: we explain the $\mathcal{R}$ $4f$ crystal field Hamilton in section 4.2 which is involved in the single-ion model for the $\mathcal{R}$ $4f$ shell (Sec. 4.3), itself involved in the two sublattice model for $\mathcal{R}-\mathcal{M}$ intermetallics (Sec. 4.4). In sections 4.5 and 4.6, we describe different approaches to this two sublattice model.

4.1 Hard magnetism, economic background and scientific motivation

$\mathcal{R}-\mathcal{M}$ intermetallics are heavily tied to the research for "hard" magnetic materials as we briefly describe in this section. For more detailed reviews, the reader can refer to [Coey, 2011, Coey, 2020, Skomski and Coey, 2016, Skomski, 2016, Skokov and Gutfleisch, 2018, Gutfleisch et al., 2011].

To explain the concept of hard magnetism, let us first consider an ideal, infinite, isotropic ferromagnet. It is characterized by a Curie temperature T_c below which it features magnetic ordering and by a temperature dependent magnetization $M(T)$. We drop the temperature dependence in this section for clarity. Under an applied external field $\boldsymbol{H}_{\text{ext}}$ along the z direction, the free energy F of the system simply consists in a Zeeman term[1]

$$F(\theta) = -\boldsymbol{M}\cdot\boldsymbol{H}_{\text{ext}} = -MH_{\text{ext}}\cos(\theta) \tag{4.1}$$

where θ is the angle between the magnetization $\boldsymbol{M}$ and $+z$ and H_{ext} the projection of the

[1] We use the convention $\mu_0 = 1$ in this thesis, see appendix A.

external field on $+z$. Minimization of this free energy with respect to θ yields $\theta = 0$ if $H_{\text{ext}} > 0$, $\theta = \pi$ if $H_{\text{ext}} < 0$, i.e. the magnetization is aligned with the external field. If the ferromagnet is initially magnetized along $+z$ for instance, an infinitely small H_{ext} applied along $-z$ is enough to flip the magnetization direction. This illustrated in figure 4.1a.

In reality however, ferromagnets are made of a crystalline material which breaks rotationnal symmetry by the presence of a magnetocrystalline anisotropy. We will describe in length the origin of this magnetic anisotropy in the next sections; for the present discussion, suffice to say that at room temperature and above (typical conditions for the use of a permanent magnet), it can be taken into account by the addition of a term in the free energy of the form $K_1 \sin^2(\theta)$. If $K_1 > 0$, the anisotropy favors alignement of the magnetization with the direction z (uniaxial anisotropy); if $K_1 < 0$, it favors $\boldsymbol{M}$ in the plane orthogonal to z (planar anisotropy). The free energy is then

$$F(\theta) = -MH_{ext}\cos(\theta) + K_1 \sin^2(\theta). \tag{4.2}$$

which can be viewed as a particular case of the Stoner-Wohlfarth model [Stoner and Wohlfarth, 1948]. Assuming for instance that K_1 is positive, it has the following minima:

- $\theta = 0$. Stable for $H_{\text{ext}} > 0$, locally stable for $H_{\text{ext}} \in]-\frac{2K_1}{M}, 0]$;
- $\theta = \pi$. Stable for $H_{\text{ext}} < 0$, locally stable for $H_{\text{ext}} \in [0, \frac{2K_1}{M}[$.

Hence, if the ferromagnet is initially magnetized along $-z$, it requires a magnetic field $H_{\text{ext}} = 2K_1/M = H_{\text{a}}$ to flip the magnetization direction, where H_{a} is called the anisotropy field (it was simply 0 in the previous case of the isotropic ferromagnet). It is a measure of how resilient the magnet is to external magnetic fields. This is illustrated in figure 4.1b. We call "easy axis" (or "easy plane") a direction for which the anisotropy term in the free energy 4.2 is minimal, "hard axis" a direction for which it is maximal.

Let us now consider a real finite ferromagnet. Except for specific shapes, it creates a magnetic field outside its volume called the stray field – which is the goal of a permanent magnet. It also generates a magnetic field inside its volume called the demagnetizing field $\boldsymbol{H}_{\text{d}}$ as it opposes the magnetization. Let us indeed suppose that the ferromagnet is an ellipsoid and the magnetization is along one of the principal axes: then $\boldsymbol{H}_{\text{d}} = -\mathcal{N}\boldsymbol{M}$ where $\mathcal{N} \in [0, 1]$ is the demagnetizing factor (more generally, $\mathcal{N}$ is a non-homogeneous second-order tensor). Furthermore, in a real ferromagnet, the internal field opposed to the magnetization which puts the latter to zero is usually much smaller than H_{a} due to magnetic domains, defects, polycrystallinity... The actual field for which $M = 0$ field is called the intrinsic coercive field[2] H_{c}^{i}, as illustrated in figure 4.1c. If $H_{\text{d}} > H_{\text{c}}^{\text{i}}$, then at nil applied field, there is no magnetization left in the compound. Hence, the first permanent magnets (i.e. ferromagnets with finite magnetization at zero applied field) had to be made in specific shapes, which reduced $\mathcal{N}$ to fulfill the criterion $H_{\text{d}} < H_{\text{c}}^{\text{i}}$, such as the elongated needle or the iconic horseshoe.

[2]Here internal, as in [Coey, 2011].

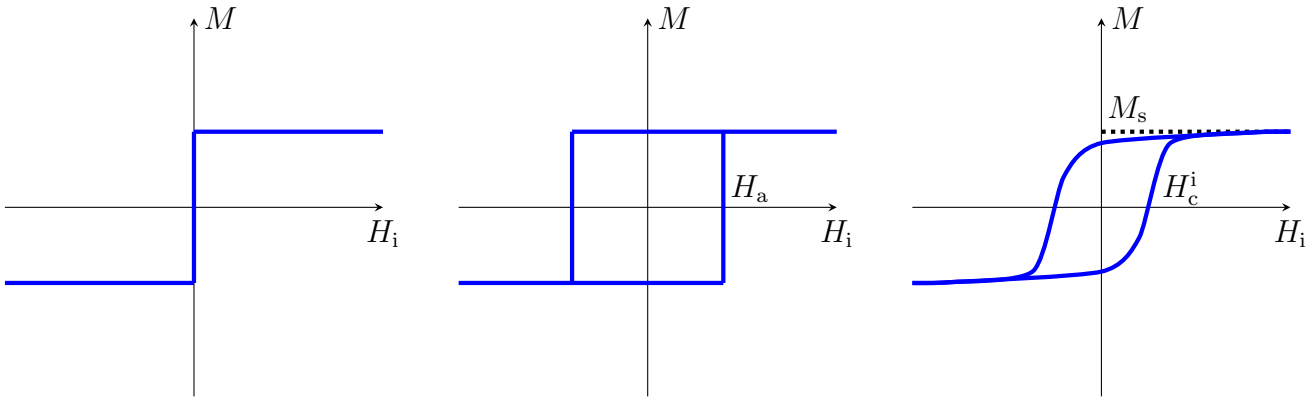

Figure 4.1: Magnetization along the direction of the internal field $H_\mathrm{i} = H_\mathrm{ext} + H_\mathrm{d}$ (hysteresis loop). a) Ideal isotropic ferromagnet. b) Ideal anisotropic ferromagnet. c) Real finite magnet.

A small value of $\mathcal{N}$ however comes at a price: a small value of the stray field. Indeed, the energy associated to the stray field is given by

$$\frac{1}{2}\int_o \boldsymbol{B}\cdot\boldsymbol{H}dV = -\frac{1}{2}\int_i \boldsymbol{B}\cdot\boldsymbol{H}dV \tag{4.3}$$

at zero applied field, where the subscript o (i) means the region outside (inside) the volume of the magnet. It is bounded by the ideal case of $M = M_\mathrm{s}$ where M_s is the magnetization at saturation (see Fig. 4.1c), which gives the following energy associated to the stray field (in the ellipsoid case)

$$\frac{1}{2}V\mathcal{N}(1-\mathcal{N})M_\mathrm{s}^2 \tag{4.4}$$

where V is the volume of the magnet. This quantity goes to zero when $\mathcal{N}$ goes to zero, i.e. the first permanent magnets described above had a relatively small stray field. On the contrary, this quantity is maximal for $\mathcal{N} = 1/2$ – which can approximately be obtained for a cylinder whose height is equal to its radius [Coey, 2011]. The minimal condition for a magnet to be called "hard" is hence that its intrinsic coercive field H_c^i is high enough to allow the shape optimization $\mathcal{N} = \frac{1}{2}$ in the ideal case, i.e. $H_\mathrm{c}^\mathrm{i} > M_\mathrm{s}/2$ [Coey, 2011]. If $H_\mathrm{c}^\mathrm{i} \ll M_\mathrm{s}/2$, the ferromagnet is called "soft"; the intermediate regime is called "semi-hard". The hard magnetism condition is difficult to realize when combined with the requirement of a high stray field, characterized by the maximum energy product

$$(BH)_\mathrm{max} = \frac{2}{V}\max_{\mathcal{N}}(-\int_i \boldsymbol{B}\cdot\boldsymbol{H}dV) \tag{4.5}$$

which takes the value $\frac{1}{4}M_\mathrm{s}^2$ in the ideal case 4.4. The stronger the stray field is (the larger M_s is), the larger the intrinsic coercive field must be.

The first major breakthrough was the discovery of the ferrimagnetic hexagonal ferrites at Philips in 1951 which featured a H_c^i larger than M_s [Coey, 2011]. The second breakthrough

was the discovery of $\mathcal{R}-\mathcal{M}$ intermetallics in the 1960s which allowed for high-performance hard magnets. In these compounds, the transition metals provide high T_c and M_s (strong ferromagnetism behavior) while the rare earths drastically increase the magnetic anisotropy due to the high spin-orbit coupling (hard magnetism behavior), as we will describe in the next sections. The current champion is $Nd_2Fe_{14}B$ which was shown to give even better performances upon substitution of some Nd by Dy.

Rare earths are difficult to extract from the soil and the process is polluting. Hence, they are usually expensive: for instance (see e.g. [Coey, 2020]), in 2018, prices were 280 USD.kg^{-1} for Dy, 70 USD.kg^{-1} for Nd and of the order of 1 USD.kg^{-1} for Fe. On the other hand, the global production of rare-earth-based permanent magnets represents more than 50% percent of the total magnet market, with roughly 1.4×10^5 tonnes produced every year [Coey, 2020]. These compounds are indeed key components of numerous energy-efficient technologies which have today to meet an increasing need, such as wind generators and electrical motors [Skokov and Gutfleisch, 2018, Coey, 2011, Gutfleisch et al., 2011]. Therefore, reducing the $\mathcal{R}$ (especially heavy ones, more scarce; light rare earths La and Ce are much more abundant) concentration in rare-earth-based permanent magnets is crucial economically- and environmentally-wise [Gutfleisch et al., 2011]. This goal can be achieved either by developing a rare-earth-free high-performance magnetic material [Skokov and Gutfleisch, 2018] or by optimizing existing materials – by increasing either their intrinsic properties arising at the atomic level (T_c, M_s, K_1) or their extrinsic properties due to the microstructure (H_c^i, $(BH)_{max}$). In this thesis, we focus on the study of intrinsic properties of two $\mathcal{R}-\mathcal{M}$ intermetallics family: the "1-5" family $\mathcal{R}Co_5$ and the "2-14-1" family $\mathcal{R}_2Fe_{14}B$. From the point of view of theoretical physics, these compounds also feature some interesting properties (spin reorientation transition, first-order magnetization process,...), in particular at low temperature, a condition at which they are usually not used in hard magnetic applications (but these properties are of interest for other uses, e.g. magnetic refrigeration [Nikitin et al., 2010]). Explaining quantitatively from first-principles all their properties is quite a challenge, as we will show in the next sections.

4.2 Crystal field theory

A crystal breaks rotational symmetry which, as is discussed in the following sections, might ultimately lead to magnetic anisotropy. Here, we introduce the main notions of the Crystal Field (CF) theory [Bethe, 1929, Van Vleck, 1932] which studies the lifting of orbital degeneracy for an atom embedded in a crystal. It can also be extended to take into account hybridization with neighboring ions in the so-called ligand field theory [Ballhausen, 1962, Griffith, 1971, Haverkort et al., 2012] which can explain bonds in a solid for instance. Let us illustrate these notions on a simple example which is illustrated in figure 4.2.

We first consider a free d shell and neglect spin-orbit coupling. The $\{|m,\sigma\rangle\}_{m\in[\![-2,2]\!]}$ orbitals are degenerate and the ground-state wavefunction is spherically symmetric. The local Hamiltonian matrix in the basis of the $\{|m,\sigma\rangle\}_{m\in[\![-2,2]\!]}$ is simply a constant (see Fig. 4.2).

We now assume that this d shell is embedded in a octahedral environment (surrounded

by ligands) and look at the effect of the Coulomb interaction with the charge density. Then, the $\{|m,\sigma\rangle\}_{m\in[\![-2,2]\!]}$ orbitals are not eigenstates of the local Hamiltonian anymore and the degeneracy is lifted. CF theory predicts indeed that the atomic levels are splitted into two high-energy e_g states and three low-energy t_{2g} states separated by the crystal field splitting Δ_{CF}. The diagonalized local Hamiltonian matrix is hence now

$$H_{t_{2g}} = 0 \tag{4.6}$$

$$H_{e_g} = \Delta_{CF}\mathbb{I} \tag{4.7}$$

with the proper choice of energy origin. This CF splitting is illustrated in figure 4.2.

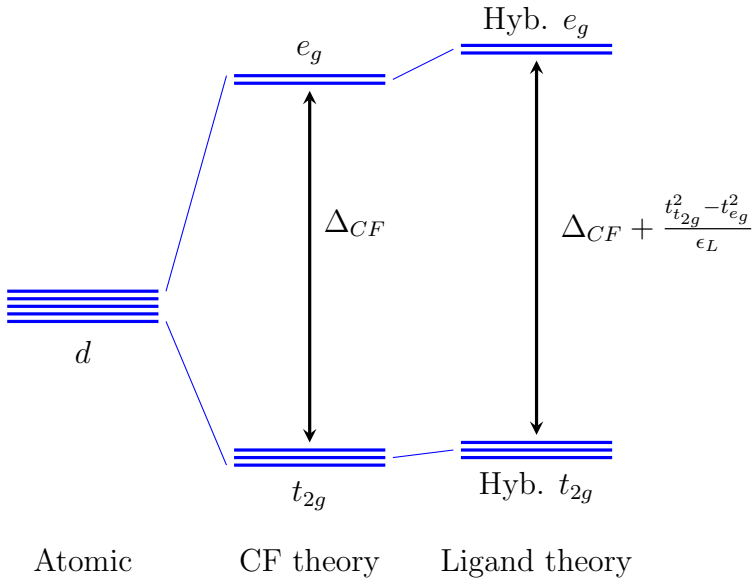

Figure 4.2: Crystal field effects on a d shell embedded in an octahedral environment, as described in the main text.

Let us now further assume that these CF orbitals can hybridize with the atomic levels $\epsilon_L < 0$ of the neighboring ligand ions via the hopping parameter t_{e_g} ($t_{t_{2g}}$) for the e_g (t_{2g}) states. Then, assuming $\epsilon_L \ll -\Delta_{CF}$ (low lying ligand orbitals), standard perturbation theory gives that the d CF orbitals now also have some ligand character, e.g. the wavefunction ψ_g of one e_g orbital interacting with one ligand orbital ψ_L is given by

$$\psi_{e_g} \approx \psi_{e_g} - \frac{t_{e_g}}{\epsilon_L}\psi_L. \tag{4.8}$$

The new Hamiltonian is approximately given by

$$H_{t_{2g}} \approx -\frac{t_{t_{2g}}^2}{\epsilon_L}\mathbb{I} \tag{4.9}$$

$$H_{e_g} \approx (\Delta_{CF} - \frac{t_{e_g}^2}{\epsilon_L})\mathbb{I}. \tag{4.10}$$

If for instance, $t_{e_g}^2 > t_{t_{2g}}^2$, the hybridization will increase the splitting. This shows that the CF splitting has two contributions: one due to electrostatic (CF theory) and one due to hybridization (ligand theory), as summarized in figure 4.2. The CF splitting can have very different effects depending on its value with respect to other quantities, such as the spin-orbit interaction H_{SO} and the local Coulomb interaction H_U. In this thesis, we consider $\mathcal{R}$s, in which we typically have $H_U > H_{\text{SO}} > H_{\text{CF}}$ (not the case in $\mathcal{M}$s where SO is usually the smallest energy scale).

After these introductory considerations, let us derive the more general CF formalism that is applied in this thesis (see e.g. [Mulak and Gajek, 2000, Newman and Ng, 2000]). Let us assume that an ion is embedded in a crystal of charge density $\rho(\boldsymbol{R})$ with which it Coulomb interacts. The potential created by this charge distribution is

$$V(\boldsymbol{r}) = \int \frac{\rho(\boldsymbol{R})}{|\boldsymbol{r}-\boldsymbol{R}|} d^3\boldsymbol{R} \tag{4.11}$$

Using the same kind of decomposition as in equation 3.16, we get

$$V(\boldsymbol{r}) = \sum_{k=0}^{\infty} \frac{4\pi}{2k+1} \sum_{q=-k}^{k} \int \frac{R_<^k}{R_>^{k+1}} \rho(\boldsymbol{R}) Y_k^{q*}(\boldsymbol{\Omega}') Y_k^q(\boldsymbol{\Omega}) d^3\boldsymbol{R} \tag{4.12}$$

$$= \sum_{k=0}^{\infty} \sum_{q=-k}^{k} \left(\sqrt{\frac{4\pi}{2k+1}} \int \frac{R_<^k}{R_>^{k+1}} \rho(\boldsymbol{R}) Y_k^{q*}(\boldsymbol{\Omega}') d^3\boldsymbol{R} \right) \sqrt{\frac{4\pi}{2k+1}} Y_k^q(\boldsymbol{\Omega}) \tag{4.13}$$

$$= \sum_{k=0}^{\infty} \sum_{q=-k}^{k} \tilde{B}_k^q(r) C_k^q(\boldsymbol{\Omega}) \tag{4.14}$$

where $\boldsymbol{r} = (r, \boldsymbol{\Omega})$ and $\boldsymbol{R} = (R, \boldsymbol{\Omega}')$ in spherical coordinates. We have used the notations $R_< = \min(r, R)$ and $R_> = \max(r, R)$. The $C_k^q(\boldsymbol{\Omega}) = \sqrt{\frac{4\pi}{2k+1}} Y_k^q(\boldsymbol{\Omega})$ are called the Wybourne spherical tensors [Wybourne, 1965].

Assuming atomic-like Wannier orbitals $w_{lm}(\boldsymbol{r}) = R_l(r) Y_l^m(\boldsymbol{\Omega})$, the CF Hamiltonian matrix H_{CF} is then given by[3]

$$[H_{CF}]_{mm'} = \sum_{k=1}^{\infty} \sum_{q=-k}^{k} \left(-\int R_l^2(r) \tilde{B}_k^q(r) dr \right) \left(\int Y_l^{m*}(\boldsymbol{\Omega}) C_k^q(\boldsymbol{\Omega}) Y_l^{m'}(\boldsymbol{\Omega}) d^2\boldsymbol{\Omega} \right) \tag{4.15}$$

$$= \sum_{k=1}^{\infty} \sum_{q=-k}^{k} B_k^q \sqrt{\frac{4\pi}{2k+1}} (-1)^m G(l, k, l, -m, q, m') \tag{4.16}$$

where $G(l, l, k, -n, m, q)$ is a Gaunt coefficient and we have defined the Crystal Field Parameters (CFPs) B_k^q. The non-vanishing CFPs are determined by the local symmetry of the ion and by the considered atomic shell ($k \leq 6$ for the $4f$ shell, as can be shown from the properties of the

[3] In this thesis, $-e = -1$ (see appendix A) and we have dropped the $k = 0$ spherical term.

Gaunt coefficients). The crystal-field Hamiltonian can hence be written as:

$$\hat{H}_{CF} = \sum_{kq} B_k^q \hat{C}_k^q \tag{4.17}$$

$$\hat{C}_k^q = \sum_{mm'\sigma} \sqrt{\frac{4\pi}{2k+1}} (-1)^m G(l,k,l,-m,q,m') f_{m\sigma}^\dagger f_{m'\sigma}. \tag{4.18}$$

Several conventions exist for the CFPs. The B_k^q are here complex numbers and in the so-called Wybourne convention. From now on, to facilitate the comparison with experimental literature, we will use the more common Stevens convention [Stevens, 1952], which uses real CFPs with a different renormalization. In this case, the crystal field Hamiltonian is expressed through the renormalized Hermitian combination of Wybourne tensors

$$\hat{T}_k^0 = \hat{C}_k^0 / \lambda_{k,0} \tag{4.19}$$

$$\hat{T}_k^{\pm|q|} = \sqrt{\pm 1} \left[\hat{C}_k^{-|q|} \pm (-1)^{|q|} \hat{C}_k^{|q|} \right] / \lambda_{k,|q|}, \tag{4.20}$$

where the $\lambda_{k,|q|}$ are tabulated in [Mulak and Gajek, 2000] for instance, as

$$\hat{H}_{CF} = \sum_{kq} A_k^q \hat{T}_k^q. \tag{4.21}$$

The CFPs A_k^q in Stevens convention[4] are real and related to B_k^q by

$$A_k^0 = B_k^0 \lambda_{k,0} \tag{4.22}$$

$$A_k^{|q|} = \mathrm{Re}\left\{ B_k^{-|q|} \right\} \lambda_{k,|q|} \tag{4.23}$$

$$A_k^{-|q|} = \mathrm{Im}\left\{ B_k^{-|q|} \right\} \lambda_{k,|q|}. \tag{4.24}$$

Furthermore, as seen in the previous example, hybridization with neighboring ions will also affect the CFPs.

4.3 The single-ion model for the $4f$ shell

Let us now consider the full local Hamiltonian of a $\mathcal{R}$ site in $\mathcal{R}-\mathcal{M}$ intermetallics. These compounds usually display the following hierarchy of inter-site magnetic exchange interactions

$$\mathcal{M}3d - \mathcal{M}3d \gg \mathcal{M}3d - \mathcal{R}4f \gg \mathcal{R}4f - \mathcal{R}4f. \tag{4.25}$$

The $\mathcal{M}3d - \mathcal{M}3d$ interaction is responsible for the strong magnetism behavior (large magnetization, Curie temperature) of the $\mathcal{M}$ sublattice. The $\mathcal{M}3d - \mathcal{R}4f$ interaction is a multi-orbital

[4] We have simplified the misleading $A_k^q \langle r^k \rangle$ notation found in the literature (which is due to historical reasons).

coupling as it has been shown to be mediated through the moment of $\mathcal{R}5d6s$ orbitals [Herbst, 1991, Coey, 1996].

Equation 4.25 justifies the so-called single-ion approximation, adopted in this thesis and explained in depth in [Kuz'min and Tishin, 2007] for instance: the $\mathcal{R}4f-\mathcal{R}4f$ coupling is neglected and the $\mathcal{M}3d-\mathcal{R}4f$ exchange interaction is modeled by an exchange field $\mathbf{B}_{\text{ex}}(T)$ which captures the combined effects of the inter-atomic $\mathcal{M}3d-\mathcal{R}5d6s$ and intra-atomic $\mathcal{R}5d6s-\mathcal{R}4f$ [Frietsch et al., 2015, Pivetta et al., 2020] interactions as an effective mean-field acting on the $\mathcal{R}$ $4f$ shell.

Within this approximation, the local Hamiltonian for a $\mathcal{R}$ $4f$ shell in the unit cell reads

$$\hat{H}_{4f}(T) = E_0\hat{\mathbb{I}} + \hat{H}_{\text{SO}} + \hat{H}_{\text{ex}}(T) + \hat{H}_{\text{Z}} + \hat{H}_{\text{CF}} + \hat{H}_U. \tag{4.26}$$

E_0 is an energy shift determining the occupancy of the shell, $\hat{H}_{\text{SO}} = \lambda\sum_i \hat{\boldsymbol{s}}_i \cdot \hat{\boldsymbol{l}}_i$ is the spin-orbit (SO) Hamiltonian, λ is the spin-orbit coupling, $\hat{H}_{\text{ex}}(T) = 2\mu_B\mathbf{B}_{\text{ex}}(T)\cdot\hat{\mathbf{S}}_{4f}$ is the $\mathcal{M}-\mathcal{R}$ exchange interaction with $\mathbf{B}_{\text{ex}}(T)$ being the exchange field at temperature T and $\hat{\mathbf{S}}_{4f}$ the $4f$ spin operator. $\hat{H}_{\text{Z}} = -\mathbf{H}_{\text{ext}}\cdot\hat{\mathbf{M}}_{4f}$ is the Zeeman interaction between the total $4f$ moment operator $\hat{\mathbf{M}}_{4f}$ and the external magnetic field $\mathbf{H}_{\text{ext}}$. $\hat{H}_{CF}$ is the crystal-field Hamiltonian 4.21. In this thesis, we neglect possible temperature dependence of CFPs [Cadogan et al., 1988]. $\hat{H}_U$ is the Coulomb interaction between $4f$ electrons (see Sec. 3.3).

4.4 The two sublattice model for $\mathcal{R}-\mathcal{M}$ intermetallics

Let us now look at the total free energy F per unit cell of the system composed of the partially filled $\mathcal{M}3d$ and $\mathcal{R}4f$ shells. Hybridization of the $4f$ is here assumed to be weak enough to be taken into account by a renormalization of CFPs (see ligand theory in Sec. 4.2). We assume that the $3d$ contribution can be factorized out in the following form:

$$F(T,\boldsymbol{\Omega}_{3d}) = \sum_i w_i F_{4f}^{(i)}(T,\boldsymbol{\Omega}_{3d}) + F_{3d}(T,\boldsymbol{\Omega}_{3d}) \tag{4.27}$$

$$F_{3d}(T,\boldsymbol{\Omega}_{3d}) = -\boldsymbol{M}_{3d}(T)\cdot\boldsymbol{H}_{ext} + K_1^{3d}(T)\sin^2\theta_{3d} \tag{4.28}$$

$$F_{4f}^{(i)}(T,\boldsymbol{\Omega}_{3d}) = -T\log\left(\text{Tr}\left\{\exp\left\{-\beta\hat{H}_{4f}^{(i)}(T,\boldsymbol{\Omega}_{3d})\right\}\right\}\right) \tag{4.29}$$

where $\beta = 1/T$. F_{3d} is the contribution from the $3d$ sublattice, $\boldsymbol{M}_{3d}$ is the $3d$ magnetization, $\boldsymbol{\Omega}_{3d} = (\theta_{3d},\phi_{3d})$, θ_{3d} (ϕ_{3d}) is the polar (azimuthal) angle of $\boldsymbol{M}_{3d}$, $\boldsymbol{H}_{ext}$ is the applied external field and K_1^{3d} is the $3d$ first anisotropy constant (in the majority of $\mathcal{R}-\mathcal{M}$ intermetallics, the $\mathcal{M}$ anisotropy is reasonably well described by such a simple anisotropy term).

F_{4f} is the contribution from the $4f$ sublattice. The index i = (site, ion) denotes the possible different $\mathcal{R}$ sites in the unit cell as well as possible different magnetic (i.e. with partially filled $4f$) $\mathcal{R}$ species occupying these sites in mixed systems (i.e. with substitutional alloys on the $\mathcal{R}$ sublattices). w_i is the corresponding occupancy, $F_{4f}^{(i)}$ the contribution from the corresponding $4f$ shell and $\hat{H}_{4f}^{(i)}$ the corresponding local Hamiltonian given by the single-ion approximation

4.26, with i specific E_0, λ, $\boldsymbol{B}_{\text{ex}}(T)$ and CFPs.

These two sublattices are linked via the definition of the exchange field

$$\boldsymbol{B}_{\text{ex}}^{(i)}(T) = -n_{3d-4f}^{(i)} \boldsymbol{M}_{3d}(T), \tag{4.30}$$

the temperature variation of the positive exchange coupling $n_{3d-4f}^{(i)}$ between the $\mathcal{M}$ and $\mathcal{R}$ sublattices being usually neglected. This relation gives the $\boldsymbol{\Omega}_{3d}$ dependency of $\hat{H}_{4f}^{(i)}$ in equation 4.29. The exchange field tends to anti-align the $4f$ spin moments with respect to $\boldsymbol{M}_{3d}$. Consequently, due to LS coupling, the total moment of a light (heavy) $\mathcal{R}$ tends to be (anti-)aligned with $\boldsymbol{M}_{3d}$.

The origin of the magnetic anisotropy in $\mathcal{R}-\mathcal{M}$ intermetallics is then explained by the following chain of interactions (see Fig. 4.3): the magnetization of the $3d$ sublattice (which usually does not exhibit high anisotropy) interacts with the $4f$ spins (via $\hat{H}_{\text{ex}}(T)$ in Eq. 4.26) which are coupled (via $\hat{H}_{\text{SO}}$ in Eq. 4.26) to the orbital degrees of freedom which are sensitive to the crystalline environment (via $\hat{H}_{\text{CF}}$ in Eq. 4.26). This chain of interaction converts a crystalline anisotropy into a magnetic one: this form of magnetic anisotropy is therefore called magnetocrystalline anisotropy. The stronger the $3d$–$4f$ exchange interaction and the crystalline anisotropy are, the stronger the magnetic anisotropy is. This also explains why $\mathcal{R}$s are needed in high-performance hard magnets: the SO coupling in the $4f$ shell of $\mathcal{R}$s is stronger than in the $3d$ shell of $\mathcal{M}$s.

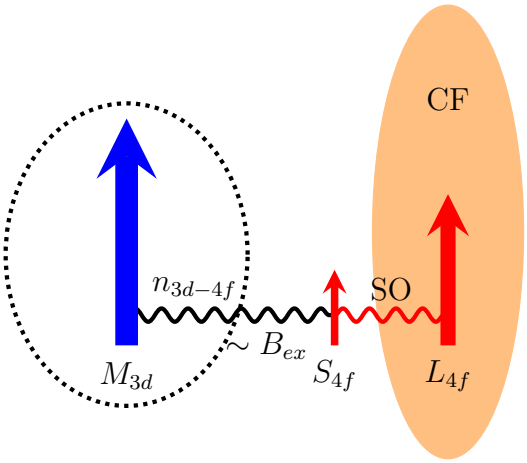

Figure 4.3: Interactions giving rise to magnetocrystalline anisotropy in $\mathcal{R}-\mathcal{M}$ intermetallics.

The total free energy 4.27 is to be minimized with respect to the direction $\boldsymbol{\Omega}_{3d}$ of $\boldsymbol{M}_{3d}$ (the directions of $4f$ moments are internal parameters) yielding macroscopic quantities that can be experimentally measured such as magnetization curves. In the next section, we describe two approaches to this two sublattice model. The latter however employs several material-specific parameters such as the CFPs which are difficult to evaluate experimentally. Indeed, extracting them by fitting experimental high field magnetization curves [Yamada et al., 1988, Cadogan et al., 1988, Kostyuchenko et al., 2020, Tie-song et al., 1991] has a limited predictive power, as

it usually neglects some CFPs, and requires the use of single crystals. Furthermore, care must be taken to properly separate contributions from the $\mathcal{R}$ and $\mathcal{M}$ sublattices [Ito et al., 2016]. Therefore, the development of a general predictive theory which can compute these parameters from first principles is crucial for the field but is also a notorious difficult problem, as we explain in section 4.6.

At this point, we define the amplitude of the magnetocrystalline anisotropy MAE as the difference of free energy between two axes (usually hard and easy) for nil applied external field (e.g. $F_{[100]} - F_{[001]}$). The contribution of a given $\mathcal{R}$ ion to this MAE that arises due to the interplay of its on-site crystal field and spin-orbit effects is also often called Single-Ion Anisotropy (SIA).

4.5 Linear-in-CF theory, anisotropy constants and the Sucksmith-Thompson method

The linear-in-CF theory [Kuz'min, 1995, Kuz'min and Tishin, 2007]) is an approximate theory for computing the anisotropy constants (one such constant K_1 was introduced in Sec. 4.1) of the $\mathcal{R} - \mathcal{M}$ intermetallics[5]. It is based on the following assumptions[6]:

1. $H_U \gg H_{\text{SO}}$, H_{ex}, H_{Z}, H_{CF}. It allows the use of the LS coupling.
2. $H_{\text{SO}} \gg H_{\text{ex}}$, H_{Z}, H_{CF}. This is not a very good approximation in light rare-earths, especially Sm.
3. $H_{\text{ex}} \gg H_{\text{Z}}$. It implies a weak to moderate magnetic field.
4. $H_{\text{ex}} \gg H_{\text{CF}}$. This criterion is called strict exchange dominance. It is usually not fulfilled in real $\mathcal{R} - \mathcal{M}$ intermetallics. However, $H_{\text{ex}} > H_{\text{CF}}$ is usually fulfilled, a criterion called broad exchange dominance.

We assume that there is a single $\mathcal{R}$ ion in the unit cell for simplicity. The first two assumptions allows to consider only the GS multiplet J in the diagonalization of the $4f$ Hamiltonian 4.26. In the GSM, the exchange Hamiltonian reduces to

$$\hat{H}^{\text{S}}_{\text{ex}} = \Delta_{\text{ex}} \mathbf{n} \cdot \hat{\mathbf{J}}; \ \Delta_{ex} = 2(g_J - 1)\mu_B B_{\text{ex}} \tag{4.31}$$

where $\boldsymbol{n}$ is the direction of the exchange field and g_J is the Landé factor for the GS multiplet J. Furthermore, in the GSM, according to [Stevens, 1952] the CF Hamiltonian reduces to

$$\hat{H}^{\text{S}}_{\text{CF}} = \sum_{kq} \Theta_k(J) A^q_k \hat{O}^q_k(J). \tag{4.32}$$

[5] We insist on the fact that this theory does not compute the parameters involved in the two sublattice which are taken as inputs.

[6] These criteria are actually more precisely defined; for more details on this point, the reader can refer to [Kuz'min and Tishin, 2007].

$\hat{O}_k^q(J)$ are the Stevens operator equivalents in the J multiplet, which have, apart from some prefactor, the same matrix elements within the J multiplet as the corresponding $\hat{T}_k^q$. The prefactors $\Theta_k(J)$ are called the Stevens factors (tabulated in [Kuz'min and Tishin, 2007] for instance); it is common to also designate $\Theta_k(J)$ as α_J, β_J and γ_J for $k = 2$, 4 and 6 respectively. The advantage of this operator equivalent technique is that the $\hat{O}_k^q(J)$ take some simple forms, e.g. $\hat{O}_2^0(J) = 3\hat{J}_z^2 - J(J+1)$.

The third and fourth assumptions allow to treat the CF and Zeeman terms in the $4f$ free-energy 4.29 as perturbations. The linear-in-CF theory then considers only first order (i.e. linear) crystal field and Zeeman corrections. This leads to the following decomposition:

$$F_{4f}^{\text{lin}}(T, \boldsymbol{\Omega}) = F_0(T) + E_{\text{anis}}(T, \boldsymbol{\Omega}) - \boldsymbol{M}_{4f}(T) \cdot \boldsymbol{H}_{ext} \tag{4.33}$$

where $F_0(T)$ is a $\boldsymbol{\Omega}$-independent term. $\boldsymbol{M}_{4f}(T)$ is the $4f$ total moment, rigid and perfectly (anti-)aligned with $\boldsymbol{M}_{3d}$ in this approximation – the angles (θ, ϕ) of the total magnetization are hence equal to (θ_{3d}, ϕ_{3d}). $E_{\text{anis}}(T, \boldsymbol{\Omega})$ is the $4f$ anisotropy energy which, in this approximation, can be written as a truncated sum of sines which depend on the symmetry of the crystal. For instance, in $\mathcal{R}\text{Co}_5$, it reads

$$E_{\text{anis}}(T, \boldsymbol{\Omega}) = K_1(T)\sin^2(\theta) + K_2(T)\sin^4(\theta) + K_3(T)\sin^6(\theta) + K_3'(T)\sin^6(\theta)\cos(6\phi) \tag{4.34}$$

in the coordination frame with $z||c$ and $x||a$. The K_i are the $\mathcal{R}$ anisotropy constants which contain only linear terms of the CFPs in this approximation [Kuz'min and Tishin, 2007]:

$$K_1(T) = -3\alpha_J A_2^0 J^2 B_J^{(2)}(x) - 40\beta_J A_4^0 J^4 B_J^{(4)}(x) - 168\gamma_J A_6^0 J^6 B_J^{(6)}(x) \tag{4.35}$$

$$K_2(T) = 35\beta_J A_4^0 J^4 B_J^{(4)}(x) + 378\gamma_J A_6^0 J^6 B_J^{(6)}(x) \tag{4.36}$$

$$K_3(T) = -231\gamma_J A_6^0 J^6 B_J^{(6)}(x) \tag{4.37}$$

$$K_3'(T) = \gamma_J A_6^6 J^6 B_J^{(6)}(x) \tag{4.38}$$

where $x = 2\beta J|g_J - 1|B_{\text{ex}}$ and $B_J^{(n)}(x)$ are the generalized Brillouin functions (GBFs). Due to the properties of the GBFs at small x, only the "20" CFP contributes in the leading order in $1/T$. Hence, at high T, it is usually reasonable to only consider K_1.

Combining the expression of the $4f$ free energy 4.33 with the $3d$ one 4.28 yields the following single-lattice-like expression for the total free energy:

$$F^{\text{lin}}(T, \boldsymbol{\Omega}) = F_0(T) - \boldsymbol{M}(T) \cdot \boldsymbol{H}_{\text{ext}} + E_{\text{anis}}^{\text{tot}}(T, \boldsymbol{\Omega}) \tag{4.39}$$

where $\boldsymbol{M}$ is the total moment and $E_{\text{anis}}^{\text{tot}}(T, \boldsymbol{\Omega})$ the total anisotropy energy written in $\mathcal{R}\text{Co}_5$ as

$$E_{\text{anis}}^{\text{tot}}(T, \boldsymbol{\Omega}) = \left(K_1(T) + K_1^{3d}(T)\right)\sin^2(\theta) + K_2(T)\sin^4(\theta) + K_3(T)\sin^6(\theta) + K_3'(T)\sin^6(\theta)\cos(6\phi). \tag{4.40}$$

While this linear-in-CF theory is formally justified only in the strict exchange dominance limit, it can be qualitatively correct in real materials as they are often broadly exchange dominated.

Typical breakdown of this theory occur in Sm where the single-multiplet approximation is especially bad. It may also break down in heavy rare-earths whose total moment is anti-aligned with the $3d$ one: even small non-collinearities (not accounted in the linear-in-CF theory, as said above) can then drastically impact the direction of the total moment.

The Sucksmith-Thompson (ST) method [Sucksmith and Thompson, 1954], widely used to extract the macroscopic anisotropy constants from experimental magnetization curves, assumes that the free energy 4.27 can be approximated by a single-lattice free energy of the type 4.39. It restricts the anisotropy constants to the first two ones, i.e. it assumes a total free energy of the form (dropping the T dependency in the remaining of this section for clarity):

$$F^{\mathrm{ST}}(\boldsymbol{H}_{\mathrm{ext}},\theta) = F_0 - \boldsymbol{M}\cdot\boldsymbol{H}_{\mathrm{ext}} + K_1^{\mathrm{tot}}\sin^2(\theta) + K_2^{\mathrm{tot}}\sin^4(\theta). \tag{4.41}$$

Let us assume for instance that a magnet is in a planar phase and that a magnetic field along the hard $+z$ direction is applied. Then, minimizing the free energy 4.41 with respect to theta yields:

$$\frac{\partial F^{\mathrm{ST}}(H_{\mathrm{ext}},\theta)}{\partial\theta} = MH_{\mathrm{ext}}\sin(\theta) + 2K_1^{\mathrm{tot}}\cos(\theta)\sin(\theta) + 4K_2^{\mathrm{tot}}\cos(\theta)\sin^3(\theta) = 0 \tag{4.42}$$

Because $\theta = 0$ is the hard axis, if the external magnetic field is not too strong, we can assume $\sin(\theta) \neq 0$. Furthermore, the magnetization along the applied field is here $M\cos(\theta)$; hence, for the angle θ which minimizes the free energy, we can write $\cos(\theta) = m(H_{\mathrm{ext}})$ where $m(H_{\mathrm{ext}})$ is the normalized magnetization along the direction of the external field. We get:

$$\frac{M}{2}\frac{H_{\mathrm{ext}}}{m(H_{\mathrm{ext}})} = -K_1^{\mathrm{tot}} - 2K_2^{\mathrm{tot}} + 2K_2^{\mathrm{tot}}m(H_{\mathrm{ext}})^2. \tag{4.43}$$

Similarly, if we assume a uniaxial phase and hence an in-plane applied external field, with m still being the normalized magnetization along the direction of the external field (this time in-plane), we get

$$\frac{M}{2}\frac{H_{\mathrm{ext}}}{m(H_{\mathrm{ext}})} = K_1^{\mathrm{tot}} + 2K_2^{\mathrm{tot}}m(H_{\mathrm{ext}})^2. \tag{4.44}$$

Equation 4.43 (4.44) is the equation governing the magnetization curve for a planar (uniaxial) magnet with the external field along the hard direction. The idea of the Sucksmith-Thompson approach is to apply an external field of varying strength H_{ext} along the hard direction, measure the magnetization along this direction and divide it by the measured M_{s} to define $m(H_{\mathrm{ext}})$[7]. Then, $\frac{M}{2}H_{\mathrm{ext}}/m(H_{\mathrm{ext}})$ is plotted as a function of $m(H_{\mathrm{ext}})^2$. This curve is fitted with the corresponding form 4.43 or 4.44 for different temperatures and the T-dependent anisotropy constants are extracted. This method has some limitations which it shares with the linear-in-CF theory: it does not work well for heavy $\mathcal{R}$s with non-collinearity effects for instance. The

[7] The ST method assumes rigid $4f$ magnetization, see Eq. 4.41.

fitting is poor in these cases. Despite these limits, we will employ the ST method in order to have a consistent comparison with experimental anisotropy constants that were extracted with it.

4.6 From an *ab initio* perspective

In this section, we summarize the *ab initio* approach for magnetic properties of $\mathcal{R}-\mathcal{M}$ intermetallics used in this thesis. The idea is to use the single-ion model for the $4f$ shell 4.26 within the two sublattice model 4.27 and to compute the different parameters involved from first principles. These parameters are: E_0, λ, $\boldsymbol{B}_{\text{ex}}(T)$ and CFPs for each $\mathcal{R}$ as well as $M_{3d}(T)$ and $K_1^{3d}(T)$ for the $\mathcal{M}$ sublattice. The calculation of the free-energy 4.29 is then performed by taking into account states up to the first excited multiplet, whose importance has been pointed out in previous works [Yamada et al., 1988] and will be stressed again in the next chapter.

In subsection 4.6.1, we detail the electronic structure LDA+HI-based approach [Delange et al., 2017] which allows to compute the parameters of the single-ion model for the $4f$ shell, namely E_0, λ, zero-temperature B_{ex} and CFPs for each $\mathcal{R}$. This electronic structure method takes as inputs the lattice parameters (taken from experiment) and the Wannier projection window (see Sec. 3.2); we will discuss the latter in length in the next chapter. In subsection 4.6.2, we explain how the zero temperature M_{3d} and K_1^{3d} are computed. Finally, in subsection 4.6.3, we give the semi-empirical formula used in this thesis to model the temperature dependence of $M_{3d}(T)$, $B_{\text{ex}}(T)$ and $K_1^{3d}(T)$. Table 4.1 is a summary of how the different parameters involved in the two sublattice model are obtained; as it will become apparent, the only parameters not extracted from first principles are the temperature dependence parameters (taken from experiment).

	E_0, λ, B_{ex}, CFPs, M_{3d}	K_1^{3d}	$B_{\text{ex}}(T)$, $M_{3d}(T)$	$K_1^{3d}(T)$	T_c, s, p
From	SIC-LDA+HI	ΔE_{SO}	Kuz'min	Zener	Exp.
Eq.	4.46	4.47	4.50	4.51	-

Table 4.1: Summary of the different parameters involved in the two sublattice model. The second row indicates how they are obtained; the last row gives the reference of the corresponding equation (if any) in the text.

4.6.1 Electronic structure approach for the single-ion model of the $4f$ shell

Computing CFPs from first principles is a notorious challenge, notably due to the localized and strongly correlated nature of $\mathcal{R}$ $4f$ states which standard DFT fails to describe properly (see Sec. 1.5). Furthermore, as suggested by [Brooks et al., 1997], the self-interaction error in LDA (see Sec. 1.4) leads to an unphysical contribution to CFPs; a proper approach to CF estimation should hence include a self-interaction suppression scheme. First works towards *ab initio* methods were still partially relying on the crude point-charge electric model [Zhong and Ching, 1989a, Zhong and Ching, 1989b]. Several DFT-based approaches have been so far

developed and applied to various $\mathcal{R}-\mathcal{M}$ intermetallics [Daalderop et al., 1992, Novák and Kuriplach, 1994, Steinbeck et al., 1994, Hummler and Fähnle, 1996, Novák, 1996, Diviš et al., 2005, Tsuchiura et al., 2018, Patrick and Staunton, 2019], usually relying on open-core-like treatment of R $4f$ shells. However, a more consistent approach to compounds with partially filled $4f$ shell is the LDA+DMFT method described in section 3.5 within the quasi-atomic Hubbard-I approximation (see Sec. 3.7). Combining the ideas used in the open-core approach to CFPs with the LDA+HI approach to $4f$ shell, [Delange et al., 2017] developed a self-interaction suppressed, self-consistent LDA+HI scheme to the computation of CFPs.

Within this scheme, adopted in this thesis, the $\mathcal{M}$ sublattice magnetism is described with LSDA and spin-orbit coupling is included within the usual second variationnal procedure (see Sec. 1.5). The $4f$ shells of the $\mathcal{R}$ ions are treated as localized and atomic-like using the HI approximation within DMFT. To eliminate the self-interaction contribution to the CFPs, the scheme enforces a spherically symmetric $4f$ shell, by averaging the Boltzmann weights of the eigenstates of the HI quasi-atomic Hamiltonian $\hat{H}_{\text{at}}$ (Eq. 3.39) belonging to the GS multiplet. To eliminate the self-interaction contribution to B_{ex}, it also suppresses the spin polarization of the $4f$ shell. Once LDA+HI self-consistency is reached, the converged quasi-atomic Hamiltonian from the HI approximation (see Sec. 3.7)

$$\hat{H}_{\text{at}} = \hat{H}_{\text{1el}} + \hat{H}_U = \sum_{uv} \epsilon_{uv} \hat{f}_u^\dagger \hat{f}_v + \hat{H}_{\text{U}} \tag{4.45}$$

should correspond to the expected form 4.26 in the single-ion approximation (without applied external field). Therefore, the CFPs, λ, E_0 and B_{ex} are extracted from the converged one electron level-position matrix ϵ (see Eq. 3.40) defining $\hat{H}_{\text{1el}}$ by the fitting

$$\hat{H}_{\text{1el}} = E_0 \hat{\mathbb{I}} + \lambda \sum_i \hat{\boldsymbol{s}}_i \cdot \hat{\boldsymbol{l}}_i + \hat{H}_{\text{ex}} + \hat{H}_{\text{CF}}. \tag{4.46}$$

With the $\mathcal{M}$ sublattice magnetism treated by zero-temperature LSDA, the term $\hat{H}_{\text{ex}}$ is obtained for $T = 0$. The computed CFPs are furthermore weakly dependent on the values of U and J [Delange et al., 2017]. From now on, this scheme is denoted as SIC-LDA+HI, where "SIC" stands for Self-Interaction-Corrected. In the next chapter, we will also add to this scheme a +U correction for the $\mathcal{M}$ $3d$ shell treated within LSDA+U (see Sec. 3.8), in order to improve the description of the $\mathcal{M}$ sublattice magnetic properties as described in the next subsection.

One remark is due here regarding the ability of HI to capture effects predicted by the ligand theory described in section 4.2. While HI neglects the hybridization function, hybridization with other states are implicitly taken into account through the shape of $4f$ orbitals in which the matrix $\sum_{\mathbf{k}} P_{\mathbf{k}} H_{KS}^{\mathbf{k}} P_{\mathbf{k}}^\dagger$ is calculated (see Eq. 3.40). The renormalization of CFPs by hybridization is hence taken into account by the present HI-based scheme if the Wannier window is not too large (see Sec. 3.2), as can be qualitatively understood by comparing equation 4.8 to equation 3.14. We will see implications of this in the next chapter.

Computational parameters used in this thesis. Calculations are performed with the $\mathcal{M}$ magnetic moment aligned along the [001] direction. $\mathcal{R}$ $4f$ Wannier orbitals are constructed from the Kohn-Sham (KS) bands enclosed in an energy window $\mathcal{W}$ of size 4 eV (see Sec. 3.2). For light $\mathcal{R}$s, whose KS $4f$ states are pinned at the Fermi level E_F, this window is centered around E_F; for heavy $\mathcal{R}$s, as the $4f$ KS bands move towards lower energies during the self-consistent calculation, the window is centered around the central weight of the $4f$ partial density of states (see Fig. 5.5). For the double counting term, the FLL with nominal occupancy is used (see Sec. 3.4). The on-site rationally-invariant Coulomb repulsion $\hat{H}_U$ (see Sec. 3.3) between $4f$ electrons is specified with the two parameters $U = 6$ (7) eV for light (heavy) $\mathcal{R}$s (to account for the increase along the series), and $J = 0.73$, 0.77, 0.85, 0.95, 0.99 and 1.02 for Pr, Nd, Sm, Tb, Dy and Ho respectively, as measured by optical spectroscopy [Carnall et al., 1989] (in the next chapter, $J = 0.85$ eV for Nd but it has a weak impact on the results). The value $J = 0.71$ eV is chosen for Ce in order to account for the increase along the series. We use the FLAPW electronic structure calculation code WIEN2k [Blaha et al., 2018, Blaha et al., 2020] in conjunction with the TRIQS library [Parcollet et al., 2015, Aichhorn et al., 2016].

4.6.2 $3d$ sublattice at zero temperature

In this thesis, the zero temperature K_1^{3d} is evaluated in a given compound by the method of [Liu et al., 2020], which we briefly derive below.

First, we introduce a coupling constant λ and parametrize the total many-body Hamiltonian describing the physics of the compound as $H(\lambda) = H_0 + \lambda H_{\mathrm{SO}}$ where H_{SO} is the spin-orbit Hamiltonian and $\lambda = 1$ corresponds to real physical magnitude of the spin-orbit coupling. The parametrized total energy is written as a perturbation expansion in λ: $E(\lambda) = \sum_n \lambda^n E_n$. Hellmann-Feynman allows us to write $E'(\lambda) = E^{\mathrm{SO}}(\lambda)/\lambda$ where $E^{\mathrm{SO}}(\lambda)$ is the parametrized spin-orbital energy. Subsequently, introducing a coupling-constant integration by λ, [Liu et al., 2020] show that $E^{\mathrm{SO}}(\lambda) = \sum_n n\lambda^n E_n$, and, to the second order in λ, $E^{\mathrm{SO}} = E^{\mathrm{SO}}(\lambda = 1) = 2E_2$. One then obtains $E = E(\lambda = 1) = E_0 + E_2 = E_0 + E^{SO}/2$ and $K_1 = E_{[100]} - E_{[001]} = (E^{\mathrm{SO}}_{[100]} - E^{\mathrm{SO}}_{[001]})/2$.

Hence, the $3d$ first anisotropy constant K_1^{3d} is evaluated from the change of $\mathcal{M}$ sublattice spin-orbital energy upon its moment rotation:

$$K_1^{3d} = \sum_i \Delta E_i^{\mathrm{SO}}/2, \tag{4.47}$$

where the sum runs over all $\mathcal{M}$ ions, $\Delta E_i^{\mathrm{SO}} = E_i^{\mathrm{SO}}(\boldsymbol{M}_{3d}||100) - E_i^{\mathrm{SO}}(\boldsymbol{M}_{3d}||001)$. The spin-orbit energy E_i^{SO} for site i is calculated as $\mathrm{Tr}\left[\rho_i^{3d}\hat{H}_{\mathrm{SO}}^{3d}\right]$, where ρ_i^{3d} is the on-site $3d$ density matrix for a given $\boldsymbol{M}_{3d}$ direction and the spin-orbit Hamiltonian $\hat{H}_{\mathrm{SO}}^{3d}$ is of the same form as for the $\mathcal{R}$ shell (see Sec. 4.3), with obviously different spin-orbit coupling λ_{3d}. In practice, for a given compound, we perform two separate SIC-LDA+HI calculations with the $\mathcal{M}$ moment aligned along [001] and [100], and a +U correction for the $\mathcal{M}$ $3d$ shells. This allows to compute ρ_i^{3d} along the two directions as well as to estimate the spin-orbit coupling λ_{3d}. K_1^{3d} then follows from equation 4.47.

At 0 K, both B_{ex} and the $3d$ spin moment are extracted from the material specific SIC-LDA+HI scheme described in subsection 4.6.1. Namely, B_{ex} is extracted from the converged one-electron $4f$ Hamiltonian. The $3d$ spin moment S_{3d} is calculated simultaneously. Since B_{ex} originates from the same $3d$ spin polarization in the same calculation, this treatment ensures consistent values of these parameters. We add to S_{3d} the computed value of L_{3d} with a +U correction for the $\mathcal{M}$ $3d$ shells.

One remark is due here regarding the choice of adding the +U correction to the $3d$ shell of $\mathcal{M}$ atoms. Describing the $\mathcal{M}$ sublattice with standard LSDA would result in poorly described magnetic properties. Indeed, the latter is well-known to significantly underestimate the orbital moment and the magnetic anistropy in $\mathcal{M}$ systems [Solovyev et al., 1998, Nguyen et al., 2018]. [Solovyev et al., 1998] showed that this orbital polarization is better described by DFT+U (see Sec. 3.8), used by [Nguyen et al., 2018] to describe magnetic properties of YCo_5 and $LaCo_5$ for instance.

Computational parameters used in this thesis. The +U correction for Fe (Co) atoms was specified with $U = 1.1$ (1.2) eV and $J = 0$ eV. The SIC-LDA+HI+U estimated spin-orbit coupling were $\lambda_{3d} = 60$ (70) meV for Fe (Co) atoms.

4.6.3 Temperature scaling of the $3d$ sublattice

Treating the $3d$ sublattice within DMFT is beyond our current possibilities as itinerant magnetism, which cannot be described by the simple HI approximation, would require the use of more advanced techniques like CTQMC (see. Sec. 2.4). This would be even more difficult for large unit cells including several crystallographically inequivalent $\mathcal{M}$ sites (like in "2-14-1" systems). Moreover, DMFT being a mean-field approximation tends to overestimate Curie temperatures by a significant uncontrolled factor.

Hence, consistently with the definition of the exchange field 4.30, $\mathbf{M}_{3d}(T)$ and $\mathbf{B}_{\text{ex}}(T)$ are assumed to be anti-aligned (as is the case in our calculations for T =0) and to follow the same temperature scaling, for which we use the semi-empirical one of [Kuz'min, 2005]:

$$M_{3d}(T) = M_{3d}\alpha(T) \tag{4.48}$$

$$B_{ex}(T) = B_{ex}\alpha(T) \tag{4.49}$$

$$\alpha(T) = \left[1 - s\left(\frac{T}{T_c}\right)^{\frac{3}{2}} - (1-s)\left(\frac{T}{T_c}\right)^{p}\right]^{\frac{1}{3}} \tag{4.50}$$

where T_c is the Curie temperature and s and p are material specific parameters. These three parameters are taken from experiment.

$K_1^{3d}(T)$ is assumed to follow the temperature scaling of [Zener, 1954]:

$$K_1^{3d}(T) = K_1^{3d}\Big(M_{3d}(T)/M_{3d}\Big)^3 \tag{4.51}$$

which gives $K_1^{3d}(T) = K_1^{3d}\alpha(T)^3$.

Computational parameters used in this thesis. According to [Kuz'min et al., 2010], $p = 5/2$, $s = 0.7$ in $Y_2Fe_{14}B$ and $p = 5/2$, $s = 0.4$ in $Gd_2Fe_{14}B$. According to [Kuz'min, 2005], $p = 5/2$, $s = 0.7$ in YCo_5. We hence used $p = 5/2$ and $s = 0.6$ (0.7) for "2-14-1" ("1-5") systems, neglecting changes along the $\mathcal{R}$ series.

Chapter 5

High-order crystal field, magnetic anisotropy and spin reorientation transition in $\mathcal{R}Co_5$ intermetallics

In this chapter, we focus on the "1-5" $\mathcal{R}Co_5$ system, which crystallizes in the hexgonal structure P6/*mmm* illustrated in figure 5.1. In the coordination frame with $z||c$ and $x||a$, the $\mathcal{R}$ $4f$ CF Hamiltonian 4.21 can be expressed as

$$\hat{H}_{CF} = A_2^0\hat{T}_2^0 + A_4^0\hat{T}_4^0 + A_6^0\hat{T}_6^0 + A_6^6\hat{T}_6^6. \tag{5.1}$$

In the next section, we analyze the CFPs along the series as computed by the SIC-LDA+HI approach described in the previous chapter.

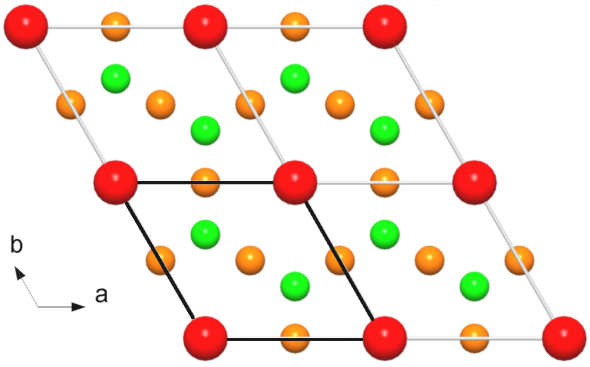

Figure 5.1: Crystal structure of the $\mathcal{R}Co_5$ family (view of the plane perpendicular to the hexagonal c = [001] direction). Red, green and orange balls represent $\mathcal{R}$, Co $2c$ and Co $3g$ atoms, respectively. The black bold lines indicate the unit cell.

The $\mathcal{R}Co_5$ family has been extensively studied experimentally. In particular, [Alameda, J. M. et al., 1982] measured the microscopic magnetization distribution on $NdCo_5$ single crystals by Polarized-Neutron Scattering (PNS) [Boucherle, J. X. et al., 1982], which allows the separation of

the $\mathcal{R}$ and $\mathcal{M}$ contributions to the magnetization. The measured Nd GS moment was found to be about 20% smaller than the saturation value of 3.27 μ_B, expected from calculations performed with values for B_{ex} and A_2^0 within acceptable ranges. This measured reduced Nd moment remained unexplained for almost 40 years. In sections 5.2-5.4, based on our work [Pourovskii et al., 2020], we present a solution to this mystery by studying the role of the high-rank A_6^6 CFP (often neglected in previous analyses) focusing on $NdCo_5$ and $TbCo_5$.

The $\mathcal{R}Co_5$ compounds also feature a rich variety of magnetic properties along the $\mathcal{R}$ series. At low temperatures, Pr and Ho systems feature an easy-cone phase; Nd, Tb and Dy an easy-plane one. These intermetallics then undergo a Spin Reorientation Transition (SRT) at higher temperatures which rotates the magnetization towards the hexagonal c = [001] axis [Tie-song et al., 1991, Kuz'min and Tishin, 2007]. Furthermore, the Sm compound was the first widely used $\mathcal{R}$-based permanent magnet [Strnat and Strnat, 1991] as it exhibits a strong uniaxial magnetic anisotropy. In section 5.5, we discuss these properties within our theoretical framework described in section 4.6.

Finally, in section 5.6, we explore a possible improvement to the Wannier projection scheme involved in the SIC-LDA+HI scheme.

5.1 Calculated rare-earth single-ion parameters

The CFPs and exchange field extracted from the converged SIC-LDA+HI[1] level positions (cf. Subsec. 4.6.1) for the $\mathcal{R}Co_5$ series are displayed in Fig. 5.2, along with the results of [Tie-song et al., 1991] obtained by fitting of experimental magnetization curves and those of [Novák, 1996] obtained from first-principles, using an open-core LDA approach.

We found for A_2^0 a non-monotonous behavior along the series, in a qualitative agreement with the experimental results of [Tie-song et al., 1991]. This is in contrast with the increasing behavior of [Novák, 1996]. A_4^0 and A_6^0 are found to have small absolute values of $\sim$ 30 K (except for Ce), which are in the same order of magnitude than those of [Tie-song et al., 1991, Novák, 1996] (not shown in Fig. 5.2 for clarity). As for the A_6^6 CFP, mostly ignored by [Tie-song et al., 1991], [Novák, 1996] computed high values decreasing along the series. We found a similar trend with values approximately twice as large (except for Ce). We discuss in depth the origin of these large A_6^6 values in section 5.4. Our computed B_{ex} is almost constant throughout the series and hence does not reproduce the decrease observed by [Tie-song et al., 1991] which was attributed to the decrease of the $4f$ radius along the series [Belorizky et al., 1987]. This discrepancy might stem from the fact that the SIC-LDA+HI scheme cannot take into account the feedback of the $4f$ moment on the $3d$ sublattice.

The SIC-LDA+HI approach also extracts E_0 and the $\mathcal{R}$ spin-orbit coupling λ, yielding for

[1] These parameters are obtained with the +U correction applied to Co and employed in Sec. 5.5. In Secs. 5.2-5.4, based on earlier work, the +U correction is not employed, leading to slightly different CFPs (mainly smaller values of the "20" CFP). For the sake of completeness, the CFPs, computed in both schemes, are given in the appendix 5.8.2.

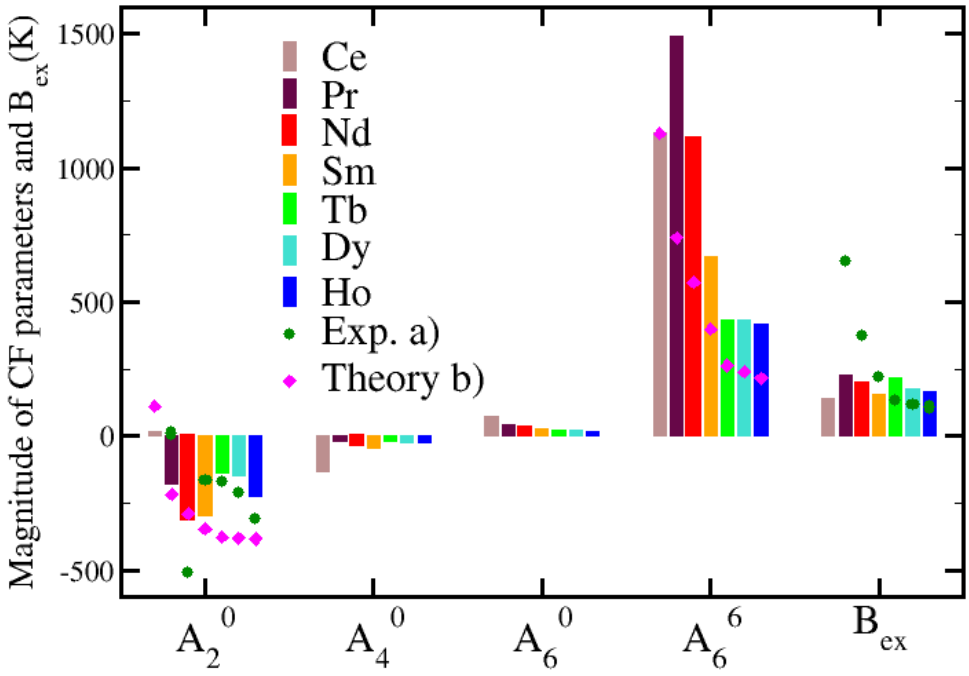

Figure 5.2: The SIC-LDA+HI calculated crystal-field parameters $A_k^q\langle r^q\rangle$ in $\mathcal{R}Co_5$ ($\mathcal{R}$= Ce, Pr, Nd, Sm, Tb, Dy, Ho). a) Experimental results of [Tie-song et al., 1991]. b) *Ab initio* results of [Novák, 1996].

instance λ =126 meV in $NdCo_5$, in good agreement with the experimental value of 110 meV for a Nd^{3+} ion in crystalline host [Carnall et al., 1989].

5.2 Magnetic properties of $NdCo_5$

5.2.1 $4f$ ground state and zero-temperature magnetization of $NdCo_5$

Nd^{3+} has the $[Xe]4f^3$ electronic configuration. According to Hund's rules (assuming LS coupling), neglecting crystal field effects for the moment, the GS multiplet of Nd^{3+} is $^4I_{9/2}$: spin $S = 3/2$, angular momentum $L = 6$ and total angular momentum $J = |L - S| = 9/2$. As the shell is less than half-filled, $\boldsymbol{L}$ and $\boldsymbol{S}$ are anti-aligned; $\boldsymbol{J}$ is aligned with $\boldsymbol{L}$. As explained in section 4.4, the exchange field tends to align $\boldsymbol{S}$ with $\boldsymbol{M}_{3d}$: for light rare-earths such as Nd it hence implies that $\boldsymbol{J}$ tends to be anti-aligned with $\boldsymbol{M}_{3d}$. Therefore, with the quantization axis along the GS magnetization direction in $NdCo_5$ [Alameda, J. M. et al., 1982] (i.e. along

$a = [100]$, see Fig. 5.1), one would expect a Nd GS wave function of the form:

$$\Psi_{\mathrm{GS}}^{\mathrm{Nd}} = |9/2; -9/2\rangle \tag{5.2}$$

with the usual notation $|J; \mu_J\rangle$ for the eigenstates of the total angular momentum. Correspondingly, one would expect a Nd moment of $M_{\mathrm{Nd}} = 3.27\mu_B$ as the Landé factor in the $J = 9/2$ multiplet is $g_J = 8/11$. Yet, [Alameda, J. M. et al., 1982] measured a value $\sim 20\%$ smaller than this expected saturated value at zero temperature.

With the SIC-LDA+HI calculated Nd single-ion parameters described in the previous section, the diagnoalization of the $4f$ Hamiltonian 4.26 (without applied field) gives however the following GS of the Nd $4f^3$ shell at zero temperature:

$$\begin{aligned}\Psi_{\mathrm{GS}}^{\mathrm{Nd}} = 0.827|9/2; -9/2\rangle - 0.536|9/2; -5/2\rangle \\ - 0.089|9/2; -1/2\rangle - 0.096|11/2; -9/2\rangle + 0.094|11/2; -5/2\rangle.\end{aligned} \tag{5.3}$$

As displayed in appendix 5.8.2, the first excited state is 220 K above in energy. The GS Nd magnetization is therefore determined by $\Phi_{\mathrm{GS}}^{\mathrm{Nd}}$ and equal to 2.66 μ_B. This reduced value compared to the saturated value of 3.27 μ_B of the GS multiplet ${}^4I_{9/2}$ of Nd^{3+} is due to the large contribution of $|9/2; -5/2\rangle$ in the GS wavefunction 5.3. Our theoretical GS is hence in an almost perfect agreement with the experimental one of [Alameda, J. M. et al., 1982] who assumed the GS wave function to be

$$\Psi_{\mathrm{GS}}^{\mathrm{Nd}} = \alpha|9/2; -9/2\rangle \pm \sqrt{1-\alpha^2}|9/2; -5/2\rangle, \tag{5.4}$$

with a factor α determining the relative weight of $\mu_J = -9/2$ and $\mu_J = -5/2$ contributions. From their measurements, [Alameda, J. M. et al., 1982] extracted $\alpha = 0.83$, yielding a Nd GS magnetic moment of 2.82 μ_B from equation 5.4. We obtain 2.84 μ_B by applying the same procedure to 5.3, i.e. by neglecting the contributions of excited multiplets and normalizing the GS wave function to 1 within the GS multiplet. If we set the "66" CFP to zero, the resulting GS wave function is purely $|9/2; -9/2\rangle$ corresponding to the fully saturated Nd moment. Hence, it is precisely this CFP that is preventing the full saturation of low-temperature Nd moment in $NdCo_5$.

In table 5.1, we compare our calculated CFPs and B_{ex} for $NdCo_5$ with previously reported experimental and theoretical values. We can notice that our "66" CFP is significantly larger than the literature values while our "20" CFP and exchange field are in the middle of them. For each set of CFPs+B_{ex}, we compute the value of α and the corresponding Nd GS moment from equation 5.4. As shown in table 5.1, none of the previous CFP evaluation approaches, despite the large scatter between their results, can reproduce the large contribution of $\mu_J = -5/2$ to the GS found by [Alameda, J. M. et al., 1982] and the corresponding reduction of the moment. The "freezing" of the Nd GS moment is hence a direct indication of the very large value of the "66" CFP in the compound.

	A_2^0	A_4^0	A_6^0	A_6^6	B_{ex}	α	M_{Nd}
[Radwański, 1986]	-210	-	-	-	101	1.0	3.26
[Tie-song et al., 1991]	-1020	0	115	150	245	0.94	3.20
[Zhang et al., 1994]	-397	-0.9	8.3	510	203	0.98	3.23
	-482	-0.9	8.3	510	393	0.99	3.25
[Novák, 1996]†	-288	-44.7	11.3	573	101	0.87	2.93
	-288	-44.7	11.3	573	302	0.96	3.18
[Patrick and Staunton, 2019]†	-415	-26	5.4	146	169	1.0	3.27
This work†	-285	-33	36	1134	196	0.84	2.84
Exp. [Alameda, J. M. et al., 1982]						0.83	2.82

Table 5.1: The CFPs and exchange field B_{ex} (in K) reported in previous theoretical and experimental works compared to the present one. The coefficient α in the GS wave function 5.4 and corresponding GS magnetic moment (in μ_B) calculated from given CFPs and B_{ex} are listed in the last two columns. *Ab initio* works are marked by †. [Zhang et al., 1994] report two sets of values for the CFPs and B_{ex}. [Novák, 1996] does not report B_{ex}, we thus employ two values representing the bounds of its generally accepted range. The measured α and Nd GS moment M_{Nd} are given in the last line.

5.2.2 Zero-temperature magnetic anisotropy of $NdCo_5$

To investigate the impact of A_6^6 on the Nd anisotropy energy E_{anis} at zero temperature, we compute the $4f$ free energy 4.29 for varying direction $\boldsymbol{n}$ of the exchange-field $\boldsymbol{B}_{ex} = B_{ex}\boldsymbol{n}$ (i.e. the direction of magnetization of the Co sublattice), as plotted in figure 5.3a. We obtain a strong Nd polar SIA favoring the in-plane phase, with the easy direction along the a direction of the hexagonal unit cell. If A_6^6 is not taken into account, we can also notice that the SIA of $NdCo_5$ is substantially reduced and favors an easy-cone phase. Therefore, the polar SIA of Nd in this compound is highly sensitive to the high-rank "66" CFP. In contrast, the azimuthal SIA is rather weak and is hence not a reliable signature for the relative magnitude of A_6^6.

In a hexagonal crystal, assuming possible truncation of the series and collinearity of the $3d$ and total moments, this anisotropy energy at zero temperature (see Eq. 4.34) reads

$$E_{anis}(\theta,\phi) = K_1 \sin^2\theta + K_2 \sin^4\theta + K_3 \sin^6\theta + K_3' \sin^6\theta \cos 6\phi, \tag{5.5}$$

where θ and ϕ are polar and azimuthal angles, respectively, of the magnetization direction in the coordination frame with $z||c$ and $x||a$. The $\mathcal{R}$ macroscopic anisotropy constants K are determined by the interplay of exchange field and CFPs. As shown in figure 5.3a, the calculated $\mathcal{R}$ anisotropy energy can be reasonably well fitted by equation 5.5 with three anisotropy constants, K_1, K_2 and K_3'. Though a more precise fitting is obtained by including K_3, we neglect it to facilitate the comparison with previous experimental measurements, in which K_3 was also neglected. The resulting values of Ks are listed in Table 5.2. The calculated anisotropy constants are in overall good agreement with experiments, taking into account a large scatter of experimental values. In particular, both our theory and experiment find a large negative value of K_1 and a positive constant K_2 of smaller magnitude. The overall negative MAE of $NdCo_5$, defined as

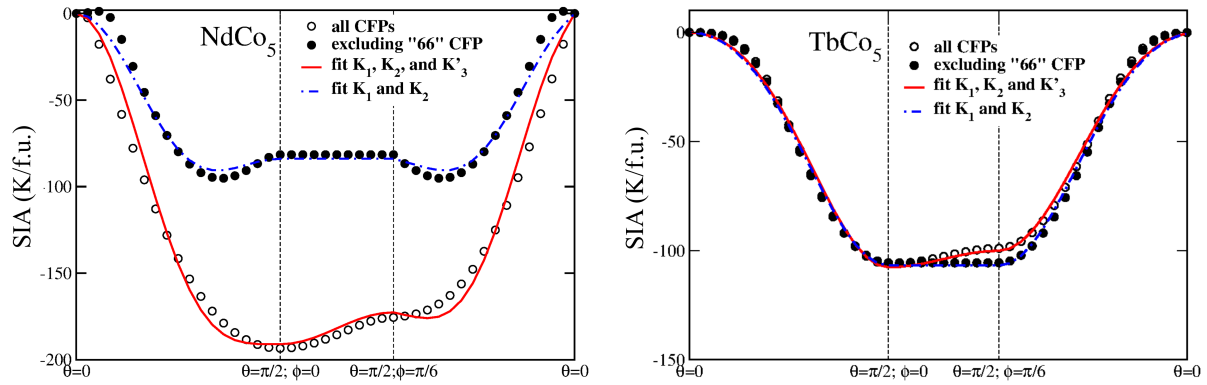

Figure 5.3: The ground state energy of rare-earth $4f$ shell in (a) $NdCo_5$ and (b) $TbCo_5$, as a function of the exchange field's direction $\boldsymbol{n}$, specified by the polar and azimuthal angles θ and ϕ. The direction $\boldsymbol{n}$ is initially along the lattice direction $c = [001]$. It is then rotated by $\pi/2$ about the y axis into the direction along the lattice a direction. This is followed by the rotation by $\phi = \pi/6$ in the ab plane and a subsequent rotation back into the uniaxial direction. Empty and filled circles indicate the values computed by direct diagonalization of the Hamiltonian 4.26 constructed with and without the CF parameter A_6^6, respectively. The solid lines are a least-square fit of calculated E_{anis} to the anisotropy-energy expression 5.5. The dashed blue and solid red line represent the obtained fits using the anisotropy constants specified in the legend.

$F(\boldsymbol{M}||a) - F(\boldsymbol{M}||c)$, is well reproduced when the "66" CFP is taken into account; without this high-rank CFP the magnitude of MAE is severely underestimated.

These results on the anisotropy constants can be compared to predictions of the standard linear-in-CF single-multiplet theory described in section 4.5. In the strictly exchange-dominated regime, A_6^6 CFP is shown to contribute only to the azimuthal dependence of $E_{\text{anis}}(\theta, \phi)$ determined by anisotropy constant K_3' (see Eq. 4.38); as follows from 5.5, it should thus have no impact on the average polar dependence of E_{anis}, in a drastic disagreement to the numerical results showing a strong enhancement of the in-plane anisotropy by the "66" CFP.

As we demonstrate in [Pourovskii et al., 2020], the conditions for broad exchange-dominance are fulfilled in $NdCo_5$ and $TbCo_5$. The strict exchange dominance regime is however not attained (see Sec. 4.5). However, the failure of the linear-in-CF theory is also due to its single-multiplet character: the large "66" CFP apparently induces strong inter-multiplet effects in $NdCo_5$, as we demonstrate explicitly in the next subsection.

$NdCo_5$

	with A_6^6	w/out A_6^6	Exp.
K_1	-393	-231	-510[c]
$K_1 + K_1^{3d}$	-348	-186	-244[a], -212[b], -468[c]
K_2	211	147	119[a], 87[b], 193[c]
K_3'	-9	-	-
MAE	-148	-37	-125[a], -125[b], -275[c]

$TbCo_5$

	with A_6^6	w/out A_6^6	Exp.
K_1	-59	-64	-99[c]
$K_1 + K_1^{3d}$	-14	-19	-57[c]
K_2	-45	-43	-36
K_3'	-4	-	-
MAE	-63	-62	-93[c]

Table 5.2: The zero-temperature rare-earth single-ion anisotropy constants and MAE (in K/f.u.). The theoretical values are extracted by fitting the angular dependence of the calculated anisotropy energy (Fig. 5.3) to equation 5.3. For the anisotropy constant of Co sublattice K_1^{3d}, we took the value of 45 K/f.u. measured in YCo_5, higher-order anisotropy constants of Co being negligible in accordance with experiment [Alameda et al., 1981]. Experimental values from [Tatsumoto, E. et al., 1971], [Ermolenko, 1976] and [Ermolenko, 1980b] are indicated by superscripts [a], [b] and [c], respectively.

5.2.3 Temperature dependence of single-ion anisotropy and role of J mixing

The previous section focused on the low-temperature magnetism of $NdCo_5$. Let us now consider the $4f$ magnetic anisotropy at elevated temperature T up to the Curie point $T_c = 910$ K of $NdCo_5$.

The calculated T-dependent Nd single-ion anisotropy SIA, defined as the difference of $4f$ free-energy between the [001] and [100] directions, is plotted in figure 5.4. The SIA exhibits the expected rapid decrease with increasing temperature. More interestingly, by comparing the SIA calculated with and without the "66" CFP one concludes that its strong impact on the anisotropy persists in the high-temperature regime. Indeed, its relative contribution $r_{66} = (\text{SIA} - \text{SIA}^*)/\text{SIA}$, where SIA^* is calculated excluding the "66" CFP, decreases rather slowly with the temperature and is still about 27% close to T_c (see inset in Fig. 5.4).

This behavior is, in fact, quite unexpected. Indeed, the high-temperature expansion of the $\mathcal{R}$ single-ion anisotropy predicts that only the "20" CFP contributes in the leading order in $1/T$ within the single-multiplet formalism (see Sec. 4.5). In order to understand better the origin of this behavior we computed the temperature evolution of SIA and SIA^* using the Stevens formalism (Eqs. 4.32 and 4.31), i.e. including only the Ground State Multiplet (GSM). As one sees in figure 5.4, excluding excited multiplets reduces the contribution of "66" CFP by about a quarter at $T = 0$ and by about 60% at $T = 300$ K. The inter-multiplet mixing thus significantly increases the "66" CFP contribution to the anisotropy, particularly, at room temperature and

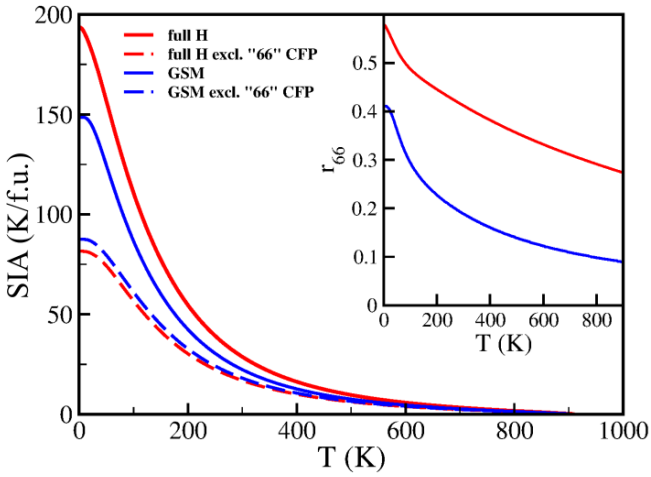

Figure 5.4: The temperature dependence of Nd SIA anisotropy in $NdCo_5$. The solid and dashed lines are calculated with all CFPs and with the "66" CFP excluded, respectively. Inset: the relative contribution of the "66" CFP to the SIA versus T.

above. Inversely, the role of inter-multiplet mixing is drastically enhanced by this CFP. Indeed, with the "66" CFP excluded the single-multiplet and full calculations produce very similar values for the $\mathcal{R}$ anisotropy energy.

5.3 Comparison to $TbCo_5$

We now turn to the case of the heavy $\mathcal{R}$ system $TbCo_5$. Tb^{3+} has the $[Xe]4f^8$ electronic configuration. According to Hund's rules, neglecting crystal field effects, the GS multiplet of Tb^{3+} is $^7F_6$: spin $S = 3$, angular momentum $L = 3$ and total angular momentum $J = L+S = 6$. As the shell is more than half-filled, $\boldsymbol{J}$ is aligned with $\boldsymbol{L}$ and $\boldsymbol{S}$; hence also with $\boldsymbol{M}_{3d}$. Therefore, one would expect a GS wavefunction of the form:

$$\Psi_{\mathrm{GS}}^{\mathrm{Tb}} = |6;6\rangle. \tag{5.6}$$

Our calculated GS wave function gives this pure total moment eigenstate 5.6 and correspondingly the fully saturated Tb moment – the first excited state is 232 K above, see appendix 5.8.2. Excluding the "66" CFP, only a negligible change in this GS wave function is observed.

We performed the same calculation of the $4f$ free energy with varying direction of the exchange field and subsequent fitting to extract the anisotropy constants. As displayed in figure 5.3b, with the"66" CFP included, the SIA favors an in-plane phase with the easy direction along the a axis, similarly to $NdCo_5$. The magnitude of the SIA is however about twice larger in $NdCo_5$ ($\sim$ 100 K versus $\sim$ 200 K). As shown in table 5.2, contrary to $NdCo_5$, we obtain negative and comparable values for K_1 and K_2 in $TbCo_5$. The overall MAE (including the Co contribution) is negative, corresponding to the in-plane a easy axis, and is about twice smaller

than in $NdCo_5$. These results are in qualitative agreement with the (to our awareness only) experimental measurements of [Ermolenko, 1980b]. Excluding the "66" CFP has a weak effect on the anisotropy energy, as shown in table 5.2 and in figure 5.3b.

Therefore, we can conclude that A_6^6 has a negligible impact on the low-temperature magnetic moment and anisotropy of Tb (apart from, obviously, inducing some planar anisotropy). This behavior is in sharp contrast to the one of $NdCo_5$, which might seem in contradiction to the approximately same ratio A_6^6/A_2^2 in these two systems (see appendix 5.8.2). However, the Stevens factor γ_J for the GS multiplet $^7F_6$ of Tb is much smaller than the the one of Nd $^4I_{9/2}$ ($-1.121 \cdot 10^{-6}$ versus $-38 \cdot 10^{-6}$). One may estimate the relative importance of "20" and "66" terms from the ratio of CF splittings generated by each of these CFPs in their GS multiplet:

$$d = \frac{\gamma_J A_6^6 (\langle \hat{O}_6^6(J) \rangle)\text{max}}{\alpha_J A_2^2 (\langle \hat{O}_2^0(J) \rangle)\text{max}}. \tag{5.7}$$

where the symbol $(\langle \hat{O}_k^q(J) \rangle)\text{max}$ designates the largest eigenvalue of the corresponding Stevens operator. Evaluating 5.7 with our SIC-LDA+HI calculated CFPs, we find d =3.28 and 0.19 for Nd and Tb, respectively. The "66" CFP is therefore about 17 times more significant in the case of $NdCo_5$. Therefore, while our calculations predict a large "66" CFP in all $\mathcal{R}Co_5$ compounds (see Fig. 5.2), the impact of this CFP on $\mathcal{R}$ magnetic moment and anisotropy is ion-dependent.

Moreover, the Tb CF states within its GS multiplet feature much smaller J-mixing as compared to the Nd ones (see tables 5.6 and 5.7 in appendix 5.8.2); hence, in contrast to the Nd case no strong impact of J-mixing on the anisotropy is expected.

5.4 Electronic structure, hybridization and rank-6 crystal-field in $\mathcal{R}Co_5$

As we have discussed in section 5.1, the SIC-LDA+HI method predicts an unexpectedly large value for A_6^6 in $\mathcal{R}Co_5$ compounds. In this section we aim at identifying physical origin of this result.

The crystalline environment of $\mathcal{R}$ site in $\mathcal{R}Co_5$ is invariant under the 6-fold rotation (Fig. 5.1), but not under an arbitrary rotation about the c axis, which is precisely the symmetry of $A_6^6 \hat{T}_6^6$ term. This points out to its likely origin in a spatially non-uniform in-plane interaction between $\mathcal{R}$ and its Co neighbors. Previous *ab initio* approaches miss the main contribution to the "66" CFP (see table 5.1) and rely on the open-core approach which completely neglects hybridization with other states. Within the Hubbard-I approximation however, the hybridization can enter into 3.39 implicitly, through the shape of $4f$ orbitals in which the matrix $\sum_{\mathbf{k}} P_{\mathbf{k}} H_{KS}^{\mathbf{k}} P_{\mathbf{k}}^\dagger$ in 3.40 is evaluated (see Subsec. 4.6.1). One may hence suspect that this contribution is due to a hybridization mixing between $\mathcal{R}$ and itinerant states. Mixing of localized $4f$s with, for example, Co $3d$ states, which are also to some degree localized, should lead in a simple tight-binding picture to the formation of directed bonds leading to the expected 6-fold symmetry of the resulting CF contribution.

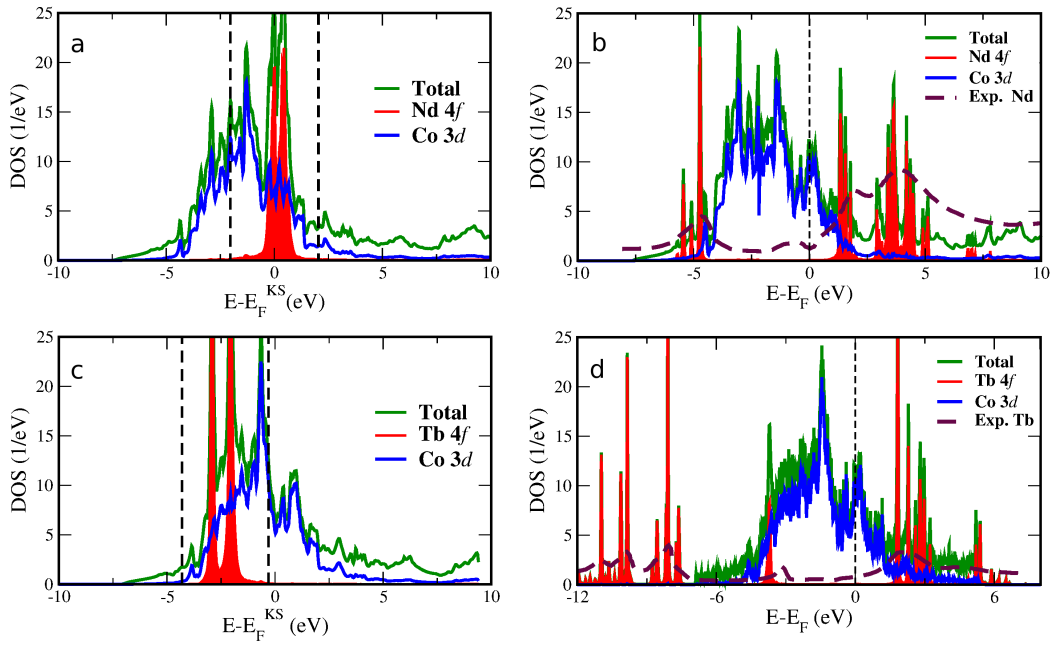

Figure 5.5: a) The density of Kohn-Sham (KS) states in $NdCo_5$ as obtained from the charge density converged in SIC-LDA+HI. In these calculations the exchange field on the Nd sublattice is suppressed by averaging (see Subsec. 4.6.1) and hence, Nd $4f$ band is not spin-polarized. The range included into the energy window $\mathcal{W} = [-2, 2]$ eV is indicated by vertical dashed lines. b) The SIC-LDA+HI spectral function of $NdCo_5$. The same plots for $TbCo_5$ are shown in panels c) and d), respectively. Notice the shift of the Tb $4f$ KS band to lower energies. The experimental photoemission and inverse-photoemission spectra displayed as brown dashed line in b) and d) are for the Nd and Tb metals [Lang et al., 1981].

These qualitative arguments can be verified within the SIC-LDA+HI approach by exploiting the flexibility of the $4f$ Wannier orbitals basis. As one sees in figure 5.5a, the Wannier window $\mathcal{W}$ used here includes all Nd $4f$, while a part of Co $3d$ bands are excluded. As explained in section 3.2, this small window results in extended Wannier orbitals due to hybridization admixture of other characters to those bands, as can be qualitatively analyzed by plotting them in the real space. The Nd $4f$ orbitals in $NdCo_5$ constructed for different magnetic quantum number m using the small energy windows are depicted in figure 5.6. One sees that the Wannier orbitals are extended and leak to neighboring Co sites, this leakage is orbitally-dependent (being rather small for $m = -1$ and large for $m = -2$ and -3), hence, directly contributing to the splitting of the corresponding one-electron levels. The matrix $\sum_{\mathbf{k}} P_{\mathbf{k}} H^{\mathbf{k}}_{KS} P^{\dagger}_{\mathbf{k}}$ computed in such an extended Wannier basis will be affected by hybridization. On the contrary, a large window would give very localized Wannier orbitals with no leakage to the Co neighbors, hence, the CFPs calculated in this case using SIC-LDA+HI approach should not include any contribution of hybridization and be solely determined by the electrostatic contribution. Indeed, using the window $[-9, 6]$ eV, the SIC-LDA+HI computed "66" CFP in $NdCo_5$ is 650 K, almost twice smaller than the value for the $\mathcal{W} = [-2, 2]$ eV window.

In figures 5.5b and 5.5d we display the calculated SIC-LDA+HI spectral function for $NdCo_5$ and $TbCo_5$, respectively. The quasiatomic multiplet structure of $\mathcal{R}$ $4f$ is compared to experimental photoemission spectra (PES) and inverse PES of the pure Nd and Tb metals [Lang et al., 1981] (we are not aware of any PES experiments on the Nd and Tb "1-5" systems). One observes a very good agreement between the positions of $4f$ peaks in SIC-LDA+HI and experimental PES.

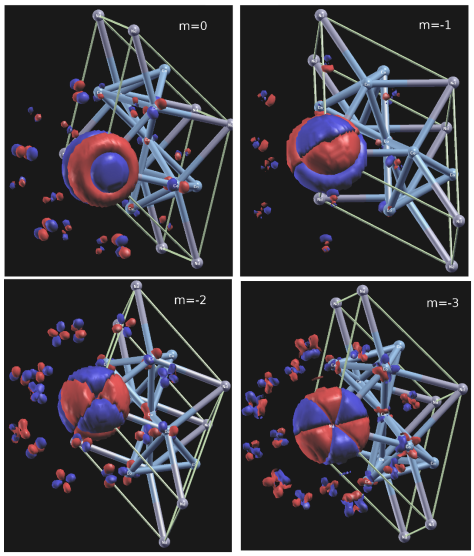

Figure 5.6: Nd $4f$ Wannier orbitals for m =0, -1 (upper row), -2, -3 (bottom row) constructed using the energy window $\mathcal{W} = [-2, 2]$ eV. The Wannier orbitals on this plot were constructed without spin-orbit to highlight the orbital dependence of their spread. The same value is used to define the isodensity surface in all cases.

Going along the $\mathcal{R}$ series, the $4f$ shell is getting more localized due to the higher atomic number Z of the atom. Hence, the hybridization is expected to go down. On the basis of this qualitative argument one expects a general decrease of "66" CFP in $\mathcal{R}Co_5$ along the $\mathcal{R}$ series, which we indeed find (except for Ce, see Fig. 5.2).

5.5 Magnetic anisotropy and spin reorientation along the series

In this section, using the SIC-LDA+HI CFPs and exchange field already described in section 5.1, we use the two sublattice model (see Sec. 4.4) to compute anisotropy constants of various $\mathcal{R}Co_5$ and study the Spin Reorientation Transition (SRT) along the $\mathcal{R}$ series.

To that end, we extracted the Co spin moment S_{3d} and orbital moment L_{3d} from the SIC-LDA+HI (with +U correction on Co) calculations for each $\mathcal{R}Co_5$, yielding the total Co moment $M_{3d} = S_{3d} + L_{3d}$. These calculations were performed with the Co moment aligned along c or in the ab plane, giving hence $M_{3d}(\theta_{3d} = 0)$ and $M_{3d}(\theta_{3d} = \pi)$. In accordance with [Tie-song et al., 1991], the total Co moment was assumed to feature some anisotropy in magnitude depending

on its direction and written as

$$M_{3d}(\theta_{3d}, T) = M_{3d}(T)(1 - p(T)\sin^2\theta_{3d}). \tag{5.8}$$

We assumed the anisotropy coefficient $p(T)$ to be temperature-independent and evaluated $p(0)$, in each compound, thanks to the ratio $M_{3d}(\theta_{3d} = \pi)/M_{3d}(\theta_{3d} = 0)$ of Co-sublattice moments aforementioned, yielding $p(0) \approx 0.04$, approximately constant throughout the series. This result is in excellent agreement with the value 0.037 of [Tie-song et al., 1991].

From these calculations with the +U correction for Co, we also computed the $\mathcal{R}$-specific Co sublattice anisotropy constant K_1^{3d} by the difference of spin-orbital energy upon rotation of the Co magnetic moment in each compound, as described in subsection 4.6.2. This yielded values between 28 and 58 K/f.u. along the series, in good agreement with the total K_1 measured in YCo_5 of $\sim$ 45 K/f.u. [Ermolenko, 1976] (under a quite reasonable assumption of Y not contributing to the anisotropy).

The temperature dependence of $M_{3d}(T)$ and $B_{ex}(T)$ ($K_1^{3d}(T)$) is assumed to follow Kuzmin (Zener) formulas, as described in subsection 4.6.3. The Curie temperatures were taken from [Tie-song et al., 1991].

$CeCo_5$ required a specific treatment. [Patrick and Staunton, 2019] suggested indeed that Ce is in an intermediate valence state for which the HI approximation is not sufficient. We hence followed an approach based on the work of [Galler et al., 2021b]. Namely, the free-energy contribution 4.29 of Ce was rescaled as

$$F_{4f}(T) \to \alpha_0(T)^2 F_{4f}(T) \tag{5.9}$$

where $\alpha_0(T) = \min\left(M_{\text{Ce}}^{\text{QMC}}(T)/M_{\text{Ce}}^{\text{HI}}(T), 1\right)$, $M_{\text{Ce}}^{\text{HI}}(T)$ is the Ce moment as calculated by SIC-LDA+HI and $M_{\text{Ce}}^{\text{QMC}}(T)$ the one calculated by a subsequent QMC calculation which can explicitly treat hybridization. Some details of this procedure are given in the appendix 5.8.1. These different parameters are summarized in table. 5.3.

	Ce	Pr	Nd	Sm	Tb	Dy	Ho
T_c (K)	650	910	910	980	980	970	1040
M_{3d} (μ_B/f.u.)	7.8	8.1	8.1	8.0	8.1	8.1	8.1
K_{3d} (K/f.u.)	40	46	28	32	58	56	55
K_{3d} (MJ.m^{-3})	6.6	7.5	4.6	5.2	9.5	9.2	9.0

Table 5.3: Summary of the parameters used in the two sublattice model of the $\mathcal{R}Co_5$. The Curie temperatures are taken from [Tie-song et al., 1991]. The $3d$ total magnetic moments and the magnetic anisotropies (in two widely used units) are computed from first principles thanks to the SIC+LDA+HI scheme with +U correction for Co, as described in the main text.

Then, by minimizing the total free energy 4.27, we computed the magnetization curves and subsequently extracted the anisotropy constants from the Sucksmith-Thompson method (see

Sec. 4.5) which are displayed in figure 5.7 and compared to experimental values of [Ermolenko, 1976], extracted with the same method. Overall, the agreement with experiment is reasonable, except for Pr at intermediate temperatures. Our calculations for instance reproduce the vanishing of K_2 at room temperatures in $NdCo_5$ and the strong uniaxial anisotropy of $SmCo_5$. Compared to the theoretical approach of [Patrick and Staunton, 2019], the present scheme treats heavy $\mathcal{R}$s (not investigated by the latter) and gives better agreement with experimental data for Ce – while maintaining similar accuracy for Pr, Nd and Sm.

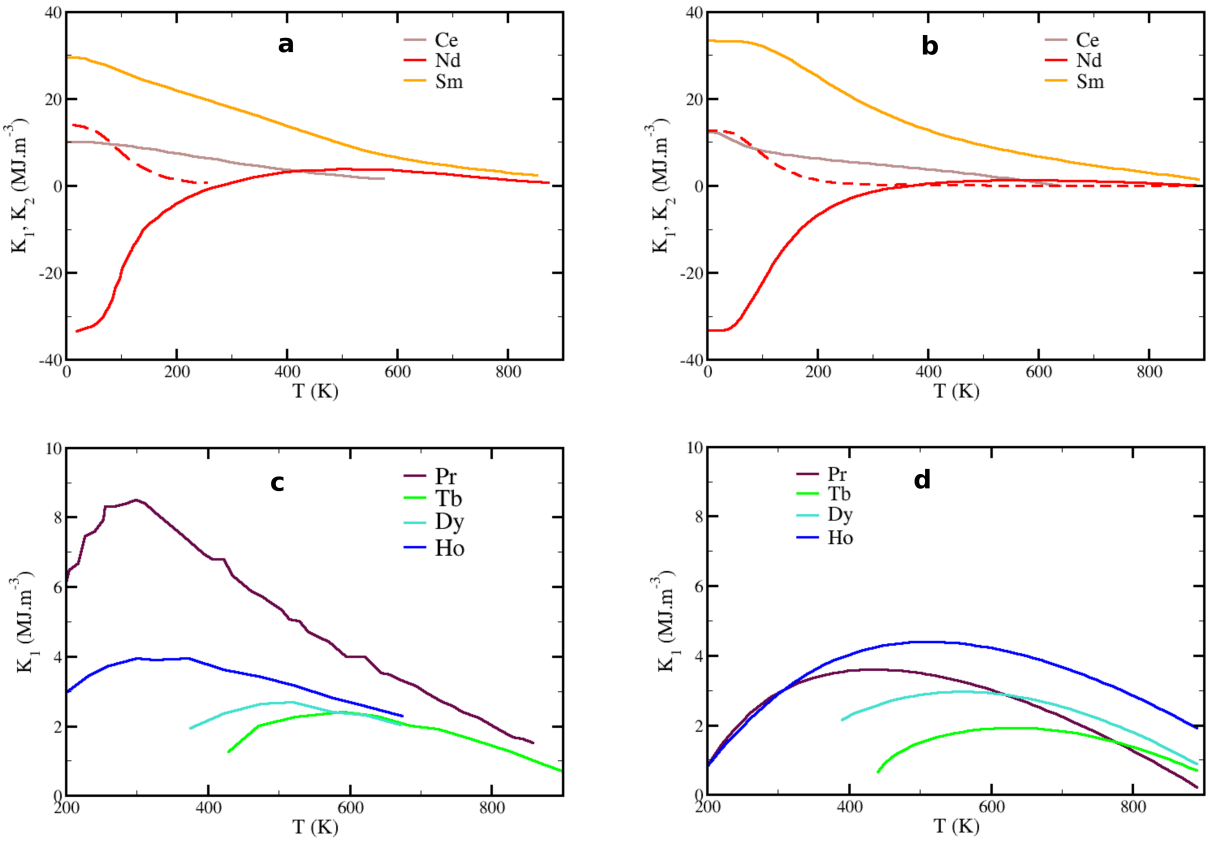

Figure 5.7: Anisotropy constants of the $\mathcal{R}Co_5$ compounds. Solid line: K_1. Dashed line: K_2. Left panel: experiment according to [Ermolenko, 1976]. Right panel: this work. Top panel: $\mathcal{R}$ = Ce, Nd, Sm for which the ST method was reasonable in the full range of temperature. Bottom panel: $\mathcal{R}$ = Pr, Tb, Dy and Ho for which the ST method was only reasonable in a restricted range of temperature.

Furthermore, the minimization of the total free energy 4.27 also gives the magnetic phase at a given temperature. As shown in figure 5.8, the approach correctly predicts the existence of a SRT in Pr, Nd, Tb, Dy and Ho and none in Ce and Sm. This SRT is due to the competition between positive K_1^{3d} (see table 5.3) and negative SIA of the $\mathcal{R}$ ions. The calculated SRT are also coherent with the calculated anisotropy constants displayed in figure 5.7: for example, Ce

and Sm have positive K_1 in the whole range of temperature (hence uniaxial phase) while the sign of K_1 in Nd changes, signalling the SRT (see [Kuz'min and Tishin, 2007]). The large negative value of the Nd SIA (and hence the planar phase) at 0 K is due to the large value of the "66" CFP discussed in the previous sections. Furthermore, our computations also predict the correct azimuthal angle according to experiment and the 'Stevens γ_J rule' (see [Kuz'min and Tishin, 2007]): at low T, $\phi = 0$ for Nd, Tb and Ho, $\phi = \pi/6$ for Pr and Dy. Comparing now the theoretical and experimental evolution of the angle θ between the total moment and the c axis, we get a moderate agreement. Our approach correctly predicts lower SRT temperatures for Pr and Ho compared to Nd, Tb and Dy and has a precision smaller than 100 K on the SRT temperatures. However, some precise features are not reproduced (conical phase for Pr and Ho, presence or not of a second "bump").

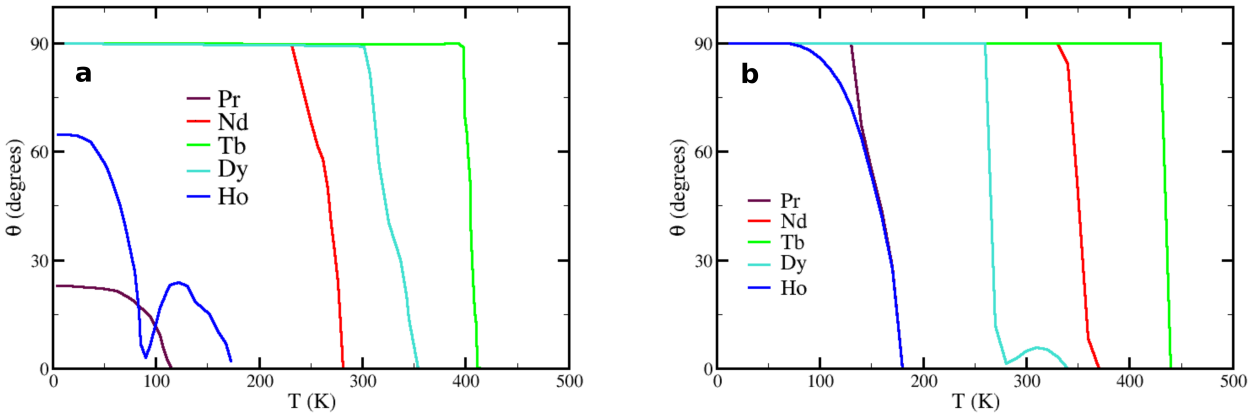

Figure 5.8: Evolution of the angle θ between the total moment and the c axis in $\mathcal{R}Co_5$ systems. a) Reproduced from the experimental results of [Ermolenko, 1979], [Ermolenko, 1980a], [Ermolenko and Rozenfeld, 1980], [Ermolenko and Rozhda, 1982], [Ermolenko and Rozhda, 1983] and [Ermolenko, 1983], as cited by [Tie-song et al., 1991]. b) This work.

5.6 Choice of the Wannier orbitals

In this chapter (and in the following one), we employed the Wannier projection scheme described in section 4.6.1, namely we chose the KS bands inside an energy window $\mathcal{W}$ of size 4 eV. As demonstrated by [Delange et al., 2017] and further discussed in the sections above, a large window results in localized $4f$ states while a small one takes into account leakage to neighboring ions due to hybridization. This choice can have a significant impact on the CFPs and hence on the calculated magnetic properties, as shown for the zero-temperature Nd moment in $NdCo_5$ (see Sec. 5.2) explained by the large value of "66" CFP arising from hybridization. It hence appears that a small window seems preferable. However, the precise size remains a parameter of the scheme. It gets even more complicated for heavy rare earths compounds as

their $4f$ KS bands are not pinned at the Fermi level in the "1-5" systems: the window must hence also be moved.

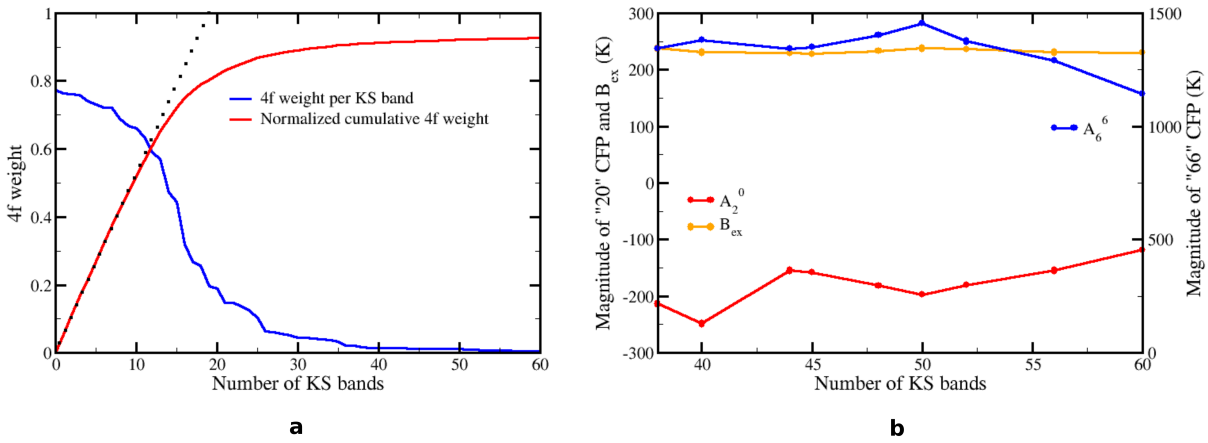

Figure 5.9: a) Pr $4f$ weight per KS band in $PrCo_5$ and their cumulative sum divided by 14. b) Pr SIC-LDA+HI CFPs and B_{ex} in $PrCo_5$ versus the number of KS bands with highest $4f$ character considered in the Wannier projection.

A more controlled way of constructing the Wannier orbitals would hence be beneficial. The idea which we explore in this section is the following. Let us take a relatively large window of $[-9, 6]$ eV and look at the $4f$ weight of the enclosed bands. To include most of this weight and have well defined Wannier functions while taking into account hybridization as discussed above, it seems reasonable to consider for the projection the KS bands with the highest $4f$ character. Figure 5.9a displays, in the case of $PrCo_5$, the (sorted) $4f$ weight per KS band inside this large window as well as the normalized cumulative weight (i.e. the sum of these weights divided by 14). It is clear that the projection cannot take all the (79) bands in the window (otherwise hybridization is not taken into account) neither too few KS bands (otherwise significant $4f$ weight is missing). To fix the exact number of projected bands N, one could try a linear fit of the low-N part of the cumulative weight (as illustrated in Fig. 5.9a) and take the intersection of this line with the asymptote at infinity, i.e. weight $= 1$. In the case of $PrCo_5$, this would yield $N \approx 19$. This value proved however to be too small, several bands with high amount of $4f$ character are indeed missing. This leads to poor $4f$ state representation as qualitatively illustrated in figure 5.10 showing $4f$ Wannier-projected $\boldsymbol{k}$-resolved spectral function in the case of $NdCo_5$: one sees that for $N = 18$ bands, the resulting spectral function $P_{\boldsymbol{k}} G_{\boldsymbol{k}}(\omega) P_{\boldsymbol{k}}^{\dagger}$ is highly discontinuous, while at $N = 30$ bands it is quite well behaving.

The number of bands therefore remains a parameter of the calculation that one needs to optimize. In our experience in the "1-5" system, it should be above ~ 30 (to ensure correct $4f$ representability) and below ~ 55 (to ensure treatment of hybridization). In this range, the CFPs exhibit moderate N dependence, as illustrated in figure 5.9b in the case of $PrCo_5$ for instance. For comparison, in the same compound, with the $[-2, 2]$ eV window which encloses ~ 43 bands,

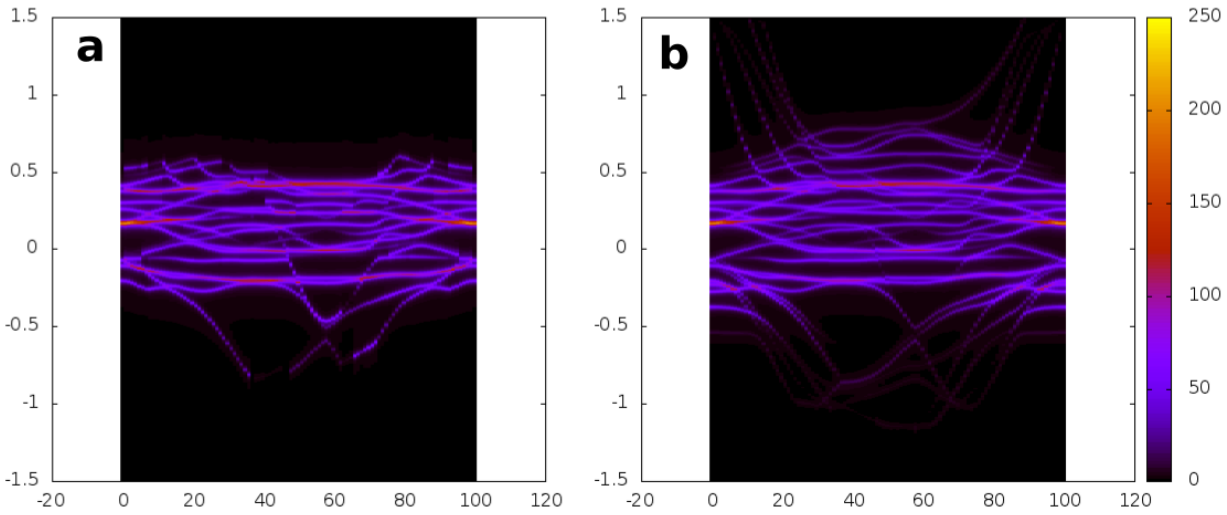

Figure 5.10: Projected-Wannier spectral function $P_{\boldsymbol{k}}G_{\boldsymbol{k}}(\omega)P_{\boldsymbol{k}}^{\dagger}$ in $NdCo_5$ with different numbers of KS bands considered for the creation of Nd Wannier orbitals as explained in the main text. a) 18 KS bands. b) 30 KS bands.

the "20" , "66" CFPs and B_{ex} were estimated as -179, 1493 and 228 K respectively (see Fig. 5.2). The number of bands N can be a better controlled input than the size and position of the window $\mathcal{W}$, since this scheme does not depend on the $4f$ band position or its precise structure (the evolution of spin-orbit splitting, which becomes larger in heavy rare earths hence increasing the total $4f$ bandwidth, see Figs. 5.5a and 5.5c).

5.7 Conclusion

In this chapter, we have calculated the $\mathcal{R}$ crystal-field parameters (CFPs) in magnetic intermetallics $\mathcal{R}Co_5$ using the *ab initio* SIC-LDA+HI methodology of [Delange et al., 2017] with the additionnal +U correction for Co $3d$ shells. The low-rank CFPs are in relatively good agreement with experimental results. Our study reveals that the high-order "66" CFP A_6^6 takes exceptionally large values in these $\mathcal{R}Co_5$ systems, especially for light $\mathcal{R}$ elements.

In particular, in $NdCo_5$, this CFP is found to freeze the ground-state Nd moment well below its fully saturated value. We show that this freezing of the GS moment, previously observed [Alameda, J. M. et al., 1982] but not explained, represents in fact an experimental fingerprint of a large A_6^6 CFP in this system. Our calculations reveal a strong impact of this CFP on the $NdCo_5$ anisotropy and its temperature dependence. In contrast, in the case of $TbCo_5$ the "66" CFP has a very weak influence on the magnetic anisotropy and does not affect the GS magnetization. This is explained by a relatively small order-six Stevens coefficient of the Tb GSM reducing the impact of order-6 CFPs on its magnetism. The influence of A_6^6 on the magnetism of $\mathcal{R}Co_5$ is thus $\mathcal{R}$-ion specific.

The large value of A_6^6 in $\mathcal{R}Co_5$ is shown to be induced by hybridization between the $\mathcal{R}$ $4f$

shell and its 6-fold coordinated crystalline environment. In our SIC-LDA+HI approach this hybridization is taken into account indirectly, through the shape of $4f$ orbitals, which become less localized due to hybridization effects. Neglecting the impact of hybridization to CFPs reduces significantly the magnitude of calculated A_6^6. Along the $\mathcal{R}$ series, the contraction of the $4f$ shell reduces this hybridization resulting in a general reduction of the "66" CFP.

More generally, this chapter shows that hybridization mixing of $\mathcal{R}$ $4f$ shell with its q-fold coordinated environment may lead to the appearance of large CFPs A_k^q, with $q \neq 0$. These high-order CFPs are traditionally considered to be much less important for the $\mathcal{R}$ single-ion magnetic anisotropy as compared to low-order A_2^0. The present chapter shows that this assumption does not always hold. By modifying the local environment of the $\mathcal{R}$ ion by $\mathcal{M}$ substitutions or small-atom insertions one can change the hybridization, and, hence, these high-order CFPs. As shown in the present chapter, using an advance *ab initio* methodology one can describe such hybridization-induced CFPs and their impact on magnetic anisotropy. This opens an opportunity for theoretical optimization of $\mathcal{R}-\mathcal{M}$ intermetallics with respect to such properties as the single-ion magnetic anisotropy, the temperature of spin-reorientation transitions, or the magnetocaloric effect [Nikitin et al., 2010, Wang et al., 2019].

We have also computed from first principles the anisotropy constant K_1^{3d} of the Co sublattice in $\mathcal{R}Co_5$ compounds and used it together with computed $\mathcal{R}$ parameters (CFPs, exchange, SO) within the two sublattice model. With this almost parameter-free approach, the calculated temperature-dependent anisotropy constants and SRT temperatures were shown to be in reasonable agreement with experimental results.

Finally, we have explored a possibly more controlled way of constructing the $4f$ Wannier orbitals, by choosing the KS bands which have the highest $4f$ character.

5.8 Appendix

5.8.1 Treatment of Ce

In the case of Ce, which is in an intermediate valence state, the HI approximation is not sufficient. To go beyond this HI treatment, we followed the method of [Galler et al., 2021b] which used a Coqblin-Schrieffer [Coqblin and Schrieffer, 1969] approach for the Anderson impurity Hamiltonian

$$\hat{H}_{\text{AIM}} \approx \hat{H}_{\text{CS}} = \hat{H}^{\text{S}}_{\text{ex}} + \hat{H}^{\text{S}}_{\text{CF}} + \hat{H}_{\text{K}} + \hat{H}_{\text{c}} \tag{5.10}$$

where $\hat{H}^{\text{S}}_{\text{ex}}$ is the exchange Hamiltonian 4.31 in the GS J multiplet, $\hat{H}^{\text{S}}_{\text{CF}}$ is the CF Hamiltonian within the Stevens formalism 4.32 in the GS J multiplet, H_{K} is a Kondo-like coupling between the impurity and the bath represented by $\hat{H}_{\text{c}}$. [Galler et al., 2021b] assumed that, for given angles $\mathbf{\Omega}$ of the exchange field (and hence $3d$ moment), the Ce GS wavefunction was given by

$$|\Psi(\mathbf{\Omega}, \alpha)\rangle = \sqrt{1-\alpha^2}\,|\Psi_{\text{Sph}}\rangle + \alpha\,|\Psi_J(\mathbf{\Omega})\rangle \tag{5.11}$$

where $|\Psi_J\rangle$ is the GS wavefunction in the case $\hat{H}_{\text{K}} = 0$ (i.e. it reduces the impurity to its atomic limit) and $|\Psi_{\text{Sph}}\rangle$ the GS wavefunction in the case $\hat{H}^{S}_{ex} = 0$, assumed to be spherically symmetric. The parameter α is to be chosen by the variational principle

$$\frac{\partial \langle\Psi(\mathbf{\Omega}, \alpha)|\hat{H}_{\text{CS}}(\alpha)|\Psi(\mathbf{\Omega}, \alpha)\rangle}{\partial \alpha} = 0. \tag{5.12}$$

Let us denote by α_0 the value of α obtained by this variational principle in the case $\mathbf{\Omega} = 0$. Following the main ideas of the [Galler et al., 2021b] (perturbation theory in CF), we approximate the difference of energy between cases $\mathbf{\Omega}$ and 0 by

$$\begin{aligned}
E_{\text{anis}}(\mathbf{\Omega}) &= E(\mathbf{\Omega}, \alpha) - E(0, \alpha_0) && (5.13)\\
&\approx E(\mathbf{\Omega}, \alpha_0) - E(0, \alpha_0) && (5.14)\\
&\approx \alpha_0^2 \langle\Psi_J(\mathbf{\Omega})|\hat{H}^{\text{S}}_{\text{CF}}|\Psi_J(\mathbf{\Omega})\rangle - \alpha_0^2 \langle\Psi_J(0)|\hat{H}^{\text{S}}_{\text{CF}}|\Psi_J(0)\rangle && (5.15)\\
&\approx \alpha_0^2\ E^{\text{at}}_{\text{anis}}(\mathbf{\Omega}) && (5.16)
\end{aligned}$$

where $E^{\text{at}}_{\text{anis}}(\mathbf{\Omega})$ is the anisotropy energy in the quasi-atomic limit, i.e. computed within HI. Following [Galler et al., 2021b], we also get for the magnetization of Ce

$$\boldsymbol{M} = \alpha_0^2 \boldsymbol{M}^{\text{at}}. \tag{5.17}$$

where $\boldsymbol{M}^{\text{at}}$ is the magnetization in the quasi-atomic limit. Hence, approximating finite temperature by the low T regime, the $4f$ contribution to the free energy for a Ce ion is approximately given by:

$$\begin{aligned}
F_{4f}(T, \mathbf{\Omega}) &\approx -\boldsymbol{M}(T) \cdot \boldsymbol{H}_{ext} + E_{anis}(T, \mathbf{\Omega}) && (5.18)\\
&\approx \alpha_0(T)^2 F^{at}_{4f}(T). && (5.19)
\end{aligned}$$

The parameter $\alpha_0(T)$ was estimated as $\alpha_0^2 = \min(M(T)/M^{\text{at}}(T), 1)$, where $M(T)$ was computed by CTQMC calculations with density-density local Coulomb interaction 3.22, neglecting the off-diagonal part of the hybridization in the basis where the effective atomic levels 3.40 are diagonal. We used the TRIQS library [Parcollet et al., 2015].

5.8.2 CFPs and CF states

In table 5.4, we list the CFPs and B_{ex} in $NdCo_5$ and $TbCo_5$ calculated from the SIC-LDA+HI scheme. In tables 5.6 and 5.7, we list the corresponding calculated $4f$ wave functions within the GSM (for Nd and Tb respectively); the coordinate system is chosen in accordance with [Alameda, J. M. et al., 1982], i.e. with the local quantization axis $z||a$ and $x||c$ and the states are written as the expansion $\sum a(J,\mu_J)|J;\mu_J\rangle$ in pure angular momentum eigenstates $|J;\mu_J\rangle$ of a given occupancy – all contributions with $a^2(J,\mu_J) > 10^{-3}$ are shown. In table 5.5, we list the SIC-LDA+HI calculated CFPs and B_{ex} in $\mathcal{R}Co_5$ with the +U correction for Co $3d$ shells.

	A_2^0	A_4^0	A_6^0	A_6^6	B_{ex}
$NdCo_5$	-285	-32	36	1134	196
$TbCo_5$	-118	-20	20	440	208

Table 5.4: SIC-LDA+HI calculated crystal-field parameters and exchange field (in K) in $\mathcal{R}Co_5$ ($\mathcal{R}$ = Nd,Tb). The quantization axis is along the hexagonal [001] direction.

	A_2^0	A_4^0	A_6^0	A_6^6	B_{ex}
$CeCo_5$	16.5	-132	72	1131	139
$PrCo_5$	-179	-21	43	1493	228
$NdCo_5$	-313	-34	34	1111	199
$SmCo_5$	-297	-46	29	669	158
$TbCo_5$	-136	-17	20	435	215
$DyCo_5$	-145	-22	20	433	179
$HoCo_5$	-234	-22	16	419	165

Table 5.5: SIC-LDA+HI with +U correction for Co calculated crystal-field parameters and exchange field (in K) in $\mathcal{R}Co_5$ ($\mathcal{R}$ = Ce, Pr, Nd, Sm, Tb, Dy, Ho). The quantization axis is along the hexagonal [001] direction.

$E - E_{GS}$ (K)	Eigenstates in $\|J;\mu_J\rangle$ basis
0	$+0.827\|9/2;-9/2\rangle - 0.536\|9/2;-5/2\rangle - 0.096\|11/2;-9/2\rangle + 0.094\|11/2;-5/2\rangle - 0.089\|9/2;-1/2\rangle$
220	$+0.702\|9/2;-3/2\rangle + 0.690\|9/2;-7/2\rangle - 0.117\|9/2;+5/2\rangle - 0.103\|11/2;-3/2\rangle - 0.063\|9/2;+1/2\rangle$
280	$+0.760\|9/2;-5/2\rangle + 0.535\|9/2;-9/2\rangle + 0.305\|9/2;-1/2\rangle - 0.158\|9/2;+3/2\rangle - 0.092\|9/2;+7/2\rangle$ $-0.079\|11/2;-1/2\rangle - 0.045\|11/2;-5/2\rangle + 0.032\|11/2;+7/2\rangle$
526	$+0.708\|9/2;-7/2\rangle - 0.687\|9/2;-3/2\rangle + 0.091\|11/2;-3/2\rangle + 0.081\|9/2;+1/2\rangle - 0.079\|9/2;+5/2\rangle$ $+0.058\|9/2;+9/2\rangle - 0.034\|11/2;-7/2\rangle - 0.032\|11/2;-11/2\rangle$
642	$+0.668\|9/2;-1/2\rangle - 0.613\|9/2;+3/2\rangle - 0.333\|9/2;-5/2\rangle - 0.189\|9/2;+7/2\rangle - 0.138\|9/2;-9/2\rangle$ $-0.087\|11/2;-1/2\rangle + 0.056\|11/2;+3/2\rangle + 0.036\|11/2;+7/2\rangle$
697	$+0.789\|9/2;+5/2\rangle + 0.567\|9/2;+1/2\rangle - 0.183\|9/2;+9/2\rangle + 0.107\|9/2;-7/2\rangle + 0.068\|9/2;-3/2\rangle$ $-0.046\|11/2;+5/2\rangle - 0.040\|11/2;+9/2\rangle - 0.032\|11/2;-3/2\rangle$
738	$+0.666\|9/2;+3/2\rangle + 0.653\|9/2;-1/2\rangle + 0.330\|9/2;+7/2\rangle - 0.094\|9/2;-5/2\rangle - 0.078\|11/2;-1/2\rangle$ $-0.056\|11/2;+7/2\rangle$
829	$+0.807\|9/2;+1/2\rangle - 0.524\|9/2;+5/2\rangle + 0.201\|9/2;+9/2\rangle - 0.102\|11/2;+1/2\rangle - 0.094\|9/2;-7/2\rangle$ $+0.075\|11/2;+5/2\rangle + 0.071\|9/2;-3/2\rangle - 0.040\|11/2;-3/2\rangle$
1070	$+0.956\|9/2;+9/2\rangle + 0.252\|9/2;+5/2\rangle - 0.102\|11/2;+5/2\rangle - 0.064\|9/2;+1/2\rangle + 0.055\|9/2;-3/2\rangle$ $-0.055\|11/2;+9/2\rangle$
1111	$+0.905\|9/2;+7/2\rangle - 0.387\|9/2;+3/2\rangle - 0.139\|11/2;+7/2\rangle - 0.065\|9/2;-1/2\rangle + 0.059\|9/2;-5/2\rangle$ $+0.041\|11/2;+11/2\rangle + 0.040\|11/2;+3/2\rangle$

Table 5.6: SIC-LDA+HI calculated eigenvalues and eigenstates of Nd $4f$ shell in $NdCo_5$

$E - E_{GS}$, K	Eigenstates in $\|J;\mu_J\rangle$ basis
0	$+1.000\|6;+6\rangle$
232	$+0.994\|6;+5\rangle + 0.091\|6;+3\rangle + 0.048\|5;+5\rangle$
428	$+0.991\|6;+4\rangle + 0.098\|6;+2\rangle + 0.080\|5;+4\rangle$
634	$+0.989\|6;+3\rangle - 0.093\|6;+5\rangle + 0.088\|5;+3\rangle + 0.076\|6;+1\rangle$
844	$+0.988\|6;+2\rangle - 0.098\|6;+4\rangle + 0.095\|5;+2\rangle + 0.059\|6;+0\rangle$
1050	$+0.989\|6;+1\rangle + 0.103\|5;+1\rangle - 0.076\|6;+3\rangle + 0.060\|6;-1\rangle$
1251	$+0.989\|6;+0\rangle + 0.109\|5;+0\rangle + 0.076\|6;-2\rangle - 0.060\|6;+2\rangle$
1448	$+0.987\|6;-1\rangle + 0.110\|5;-1\rangle + 0.090\|6;-3\rangle - 0.062\|6;+1\rangle$
1647	$+0.987\|6;-2\rangle + 0.104\|5;-2\rangle + 0.088\|6;-4\rangle - 0.078\|6;+0\rangle$
1852	$+0.989\|6;-3\rangle + 0.093\|5;-3\rangle - 0.091\|6;-1\rangle + 0.063\|6;-5\rangle$
2059	$+0.992\|6;-4\rangle - 0.087\|6;-2\rangle + 0.083\|5;-4\rangle$
2260	$+0.995\|6;-5\rangle + 0.071\|5;-5\rangle - 0.061\|6;-3\rangle$
2440	$+1.000\|6;-6\rangle$

Table 5.7: SIC-LDA+HI calculated eigenvalues and eigenstates of Tb $4f$ shell in $TbCo_5$

Chapter 6

Ce and Dy substitutions in $Nd_2Fe_{14}B$: site-specific magnetic anisotropy from first principles

As detailed in section 4.1, $Nd_2Fe_{14}B$ is currently the most widely used high-performance permanent magnet in the industry and the properties of this intermetallic can be further enhanced by doping with Dy or Tb. However, mining rare-earths is polluting and these elements can be quite expensive, especially heavy ones. Therefore, efforts are being made to find alternative high-performance magnets with reduced (heavy) rare-earth concentration; Ce-substituted compounds have especially gained attention as this element is more abundant and cheaper than Nd. In this chapter based on our work [Boust et al., 2022a], we study the optimization of the intrinsic properties of Ce and Dy doped $Nd_2Fe_{14}B$ systems.

Below, we hence apply the SIC-LDA+HI methodology (see Sec. 4.6.1) to compounds of the form $(Nd_{1-x}\mathcal{R}_x)_2Fe_{14}B$ ($\mathcal{R}$ = Ce, Dy) which crystallize in the $P4_2/mnm$ structure shown in figure 6.1. This crystal structure features two different planes $z = 0$ and $z = 1/2$ as well as two inequivalent $\mathcal{R}$ sites: the smaller one is labeled f, the larger one g. The unit cell is large (68 atoms), which makes *ab initio* calculations challenging. This chapter is organized as follows: in section 6.1, we present our calculational approach to $3d$-sublattice parameters, namely $M_{3d}(T)$ and $K_1^{3d}(T)$, and list their obtained values; in section 6.2, we detail the computed Nd and Dy CFPs and exchange field B_{ex} for each inequivalent $\mathcal{R}$ site in the unit cell; basing on these parameters, we analyze in section 6.3 the magnetic properties of pure $Nd_2Fe_{14}B$. In section 6.4 (6.5) the partial Nd substitution by Ce (Dy) is discussed, focusing on the impact of site occupancy. The reader can refer to the famous review of [Herbst, 1991] for more details on $Nd_2Fe_{14}B$-based systems.

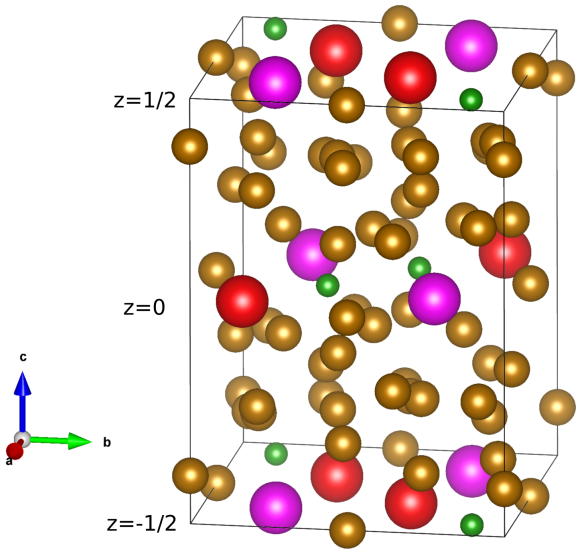

Figure 6.1: "2-14-1" crystal structure showing the different z planes and inequivalent $\mathcal{R}$ sites: $\mathcal{R}$ f site in purple, $\mathcal{R}$ g site in red (Fe: large brown, B: small green). These sites are also often labeled as $4f$ and $4g$ in the literature but we keep f and g in this chapter to avoid confusion with the notation for the $\mathcal{R}$ $4f$ electrons. Plotted with VESTA [Momma and Izumi, 2011].

6.1 Parameters of the 3d sublattice

We assume the zero-temperature $\mathcal{M}$ anisotropy constant K_1^{3d} in $\mathcal{R}_2Fe_{14}B$ systems to be independent on the $\mathcal{R}$ ions and evaluate it in $La_2Fe_{14}B$ by performing two separate LDA+U calculations with the 3d moment aligned along [001] and [100]. K_1^{3d} is evaluated as the difference of spin-orbital energy upon rotation of the $\boldsymbol{M}_{3d}$, as described in subsection 4.6.2. This approach yields the value $K_1^{3d} = 0.4$ MJ.m^{-3} for $La_2Fe_{14}B$, in reasonable agreement with experimentally measured value $K_1^{3d} = 0.7$ MJ.m^{-3} [Bolzoni et al., 1987]. We also expect the 3d zero-temperature orbital moment L_{3d} to be essentially independent on the $\mathcal{R}$ ions in the system. We therefore evaluate it by LDA+U in $La_2Fe_{14}B$ with $\boldsymbol{M}_{3d}$ aligned with [001], yielding 0.06 μ_B/atom, in reasonable agreement with the experimental value of ~ 0.08 μ_B/atom [García et al., 2000a].

The 3d spin moment S_{3d} computed by the material specific SIC-LDA+HI as described in subsection 4.6.2 yields essentially the same value 30 μ_B/f.u. in $Nd_2Fe_{14}B$ and $Dy_2Fe_{14}B$. It hence gives a total moment per unit cell of $M_{3d} = L_{3d} + S_{3d} = 30.8$ μ_B at zero temperature.

A special treatment is necessary for Ce-based compounds. Indeed, according to the measurements of [Colin et al., 2016], Ce is found in an intermediate valence state dominated by Ce^{4+} in "2-14-1" intermetallics, the description of which would require the use of more sophisticated and computationally heavy many-body approaches such as Quantum Monte-Carlo [Galler et al., 2021b], as done for $CeCo_5$ in section 5.5. Moreover, in "2-14-1" systems with localized rare earths, those localized $\mathcal{R}$ ions (Nd, Dy etc.) provide a dominant contribution to the magnetic anisotropy. The contribution of Ce, whether with an itinerant or localized $4f$ shell, is expected

to be relatively small, in particular at room temperature and above (as shown by [Galler et al., 2021b]). Therefore, in mixed compounds $(Nd_{1-x}Ce_x)_2Fe_{14}B$:

- In CFP calculations of Nd by the SIC-LDA+HI scheme described above, Ce is treated within LDA;
- Ce contributions to the magnetic moment and anisotropy in the two sublattice model are described by a mere renormalization of the same $3d$ quantities at zero temperature. Specifically, as the total experimental moment per unit cell in $Ce_2Fe_{14}B$ is 29.4 μ_B at 4.2 K [Herbst, 1991], we adapt $M_{3d} = 30.8(1-x) + 29.4x$ μ_B per unit cell. Furthermore, as our experimental collaborators measured a larger zero temperature $K_1 = 1.6$ MJ.m^{-3} in $Ce_2Fe_{14}B$ (in agreement with previous measurements [Bolzoni et al., 1987, Hirosawa et al., 1986]) compared to $La_2Fe_{14}B$, we adapt $K_1^{3d} = 0.4(1-x) + 1.6x$ MJ.m^{-3} (see table 6.1).

The temperature dependences of $M_{3d}(T)$ (and therefore also of $B_{ex}(T)$) and $K_1^{3d}(T)$ are assumed to follow Kuz'min and Zener formulas respectively, as described in subsection 4.6.3. The Curie temperature is taken from experiment [Herbst, 1991] for pure compounds and computed as the weighted sum of parent pure compounds for mixed systems. Table 6.1 summarizes the different parameters explained in this section.

	T_c	K_1^{3d}
$Nd_2Fe_{14}B$	585	0.4
$Ce_2Fe_{14}B$	424	1.6
$(Ce_{0.63}Nd_{0.37})_2Fe_{14}B$	484	1.16
$(Ce_{0.36}Nd_{0.64})_2Fe_{14}B$	527	0.83
$Dy_2Fe_{14}B$	598	0.4
$(Dy_{0.36}Nd_{0.64})_2Fe_{14}B$	590	0.4

Table 6.1: Values of the Curie temperature T_c (in K) and of the $3d$ first anisotropy constant at 0 K K_1^{3d} (in MJ.m^{-3}) involved in the two sublattice model for different compounds studied in this chapter.

6.2 Calculated $4f$ crystal field parameters and exchange field

In "2-14-1" systems, the CF Hamiltonian 4.21 for a given $\mathcal{R}$, in the coordinate system x$\|$[100] and z$\|$[001], site can be written as [Yamada et al., 1988]

$$\hat{H}_{CF} = A_2^0\hat{T}_2^0 + A_2^{-2}\hat{T}_2^{-2} + A_4^0\hat{T}_4^0 + A_4^{-2}\hat{T}_4^{-2} + A_4^4\hat{T}_4^4 + A_6^0\hat{T}_6^0 + A_6^{-2}\hat{T}_6^{-2} + A_6^4\hat{T}_6^4 + A_6^{-6}\hat{T}_6^{-6}. \quad (6.1)$$

Nd CFPs and B_{ex} computed within our approach (see Sec. 4.6) in pure $Nd_2Fe_{14}B$, together with experimental [Cadogan et al., 1988] and previous *ab initio* [Sato et al., 2021] values, are summarized in figure 6.2 for f and g inequivalent sites in the unit cell (see Fig. 6.1). Our theoretical parameters have the same sign and order of magnitude than the ones extracted by [Cadogan

et al., 1988] from experimental magnetization curves (only a subset of CFPs was assumed to be non-zero in their fitting). The only significant discrepancy with respect to [Cadogan et al., 1988] is the underestimation of A_6^4 on the g site. Overall, the results of our *ab initio* approach are comparable with those of [Sato et al., 2021].

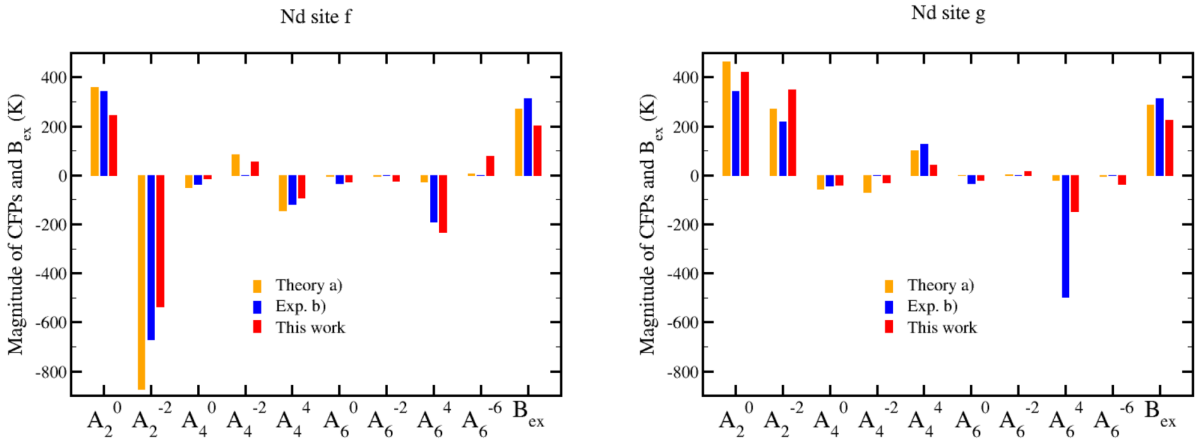

Figure 6.2: Nd CFPs and B_{ex} (in K) for both inequivalent sites in the "2-14-1" system. The values are for the $z = 0$ plane of the unit cell (the signs of A_2^{-2}, A_4^{-2}, A_6^{-2} and A_6^{-6} change for the middle plane). a) [Sato et al., 2021]. b) [Cadogan et al., 1988] ([Li et al., 1988] for B_{ex}).

The precise values are summarized in table 6.3 in appendix 6.7, which also lists computed CFPs for Dy in $Dy_2Fe_{14}B$ as well as our results for various mixed systems with Ce or La (both treated within LDA) occupying one of the two sites. These calculations with partial substitution give, for Nd and Dy, essentially the same CFPs and B_{ex} as in the corresponding pure compounds. This shows that the CFPs on one $\mathcal{R}$ site are insensitive to substitution of the $\mathcal{R}$ element at the other site, therefore justifying the use of equation 4.27.

Furthermore, in all cases, the g site exhibits higher or equal values of the key low-rank CFP A_2^0 as well as that of B_{ex} compared to the f site. This suggests that this site exhibits a higher SIA than the f one (in agreement with the results of [Chouhan et al., 2018, Sato et al., 2021]), at least at high temperature, where higher order CFPs are essentially negligible (as explained in Sec. 4.5). This idea is explored in sections 6.4 and 6.5.

6.3 Magnetic properties of pure $Nd_2Fe_{14}B$

In this section, we employ the *ab initio* Nd CFPs shown in figure 6.2 and parameters summarized in table 6.1 within the two sublattice picture (see Sec. 4.4) to compute magnetic properties of $Nd_2Fe_{14}B$ and compare our predictions with experimental data.

Figure 6.3a displays the computed $Nd_2Fe_{14}B$ magnetization curves along the [100] and [110] directions together with the experimental ones [Gomez Eslava et al., 2021] at $T = 10$ K and 300 K. The experimental curves are well reproduced, including some subtle features such as the First-Order Magnetization Process (FOMP) along [100] at $T = 10$ K (at $H_{ext} \sim 17$ T) as well as

the saturation (∼37 μ_B/f.u. along [100] at 10 K) and spontaneous magnetizations (∼13 μ_B/f.u. and ∼17 μ_B/f.u. at 10 K along [100] and [110] respectively).

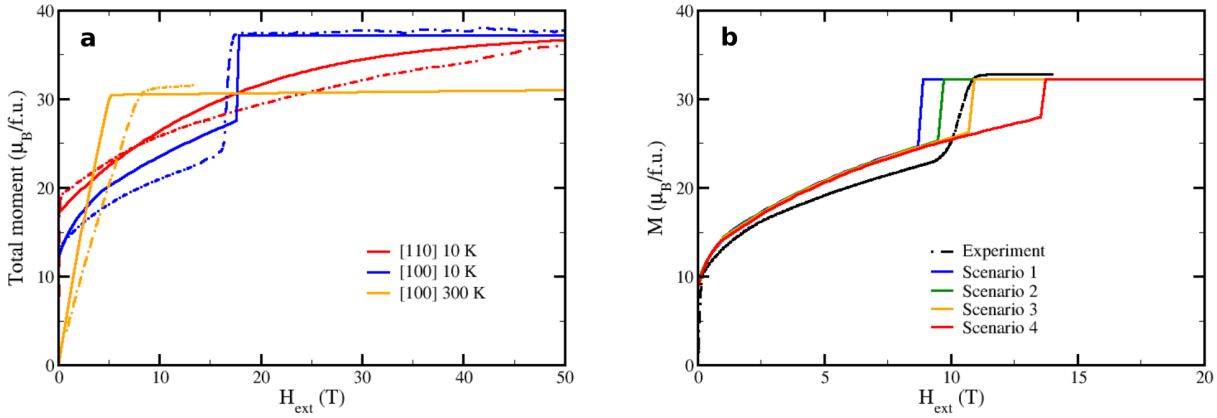

Figure 6.3: a) $Nd_2Fe_{14}B$ magnetization curves along [100] and [110], at $T = 10$ and 300 K. Dotted lines: experiment [Gomez Eslava et al., 2021]. Solid lines: theory. b) Magnetization curve of $(Nd_{0.37}Ce_{0.63})_2Fe_{14}B$ along [100] at 10 K, according to experiment and computed for the different occupancy scenarios 1-4 (see table 6.2).

Figure 6.4a shows the evolution of the angle θ between the total spontaneous magnetization (in the $(\bar{1}10)$ plane) and the [001] axis in $Nd_2Fe_{14}B$. Our calculations reproduce the Spin Reorientation Transition (SRT) occurring at low temperature. The low temperature angle is also reproduced (∼30°), which is consistent with the excellent agreement of the low temperature magnetizations at zero field (see Fig. 6.3). The SRT temperature is however underestimated (∼75 K instead of ∼135 K). There has been a lot of debate regarding the magnetic structure of the compound at 4 K: some works [Cadogan et al., 1988, Yamada et al., 1988, Nowik et al., 1990] predicted a very small canting angle between Nd moments and the total one ($\leq 7°$), while others suggested a large one [Onodera et al., 1987, Bartolomé et al., 2000, García et al., 2000b, Wolfers et al., 2001]. Our calculations support the small canting angle picture, with a maximum angle of 5° between a Nd moment and the total one.

Figure 6.4b displays the evolution of $Nd_2Fe_{14}B$ anisotropy constants K_1 and K_2 extracted with the Sucksmith-Thompson (ST) method (see Sec. 4.5). The agreement is fairly good. It is also consistent with figure 6.4: at high temperatures, both anisotropy constants are positive and the phase is therefore uniaxial. At low temperature, the competition between negative K_1 and positive K_2 results in the conical phase. The temperature at which K_1 changes signs is underestimated, consistently with the underestimation of the spin reorientation transition temperature (see Fig. 6.4).

Our method therefore proves to be a reliable *ab initio* approach to the magnetic properties of the complicated $Nd_2Fe_{14}B$ system: it provides site-specific Nd CFPs as well as exchange field and explains different subtle experimental features (SRT, FOMP, etc.), with the crystal structure, T-dependence of the $3d$ sublattice and Wannier projection window as the only parameters.

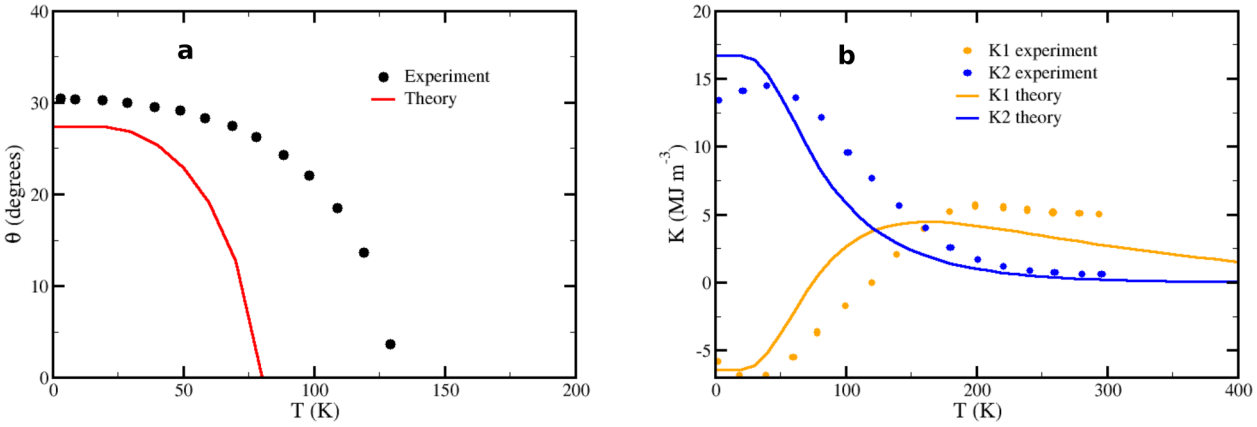

Figure 6.4: a) Temperature evolution of the angle θ between the total moment (in the $(\bar{1}10)$ plane) and the [001] axis in $Nd_2Fe_{14}B$. Experiment is from [Cadogan et al., 1988]. b) Evolution of $Nd_2Fe_{14}B$ anistropy constants K_1 and K_2 with temperature, extracted by the Sucksmith-Thompson method (see Sec. 4.5). The experimental data was taken from [Andreev et al., 1986].

6.4 Ce substitution

In this section, we employ the *ab initio* Nd CFPs shown in figure 6.2 and parameters summarized in table 6.1 within the two sublattice picture (see Sec. 4.4) to study partial substitution of Nd by lighter, more abundant and cheaper Ce. Ce preferred site in these $(Nd_{1-x}Ce_x)_2Fe_{14}B$ systems is still controversial. Indeed, [Colin et al., 2016] showed that Ce favors the smaller f site in their compounds (consistently with a valence dominated by Ce^{4+}). However, [Lin et al., 2020] suggested the opposite. To investigate this issue, we compared the experimental FOMP at 10 K along [100] in $(Nd_{0.37}Ce_{0.63})_2Fe_{14}B$ with theoretical calculations for different occupancy scenarios (see table 6.2): Ce with a slight g preference as measured by [Lin et al., 2020] (scenario 1), no site preference between Ce and Nd (scenario 2), Ce with a slight f preference as measured by [Colin et al., 2016] (scenario 3) and Ce fully occupying the f site (scenario 4). As illustrated in figure 6.3b, gauged by the FOMP field, scenario 3 gives the best agreement with experiment. However, one may notice that the relative error in the determination of the FOMP field for the pure compound (about 2 Teslas) suggests an accuracy of about 1 Tesla for the mixed case with the error scaled correspondingly to the lower Nd concentration. Within this uncertainty, we cannot discriminate between the scenarios 2 and 3; however, Nd preference for f site (scenario 1) and purely g Nd occupancy (scenario 4) are unlikely. Therefore, the experimental situation likely corresponds to either no preference or a slight Ce preference for the f site. This implies that there is potentially room for site occupancy optimization which is studied below.

We then computed the magnetocrystalline anisotropy MAE $= F_{[100]} - F_{[001]}$ for different Ce concentration: $Nd_2Fe_{14}B$, $(Nd_{0.64}Ce_{0.36})_2Fe_{14}B$, $(Nd_{0.37}Ce_{0.63})_2Fe_{14}B$ and $Ce_2Fe_{14}B$. We directly evaluated the MAE from equation 4.27 using the experimental occupancy of [Colin et al.,

Compound	Scenario	Nd f	Nd g	$\mathcal{R}$ f	$\mathcal{R}$ g
$(Nd_{0.37}Ce_{0.63})_2Fe_{14}B$	1. [Lin et al., 2020]	0.45	0.29	0.55	0.71
	2. No pref.	0.37	0.37	0.63	0.63
	3. [Colin et al., 2016]	0.25	0.49	0.75	0.51
	4. Ce on f	0.0	0.74	1.0	0.26
$(Nd_{0.64}Ce_{0.36})_2Fe_{14}B$	5. [Colin et al., 2016]	0.56	0.72	0.44	0.28
	6. Ce on f	0.28	1.0	0.72	0.0
$(Nd_{0.64}Dy_{0.36})_2Fe_{14}B$	7. [Saito et al., 2017]	0.51	0.77	0.49	0.23
	8. Dy on g	1.0	0.28	0.0	0.72

Table 6.2: Site-detailed stoichiometry of $(Nd_{1-x}\mathcal{R}_x)_2Fe_{14}B$ compounds ($\mathcal{R}$ = Ce, Dy), depending on various occupancy scenarios. Numbers labeling the scenarios are used for clear reference in the main text and figures. No pref. = no site preference between Nd and $\mathcal{R}$. $\mathcal{R}$ on i = ion $\mathcal{R}$ occupies first the site i. [Lin et al., 2020] = Ce has a slight preference for the g site. [Colin et al., 2016] = Ce has a slight preference for the f site. [Saito et al., 2017] = Dy has a slight preference for the f site. The actual occupation numbers of scenarios 1, 3, 5 and 7 were extracted by interpolation of the measured data displayed in the respective references.

2016] for the mixed systems (scenarios 3 and 5 in table 6.2). The results are displayed in figure 6.5 together with the experimental results of our collaborators. The MAE decreases, as expected, as a function of the Ce concentration which contributes weakly to the MAE (only through the renormalization of K_1^{3d} in this chapter) compared to Nd. The overall agreement between theory and experiment is fairly good which shows the ability of our approach to treat complex substituted systems.

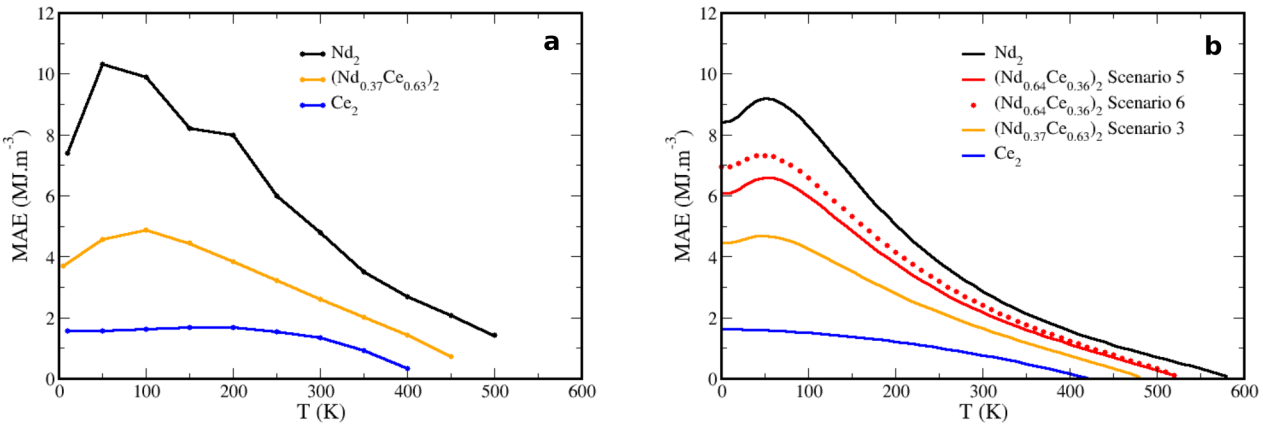

Figure 6.5: Magnetocrystalline anisotropy as a function of temperature of $(Nd_{1-x}Ce_x)_2Fe_{14}B$ compounds. a) experiment (see [Boust et al., 2022a] for details). b) theory according to occupancy scenarios of table 6.2. In the case of $Ce_2Fe_{14}B$, the theoretical MAE amounts to $K_1^{3d}(T)$ as explained in section 6.1.

To investigate the importance of site occupancy, we also computed the MAE with Ce occupying only the f site, for the $(Nd_{0.64}Ce_{0.36})_2Fe_{14}$ stoichiometry (scenario 6 in table 6.2); the result is displayed in figure 6.5. Compared to the experimental occupancy of [Colin et al., 2016], we computed an increase of anisotropy over the whole range of temperature (+9% at 300 K for instance, from 2.2 to 2.4 MJ.m^{-3}). This effect arises from the larger Nd g SIA due to larger A_2^0 and B_{ex} (as discussed above, see Fig. 6.2). Therefore, by further enhancing f site Ce occupancy (and, correspondingly, Nd g occupancy), one should be able to increase the MAE of $(Nd,Ce)_2Fe_{14}B$ substituted compounds. It also means that when it comes to non-magnetic Nd substitutions, it is, in principle, preferable to use elements with smaller ionic radii in order to keep Nd at the larger g site.

6.5 Dy substitution

In this section, we employ the *ab initio* Nd and Dy CFPs summarized in table 6.2 and parameters summarized in table 6.1 within the two sublattice picture (see Sec. 4.4) to study partial substitution of Nd by Dy, which is routinely done in the industry to enhance the anisotropy. According to [Saito et al., 2017], Dy has a preference for the f site, which is consistent with its smaller atomic radius compared to Nd (lanthanide contraction). As in the case of Ce, the experimental occupancy is still close to equal occupation between sites, but the situation is reversed: here, heavy $\mathcal{R}$ occupying the f site is expected to be detrimental to the anisotropy. Indeed, as shown in figure 6.6a, Dy has a larger SIA and also features a larger contribution arising from the g site. It results in $MAE^g_{Dy} - MAE^f_{Dy} > MAE^g_{Nd} - MAE^f_{Nd}$ which means that, for a given Dy content, forcing Dy to occupy the g site is predicted to enhance the anisotropy. This is illustrated in figure 6.6b: theoretical MAE of $(Nd_{0.64}Dy_{0.36})_2Fe_{14}B$ with the experimental occupancy from [Saito et al., 2017] (scenario 7 in table 6.2) is larger than in pure $Nd_2Fe_{14}B$ but can be further increased by assuming Dy to occupy the g site (scenario 8 in table 6.2). We computed for instance an increase of 10% at 300 K (from 4.1 to 4.5 MJ.m^{-3}). Therefore, were we able to force Dy on the g site in Nd-Dy compounds, we could increase, though moderately, the anisotropy per Dy content. The same kind of phenomenon is expected to occur with Tb substitution.

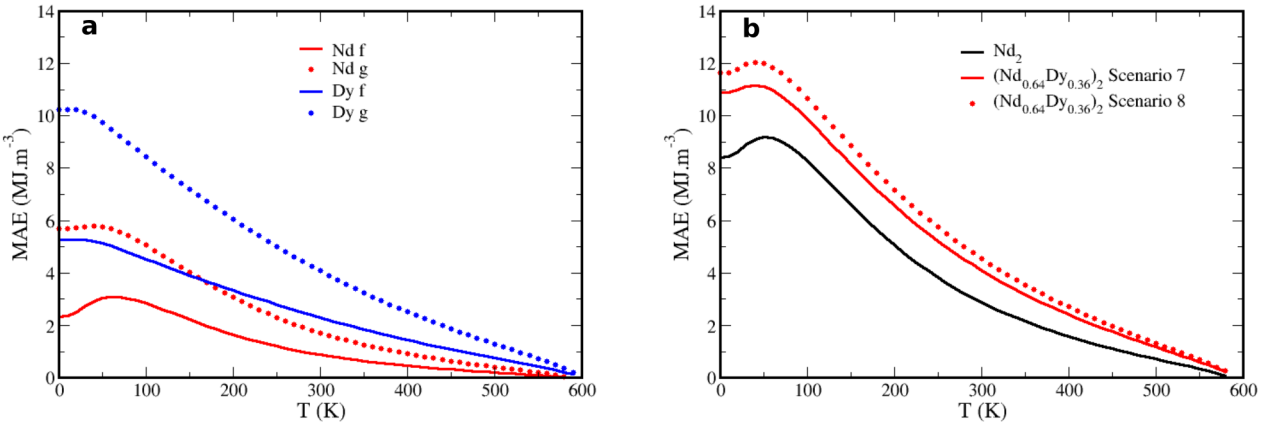

Figure 6.6: Evolution of theoretical MAE with temperature. a) Contribution of ($\mathcal{R}$, site). b) $Nd_2Fe_{14}B$ and $(Nd_{0.64}Dy_{0.36})_2Fe_{14}B$ according to occupancy scenarios of table 6.2.

6.6 Conclusion

In this chapter, we computed from the first-principles SIC-LDA+HI approach site specific crystal field and exchange field parameters of Nd in the theoretically challenging $Nd_2Fe_{14}B$ intermetallic, which is the most widely used high-performance hard magnet in the industry. The resulting values are in excellent agreement with previously computed and experimental ones. Moreover, we showed that these parameters are essentially insensitive to substitutions on the other $\mathcal{R}$ site in the "2-14-1" structure, an assumption usually made in the literature but not proven. We also showed that with these parameters one may construct an almost fully *ab initio* two sublattice model that reproduces various measured magnetic properties of $Nd_2Fe_{14}B$.

Next, we studied industrially motivated partial substitution of Nd by Ce or Dy, focusing on the substitution site preference and its impact on magnetic properties. In Ce substituted compounds – often considered in the quest to reduce the scarce heavy rare-earth content in hard magnets – comparison of experimental data [Colin et al., 2016, Lin et al., 2020] with our theoretical calculations supports a slight Ce preference for the f site. Our theoretical predictions are found to be in good agreement with experimental measurements of MAE in Ce substituted single crystals. Our calculations also predict that enhancing Nd preferential g-site occupancy leads to a higher SIA. This theoretical observation implies that one might be able to enhance (though moderately) the magnetic anisotropy in $(Nd,Ce)_2Fe_{14}B$ compounds by engineering higher Ce f-site occupancy.

In Dy substituted compounds, routinely used in the industry, we also showed that an increase (though moderate) of the magnetic anisotropy is theoretically expected when Dy occupies the g site. This could perhaps be achieved by adding a third $\mathcal{R}$ element with an even smaller radius (therefore occupying preferably the f site), such as Ce^{4+}: while this kind of doping would lower the anisotropy of the compound, it could increase the anisotropy per Dy atom by the mechanism

aforementioned as well as reduce the total economic cost (as Ce is cheaper than Dy), resulting in an overall better anisotropy/price ratio.

Overall, our *ab initio* approach is shown to be a reliable tool to predict and analyze intrinsic properties of complex, substituted, hard magnetic materials. It may provide useful insight into site occupancy optimization and its impact on magnetic properties.

6.7 Appendix

Table 6.3 summarizes CFPs and exchange fields computed in this chapter for various "2-14-1" systems.

	Site	A_2^0	A_2^{-2}	A_4^0	A_4^{-2}	A_4^4	A_6^0	A_6^{-2}	A_6^4	A_6^{-6}	B_{ex}
$Nd_2Fe_{14}B$	f	246	-537	-14	54	-91	-27	-24	-232	78	203
	g	420	349	-41	-29	42	-19	15	-149	-37	222
$NdLaFe_{14}B$	f	297	-641	-22	73	-119	-25	-16	-228	27	212
$CeNdFe_{14}B$	g	414	334	-45	-28	54	-20	9	-154	-56	223
$Dy_2Fe_{14}B$	f	113	-345	-4	29	-19	-12	27	-93	115	209
	g	186	180	-16	-17	19	-10	-14	-25	72	207
$DyCeFe_{14}B$	f	115	-381	-6	32	-21	-14	32	-95	123	189
$CeDyFe_{14}B$	g	190	129	-18	-7	8	-11	-21	-15	86	210

Table 6.3: Site specific theoretical CFPs and B_{ex} (in K) for Nd and Dy computed in different compounds. The values are for the $\mathcal{R}$ ions in the $z = 0$ plane of the unit cell (the signs of A_2^{-2}, A_4^{-2}, A_6^{-2} and A_6^{-6} change for the middle plane). In substituted compounds, Nd/Dy occupies the site indicated in the second column, which is also highlighted by the order of the ions in the compound formula (first ion on site f, second on site g).

Part III

Optical and spectral properties of rare-earth-based semiconductors

Chapter 7

Combining semi-local exchange with dynamical mean-field theory: electronic structure and optical response of $\mathcal{R}_2O_3$ and $\mathcal{R}$SF

In this chapter based on our works [Galler et al., 2021a, Boust et al., 2022b], we propose a first-principles approach combining DMFT and the modified Becke-Johnson potential (see Sec. 1.6) which we apply it to study the optical and spectral properties of rare-earth sesquioxides $\mathcal{R}_2O_3$ and fluorosulfides $\mathcal{R}$SF. This method was also applied with success to rare-earth mononitrides $\mathcal{R}$N by [Galler and Pourovskii, 2022]. The chapter, which mainly focuses on $\mathcal{R}_2O_3$, leaving the discussion of $\mathcal{R}$SF at the end, is organized as follows. We start by explaining the motivations behind it in section 7.1. In section 7.2, we briefly review previous theoretical methods applied to the $\mathcal{R}_2O_3$ family. We then describe the mBJ and DMFT combined approach in section 7.3. In section 7.4, we discuss hybridization effects in $\mathcal{R}_2O_3$ compounds. Finally, we use the combined mBJ and DMFT methodology to analyse the spectral and optical properties of $\mathcal{R}_2O_3$ and $\mathcal{R}$SF in sections 7.5, 7.6 and 7.7.

7.1 Motivation

Rare-earth oxides are semiconductors with a wide range of potential applications, e.g., in electronics, optics and catalysis [Gasgnier, 1989, Trovarelli, 1999, Päiväsaari et al., 2005, Leskelä et al., 2006, Chiu et al., 2012, Goh et al., 2017]. In particular, the sesquioxide series $\mathcal{R}_2O_3$ has been the subject of numerous experimental and theoretical studies. These oxides are promising high K-gate dielectrics [Leskelä et al., 2006, Chiu et al., 2012, Goh et al., 2017]; they also represent a prototypical case of $\mathcal{R}$ semiconductors for testing various theoretical approaches to correlated semiconductors in general [Skorodumova et al., 2001, Petit et al., 2005, Hay et al., 2006, Loschen et al., 2007, Pourovskii et al., 2007, Tomczak, 2007, Jacob et al., 2008, Jiang

et al., 2009, Jiang et al., 2012, Amadon, 2012, Gillen et al., 2013, Jiang, 2018, El-Kelany et al., 2018].

The $\mathcal{R}$ fluorosulfides have recently attracted attention due to the brilliant color exhibited by some of them: yellow for SmSF and GdSF, red for CeSF. These compounds are potential candidates for the replacement of the common, more toxic, yellow-red cadmium-based pigments and have been extensively studied experimentally [Demourgues et al., 2001b, Demourgues et al., 2001a, Pauwels et al., 2002, Pauwels, 2003]. As for theoretical works, we can cite for example the CeSF study of [Tomczak et al., 2013].

Typically, the electronic structure of such $\mathcal{R}$ semiconductors comprises wide semiconducting ligand (oxygen, sulfur,...) p and $\mathcal{R}$ $5d$ bands together with strongly correlated and localized $\mathcal{R}$ $4f$ orbitals. Their spectroscopy and optical response are strongly affected by the location of the $4f$ quasi-atomic states, which may appear inside or outside the $p-d$ gap, as illustrated in figure 7.1. This may lead to a non-monotonous evolution of the optical gap along the $\mathcal{R}$ series as, for example, observed in the $\mathcal{R}$ sesquioxides, -sulfides and -selenides $\mathcal{R}_2X_3$ (where $\mathcal{R}$ = La...Lu, X = O, S, or Se) [Golubkov et al., 1995, Prokofiev et al., 1996] .

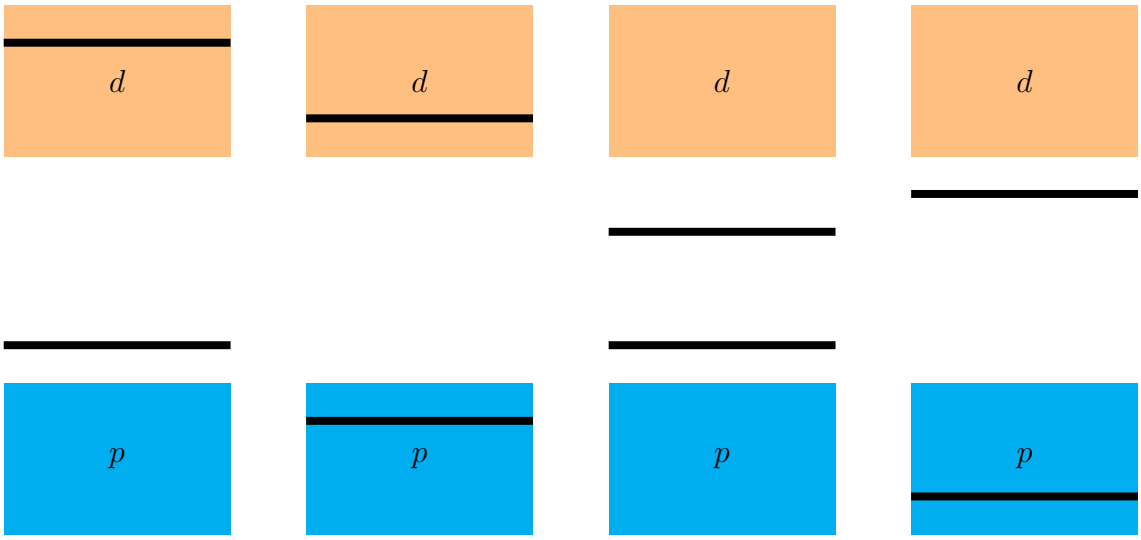

Figure 7.1: Possible positions of the $\mathcal{R}$ $4f$ lower and upper Hubbard bands (thick black lines) with respect to the $p-d$ gap in rare-earth semiconductors.

Formulating a predictive first-principles theory for these systems is challenging, since it should properly treat both non-local and local exchange-correlation effects: the former are involved in the formation of the $p-d$ gap, while the latter stem from strong local Coulomb interactions in the $\mathcal{R}$ $4f$ shells. Density Functional Theory (DFT) fails at both levels, when the Kohn-Sham band structure is used as an approximation to the electronic excitation spectrum. First, when employed in conjunction with the standard local density (LDA) or generalized gradient approximation (GGA) exchange-correlation (XC) potentials, it systematically underestimates the $p-d$ gap, missing, in particular, the contribution due to the exchange-correlation derivative discontinuity, as described in section 1.5. Second, the KS band structure cannot capture the Mott phenomenon, usually predicting an incorrect metallic behavior for strongly

correlated narrow bands, like the $\mathcal{R}$ $4f$ states, as also discussed in section 1.5.

7.2 Previous theoretical methods applied to $\mathcal{R}_2O_3$

Two approaches have gained importance to address these limitations of standard DFT described in the previous section. The first one is based on hybrid XC functionals that partially substitute the LDA or GGA exchange by the exact one. These approaches substantially improve the optical gap evolution along the $\mathcal{R}_2O_3$ series [Gillen et al., 2013, El-Kelany et al., 2018] as compared to the standard LDA or GGA. However, the results depend on the amount of exact exchange admixture α (though some approaches to fix α self-consistently have been proposed [El-Kelany et al., 2018]). Moreover, predictions of the $4f$ states position vary strongly between different types of hybrid functionals [Gillen et al., 2013]. Another significant limitation is the inability of this approach to treat paramagnetic phases. The sesquioxides $\mathcal{R}_2O_3$ order magnetically at low temperatures of at most several Kelvins [Kolodiazhnyi et al., 2018, Lejus et al., 1976, Sala et al., 2018]; their optical properties in the paramagnetic phase are the most relevant to experiment. Though unlikely in the case of $\mathcal{R}$ sesquioxides, the absorption edge in $\mathcal{R}$ semiconductors may generally undergo a significant change upon the onset of magnetic order [Granville et al., 2006].

The second approach involves Green's functions many-body methods, such as the Dynamical Mean-Field Theory (DMFT) (see chapter 2) or GW [Hedin, 1965]. The combination of DFT+DMFT approach (see chapter 3) successfully captures the Mott phenomenon in correlated narrow bands, even in the absence of magnetic ordering. Such an improved description of the $\mathcal{R}$ $4f$ states by DFT+DMFT resulted in a qualitatively correct shape of the optical gap evolution along the $\mathcal{R}$ sesquioxide series [Tomczak, 2007, Kolorenč, 2016], reproducing also the experimental value of the gap in Ce_2O_3 [Tomczak, 2007, Pourovskii et al., 2007, Amadon, 2012, Kolorenč, 2016]. However, the underestimation of the KS $p-d$ gap is not corrected within DFT+DMFT, resulting in systematically underestimated gaps in the Pr and Nd compounds.

It is well known that the underestimation of semiconducting gaps in the Kohn-Sham band structure of DFT can be corrected by the GW approach. Being a weak-coupling perturbative correction to DFT, GW is not suitable for the strongly localized $4f$ states. Hence, a combination of GW with DFT+U has been applied to $\mathcal{R}$ sesquioxides [Jiang et al., 2009, Jiang et al., 2012, Jiang, 2018]; in this method, the GW electronic structure is calculated from self-consistent DFT+U bands. The method predicts the $\mathcal{R}_2O_3$ gap evolution in an overall good agreement with experiment, though a careful description for a very wide range of conduction band states is required to compute the screening [Jiang, 2018]. Similarly to the hybrid XC approach, GW@DFT+U of [Jiang et al., 2009, Jiang et al., 2012, Jiang, 2018] is computationally heavy and may treat only magnetically ordered phases. In these calculations, U has been treated as a parameter generally fixed at a certain value for the whole series.

A fully consistent first-principles many-body treatment of both long-range and local correlations, e.g. by the GW+DMFT approach [Biermann et al., 2003], remains currently computationally heavy for applications to realistic $\mathcal{R}$ semiconductors, despite some recent progress

[Pashov et al., 2020, Kutepov, 2020]. Alternatively, a many-body DMFT approach to the $\mathcal{R}$ $4f$ states has been combined with advanced XC functionals for wide semiconducting bands. Such an implementation based on a hybrid functional was applied to Ce_2O_3 [Jacob et al., 2008]. The Hartree-Fock contribution to the hybrid correction was however found to lead to a large unphysical crystal field splitting [Jacob et al., 2008], inducing an orbital symmetry breaking.

In the present chapter, we employ the Tran-Blaha modified Becke-Johnson (mBJ) XC potential [Becke and Johnson, 2006, Tran and Blaha, 2009] described in section 1.6 to address the problem of the underestimation of the $p-d$ gap within DFT+DMFT at very moderate computational cost. [Huang and Lu, 2016] proposed to use mBJ to replace DFT in DFT+DMFT and presented interesting results for the spectral and optical properties of the band insulator YbS. However, to the best of our knowledge, using a combination of this type to address the physics of a material with a partially filled correlated shell was never attempted.

7.3 The mBJ@DFT+DMFT approach

The mBJ exchange potential can be employed either self-consistently, as e.g. in [Koller et al., 2011], or as a perturbative correction on top of self-consistent DFT calculations [Jiang, 2013]. As noted in section 1.6, the mBJ potential is not variational, i.e., it is not derived from any XC energy functional. Correspondingly, its self-consistent application lacks a theoretical justification. Moreover, we found that such a self-consistent application of mBJ tends to induce a symmetry breaking of the $4f$ states, similarly to the case of hybrid functionals+DMFT [Jacob et al., 2008]. This mBJ induced splitting of the $4f$ states becomes problematic in the DFT+DMFT context, since it stems from $4f$ exchange-correlation effects and needs to be removed in order to avoid a double counting (see Sec. 3.4). Designing such a specific double-counting term for a semilocal non-variational XC potential is highly non-trivial. However, we found that the perturbative "one-shot" application of mBJ, which is in this case evaluated from the charge density previously converged within standard LDA(+DMFT), induces a negligible $4f$ splitting. Hence, following the previous implementation of mBJ@DFT+U [Jiang, 2013], we also employed mBJ in a perturbative fashion; we correspondingly abbreviate our approach as mBJ@DFT+DMFT.

The mBJ@DFT+DMFT scheme can be divided into two steps. We first carry out charge-self-consistent DFT+DMFT calculations using LDA as the XC potential, together with the Hubbard-I (HI) approximation [Hubbard, 1963] for the DMFT impurity problem (see Sec. 3.7). The quasi-atomic HI approximation has proven to reliably reproduce the multiplet structure of localized $4f$ states [Pourovskii et al., 2009, Locht et al., 2016]; the self-consistent DFT+HI [Pourovskii et al., 2007] has further shown to provide a qualitatively correct evolution of the gap along the $\mathcal{R}_2O_3$ series [Tomczak, 2007]. We subsequently apply the perturbative mBJ correction to the Kohn-Sham (KS) bands and recalculate the final electronic structure by performing a DMFT cycle using the HI approximation for the mBJ-corrected KS bands.

Computational details for $\mathcal{R}_2O_3$. We restricted ourselves to $\mathcal{R}$ sesquioxides with the hexagonal structure P$\bar{3}m1$ (space group 164), namely $\mathcal{R}$ = La, Ce, Pr and Nd [Adachi and Imanaka, 1998], and employed experimental lattice parameters [Adachi and Imanaka, 1998].

We employed the FLAPW electronic structure calculation code WIEN2k [Blaha et al., 2018, Blaha et al., 2020] for DFT-LDA and mBJ calculations. The spin-orbit coupling was included within the usual second variational procedure. We used the TRIQS [Parcollet et al., 2015, Aichhorn et al., 2016] implementation for DMFT and performed calculations for room temperature. Wannier orbitals representing the $4f$ states (see Sec. 3.2) were constructed from the KS bands inside a large energy window $[-9.5, 13.6]$ eV including the O $2p$ states and most of the $\mathcal{R}$ $5d$ states. The on-site rotationally-invariant Coulomb repulsion $\hat{H}_U$ between $4f$ electrons was specified with the two parameters U and J (see. Sec. 3.3). The values of U were computed by a constrained-LDA+HI (cLDA+HI, see Sec. 3.7) approach [Galler and Pourovskii, 2022] yielding U = 7.5, 7.8, 8.0 eV for Ce, Pr and Nd respectively. The values of J (which is an intra-atomic parameter that is, for rare-earth ions, independent of the crystalline environment) were chosen as J = 0.71, 0.73, 0.77 eV for Ce, Pr and Nd respectively, as measured by optical spectroscopy [Carnall et al., 1989]. The Fully Localized Limit (FLL) double-counting with the nominal atomic occupancy [Pourovskii et al., 2007] was used throughout (see Sec. 3.4). $\hat{H}_{\rm DC}$ was also included for the empty $4f$ energy levels in La_2O_3. For the La $4f^0$ shell, this amounts to an upward shift due to the negative FLL DC potential[1] by $(U-J)/2$, which was evaluated with the extrapolated values of U = 7.3 eV and J = 0.69 eV.

The optical conductivity was calculated within the Kubo linear response formalism [Kotliar et al., 2006] using the implementation of [Aichhorn et al., 2016] and neglecting excitonic effects. We employed 14 000 $\boldsymbol{k}$ points in the full Brillouin zone to evaluate transport integrals.

7.4 Treatment of hybridization effects in $\mathcal{R}_2O_3$

To elucidate the impact of hybridization, missed in HI, we also compared the HI spectral functions of $\mathcal{R}_2O_3$ with those computed using the numerically exact hybridization-expansion Continuous-Time Quantum Monte-Carlo method (CTQMC) [Werner et al., 2006, Parcollet et al., 2015, Seth et al., 2016] (see Sec. 2.4). The use of a full rotationally-invariant interaction vertex in the presence of significant spin-orbit effects and for multi-electron $4f$ filling is prohibitively computationally expensive for the CTQMC method at present and also prone to the sign problem [Gull et al., 2011]. Hence, we were able to carry out such a CTQMC calculation with full $\hat{H}_U$ only for Ce_2O_3. Starting from the converged DFT+HI electronic structure with the mBJ correction included as described above, we carry out a DMFT cycle with the CTQMC solver. In the case of Pr_2O_3 and Nd_2O_3 we employed a simplified density-density form for $\hat{H}_U$ (see Sec. 3.3) in both the CTQMC and HI calculations in order to investigate the impact of hybridization (see

[1] mBJ seems to have some limitations regarding empty 4f states which it barely impacts: we here use this DC correction to mimic the GW correction in a computationally cheap way, as often done in the literature.

appendix 7.9.1). The off-diagonal elements of the hybridization function in the basis which diagonalizes the local $4f$ one-electron Hamiltonian $\hat{H}_{\text{1el}}$ (see Eq. 3.39) were neglected in all the CTQMC calculations.

Independently of the vertex employed, the CTQMC solver induces a significant upward shift for the occupied $4f$ peak but barely affects the position of the unoccupied $4f$ states (see Fig. 7.7 in appendix 7.9.1)[2]. Although this shift could be due to the analytic continuation procedure required with the CTQMC solver (see Sec. 2.5), we interpret it as a hybridization effect. Indeed, this shift was shown to disappear for calculations with a smaller Wannier window excluding the O $2p$ states, suggesting that it stems from the $4f$ hybridization with them. This interpretation is also qualitatively consistent with a simple analytical model proposed in appendix 7.9.2. From now, we will hence assume that this shift is due to hybridization.

Therefore, in the calculation of the final electronic structure, we effectively include these hybridization effects through a renormalization of the on-site interaction and double-counting correction, as follows. Since the effect of hybridization can be effectively included through a simple shift of the LHB, we evaluated the final electronic structure and optical response from mBJ KS bands within the HI approximation. The latter, in contrast to CTQMC, allows us to correctly take into account multiplet effects for all $\mathcal{R}_2O_3$, as well as to directly obtain the real-axis spectral function. To include the hybridization shift, we renormalized U and the double-counting (DC) terms by $U \rightarrow U - X$ and $\Sigma_{\text{DC}} \rightarrow \Sigma_{\text{DC}} - N_{\text{at}}X$, with the value of X chosen to align the HI and CTQMC spectral functions, yielding $X = 1.4$, 1.6, 1.7 eV for Ce, Pr and Nd respectively. The resulting values for the normalized parameters, summarized in table 7.1, were then used for the final electronic spectra with HI and full rotationally-invariant Coulomb interaction.

	Ce	Pr	Nd
Calculated U	7.5	7.8	8.0
Renormalized U	6.1	6.2	6.3
Calculated DC	3.75	11.34	19.23
Renormalized DC	2.35	8.14	14.13

Table 7.1: The value of U (in eV) calculated by the cLDA+HI method and the corresponding double-counting correction $U(N_{\text{at}}-1/2)-J(N_{\text{at}}/2-1/2)$ (see Sec. 3.4) for the correlated $\mathcal{R}_2O_3$ insulators, where N_{at} is the atomic occupancy. The renormalized values are reduced due to hybridization effects (see appendix 7.9.1).

[2] In $\mathcal{R}$SF, this CTQMC shift was small.

7.5 Spectral properties of $\mathcal{R}_2O_3$

We first present our results for the electronic structure along the $\mathcal{R}_2O_3$ series as encoded by the $\boldsymbol{k}$-resolved and integrated spectral functions shown in figures 7.2 and 7.3, respectively.

In La_2O_3, the empty $4f$ states are located about 3 eV above the bottom of the La $5d$ band, therefore, this system is an ordinary $p-d$ band insulator (Fig. 7.2a). The calculated value of 5.6 eV for the optical gap between O $2p$ and La $5d$ is in excellent agreement with experimental 5.4 eV [Prokofiev et al., 1996]. Hence, the perturbative mBJ approach successfully corrects the large underestimation of the gap within LDA, which predicts [Tomczak, 2007] the value of 3.7 eV for the optical gap in La_2O_3.

For Ce_2O_3, our calculations predict an occupied $4f$ lower Hubbard band located within the $p-d$ gap. The absorption edge is then due to the Ce $4f$ − Ce $5d$ optical transition as can be seen in figure 7.2b. In figure 7.3b, our calculated integrated spectral function is compared to a X-ray photoemission (XPS)+inverse photoemission (BIS) measurement [Allen, 1985]. The peak observed inside the $p-d$ gap agrees very well with the computed LHB position. The width of this peak obtained by our DMFT calculations using the CTQMC method and full rotationally invariant $\hat{H}_U$ agrees with the experimental width of the LHB. Within the HI approximation, the width of the LHB is strongly underestimated as expected (see Sec. 3.7). The computed position of the UHB is ∼2 eV below the one measured in [Allen, 1985]. The overall width of the UHB in HI is controlled by multiplet splitting and is in good agreement with the CTQMC one. Separate multiplet peaks are not resolved in the latter since they are likely washed away by the analytical continuation procedure (see Sec. 2.5).

The $\boldsymbol{k}$-resolved and integrated spectral functions of Pr_2O_3 (Figs. 7.2c and 7.3c, respectively) feature a narrow $4f$ LHB located just above the top of the O $2p$ band. The UHB has the total width of about 5 eV and is split due to multiplet effects into four main peaks. The UHB bottom is just above that of the $5d$ conduction band, as is seen in figure 7.2c. The optical gap in Pr_2O_3 is thus between the $4f$ LHB and the $5d$ band. In Nd_2O_3, the optical transition is between the O $2p$ states and the $4f$ UHB (Figs. 7.2d and 7.3d), which is located almost precisely at the Nd $5d$ band bottom. The magnitude of the optical gap in Nd_2O_3 is thus predicted to be close to that in La_2O_3. The LHB in Nd_2O_3 features a significant hybridization with the O $2p$ valence band (Fig. 7.3d). The multiplet structure of the Nd $4f$ UHB, with a prominent peak at the bottom of the conduction band and three more closely spaced peaks centered about 2 eV above it, is in agreement with previous calculations [Locht et al., 2016, Galler et al., 2021a] and measurements [Lang et al., 1981, Pauwels, 2003] for other Nd systems. To our awareness, no high-resolution photoemission measurements have been reported for Pr_2O_3 and Nd_2O_3.

Our values for the optical gap extracted from the $\boldsymbol{k}$-resolved spectral functions in figure 7.2 (and consistent with the calculated onsets of the optical conductivities) are listed in table 7.2 together with the results of previous calculations and experimental measurements [Prokofiev et al., 1996]. Looking at the overall picture along the series, the evolution of the optical gap is due to a progressive downwards shift of the Hubbard bands and their changing width due to multiplet effects. The semiconducting $p-d$ gap remains, to a good precision, constant

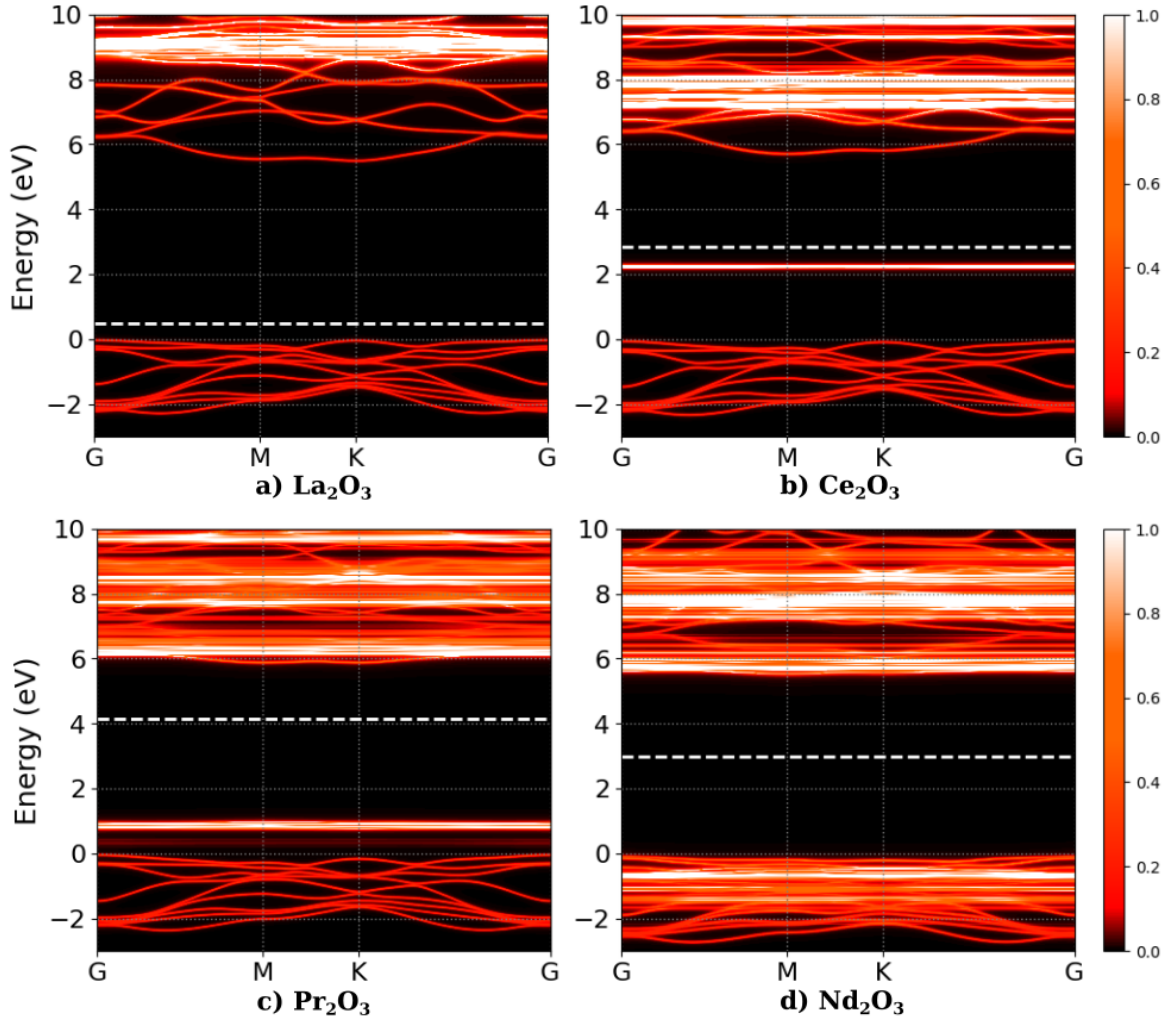

Figure 7.2: $\boldsymbol{k}$-resolved spectral functions of $\mathcal{R}_2O_3$ calculated by the mBJ@DFT+DMFT method. White color indicates a high contribution of the $\mathcal{R}$ $4f$ character. The energy is relative to the top of the O $2p$ band. The thick dashed line is the computed chemical potential at room temperature.

along the series. Overall, our predicted gap values are in good agreement with experiment. In particular, both band (La_2O_3) and correlated insulators are well described, in contrast to the previous LDA+DMFT study [Tomczak, 2007] (see table 7.2) which exhibited a consistent underestimation of the $p-d$ gap throughout the series. This resulted in a poorly described La_2O_3 optical gap and in a saturation of the optical gap between Pr_2O_3 and Nd_2O_3, not observed in experiment, due to f states being outside the small $p-d$ gap. Moreover, the seemingly good agreement with the measured gap of Ce_2O_3 was due to the simultaneous underestimation of the $p-d$ and $p-f$ gaps leading to an error cancellation.

However, one may also notice some systematic overestimation of the gaps by our calculations. This overestimation can be partially due to lifetime broadening of the $4f$ states, which is neglected within the HI approximation. For example, the HI gap in Ce_2O_3 is reduced to 3 eV

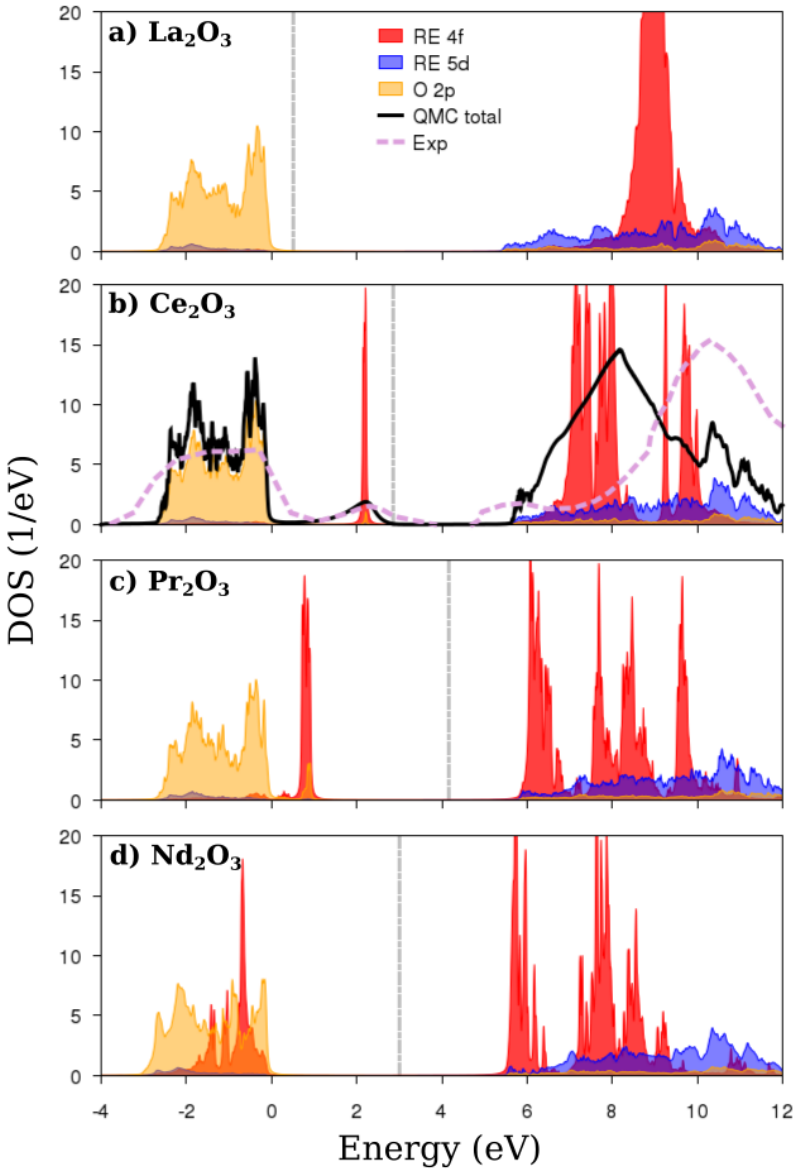

Figure 7.3: Integrated spectral functions of $\mathcal{R}_2O_3$ compounds calculated by the mBJ@DFT+DMFT method. The energy axis zero is placed at the top of the O $2p$ band. For Ce_2O_3, we also show the result of the CTQMC calculation with full rotationally invariant $\hat{H}_U$, as well as the X-ray photoemission (XPS)+inverse photoemission (BIS) measurement of [Allen, 1985]. The experimental curve was normalized to yield 18 electrons in the O $2p$ states and 2 electrons in the Ce $4f$ LHB. The vertical thick dashed line is the computed chemical potential at room temperature.

with the full CTQMC treatment (see Fig. 7.3b). Moreover, in the case of Ce_2O_3, there is only a single optical gap measurement reported in the literature and the conduction band onsets of XPS+BIS [Allen, 1985] and XPS+XAS [Mullins et al., 1998] spectra do not agree: the latter does not exhibit the shoulder at ∼5 eV in figure 7.3b, resulting in a larger $f-p$ gap in agreement

	La	Ce	Pr	Nd
Exp. [Prokofiev et al., 1996]	5.4	2.4	3.9	4.7
HSE03 [Gillen et al., 2013]	4.5	2.37	3.5	4.32
sX-LDA [Gillen et al., 2013]	5.5	1.75	3.8	4.65
GW@LDA+U	4.95^a, 5.8^b	1.5^a, 3.57^b	2.86^a	4.5^a
LDA+DMFT [Tomczak, 2007]	3.7	2.1	3.8	4.1
mBJ@DFT+DMFT	5.6	3.3	4.7	5.6

Table 7.2: Calculated optical gaps (in eV) of the $\mathcal{R}$ sesquioxides compared to experiment as well as to previous theories. The experimental values given here are the most reliable according to [Prokofiev et al., 1996] as they were measured on single crystals. a) [Jiang et al., 2012]. b) [Jiang, 2018].

with our calculations. The actual optical gap of Ce_2O_3 might therefore be larger than 2.4 eV, as already argued by [Jiang, 2018].

7.6 Optical conductivity of $\mathcal{R}_2O_3$

Our calculated optical conductivities are shown in figure 7.4 together with the corresponding experimental data of [Kimura et al., 2000].

In the correlated oxides Ce_2O_3, Pr_2O_3 and Nd_2O_3, the theoretical optical conductivity (Fig. 7.4b) exhibits a characteristic shape. Its onset differs significantly between the three systems, in agreement with their calculated optical gaps (table 7.2). However, all three optical conductivities are seen to merge at roughly 6.3 eV. At this point the conductivity is dominated by $p-d$ transitions; therefore, the approximately constant $p-d$ gap along the series results in a similar magnitude of the corresponding contribution to the conductivity. The evolution of the optical conductivity before this turning point is a signature of $4f$ states involved into the absorption edge. Correspondingly, the theoretical optical conductivity for Pr_2O_3 and Nd_2O_3 features a shallow peak (highlighted by a thick line in Fig. 7.4b) due to the presence of the f states inside the $p-d$ gap (or at its edges, as in Nd_2O_3). Schematically, the optical conductivity increases until the whole spectral weight of the f states within the $p-d$ gap is involved in the optical transitions; then a saturation occurs until $p-d$ transitions start contributing significantly. We observe the same kind of behavior in Ce_2O_3 though the magnitude of the initial plateau is significantly weaker due to a small spectral weight of Ce $4f$ states within the gap. In La_2O_3, there are no $4f$ states in the gap, hence, the initial shallow peak is missed.

Our theoretical picture is in a good qualitative agreement with the measured optical conductivity (Fig. 7.4a) in La_2O_3, Pr_2O_3 and Nd_2O_3: an initial plateau (highlighted by a thick line in figure 7.4a) followed by a rapid increase of conductivity at the $p-d$ edge is also observed in the experimental curves of correlated insulators, but is absent in La_2O_3. The shift between experimental and theoretical onsets of the conductivity is consistent with our general

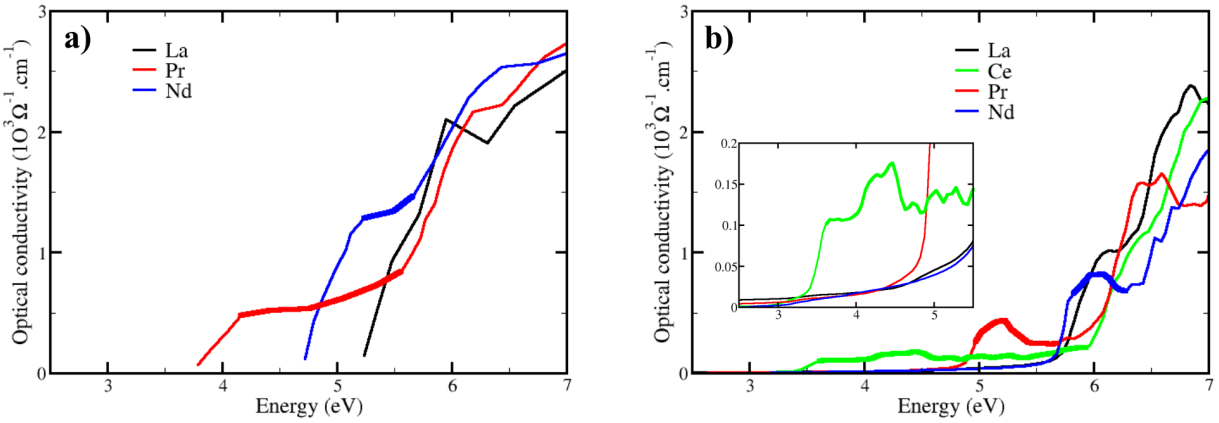

Figure 7.4: Optical conductivity of $\mathcal{R}_2O_3$. a) measured [Kimura et al., 2000]. b) calculated by mBJ@DFT+DMFT. Inset: zoom in the low energy region. The thick lines highlight the characteristic features discussed in the main text.

$\sim$0.8 eV overestimation of the optical gaps in the correlated insulators. No optical conductivity measurement for Ce_2O_3 has been, to our awareness, reported in the literature.

We note that previous DFT+U [Singh et al., 2006] and DFT+DMFT [Tomczak, 2007] works could not explain the occurrence of the initial plateaus in Pr_2O_3 and Nd_2O_3. Due to their systematic underestimation of the $p-d$ gap, these calculations predicted no $4f$ states within it. Furthermore, at higher energies, these previous works yielded theoretical values of the conductivity which were larger than the experimental ones by a factor $\sim$2; although not shown in figure 7.4, our results exhibit the same discrepancy.

7.7 Spectral properties of $\mathcal{R}$SF

In this section, we use the same mBJ@DFT+DMFT metholodgy described in section 7.3 to the rare-earth fluorosulfides $\mathcal{R}$SF. The precise computational details can be found in [Galler et al., 2021a].

Figure 7.5 compares the computed and experimental XPS [Pauwels, 2003] integrated spectral functions for PrSF, NdSF, SmSF anf GdSF. As expected by the high electronegativity of F, the F $2p$ states are located below the S $3p$ band. The latter has a double-peak structure, clearly seen in both theory and experiment, and is separated from the $\mathcal{R}$ 5d states by the $p-d$ gap which is approximately the same for all compounds. Like in $\mathcal{R}$ sesquioxides, we notice a progressive downwards shift of the $4f$ LHB and UHB along the $\mathcal{R}$ series, due to the increase of $4f$ binding energy. In GdSF, the $4f$ Hubbard bands do not exhibit multiplet splitting as the shell is half-filled. Overall, our approach correctly predicts the position of occupied $\mathcal{R}$ $4f$ and F $2p$ states.

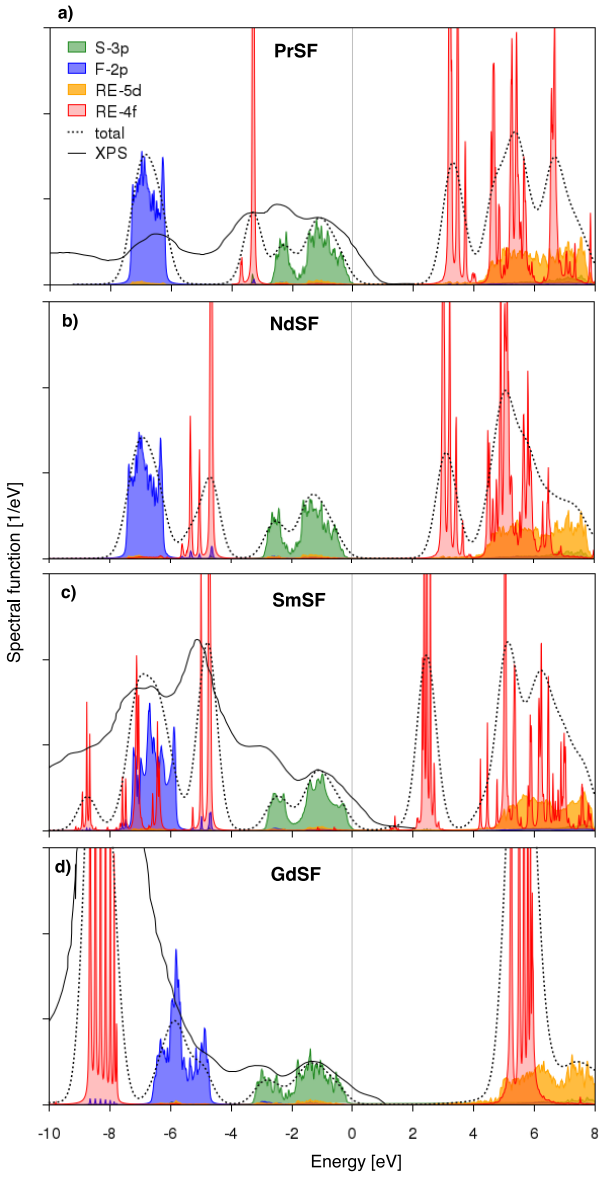

Figure 7.5: Integrated spectral functions for various $\mathcal{R}$SF calculated by the mBJ@DFT+DMFT method. The energy axis zero is placed at the top of the S $3p$ band. Dotted black line: total broadened (0.4 eV) spectral function (with the ratio of $4f$ and $3p$ contributions adjusted to the experimental one, see [Galler et al., 2021a]). Solid black line: XPS experiment [Pauwels, 2003].

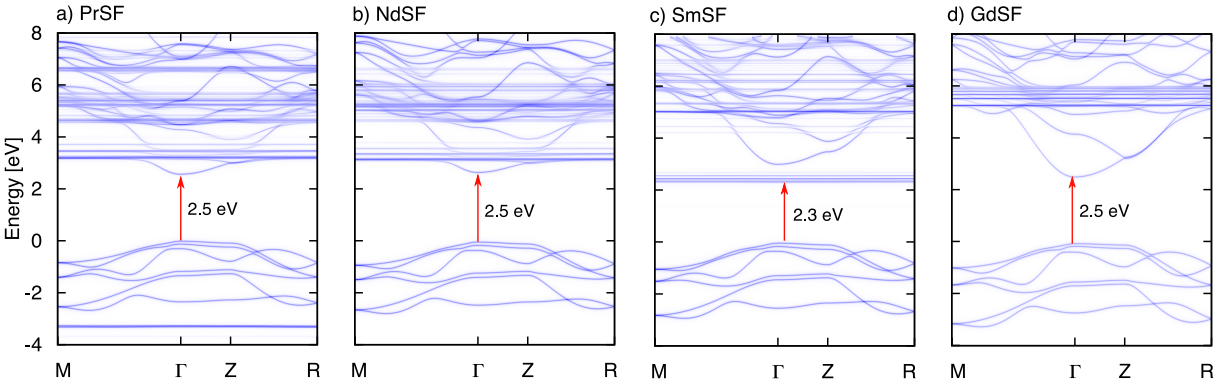

Figure 7.6: $\boldsymbol{k}$-resolved spectral functions of $\mathcal{R}$SF. calculated by the mBJ@DFT+DMFT method. The energy axis zero is placed at the top of the S $3p$ band. Arrows show the transitions defining the optical gaps.

In figure 7.6, we show the computed $\boldsymbol{k}$-resolved spectral functions. As in sesquioxides, the transitions defining the optical gap vary along the $\mathcal{R}$ series. In Pr and Nd compounds, the 2.5 eV gap is formed between a S $3p$ band and a strongly hybridized $\mathcal{R}$ $5d$−$4f$ band. In SmSF, the gap is of S$3p$−Sm$4f$ nature; in GdSF, it is of S$3p$−Gd$5d$ nature. The theoretical gap values in these compounds, 2.3 eV for SmSF and 2.5 eV for GdSF, are in excellent agreement with experiment. Indeed, both compounds, which are of a yellow color as evoked in section 7.1, feature experimentally an optical absorption edge of 2.4-2.5 eV [Demourgues et al., 2001b].

7.8 Conclusion

In this chapter, we proposed an *ab initio* approach to the electronic structure and optical properties of rare-earth semiconductors with coexisting semiconducting bands and correlated $4f$ states. Our methodology combines a DMFT treatment of strong local correlations in partially filled $4f$ shells with an improved treatment of $p-d$ semiconducting gaps by the semi-local modified Becke-Johnson (mBJ) exchange potential. The mBJ correction is implemented in a perturbative way on top of the fully self-consistent DFT+DMFT electronic structure. In contrast to previous advanced theoretical approaches to such correlated $4f$ electron semiconductors [Jiang et al., 2012, Gillen et al., 2013], our method is applicable to the paramagnetic phases of correlated semiconductors. Given the typical low magnetic ordering temperatures, those paramagnetic phases are more readily accessible experimentally than the ordered ground states.

Applying the present method to the light rare-earth sesquioxide series $\mathcal{R}_2O_3$ ($\mathcal{R}$ = La...Nd), we obtain a qualitatively correct evolution for the optical gaps and optical conductivities along this series using *ab initio* values for the on-site Coulomb repulsion U in the $4f$ shells. The precision of our scheme for the optical gaps is comparable to previous advanced *ab initio* methods [Jiang et al., 2012, Gillen et al., 2013]. The overall evolution of the electronic spectra and optical conductivity originates from a progressive downward shift of the $4f$ Hubbard bands along the series as well as in the multiplet structure of those bands. Our calculations explain a characteristic shape of the measured optical conductivity in the Pr and Nd sesquioxides, in

which a plateau right above the absorption edge is shown to be induced by $4f$ states located inside the semiconducting $p-d$ gap.

Though the $4f$ shells are usually assumed to be quasi-atomic, our CTQMC calculations reveal a significant shift of the occupied $4f$ states position compared to HI in $\mathcal{R}_2O_3$. Although this shift could be due to analytic continuation, we interpreted it as a O2p-hybridization effect as supported by calculations neglecting the latter and by a simple analytical model. Though the simultaneous treatment of multiplet and hybridization effects require the use of the computationally heavy CTQMC approach as well as additional approximations (renormalization of U and DC, etc.), our method is entirely parameter-free. Furthermore, these hybridization effects are not always as strong, such as in $\mathcal{R}$SF. Our theoretical optical gap values are in good agreement with experimental results in these fluorosulfides which are potential replacements for cadmium-based pigments. Therefore, we believe that the present approach is a promising tool for predicting and analyzing the optical response in correlated $4f$ semiconductors.

7.9 Appendix

7.9.1 Spectral function of $\mathcal{R}_2O_3$: HI vs CTQMC

Figure 7.7 shows the integrated spectral function of Pr_2O_3 computed with different approaches to the quantum impurity problem in the final DMFT run of the mBJ@DFT+DMFT scheme. The density-density approximation for the Coulomb interaction was employed in all these benchmarks. Our CTQMC calculations within the density-density approximation were performed with $1.6 \cdot 10^8$ Monte Carlo cycles and 400 moves per cycle. Analytical continuation of the CTQMC self-energies, which are calculated on the imaginary-frequency Matsubara grid, was performed using the maximum entropy method implemented in the TRIQS library [Kraberger et al., 2017].

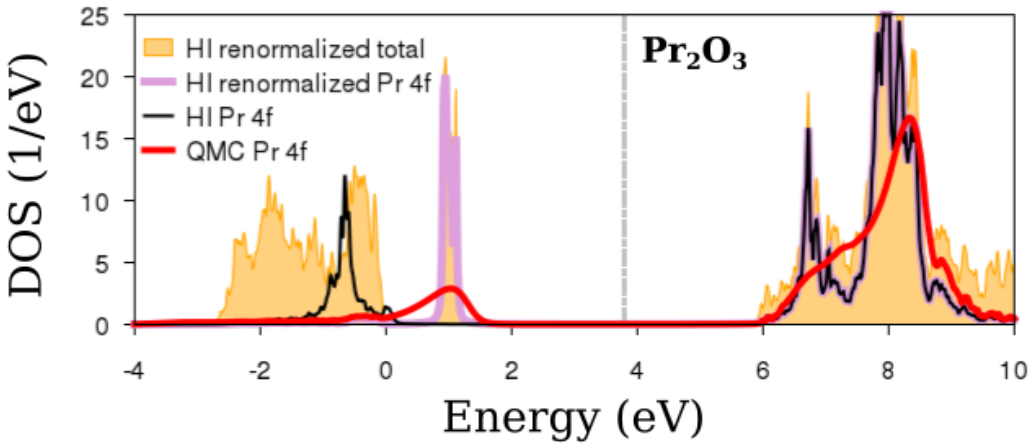

Figure 7.7: Total and partial $4f$ integrated spectral functions of Pr_2O_3 computed within the density-density approximation for the Coulomb interaction, with different flavors of the mBJ@DFT+DMFT approach: HI, CTQMC and HI with renormalized U and DC. The vertical thick dashed line is the chemical potential at room temperature computed within HI with renormalized parameters.

The comparison between Hubbard-I and CTQMC, both with *ab initio* values of U and DC, illustrates the CTQMC induced shift of the $4f$ LHB, with the UHB being unaffected. This shift can effectively be taken into account at the level of HI by renormalizing U and correcting correspondingly the DC term. By setting $U \to U - X$ and $\Sigma_{\mathrm{DC}} \to \Sigma_{\mathrm{DC}} - N_{\mathrm{at}} X$ one may align the HI spectra with the CTQMC one, as illustrated in figure 7.7. This unambiguous renormalization scheme yields $X = 1.6$ eV for Pr_2O_3. The same procedure was applied to the other correlated insulators and the renormalized parameters are summarized in table 7.1.

7.9.2 Perturbative treatment of hybridization

The CTQMC shift of the LHB observed in the $\mathcal{R}_2O_3$ spectral function (e.g. in Pr_2O_3 in Fig. 7.7) can be qualitatively understood within a simplified model using a second-order

perturbation-theory treatment of the $\mathcal{R}4f-\mathrm{O}2p$ hybridization.

We consider the $4f$ quasi-atomic Hamiltonian with a scalar ($J = 0$) interaction vertex:

$$\hat{H}_{4f} = \sum_i (\epsilon_i - \Sigma_{DC}) f_i^\dagger f_i + \frac{1}{2} U \sum_{i \neq j} \hat{n}_i \hat{n}_j \tag{7.1}$$

where ϵ_i is the KS energy level of the orbital i of the $4f$ shell, U is the Coulomb parameter and $\Sigma_{\mathrm{DC}} = U(N_{\mathrm{at}} - 1/2)$ is the FLL double counting correction with the nominal atomic occupancy N_{at}. The ϵ_i are close to the Fermi level, which we set as the zero energy; we will therefore take $\epsilon_i \approx 0$ eV.

We then add the hybridization of the $4f$ shell with $2p$ shells of the seven O ions that are the nearest neighbors of the $\mathcal{R}$ site. Hence, we include $N_p = 7 \times 6$ occupied $2p$ levels at an average energy ϵ_p:

$$\hat{H} = \hat{H}_{4f} + \epsilon_p \sum_j c_j^\dagger c_j - \sum_{ij} t (f_i^\dagger c_j + c_j^\dagger f_i) \tag{7.2}$$

where t is the hybridization matrix element.

Diagonalizing the full Hamiltonian (7.2) with finite t is analogous to an exact approach taking into account the hybridization of $4f$ orbitals with O $2p$ states; assuming $t = 0$ is analogous to the HI approximation[3].

We first consider the limit $t = 0$ of this simplified model. The eigenstates with fully occupied p states can be labelled by the number N of electrons in the $4f$ shell, the ground-state occupancy being N_{at}. We can compute the following eigenenergies:

$$E_{N_{\mathrm{at}}} = N_p \epsilon_p - U \frac{N_{\mathrm{at}}^2}{2} \tag{7.3}$$

$$E_{N_{\mathrm{at}}-1} = E_{N_{\mathrm{at}}+1} = N_p \epsilon_p - U \frac{N_{\mathrm{at}}^2 - 1}{2}. \tag{7.4}$$

The LHB and UHB energies are given by:

$$E_{\mathrm{LHB}} = E_{N_{\mathrm{at}}} - E_{N_{\mathrm{at}}-1} = -\frac{U}{2} \tag{7.5}$$

$$E_{\mathrm{UHB}} = E_{N_{\mathrm{at}}+1} - E_{N_{\mathrm{at}}} = \frac{U}{2}. \tag{7.6}$$

We now consider the effect of small finite hybridization t within the second-order perturbation theory on these different energy levels – the first order has no contribution. As the O $2p$ states are occupied, the only possible processes are the hopping of their N_p electrons to the empty $4f$

[3]Within HI, hybridization shifts can arise when the self-energy is put in the lattice Green's functions, resulting in a difference between the impurity and local spectral functions. Here, in the $\mathcal{R}_2\mathrm{O}_3$ compounds, we checked that this difference and, hence, hybridization effects at the level of HI were essentially negligible.

states and back, hence, with $N_f = 14 - N_{\text{at}}$ the number of empty $4f$ levels in the ground state,

$$E_{N_{\text{at}}}(t) \approx E_{N_{\text{at}}} - \frac{N_p N_f t^2}{-\epsilon_p + U/2} \tag{7.7}$$

$$E_{N_{\text{at}}-1}(t) \approx E_{N_{\text{at}}-1} - \frac{N_p (N_f+1) t^2}{-\epsilon_p - U/2} \tag{7.8}$$

$$E_{N_{\text{at}}+1}(t) \approx E_{N_{\text{at}}+1} - \frac{N_p (N_f-1) t^2}{-\epsilon_p + 3U/2} \tag{7.9}$$

and therefore

$$E_{\text{LHB}}(t) \approx E_{\text{LHB}} - \frac{N_p N_f t^2}{-\epsilon_p + U/2} + \frac{N_p (N_f+1) t^2}{-\epsilon_p - U/2} \tag{7.10}$$

$$E_{\text{UHB}}(t) \approx E_{\text{UHB}} - \frac{N_p (N_f-1) t^2}{-\epsilon_p + 3U/2} + \frac{N_p N_f t^2}{-\epsilon_p + U/2}. \tag{7.11}$$

In the $\mathcal{R}_2O_3$ systems studied in this work, we typically have $\epsilon_p \sim -5$ eV and $U \sim 8$ eV, which gives $1/(-\epsilon_p + U/2) \sim 0.1$ eV^{-1}, $1/(-\epsilon_p + 3U/2) \sim 0.06$ eV^{-1} and $1/(-\epsilon_p - U/2) \sim 1$ eV^{-1}. Therefore, as a first approximation, hybridization induces a shift of the LHB towards higher energies by lowering the energy of the $N = N_{\text{at}} - 1$ sector, but does not affect the UHB:

$$\begin{aligned} E_{\text{LHB}}(t) &\approx E_{\text{LHB}} + N_p (N_f+1) \frac{t^2}{-\epsilon_p - U/2} \\ E_{\text{UHB}}(t) &\approx E_{\text{UHB}} \end{aligned} \tag{7.12}$$

The value of t^2 in the $\mathcal{R}$ sesquioxides was estimated by the average over all p and f orbitals $t^2 = \frac{1}{14 N_p} \sum_{i \in [\![1,14]\!], j \in [\![1,N_p]\!]} |V_{ij}|^2$ where V_{ij} is the hopping between f orbital i and p orbital j. The matrix V was computed within the mBJ@DFT+DMFT approach by $V = \sum_{\mathbf{k}} P^f_{\mathbf{k}} H^{KS}_{\mathbf{k}} (P^p_{\mathbf{k}})\dagger$ where $H^{KS}_{\mathbf{k}}$ is the KS Hamiltonian and $P^{f(p)}_{\mathbf{k}}$ the projection to $\mathcal{R}$ $4f$ (O $2p$) Wannier orbitals. This procedure yielded $t^2 \sim 0.009$ eV^2 in Ce_2O_3, hence a LHB shift of ~ 5.2 eV from 7.12 (for $N_{\text{at}} = 1$).

The results of this very simplified model are thus consistent with the significant upward shift of the LHB computed by the CTQMC approach (illustrated in Fig. 7.7) which could therefore be explained by hybridization effects, specifically by the hopping of O $2p$ electrons to the $4f$ states and back.

Part IV

Localized correlated shells beyond Hubbard-I

Chapter 8

Equation of motion method for the strong-coupling Anderson impurity model

In this chapter, we develop a new solver for the Anderson Impurity Model (AIM, see Sec. 2.3) involved in the Dynamical Mean-Field Theory (DMFT, see Sec. 2.2), in the strong coupling limit which is especially relevant for the rare earths $4f$ shell (see. Sec. 3.7)

8.1 Motivation

While exact approaches to the AIM exist, they are in practice not applicable in the whole range of the parameters (Coulomb interaction, temperature, number of orbitals, etc.) and can show additional deficiencies. Exact Diagonalization (ED) [Caffarel and Krauth, 1994], for instance, can only treat a small number of bath sites and therefore usually gives a poor energy resolution in multi-orbital systems. Numerical Renormalization Group (NRG) [Wilson, 1975, Bulla et al., 2008] and Density Matrix Renormalization Group (DMRG) [White, 1992, Schollwöck, 2011] approaches usually scale poorly with the number of orbitals – though recent improvements for multi-orbital systems within DMRG were proposed by [Bauernfeind et al., 2017]. Quantum Monte-Carlo (QMC, see. Sec. 2.4) methods require analytic continuation to extract real frequency properties (which can wash out complicated spectral structures as discussed in Sec. 2.5) [Rubtsov et al., 2005, Werner et al., 2006, Gull et al., 2008] and/or suffer from the sign-problem [Prokof'ev and Svistunov, 2007, Gull et al., 2010], the latter being especially prevalent in the cases of realistic multi-orbital interaction vertices and in the presence of large spin-orbit. Generally speaking, dealing with an f shell impurity with an arbitrary Coulomb interaction embedded in an arbitrary bath is computationally too heavy with exact approaches.

However, as discussed in section 3.7, the $4f$ shell of rare earths in real materials is expected to be in the strong-coupling $U \gg \Delta$ regime for which the most drastic approximation is Hubbard-I (HI). This approximation, used extensively throughout this thesis, neglects the hybridization Δ but exhibits many advantages: it is fast even in the relevant case of the multi-orbital f shell, it

can give quantities on the imaginary and real frequency axes, etc. Yet, it cannot describe some key phenomenons which occur in the strong-coupling regime such as:

- mixed-valence states and the Kondo effect [Hewson, 1993], crucial in the physics of some Ce$-\mathcal{M}$ intermetallics for instance (see [Galler et al., 2021b] as well as chapters 5 and 6);
- the low-T antiferromagnetic order in the one band Hubbard model as expected by the spin-1/2 Heisenberg model (the low energy physics the one band Hubbard model is well-known to be be reducible to the Heisenberg Hamiltonian in the strong-coupling limit) – such magnetic orders are ubiquitous in real f-electron compounds, where the intersite magnetic coupling is mediated through RKKY or superexchange, both mechanisms being missed by the HI approximation;
- finite lifetime effects and broadening of the spectrum which are completely neglected as the HI self-energy on the real axis is purely real.

All these limitations have driven the research for an efficient strong-coupling, causal, beyond HI approach to the AIM. Various methods have been proposed to construct an approximation for the impurity Green's function which is correct, at least, to the first order in the hybridization. We briefly review them below.

The Non-Crossing Approximation (NCA) and its extensions. NCA was successfully applied to Ce [Zölfl et al., 2001] and $La_{1-x}Sr_xTiO_3$ [Zölfl et al., 2000] for instance. It nonetheless requires the computationally heavy self-consistent calculation of the pseudoparticles self-energies and is hard to formulate on the imaginary axis [Haule et al., 2010].

The different-time decoupling [Stasyuk and Hera, 2005]. This approach is more general than the Hubbard-III approximation [Hubbard, 1964]. The formalism is however single-orbital and requires the self-consistent calculation of Hubbard operators averages.

The perturbation theory around the atomic limit. The methods of [Dai et al., 2005] and [Jia-Ning et al., 2010] can reproduce the Néel temperature in the strong coupling regime but the former violates causality in the metallic phase and the latter has to make several approximations (e.g. limitation to real self-energies).

The projective truncation approximation [Fan et al., 2018, Fan and Tong, 2019]. In the single-orbital case, this technique qualitatively captures the Kondo effect and ensures causality. The extension to multi-orbital systems seems however difficult.

The equation of motion (EOM) [Jeschke and Kotliar, 2005, Tong, 2015, Ma and Tong, 2019]. The approach of [Jeschke and Kotliar, 2005] is limited to infinite U. To avoid causality violation, [Tong, 2015, Ma and Tong, 2019] had to perform a continued-fraction resummation of the impurity Green's function – which is not trivial in multi-orbital cases.

In this chapter, we develop a new EOM method to solve the AIM which is exact at first order in the hybridization. EOM approaches are based on a formula for the time derivative of two-times Green's functions which we explicit below.

Let us consider a general time-independent Hamiltonian $\hat{H}$ and a fermionic retarded Green's function[1]

$$\langle\langle \hat{O}, \hat{Q}^\dagger \rangle\rangle_{t-t'} = -i\theta(t-t')\langle\{\hat{O}(t), \hat{Q}^\dagger(t')\}\rangle \tag{8.1}$$

of two arbitrary operators in the Heisenberg representation $\hat{O}(t)$ and $\hat{Q}^\dagger(t')$ at real times t and t' – where $\{\ \}$ denotes the anticommutator and $\langle\ \rangle$ the average value. Then, taking the derivative with respect to t or t' gives:

$$\partial_t \langle\langle \hat{O}, \hat{Q}^\dagger \rangle\rangle_{t-t'} = -i\delta(t-t')\langle\{\hat{O}, \hat{Q}^\dagger\}\rangle - \theta(t-t')\langle\{[\hat{O}(t), \hat{H}], \hat{Q}^\dagger(t')\}\rangle \tag{8.2}$$

$$\partial_{t'} \langle\langle \hat{O}, \hat{Q}^\dagger \rangle\rangle_{t-t'} = i\delta(t-t')\langle\{\hat{O}, \hat{Q}^\dagger\}\rangle - \theta(t-t')\langle\{\hat{O}(t), [\hat{Q}^\dagger(t'), \hat{H}]\}\rangle. \tag{8.3}$$

By taking the Fourier transform, we get, with the usual $[\ ]$ notation for the commutator,

$$\omega\langle\langle \hat{O}, \hat{Q}^\dagger \rangle\rangle_\omega = \langle\{\hat{O}, \hat{Q}^\dagger\}\rangle + \langle\langle [\hat{O}, \hat{H}], \hat{Q}^\dagger \rangle\rangle_\omega \tag{8.4}$$

$$= \langle\{\hat{O}, \hat{Q}^\dagger\}\rangle + \langle\langle \hat{O}, [\hat{Q}, \hat{H}]^\dagger \rangle\rangle_\omega, \tag{8.5}$$

which is the equation of motion of the Green's function $\langle\langle \hat{O}, \hat{Q}^\dagger \rangle\rangle_\omega$. It can be generalized to complex frequencies z – from now on, we will drop the index z in $\langle\langle \hat{O}, \hat{Q}^\dagger \rangle\rangle_z$. The EOM 8.4 generates a new Green's function $\langle\langle [\hat{O}, \hat{H}], \hat{Q}^\dagger \rangle\rangle$ for which a new EOM should be written. Except in some specific cases, this procedure hence generates an infinite set of EOMs and a truncation (by some decoupling) of these equations is therefore usually applied at some order. However, as shown by [Tong, 2015] and illustrated in section 8.3, truncation schemes do not in general preserve the analytical properties of the Green's function. The latter can be recasted into a continued fraction (CF[2]) form to avoid this issue [Tong, 2015, Ma and Tong, 2019], as there exist some simple criteria to ensure causality of CF Green's functions (see Sec. 8.2).

Interestingly, [Tserkovnikov, 1981] developed a general EOM framework which directly expresses a two-time Green's function into an infinite CF form. The idea behind this chapter is therefore to use the formalism of [Tserkovnikov, 1981] to express the Anderson impurity Green's function and to truncate at first order in the hybridization to get a finite CF. The EOM-based AIM solver presented in this chapter hence does not need to perform the CF resummation of [Tong, 2015, Ma and Tong, 2019]. In section 8.2, we give criteria for a CF Green's function to be causal. We illustrate the causality violation of usual truncated EOMs on a simple solvable model in section 8.3. Then, in sections 8.4 and 8.5, we derive the EOM solver equations. Finally, we numerically benchmark the approach on the single-orbital case in section 8.6.

[1] See appendix A for the Green's functions notations used in this thesis.
[2] In this chapter, "CF" does not mean "Crystal Field".

8.2 Causality and continued fraction

Theorem. A matrix Green's function of the form

$$G(z) = I\Big(zI - L - Y(z)\Big)^{-1} I \tag{8.6}$$

is causal if the following criteria are all met:

1. I is Hermitian positive definite;
2. L is Hermitian;
3. $Y(z)$ is causal.

Proof. Let us assume that the aforementioned criteria are met. Then,

$$i\Big(G(z) - [G(z)]^\dagger\Big) = iG(z)\Big(\big([G(z)]^\dagger\big)^{-1} - \big(G(z)\big)^{-1}\Big)[G(z)]^\dagger \tag{8.7}$$

$$= iG(z)I^{-1}\Big(\bar{z}I - L - [Y(z)]^\dagger - zI + L + Y(z)\Big)I^{-1}[G(z)]^\dagger \tag{8.8}$$

$$= G(z)I^{-1}\Big(i(\bar{z} - z)I + i\big(Y(z) - [Y(z)]^\dagger\big)\Big)I^{-1}[G(z)]^\dagger. \tag{8.9}$$

If $z \in \mathcal{H}$ where $\mathcal{H}$ is the upper half of the complex plane, then $i(\bar{z} - z) > 0$, hence $i(\bar{z} - z)I$ is positive definite. Because Y is causal, $i\big(Y(z) - [Y(z)]^\dagger\big)$ is positive semidefinite for all $z \in \mathcal{H}$. Hence,

$$\Big(i(\bar{z} - z)I + i\big(Y(z) - [Y(z)]^\dagger\big)\Big) = P(z) \tag{8.10}$$

is positive semidefinite for all $z \in \mathcal{H}$. Finally, as

$$i\Big(G(z) - [G(z)]^\dagger\Big) = \big[G(z)I^{-1}\big]P(z)\big[G(z)I^{-1}\big]^\dagger \tag{8.11}$$

is positive semidefinite for all $z \in \mathcal{H}$, G is causal, which completes the proof.

This theorem can be applied to multi-level continued fraction (i.e. when $Y(z)$ is itself expressed in a form similar to Eq. 8.6, etc.) by applying it recursively. It then gives criteria on each coefficient of the CF for it to be causal.

8.3 Truncated equation of motion on a simple example

Let us now illustrate, on a simple solvable example, how truncation of EOMs can violate causality. We consider in this section the Hamiltonian

$$\hat{H} = \epsilon(\hat{f}^\dagger \hat{f} + \hat{c}^\dagger \hat{c}) + t(\hat{f}^\dagger \hat{c} + \hat{c}^\dagger \hat{f}) \tag{8.12}$$

and aim to compute $\langle\langle \hat{f}, \hat{f}^\dagger \rangle\rangle$ at second order in t. Using the equation of motion 8.4, we get

$$z\langle\langle \hat{f}, \hat{f}^\dagger \rangle\rangle = 1 + \epsilon\langle\langle \hat{f}, \hat{f}^\dagger \rangle\rangle + t\langle\langle \hat{c}, \hat{f}^\dagger \rangle\rangle. \tag{8.13}$$

Subsequently applying the EOM 8.5 to $\langle\langle \hat{c}, \hat{f}^\dagger \rangle\rangle$, we obtain

$$z\langle\langle \hat{c}, \hat{f}^\dagger \rangle\rangle = \epsilon\langle\langle \hat{c}, \hat{f}^\dagger \rangle\rangle + t\langle\langle \hat{c}, \hat{c}^\dagger \rangle\rangle. \tag{8.14}$$

Combining equations 8.13 and 8.14, we get

$$\langle\langle \hat{f}, \hat{f}^\dagger \rangle\rangle = \frac{1}{z-\epsilon} + \frac{t^2}{(z-\epsilon)^2}\langle\langle \hat{c}, \hat{c}^\dagger \rangle\rangle. \tag{8.15}$$

We now truncate 8.15 at second order in t, and hence, at zeroth order for $\langle\langle \hat{c}, \hat{c}^\dagger \rangle\rangle$ (i.e. we take $\langle\langle \hat{c}, \hat{c}^\dagger \rangle\rangle = \frac{1}{z-\epsilon}$):

$$\langle\langle \hat{f}, \hat{f}^\dagger \rangle\rangle = \frac{1}{z-\epsilon} + \frac{t^2}{(z-\epsilon)^3}. \tag{8.16}$$

This form of the Green's function is not causal because of the pole of order 3. Indeed, at $z = \epsilon + i\eta$, we get

$$\langle\langle \hat{f}, \hat{f}^\dagger \rangle\rangle_{\epsilon+i\eta} = -i\frac{1}{\eta} + i\frac{t^2}{\eta^3}. \tag{8.17}$$

and the imaginary part is not always negative for $\eta > 0$.

This model is however solvable by applying the EOM 8.4 to $\langle\langle \hat{c}, \hat{f}^\dagger \rangle\rangle$:

$$z\langle\langle \hat{c}, \hat{f}^\dagger \rangle\rangle = \epsilon\langle\langle \hat{c}, \hat{f}^\dagger \rangle\rangle + t\langle\langle \hat{f}, \hat{f}^\dagger \rangle\rangle. \tag{8.18}$$

Combining equations 8.13 and 8.18, we get the true Green's function

$$\langle\langle \hat{f}, \hat{f}^\dagger \rangle\rangle = \frac{1}{z - \epsilon - \frac{t^2}{z-\epsilon}}. \tag{8.19}$$

This form is a 2-level CF which is causal (it can be checked with the theorem of the previous section). At second order in t, it is also equal to the Green's function 8.16.

As a summary, general EOM approaches need to be truncated at a given order which leads to expressions for the Green's function of a form similar to 8.16. This expression is in general not causal. [Tong, 2015] hence resummed their truncated-EOM expression in a continued fraction

which, at the given expansion order, is equal to the EOM-derived expression. This resummation leads to a form analogous to 8.19. The EOM approach proposed below directly writes the Anderson impurity Green's function in a CF form similar to 8.19 thanks to the EOM formalism of [Tserkovnikov, 1981]. It hence does not require CF resummation and the analyticity can be checked with the theorem of the previous section.

8.4 Equation of motion: Tserkovnikov's formalism

In this section, we review the general EOM formalism behind our approach, based on the work of [Tserkovnikov, 1981]. This general framework will then be applied to the specific case of the AIM in the next section.

Let us consider a Hamiltonian $\hat{H}$ and the Green's function $\langle\langle \hat{\boldsymbol{A}}, \hat{\boldsymbol{A}}^\dagger \rangle\rangle$ where $\hat{\boldsymbol{A}}$ is a vector of operators. We decompose the Hamiltonian $\hat{H} = \hat{H}_0 + \hat{H}_+$ and introduce the Liouville operator $\mathcal{L} = \mathcal{L}_0 + \mathcal{L}_+$ such that $\mathcal{L}_0 \hat{\boldsymbol{A}} = [\hat{\boldsymbol{A}}, \hat{H}_0] = M\hat{\boldsymbol{A}}$, and $\mathcal{L}_+ \hat{\boldsymbol{A}} = [\hat{\boldsymbol{A}}, \hat{H}_+] = P\hat{\boldsymbol{B}}$, where M, P are matrices and $\hat{\boldsymbol{B}}$ a vector of operators. Following [Tserkovnikov, 1981], we also introduce the following quantities for arbitrary vector of operators $\hat{\boldsymbol{O}}$ and $\hat{\boldsymbol{Q}}$:

$$\langle \hat{\boldsymbol{O}}, \hat{\boldsymbol{Q}}^\dagger \rangle = \langle \{\hat{\boldsymbol{O}}, \hat{\boldsymbol{Q}}^\dagger\} \rangle \tag{8.20}$$

$$\langle\langle \hat{\boldsymbol{O}}, \hat{\boldsymbol{Q}}^\dagger \rangle\rangle_1 = \langle\langle \hat{\boldsymbol{O}}, \hat{\boldsymbol{Q}}^\dagger \rangle\rangle - \langle\langle \hat{\boldsymbol{O}}, \hat{\boldsymbol{A}}^\dagger \rangle\rangle \langle\langle \hat{\boldsymbol{A}}, \hat{\boldsymbol{A}}^\dagger \rangle\rangle^{-1} \langle\langle \hat{\boldsymbol{A}}, \hat{\boldsymbol{Q}}^\dagger \rangle\rangle \tag{8.21}$$

$$\langle \hat{\boldsymbol{O}}, \hat{\boldsymbol{Q}}^\dagger \rangle_1 = \langle \hat{\boldsymbol{O}}, \hat{\boldsymbol{Q}}^\dagger \rangle - \langle \hat{\boldsymbol{O}}, \hat{\boldsymbol{A}}^\dagger \rangle \langle \hat{\boldsymbol{A}}, \hat{\boldsymbol{A}}^\dagger \rangle^{-1} \langle \hat{\boldsymbol{A}}, \hat{\boldsymbol{Q}}^\dagger \rangle \tag{8.22}$$

$$\langle\langle \hat{\boldsymbol{O}}, \hat{\boldsymbol{Q}}^\dagger \rangle\rangle_2 = \langle\langle \hat{\boldsymbol{O}}, \hat{\boldsymbol{Q}}^\dagger \rangle\rangle_1 - \langle\langle \hat{\boldsymbol{O}}, \hat{\boldsymbol{B}}^\dagger \rangle\rangle_1 \langle\langle \hat{\boldsymbol{B}}, \hat{\boldsymbol{B}}^\dagger \rangle\rangle_1^{-1} \langle\langle \hat{\boldsymbol{B}}, \hat{\boldsymbol{Q}}^\dagger \rangle\rangle_1. \tag{8.23}$$

In the right-hand side of equations 8.21 and 8.22 (8.23), the second term cancels all contributions to the first term that are linear in $\hat{\boldsymbol{A}}$ ($\hat{\boldsymbol{B}}$). $\langle \hat{\boldsymbol{A}}, \hat{\boldsymbol{Q}}^\dagger \rangle_1 = 0$ for example.

Then, the equation of motion of $\langle\langle \hat{\boldsymbol{A}}, \hat{\boldsymbol{A}}^\dagger \rangle\rangle$ is, according to [Tserkovnikov, 1981] (Eq. 1.18a therein)

$$z\langle\langle \hat{\boldsymbol{A}}, \hat{\boldsymbol{A}}^\dagger \rangle\rangle = \langle \hat{\boldsymbol{A}}, \hat{\boldsymbol{A}}^\dagger \rangle + \Big(\langle \mathcal{L}\hat{\boldsymbol{A}}, \hat{\boldsymbol{A}}^\dagger \rangle + \langle\langle \mathcal{L}\hat{\boldsymbol{A}}, (\mathcal{L}\hat{\boldsymbol{A}})^\dagger \rangle\rangle_1 \Big) \langle \hat{\boldsymbol{A}}, \hat{\boldsymbol{A}}^\dagger \rangle^{-1} \langle\langle \hat{\boldsymbol{A}}, \hat{\boldsymbol{A}}^\dagger \rangle\rangle \tag{8.24}$$

$$\implies \langle\langle \hat{\boldsymbol{A}}, \hat{\boldsymbol{A}}^\dagger \rangle\rangle = \langle \hat{\boldsymbol{A}}, \hat{\boldsymbol{A}}^\dagger \rangle \Big(z\langle \hat{\boldsymbol{A}}, \hat{\boldsymbol{A}}^\dagger \rangle - \langle \mathcal{L}\hat{\boldsymbol{A}}, \hat{\boldsymbol{A}}^\dagger \rangle - P\langle\langle \hat{\boldsymbol{B}}, \hat{\boldsymbol{B}}^\dagger \rangle\rangle_1 P^\dagger \Big)^{-1} \langle \hat{\boldsymbol{A}}, \hat{\boldsymbol{A}}^\dagger \rangle \tag{8.25}$$

which generates the new Green's function $\langle\langle \hat{\boldsymbol{B}}, \hat{\boldsymbol{B}}^\dagger \rangle\rangle_1$. According to [Tserkovnikov, 1981] (Eq. 1.29a therein), its equation of motion is

$$\begin{aligned} z\langle\langle \hat{\boldsymbol{B}}, \hat{\boldsymbol{B}}^\dagger \rangle\rangle_1 = \langle \hat{\boldsymbol{B}}, \hat{\boldsymbol{B}}^\dagger \rangle_1 + \Big(& \langle \mathcal{L}\hat{\boldsymbol{B}}, \hat{\boldsymbol{B}}^\dagger \rangle_1 - \langle \hat{\boldsymbol{B}}, \hat{\boldsymbol{A}}^\dagger \rangle \langle \hat{\boldsymbol{A}}, \hat{\boldsymbol{A}}^\dagger \rangle^{-1} \langle \mathcal{L}\hat{\boldsymbol{A}}, \hat{\boldsymbol{B}}^\dagger \rangle_1 \\ & + \langle\langle \mathcal{L}\hat{\boldsymbol{B}}, (\mathcal{L}\hat{\boldsymbol{B}})^\dagger \rangle\rangle_2 \Big) \langle \hat{\boldsymbol{B}}, \hat{\boldsymbol{B}}^\dagger \rangle_1^{-1} \langle\langle \boldsymbol{B}, \boldsymbol{B}^\dagger \rangle\rangle_1 \end{aligned} \tag{8.26}$$

which gives

$$\langle\langle \hat{\boldsymbol{B}}, \hat{\boldsymbol{B}}^\dagger \rangle\rangle_1 = \langle \hat{\boldsymbol{B}}, \hat{\boldsymbol{B}}^\dagger \rangle_1 \Bigg(z\langle \hat{\boldsymbol{B}}, \hat{\boldsymbol{B}}^\dagger \rangle_1 - \langle \mathcal{L}\hat{\boldsymbol{B}}, \hat{\boldsymbol{B}}^\dagger \rangle_1 + \langle \hat{\boldsymbol{B}}, \hat{\boldsymbol{A}}^\dagger \rangle \langle \hat{\boldsymbol{A}}, \hat{\boldsymbol{A}}^\dagger \rangle^{-1} \langle \mathcal{L}\hat{\boldsymbol{A}}, \hat{\boldsymbol{B}}^\dagger \rangle_1 - \langle\langle \mathcal{L}\hat{\boldsymbol{B}}, (\mathcal{L}\hat{\boldsymbol{B}})^\dagger \rangle\rangle_2 \Bigg)^{-1} \langle \hat{\boldsymbol{B}}, \hat{\boldsymbol{B}}^\dagger \rangle_1. \tag{8.27}$$

It generates the new Green's function $\langle\langle \mathcal{L}\hat{\boldsymbol{B}}, (\mathcal{L}\hat{\boldsymbol{B}})^\dagger \rangle\rangle_2$. [Tserkovnikov, 1981] then reiterates this procedure and shows that one can construct an infinite CF for $\langle\langle \hat{\boldsymbol{A}}, \hat{\boldsymbol{A}}^\dagger \rangle\rangle$. We will however only consider terms up to the second order in $\hat{H}_+$ in the Anderson impurity model, which will put an end to this infinite set of equations.

8.5 Anderson impurity model to first order in the hybridization

Let us now consider the specific case of the Anderson impurity model (see Sec. 2.3):

$$\hat{H} = \hat{H}_{\text{AIM}} = \hat{H}_f + \hat{H}_c + \hat{H}_{fc} \tag{8.28}$$

where $\hat{H}_f$ is the local impurity Hamiltonian, $\hat{H}_c = \sum_a e_a \hat{c}_a^\dagger \hat{c}_a$ is the bath Hamiltonian and $\hat{H}_{fc} = \sum_{ua}(V_{au}^* \hat{f}_u^\dagger \hat{c}_a + V_{au} \hat{c}_a^\dagger \hat{f}_u)$ is the coupling between the impurity and the bath. We assume that we have diagonalized $\hat{H}_f$ (using a HI solver of the AIM), i.e. we know orthonormal states $|A\rangle$ such that $\hat{H}_f |A\rangle = E_A |A\rangle$. We can then write the Hamiltonian $\hat{H}$ using the Hubbard X operators (or standard basis operators), defined by $\hat{X}^{AB} = |A\rangle \langle B|$, as:

$$\hat{H}_{\text{AIM}} = \sum_A E_A \hat{X}^{AA} + \hat{H}_c + \sum_{uaAB} \left(V_{au}^* \langle B| \hat{f}_u^\dagger |A\rangle \hat{X}^{BA} \hat{c}_a + V_{au} \langle A| \hat{f}_u |B\rangle \hat{c}_a^\dagger \hat{X}^{AB} \right) \tag{8.29}$$

$$= \sum_A E_A \hat{X}^{AA} + \hat{H}_c + \sum_{ai} \left(W_1^{ai} (\hat{X}_{-1}^i)^\dagger \hat{c}_a + W_{-1}^{ai} \hat{c}_a^\dagger \hat{X}_{-1}^i \right) \tag{8.30}$$

where $\hat{X}_{\Delta(i)}^i = \hat{X}^{i(1)i(2)}$, $\Delta(i)$ is a reminder of the difference of electrons between state $i(1)$ and state $i(2)$, $W_{-1}^{ai} = \sum_u V_{au} f_u^i$, $f_u^i = \langle i(1)| \hat{f}_u |i(2)\rangle$ and $W_{+1}^{ai} = (W_{-1}^{ai})^*$. We introduce the hybridization function

$$\Delta_{uv}(z) = \sum_a \frac{V_{au}^* V_{av}}{z - e_a}. \tag{8.31}$$

Our aim is to compute the impurity Green's function

$$[G_{\text{imp}}]_{uv} = \langle\langle \hat{f}_u, \hat{f}_v^\dagger \rangle\rangle = \sum_{ij} f_u^i f_v^{j*} \langle\langle \hat{X}_{-1}^i, (\hat{X}_{-1}^j)^\dagger \rangle\rangle = \sum_{ij} f_u^i f_v^{j*} G_{ij}, \tag{8.32}$$

with $G_{ij} = \langle\langle \hat{X}_{-1}^i, (\hat{X}_{-1}^j)^\dagger \rangle\rangle$, to the first order in the hybridization 8.31 or, equivalently, to the second order in the coupling V. To this end, we apply the general EOM formalism described in

the previous section to $G = \langle\langle \hat{\boldsymbol{X}}_{-1}, (\hat{\boldsymbol{X}}_{-1})^\dagger \rangle\rangle$. Using the same notations as above, we have:

$$\hat{\boldsymbol{A}} = \hat{\boldsymbol{X}}_{-1} \tag{8.33}$$
$$\hat{H}_0 = \hat{H}_f + \hat{H}_c \tag{8.34}$$
$$\hat{H}_+ = \hat{H}_{fc} \tag{8.35}$$
$$M_{ij} = \Delta E_i \delta_{ij} = (E_{i(2)} - E_{i(1)})\delta_{ij} \tag{8.36}$$
$$\hat{\boldsymbol{B}} = (\hat{\boldsymbol{B}}_{-1}, \hat{\boldsymbol{B}}_1) \tag{8.37}$$
$$\hat{B}_1^{(aj)} = (\hat{X}_0^j)^\dagger \hat{c}_a \tag{8.38}$$
$$\hat{B}_{-1}^{(aj)} = \hat{c}_a^\dagger \hat{X}_{-2}^j \tag{8.39}$$
$$P_s^{i,(aj)} = s \sum_l W_s^{al} \eta_s^{li}(j) \tag{8.40}$$
$$\{\hat{X}_{-1}^i, \hat{X}_{-1}^l\} = \sum_j \eta_{-1}^{li}(j) \hat{X}_{-2}^j \tag{8.41}$$
$$\{\hat{X}_{-1}^i, (\hat{X}_{-1}^l)^\dagger\} = \sum_j \eta_1^{li}(j) (\hat{X}_0^j)^\dagger \tag{8.42}$$

The label $s = \pm 1$ accounts for the two hopping possibilities: from the impurity to the bath and back (-1) or the reverse (+1). To truncate equation 8.25 to the second order in $\hat{H}_{fc}$ (and hence Eq. 8.27 to the zeroth order), we shall assume:

$$\langle\langle \mathcal{L}\hat{\boldsymbol{B}}, (\mathcal{L}\hat{\boldsymbol{B}})^\dagger \rangle\rangle_2 = \langle\langle \mathcal{L}_0\hat{\boldsymbol{B}}, (\mathcal{L}_0\hat{\boldsymbol{B}})^\dagger \rangle\rangle_2 = N \langle\langle \hat{\boldsymbol{B}}, \hat{\boldsymbol{B}}^\dagger \rangle\rangle_2 N^\dagger = 0 \tag{8.43}$$
$$\langle \mathcal{L}\hat{\boldsymbol{A}}, \hat{\boldsymbol{B}}^\dagger \rangle_1 = \langle \mathcal{L}_0\hat{\boldsymbol{A}}, \hat{\boldsymbol{B}}^\dagger \rangle_1 = M \langle \hat{\boldsymbol{A}}, \hat{\boldsymbol{B}}^\dagger \rangle_1 = 0 \tag{8.44}$$
$$\langle \mathcal{L}\hat{\boldsymbol{B}}, \hat{\boldsymbol{B}}^\dagger \rangle_1 = \langle \mathcal{L}_0\hat{\boldsymbol{B}}, \hat{\boldsymbol{B}}^\dagger \rangle_1 = N \langle \hat{\boldsymbol{B}}, \hat{\boldsymbol{B}}^\dagger \rangle_1 \tag{8.45}$$
$$N_{ss'}^{(ai)(bj)} = (-s\Delta E_i + s e_a)\delta_{ij}\delta_{ss'}\delta_{ab}. \tag{8.46}$$

Hence, we finally get for $G(z)$ to first order in Δ:

$$G(z) = I \Big(zI - L - Y(z) \Big)^{-1} I \tag{8.47}$$
$$I = \langle \hat{\boldsymbol{X}}_{-1}, (\hat{\boldsymbol{X}}_{-1})^\dagger \rangle \tag{8.48}$$
$$L = \langle \mathcal{L}\hat{\boldsymbol{X}}_{-1}, (\hat{\boldsymbol{X}}_{-1})^\dagger \rangle \tag{8.49}$$
$$Y(z) = PJ \Big(zJ - NJ \Big)^{-1} JP^\dagger, \tag{8.50}$$

where $J = \langle \hat{\boldsymbol{B}}, \hat{\boldsymbol{B}}^\dagger \rangle_1$. Thanks to the formalism of [Tserkovnikov, 1981], we have hence arrived at a 2-level CF form for the X Green's function and do not need to perform CF resummation like [Tong, 2015]. I, L and $Y(z)$ are to be computed at first order in the hybridization; we derive the corresponding expressions in the following subsections. As demonstrated above, this expression for the Green's function is causal as long as I is Hermitian positive definite, L is Hermitian and

$Y(z)$ is causal. We will discuss the fulfillment of these criteria along the way.

We will use the following notations for the Fermi-Dirac function, the X operators atomic Green's function, the X operators atomic average and the product of f matrix elements:

$$f(\omega) = \frac{1}{1+e^{\beta\omega}} \tag{8.51}$$

$$G^{(0)}_{kl}(z) = \frac{X_{k(1)} + X_{k(2)}}{z - \Delta E_k}\delta_{kl} \tag{8.52}$$

$$X_A = \frac{1}{Z_0}e^{-\beta E_A}, \quad Z_0 = \sum_A e^{-\beta E_A} \tag{8.53}$$

$$F^{pk}_{-1}(u,v) = f^p_u f^{k*}_v, \quad F^{pk}_1(u,v) = F^{kp}_{-1}(u,v). \tag{8.54}$$

We will also use the following quantities defined by [Dai et al., 2005]:

$$R_{vu}(A,B) = \Big(X_A + X_B\Big)T\sum_{n'}\frac{\Delta_{vu}(i\omega_{n'})}{i\omega_{n'} - E_A + E_B} \tag{8.55}$$

$$Q_{vu}(i\omega_n, A, B) = \Big(X_A - X_B\Big)T\sum_{n'}\frac{\Delta_{vu}(i\omega_{n'})}{i\omega_{n'} - i\omega_n - E_A + E_B} \tag{8.56}$$

using the imaginary axis or

$$R_{vu}(A,B) = \mathrm{Re}\big\{X_A\Delta^-_{vu}(E_A - E_B) - X_B\Delta^+_{vu}(E_A - E_B)\big\} \tag{8.57}$$

$$Q_{vu}(z,A,B) = X_A\Delta^-_{vu}(z + E_A - E_B) + X_B\Delta^+_{vu}(z + E_A - E_B) \tag{8.58}$$

$$\Delta^{\pm}(z) = -\frac{1}{\pi}\int\frac{f(\pm\omega')\Delta''(\omega')}{z-\omega'}d\omega' \tag{8.59}$$

$$\Delta''(z) = \frac{1}{i}\left(\Delta(z) - \Big(\Delta(z)\Big)^{\dagger}\right) \tag{8.60}$$

using the real axis.

8.5.1 Calculation of L

Decomposing $\mathcal{L} = \mathcal{L}_0 + \mathcal{L}_+$ we get

$$L = \langle \mathcal{L}\hat{\boldsymbol{X}}_{-1}, (\hat{\boldsymbol{X}}_{-1})^\dagger \rangle \tag{8.61}$$
$$= MI + P\langle \hat{\boldsymbol{B}}, (\hat{\boldsymbol{X}}_{-1})^\dagger \rangle \tag{8.62}$$
$$= MI + L_1 \tag{8.63}$$

where L_1 is to be taken at first order in the hybridization. It gives terms of the form

$$\langle \hat{B}_s^{(al)}, (\hat{X}_{-1}^j)^\dagger \rangle = -s \sum_k \gamma_s^{lj}(k) \langle \hat{C}_s^{ak} \rangle \tag{8.64}$$

where

$$[\hat{X}_{-2}^l, (\hat{X}_{-1}^j)^\dagger] = \sum_k \gamma_{-1}^{lj}(k) \hat{X}_{-1}^k, \quad [(\hat{X}_0^l)^\dagger, (\hat{X}_{-1}^j)^\dagger] = \sum_k \gamma_1^{lj}(k) (\hat{X}_{-1}^k)^\dagger \tag{8.65}$$
$$\hat{C}_{-1}^{ak} = \hat{c}_a^\dagger \hat{X}_{-1}^k, \quad \hat{C}_1^{ak} = (\hat{X}_{-1}^k)^\dagger \hat{c}_a. \tag{8.66}$$

Using the equation of motion for $\langle\langle \hat{c}_a, (\hat{X}_{-1}^k)^\dagger \rangle\rangle$ one can show that, at first order in V,

$$\langle \hat{C}_s^{ak} \rangle = T \sum_{n'} e^{i\omega_{n'} 0^+} W_{-s}^{ak} G_{kk}^{(0)}(i\omega_{n'}) \frac{1}{i\omega_{n'} - e_a}. \tag{8.67}$$

Hence, at second order in V,

$$L_{ij} = M_{ii} I_{ij} - \sum_{slapk} W_s^{ap} \eta_s^{pi}(l) \gamma_s^{lj}(k) \langle \hat{C}_s^{ak} \rangle \tag{8.68}$$
$$= M_{ii} I_{ij} - T \sum_{slapkn'} W_s^{ap} \eta_s^{pi}(l) \gamma_s^{lj}(k) e^{i\omega_{n'} 0^+} W_{-s}^{ak} G_{kk}^{(0)}(i\omega_{n'}) \frac{1}{i\omega_{n'} - e_a} \tag{8.69}$$
$$= M_{ii} I_{ij} - T \sum_{slpkn'uv} \eta_s^{pi}(l) \gamma_s^{lj}(k) e^{i\omega_{n'} 0^+} G_{kk}^{(0)}(i\omega_{n'}) F_s^{pk}(u,v) \Delta_{vu}(i\omega_{n'}) \tag{8.70}$$
$$= M_{ii} I_{ij} - \sum_{slpkuv} \eta_s^{pi}(l) \gamma_s^{lj}(k) F_s^{pk}(u,v) R_{vu}(k(2), k(1)). \tag{8.71}$$

The only approximation made here is the truncation at first order in the hybridization (from Eq. 8.67); without it, L is Hermitian from equation 8.61. Hence, if I is exact at first order in the hybridization, because equation 8.71 gives the zeroth and first order in the hybridization exactly, taking the Hermitian part of L still gives correct results at zeroth and first order in the hybridization. One can, this way, ensure that the L criterion for a causal Green's function 8.47 is fulfilled.

8.5.2 Calculation of Y(z)

To truncate $Y(z)$ at first order in the hybridization, one must take the zeroth order for $J = \langle \hat{\boldsymbol{B}}, \hat{\boldsymbol{B}}^\dagger \rangle_1$ and hence decouple the bath and the impurity degrees of freedom, i.e. $\langle \hat{c}_a^\dagger \hat{X}^i_{-1} \rangle = 0$ and $\langle \hat{X}^l_0 \hat{c}_a^\dagger \hat{c}_b \rangle = X_{l(1)} \langle \hat{c}_a^\dagger \hat{c}_a \rangle_0 \delta_{ab} \delta_{l(1)l(2)}$ where $\langle\ \rangle_0$ means the average in the atomic limit.

We therefore get

$$J^{(ai)(bj)}_{ss'} = \langle \hat{B}^{(ai)}_s, (\hat{B}^{(bj)}_{s'})^\dagger \rangle_1 \tag{8.72}$$

$$= \langle \hat{B}^{(ai)}_s, (\hat{B}^{(bj)}_{s'})^\dagger \rangle \tag{8.73}$$

$$= \delta_{ij} \delta_{ss'} \delta_{ab} \left(X_{j(1)} \langle \hat{c}_a^\dagger \hat{c}_a \rangle_0 + X_{j(2)} \langle \hat{c}_a \hat{c}_a^\dagger \rangle_0 \right) \tag{8.74}$$

and hence

$$Y_{ij}(z) = \sum_{sal} P^{i,(al)}_s J^{(al)}_s \left(z - N^{(al)}_s \right)^{-1} P^{j,(al)*}_s \tag{8.75}$$

$$= \sum_{slapk} W^{ap}_s \eta^{pi}_s(l) W^{ak}_{-s} \eta^{kj}_s(l) \frac{1}{z + s\Delta E_l - s e_a} \left(X_{l(1)} \langle \hat{c}_a^\dagger \hat{c}_a \rangle_0 + X_{l(2)} \langle \hat{c}_a \hat{c}_a^\dagger \rangle_0 \right) \tag{8.76}$$

$$= \sum_{slapk} W^{ap}_s \eta^{pi}_s(l) W^{ak}_{-s} \eta^{kj}_s(l) \frac{1}{z + s\Delta E_l - s e_a} \tag{8.77}$$

$$\int d\omega' \left(X_{l(1)} f(\omega') \delta(\omega' - e_a) + X_{l(2)} f(-\omega') \delta(\omega' - e_a) \right) \tag{8.78}$$

$$= \sum_{slpkuv} s \eta^{pi}_s(l) \eta^{kj}_s(l) F^{pk}_s(u,v) \left(X_{l(1)} \Delta^+_{vu}(sz + \Delta E_l) + X_{l(2)} \Delta^-_{vu}(sz + \Delta E_l) \right) \tag{8.79}$$

$$= \sum_{slpkuv} s \eta^{pi}_s(l) \eta^{kj}_s(l) F^{pk}_s(u,v) Q_{vu}(sz, l(2), l(1)). \tag{8.80}$$

The only approximation made here is also the truncation to first order in the hybridization (to obtain Eq. 8.74). In equation 8.75, because J is diagonal positive and N is diagonal, the calculated $Y(z)$ in 8.80 is causal (this can be checked with the theorem of Sec. 8.2) and hence fulfill its criterion for causal Green's function 8.47.

8.5.3 Calculation of I

We have

$$I_{ij} = \langle \{\hat{X}^i_{-1}, (\hat{X}^j_{-1})^\dagger\}\rangle \tag{8.81}$$

$$= \langle \hat{X}_0^{i(1)j(1)}\delta_{i(2),j(2)} + \hat{X}_0^{j(2)i(2)}\delta_{i(1),j(1)}\rangle \tag{8.82}$$

which gives terms of the form

$$\langle \hat{X}_0^{AB}\rangle = \frac{1}{Z}\,\mathrm{Tr}\Big\{e^{-\beta\hat{H}}\hat{X}_0^{AB}\Big\} \tag{8.83}$$

$$= \frac{1}{Z}\,\mathrm{Tr}\Big\{e^{-\beta\hat{H}_0}\hat{S}(\beta,0)\hat{X}_0^{AB}\Big\} \tag{8.84}$$

$$= \frac{\langle \hat{S}(\beta,0)\hat{X}_0^{AB}\rangle_0}{\langle \hat{S}(\beta,0)\rangle_0} \tag{8.85}$$

where

$$\hat{S}(\beta,0) = \mathcal{T}\exp\left\{-\int_0^\beta\int_0^\beta d\tau d\tau' \sum_{uv}\hat{f}_v^\dagger(\tau)\Delta_{vu}(\tau-\tau')\hat{f}_u(\tau')\right\} \tag{8.86}$$

with $\mathcal{T}$ the time-ordering operator (and within the interaction picture). To ensure causality of the Green's function 8.47, the matrix I should be Hermitian positive definite. To ensure the Green's function 8.47 to be exact at first order in the hybridization, the matrix I should also be exact at first order in the hybridization. Finding a way to meet both these conditions is still work in progress; for the moment, we have only implemented the following approximation, exact at first order in Δ but which can break positive definiteness of I:

$$\hat{S}(\beta,0) = 1 - \mathcal{T}\int_0^\beta\int_0^\beta d\tau d\tau' \sum_{uv}\hat{f}_v^\dagger(\tau)\Delta_{vu}(\tau-\tau')\hat{f}_u(\tau'). \tag{8.87}$$

The denominator in equation 8.85 then becomes, because the X atomic Green's function is diagonal,

$$\langle \hat{S}(\beta,0)\rangle_0 = 1 - \sum_{uvi}F^{ii}_{-1}(u,v)\int_0^\beta\int_0^\beta d\tau d\tau'\Delta_{vu}(\tau-\tau')\langle\langle \hat{X}^i_{-1};(\hat{X}^i_{-1})^\dagger\rangle\rangle_0^{\tau'-\tau} \tag{8.88}$$

$$= 1 - T\sum_{uvim}F^{ii}_{-1}(u,v)\int_0^\beta\int_0^\beta d\tau d\tau'\Delta_{vu}(i\omega_m)e^{-i\omega_m(\tau-\tau')} \tag{8.89}$$

$$\frac{1}{Z_0}\Big(\theta(\tau-\tau')e^{-\beta E_{i(2)}}e^{(\tau-\tau')(E_{i(2)}-E_{i(1)})} - \theta(\tau'-\tau)e^{-\beta E_{i(1)}}e^{(\tau'-\tau)(E_{i(1)}-E_{i(2)})}\Big) \tag{8.90}$$

$$= 1 - \sum_{uvi}F^{ii}_{-1}(u,v)\Big(X_{i(1)} + X_{i(2)}\Big)\sum_m\frac{\Delta_{vu}(i\omega_m)}{i\omega_m - \Delta E_i} \tag{8.91}$$

$$= 1 - \sum_{uvi}\beta F^{ii}_{-1}(u,v)R_{vu}(i(2),i(1)). \tag{8.92}$$

Similarly, the numerator in equation 8.85 becomes

$$\langle \hat{S}(\beta,0)\hat{X}_0^{AB}\rangle_0 = X_A\delta_{A,B} - \sum_{uvij} F_{-1}^{ij}(u,v)\int_0^\beta\int_0^\beta d\tau d\tau' \Delta_{vu}(\tau-\tau')\langle \mathcal{T}(\hat{X}_{-1}^j)^\dagger(\tau)\hat{X}_{-1}^i(\tau')\hat{X}_0^{AB}\rangle_0 \tag{8.93}$$

$$= X_A\delta_{A,B} - T\sum_{uvijm} F_{-1}^{ij}(u,v)\int_0^\beta\int_0^\beta d\tau d\tau' \Delta_{vu}(i\omega_m)e^{-i\omega_m(\tau-\tau')} \tag{8.94}$$

$$\frac{1}{Z_0}e^{-\beta E_B}\Bigg(\theta(\tau-\tau')e^{\tau E_B}e^{-\tau' E_A}e^{(\tau'-\tau)E_{i(1)}}\delta_{i(2),A}\delta_{j(2),B}\delta_{i(1),j(1)} \tag{8.95}$$

$$-\theta(\tau'-\tau)e^{\tau' E_B}e^{-\tau E_A}e^{(\tau-\tau')E_{i(2)}}\delta_{j(1),A}\delta_{i(1),B}\delta_{i(2),j(2)}\Bigg) \tag{8.96}$$

$$= X_A\delta_{A,B} - \frac{1}{E_B-E_A}\sum_{uvij} F_{-1}^{ij}(u,v)\Bigg(\tag{8.97}$$

$$\Big(R_{vu}(A,i(1)) - R_{vu}(B,i(1))\Big)\delta_{i(2),A}\delta_{j(2),B}\delta_{i(1),j(1)} \tag{8.98}$$

$$+\Big(R_{vu}(i(2),A) - R_{vu}(i(2),B)\Big)\delta_{j(1),A}\delta_{i(1),B}\delta_{i(2),j(2)}\Bigg). \tag{8.99}$$

Combining equations 8.82, 8.85, 8.92 and 8.99, the matrix I can be written as:

$$I = \frac{I_0 + I_1}{1 + D_1} \tag{8.100}$$

where I_0 is the atomic part of I, I_1 is the first order correction arising from the numerator 8.99 and $D_1 = -\sum_{uvi}\beta F_{-1}^{ii}(u,v)R_{vu}(i(2),i(1))$ is the first order correction arising from the denominator 8.92. The only approximation made here is again the truncation at first order in the hybridization (in Eq. 8.87).

In summary, the EOM-based, strong-coupling, AIM solver presented here works as follows:

1. Provide, as inputs, the hybridization function Δ and the local Hamiltonian $\hat{H}_f$.
2. Diagonalize $\hat{H}_f$ to extract the atomic eigenstates $\{|A\rangle\}$, eigenenergies $\{E_A\}$ and matrix elements $\{\langle A|\,\hat{f}_u\,|B\rangle\}$.
3. Compute the quantities L, $Y(z)$ and I at first order in Δ through equations 8.71, 8.80 and 8.100 respectively.
4. Compute the X operators Green's function $G(z)$ at first order in Δ through

$$G(z) = I\Bigg(zI - L - Y(z)\Bigg)^{-1}I.$$

5. Compute the impurity Green's function G_{imp} at first order in Δ through equation 8.32.

It relies on a single approximation: the truncation to first order in the hybridization (i.e. Eqs. 8.67, 8.74 and 8.87). While this truncation is standard in EOM approaches, it usually lead to non-CF forms (see Sec. 8.3). The formalism of [Tserkovnikov, 1981] allowed here to maintain a CF expression for the Green's function. The causality condition of such a form can be expressed through simple criteria on L, $Y(z)$ and I (see Sec. 8.2). While the expressions for L and $Y(z)$ exhibit the correct properties (Hermicity and causality respectively), the present approach for the calculation of I might break its positive definiteness and hence violate causality of the impurity Green's function.

8.6 Benchmark in the single-orbital case

We first benchmark the EOM to first order in Δ approach in the one-orbital AIM with the spin-polarized Lorentzian hybridization as previously employed by [Tong, 2015] to test their EOM formalism:

$$-\frac{1}{\pi}\Delta''_\sigma(w) = \frac{\Gamma\omega_c^2}{(\omega+\sigma\Delta\omega)^2+\omega_c^2} \tag{8.101}$$

where $\omega_c = 1$ was set as the energy unit, $\Gamma = 0.1$ is the hybridization strength, $\Delta\omega = 0.2$ is the polarization of the bath. Figure 8.1 compares the spin-up impurity spectral function $A_\uparrow(\omega)$ at half-filling $\mu = U/2$ and at $T = 0.1$ for various values of U, as given by the HI approximation, the present EOM approach and the NRG results extracted in [Tong, 2015]. It shows that, while at large values of U both NRG and the EOM approach tend to the HI results as expected, the EOM approach improves the HI spectrum on several aspects.

First, in agreement with NRG, it exhibits a central peak which decreases in amplitude with increasing U while the HI approximation displays no spectral weight at the Fermi level for any finite U. Second, it captures the shift of the Hubbard bands due to hybridization: for $U = 2$ for instance, the upper Hubbard band move from 1 within HI, to 1.3 within the EOM approach and NRG. Third, it captures the antiferromagnetic response of the impurity to the spin-polarized bath as shown by the larger spectral weight above $\omega = 0$ for the spin up with a positive $\Delta\omega$ – while the HI spectrum is symmetric with respect to $\omega = 0$. Finally, the EOM approach qualitatively reproduces finite-lifetime effects as its spectrum is broadened and does not exhibit Dirac-like peaks as in the HI approximation. One may note, however, that the EOM approach fails to capture the quasiparticle peak at the intermediate U value of 2. This is likely linked to the EOM method underestimating the value of critical U_c for the Mott transition, as we will now discuss.

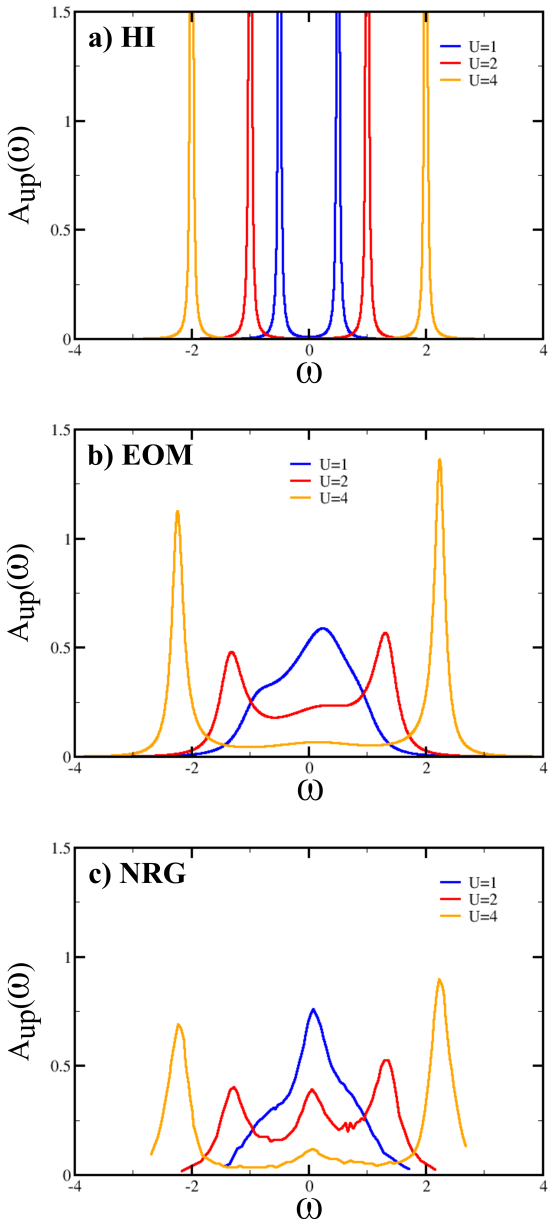

Figure 8.1: Spin-up Anderson impurity spectral function $A_\uparrow(\omega)$ for a Lorentzian hybridization 8.101 with $\omega_c = 1$, $\Gamma = 0.1$, $\Delta\omega = 0.2$, at half-filling $\mu = U/2$ and at $T = 0.1$, for different values of U. a) Hubbard-I approximation. b) The first-order in hybridization EOM approach presented in this work. c) NRG results from [Tong, 2015].

We also benchmark the approach as a DMFT impurity solver for the single-orbital Hubbard model (see Sec. 2.1) on the Bethe lattice in infinite dimensions and paramagnetic phase. In this case (see for instance [Georges et al., 1996]), the DMFT cycle described in section 2.2 is particularly simple as $\Delta = t^2 G_{\text{imp}}$ where t is the nearest-neighbor hopping; the non-interacting

Density Of States (DOS) is semi-elliptic, given by

$$A(\omega) = \frac{2}{\pi D^2}\sqrt{D^2 - \omega^2}\theta(D - |\omega|) \tag{8.102}$$

where $D = 2t$ is the half bandwidth. Figure 8.2 displays the DMFT local spectral function obtained with our EOM solver at low temperature $T = 0.001$, for $\mu = U/2$ (half-filling) and various values of U, the energy unit being $D = 1$. The approach qualitatively captures the Mott Insulator Transition (MIT) missed by HI (which would give the spectrum shown in Fig. 8.1a), the calculated critical value of U being $U_c \approx 1.7$. This value is an underestimation, as expected from the truncation at first order in the hybridization: [Bulla, 2006] indeed reported a NRG-estimated value of $U_c \approx 2.94$ at $T = 0$. We can notice an excellent agreement with the exact NRG result from [Bulla, 2006] at $U = 4$. This benchmark hence shows that our EOM approach can be used as a DMFT impurity solver and gives improved description compared to HI.

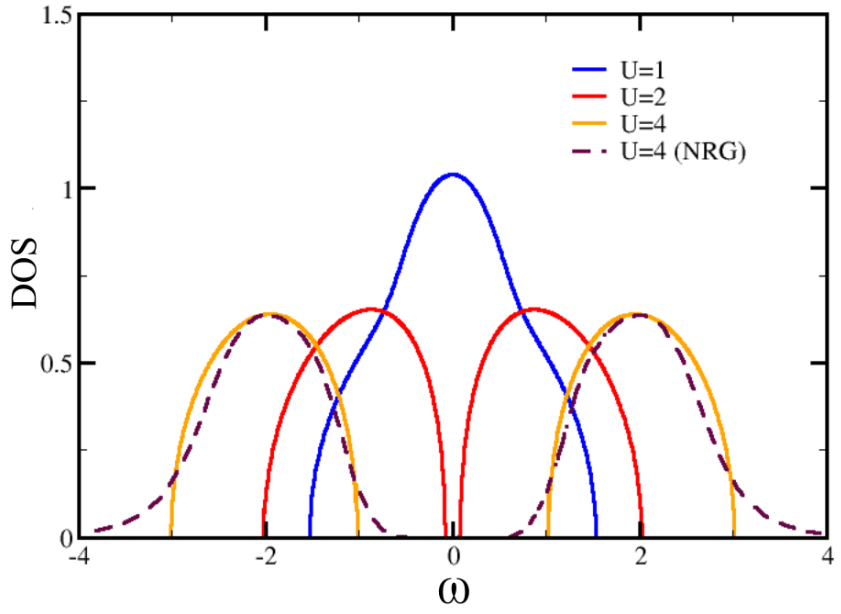

Figure 8.2: DMFT local spectral function for the single-orbital Hubbard model on the Bethe lattice with the EOM approach as the AIM solver. Calculations were performed at low temperature $T = 0.001$, for $\mu = U/2$ (half-filling) and various values of U. NRG results are at $T = 0$ and from [Bulla, 2006].

8.7 Conclusion

In this chapter, we have derived a strong-coupling EOM approach for the AIM which is correct to first order in the hybridization. Contrary to [Tong, 2015, Ma and Tong, 2019], this approach does not need the complicated CF resummation as it directly gives a CF form for the impurity Green's function. It also does not require the computationally heavy self-consistent calculation of X operators averages by calculating these to first order with standard perturbation theory techniques. Furthermore, the formalism works on both the real and imaginary frequency axes and therefore does not require analytic continuation. In the one-orbital AIM with spin-polarized Lorentzian hybridization, the present EOM approach was shown to significantly improve the HI spectrum. Similar improvements over HI were also obtained when the EOM approach was used as a DMFT impurity solver for the single-orbital Hubbard model on the Bethe lattice.

Moreover, the approach can be viewed as the CF version of the form of [Dai et al., 2005]. Indeed, with the additional following approximations which are correct at first order in the hybridization but break the CF form of the GF and can violate causality (in the metallic phase for instance):

$$G(z) \approx \Big(z - M\Big)^{-1} I + \Big(z - M\Big)^{-1} \Big(L_1 + Y(z)\Big) \Big(z - M\Big)^{-1} \tag{8.103}$$

$$I \approx I_0(1 - D_1) + I_1 \tag{8.104}$$

(with notations from Eqs. 8.63 and 8.100), one can show that the EOM approach is equivalent to the one of [Dai et al., 2005]. Their method gives, in the paramagnetic phase of the single-orbital AIM at half-filling, the following self-energy:

$$\Sigma(z) = \frac{U}{2} + \left(\frac{U}{2}\right)^2 \frac{1}{z} \left(1 + \frac{3\Delta(z)}{z}\right). \tag{8.105}$$

In order to avoid causality violation in the metallic state, [Dai et al., 2005] performed a CF resummation of this self-energy, yielding

$$\Sigma(z) = \frac{U}{2} + \left(\frac{U}{2}\right)^2 \frac{1}{z - 3\Delta(z)}. \tag{8.106}$$

One can show that the self-energy computed by our approach reduces to equation 8.106 in this case: on the Bethe lattice, our estimated $U_c \approx 1.7$ at low temperature is indeed consistent with the expected $U_c = \sqrt{3}$ and our results (see Fig. 8.2) are consistent with those of [Dai et al., 2005] with the self-energy 8.106 (Fig. 5 therein). Hence, our approach is the CF equivalent of the method of [Dai et al., 2005].

However, the present approach does also face several difficulties. It first misses the Kondo effect which the method of [Fan et al., 2018, Fan and Tong, 2019], based on the decoupling

of [Lacroix, 1981], was able to qualitatively capture for instance. Furthermore, the impurity Green's function of the present approach is causal if I is Hermitian positive definite and L is Hermitian. While the latter can be enforced to first order in Δ by taking the Hermitian part, the former cannot and equation 8.87 cannot ensure the positive definiteness of I and therefore the causality of the impurity Green's function. Finding a positive definite form for I correct to first order in the hybridization might be the subject of future work. The present approach does not however violate causality as long as the hybridization is low enough for I_1 to be small compared to I_0. Moreover, like all first-order in the hybridization approaches, the present solver is expected to give accurate results only in the case where $\Delta \ll U$; additionally, it might struggle in the regime $\Delta \gtrsim T$ (which can be seen in Eq. 8.87). Finally, the present approach scales poorly with the number of impurity orbitals n as equation 8.47 requires the inversion of a matrix of dimension $\sum_{k=1}^{n} \binom{n}{k}\binom{n}{k-1}$. Some ways to deal with this issue could be to consider only relevant transitions (additions and removals of one electron from the GS multiplet), neglect small matrix elements f_u^i and/or assume diagonal hybridization. This could also be subject of future work.

Part V

Conclusion

Chapter 9

Summary and outlook

This thesis focused on *ab initio* calculations of various properties of real materials, as opposed to model Hamiltonians. The compounds which we studied were based on rare earths ($\mathcal{R}$) which usually feature a partially filled $4f$ shell and hence strong electronic correlations.

The study of such realistic correlated materials requires computationally efficient *ab initio* approaches. Significant progress has been made in the design of numerically exact methods for quantum many-body problems [Bulla et al., 2008, Gull et al., 2011, Schollwöck, 2011]. However, one challenge of the $4f$ shell is that its associated Hilbert space is very large (2^{14}); these sophisticated methods hence still remain hardly applicable to the rare-earth compounds. On the other hand, one can take advantage of the very localized nature of the $4f$ shell for which strong coupling approaches are expected to perform well. One of them is the numerically efficient quasi-atomic Hubbard-I (HI) approximation, described in the first part of this thesis. We have hence focused on the design of such approaches (SIC-LDA+HI, mBJ@DFT+HI, first-order in hybridization impurity solver,...) and applied them to two scientifically and technologically relevant classes of f-electron compounds: magnetic intermetallics and correlated semiconductors.

The second part of this thesis dealt with the magnetic properties of rare-earth transition metal intermetallics. In the fourth chapter, we explained the mechanism giving rise to magnetic anisotropy in these compounds, namely the interplay between $3d-4f$ exchange coupling, crystal field effects and strong $4f$ spin-orbit coupling. We proposed an almost parameter-free approach to account for this mechanism in real materials, which is based on a (previously developed) self-interaction corrected (SIC) LDA+HI approach. This SIC-LDA+HI method can compute rare-earth crystal field parameters and exchange coupling as well as $3d$ zero-temperature magnetization. It is extended in this thesis to construct a full two-sublattice model describing the magnetic behavior of the system as a function of temperature and applied field, with all relevant quantities (excluding temperature evolution of $3d$ sublattice magnetization and anisotropy) obtained from theoretical calculations for both rare-earth and transition metal sublattices.

In the fifth and sixth chapters, we applied this methodology to two important families of hard-magnetic intermetallics: the "1-5" family $\mathcal{R}Co_5$ and "2-14-1" $\mathcal{R}_2Fe_{14}B$ compounds. We showed that our methodology yielded anisotropy constants and Spin Reorientation Transitions

(SRTs) generally in good agreement with experiment, in $\mathcal{R}Co_5$ and pure/substituted $Nd_2Fe_{14}B$-based compounds. We also demonstrated that hybridization effects taken into account by the choice of a small Wannier window led to a large "66" crystal field parameter in $\mathcal{R}Co_5$ compounds. In $NdCo_5$, this large value was shown to be responsible for the measured reduced zero-temperature Nd moment which remained unexplained for 40 years. Finally, we studied partial substitution of Nd by industrially motivated Ce and Dy in $Nd_2Fe_{14}B$. We showed that the rare-earth crystal field and exchange parameters (i) depend on the crystallographic site, the g site providing a higher contribution to the magnetic anisotropy but (ii) are independent on the precise rare-earth occupying the other crystallographic site. This led to the theoretical prediction that optimizing Ce (Dy) f (g) site occupancy should enhance the magnetic anisotropy of corresponding substituted compounds.

In the third part, we tried to improve the estimation of optical gaps computed by DFT+DMFT in rare-earth semiconductors. This gap is indeed determined by the position of the $4f$ Hubbard bands with respect to the non-correlated $p-d$ gap and by the amplitude of the latter which DFT systematically underestimates. We hence proposed to employ, as a perturbative treatment to DFT+HI, the computationally cheap modified Becke-Johnson (mBJ) exchange potential which was shown to give better non-correlated gap estimations. With this methodology, our calculated optical gap values in light rare-earth fluorosulfides $\mathcal{R}SF$ are in excellent agreement with experiment. In the rare-earth sesquioxides $\mathcal{R}_2O_3$, we qualitatively reproduced the non-monotonous evolution of the optical along the $\mathcal{R}$ series and explained the characteristic onset of the measured optical conductivity. Furthermore, the use of the numerically exact CTQMC approach yielded a significant shift of the $4f$ lower Hubbard band compared to HI. This shift was interpreted as a hybridization effect by a study on a simple analytical model.

The HI approach has however significant limitations even in applications to localized systems. For example, in rare-earth transition metal intermetallics, treating crystal field effectively by the use of extended Wannier functions is not free from arbitrariness; in rare-earth-based semiconductors, HI cannot treat hybridization effects which may modify significantly the optical gap. Therefore, in the fourth part, we developed a new beyond HI impurity solver for the strong coupling regime, relevant to rare earths. This approach is based on an equation of motion formalism, is exact at first order in the hybridization and yields an impurity Green's function in a continued fraction form which has simple criteria ensuring its causal character. We benchmarked the method in the single-orbital case: on the Anderson impurity model with Lorentzian hybridization and as a DMFT solver for the Hubbard model on the Bethe lattice.

In future work, we could try to overcome several limitations of the present thesis. Our theoretical treatment of rare-earth transition metal intermetallics indeed still features some parameters, one of them being the choice of the Wannier window. While we have demonstrated that a small window was necessary in order to take into account hybridization effects, the precise choice is still somewhat arbitrary. A more controlled way of constructing the Wannier orbitals

might be to choose bands with the highest $4f$ character in a large window, as we have proposed in this thesis. Further exploring this route might the topic of future research. Furthermore, this SIC-LDA+HI-based scheme cannot properly treat compounds containing Ce ions which are usually in an intermediate valence state. A previously introduced CTQMC-based method that we have applied to $CeCo_5$ can approximately circumvent this issue. The development of the EOM-based beyond HI impurity solver could improve this Ce description.

This beyond-HI solver could also help confirming our interpretation of the CTQMC-induced shift in $\mathcal{R}_2O_3$ as a hybridization effect. However, in its current state, the solver is numerically too expensive to be applied to the relevant 14 orbitals of a $4f$ shell; improving its scalability might hence be the subject of future work.

Appendix A

Conventions

- $m_e = e = \hbar = 4\pi\epsilon_0 = k_B = \mu_0 = 1$
- Vectors are marked by bold symbols, their norm are in normal font (e.g. V is the norm of $\boldsymbol{V}$)
- Operators are marked by the hat notation, their corresponding matrix representation use the same symbol without the hat (e.g. $O_{mm'}$ is the matrix representation of $\hat{O}$ in a particular basis)
- $\boldsymbol{x} = (\boldsymbol{r}, \sigma)$ and $\int d^4\boldsymbol{x} = \sum_\sigma \int d^3\boldsymbol{r}$ and $\bar{\sigma}{=}{-}\sigma$
- From chapter 4, notations like "LDA+DMFT" assume, unless stated otherwise: spin-polarization, spin-orbit coupling included, self-consistency over the charge density, DMFT correction only for partially filled $4f$ shells
- Fourier transforms in real time:

$$g(\omega) = \int_{-\infty}^{+\infty} g(t) e^{i\omega t} dt \tag{A.1}$$

$$g(t) = \frac{1}{2\pi} \int_{-\infty}^{+\infty} g(\omega) e^{-i\omega t} d\omega \tag{A.2}$$

- Fourier transforms in imaginary time:

$$g(i\omega_n) = \int_0^\beta g(\tau) e^{i\omega_n \tau} d\tau \tag{A.3}$$

$$g(\tau) = \frac{1}{\beta} \sum_{n=-\infty}^{+\infty} g(i\omega_n) e^{-i\omega_n \tau} \tag{A.4}$$

- Zubarev notation for Green's functions: for two operators $\hat{O}$ and $\hat{Q}$ we define the retarded Green's function in real time

$$\langle\langle \hat{O}, \hat{Q}^\dagger \rangle\rangle_{t-t'} = -i\theta(t-t') \langle \{ \hat{O}(t), \hat{Q}^\dagger(t') \} \rangle \tag{A.5}$$

and in imaginary time

$$\langle\langle \hat{O}, \hat{Q}^\dagger \rangle\rangle_{\tau-\tau'} = -\langle \mathcal{T} \hat{O}(\tau) \hat{Q}^\dagger(\tau') \} \rangle. \tag{A.6}$$

where $\mathcal{T}$ is the time-ordered product.

Correspondingly, in the complex frequency plane, we write $\langle\langle \hat{O}, \hat{Q}^\dagger \rangle\rangle_z$, the frequency z subscript being often dropped for clarity.

Appendix B

Glossary

- AIM: Anderson Impurity Model
- AMF: Around Mean-Field
- BIS: Bremsstrahlung Isochromate Spectroscopy
- (m)BJ: (modified) Becke-Johnson
- BR: Becke-Roussel
- CF: Crystal Field (Continued Fraction in chapter 8)
- CFP: Crystal Field Parameter
- DC: Double Counting
- DFT: Density Functional Theory
- DMFT: Dynamical Mean Field Theory
- DMRG: Density Matrix Renormalization Group
- DOS: Density Of States
- ED: Exact diagonalization
- EOM: Equation Of Motion
- FLAPW: Full-potential Linearized Augmented Plane Wave
- FLL: Fully Localized Limit
- FOMP: First-Order Magnetization Process
- GBF: Generalized Brillouin Function
- GF: Green's function

- GGA: Generalized Gradient Approximation
- GS(M): Ground State (Multiplet)
- HI: Hubbard-I
- HK: Hohenberg-Kohn
- HM: Hubbard Model
- KS: Kohn-Sham
- LDA: Local Density Approximation
- LHB: Lower Hubbard Band
- LMTO: Linearized Muffin-Tin Orbital
- LP: Lattice Parameter
- $\mathcal{M}$: transition Metal
- MaxEnt: Maximum Entropy
- MIT: Mott Insulator Transition
- NRG: Numerical Renormalization Group
- NMTO: N^{th} order Muffin-Tin Orbital
- PES: Photoemission Spectroscopy
- PNS: Polarized-Neutron Scattering
- (CT)QMC: (Continuous-Time) Quantum Monte-Carlo
- $\mathcal{R}$: Rare-earth
- RKKY: Ruderman–Kittel–Kasuya–Yosida
- UEG: Uniform Electron Gas
- SIC: Self-Interaction Corrected
- SO: Spin-Orbit
- SRT: Spin Reorientation Transition
- ST: Sucksmith-Thompson
- UHB: Upper Hubbard Band
- X: Hubbard operator

- XAS: X-ray Absorption Spectroscopy
- XPS: X-ray Photoemission Spectroscopy

Bibliography

[Adachi and Imanaka, 1998] Adachi, G.-Y. and Imanaka, N. (1998). *Chem. Rev.*, 98:14791514.

[Aichhorn et al., 2011] Aichhorn, M., Pourovskii, L., and Georges, A. (2011). Importance of electronic correlations for structural and magnetic properties of the iron pnictide superconductor lafeaso. *Phys. Rev. B*, 84:054529.

[Aichhorn et al., 2016] Aichhorn, M., Pourovskii, L., Seth, P., Vildosola, V., Zingl, M., Peil, O. E., Deng, X., Mravlje, J., Kraberger, G. J., Martins, C., Ferrero, M., and Parcollet, O. (2016). Triqs/dfttools: A triqs application for ab initio calculations of correlated materials. *Computer Physics Communications*, 204:200 – 208.

[Aichhorn et al., 2009] Aichhorn, M., Pourovskii, L., Vildosola, V., Ferrero, M., Parcollet, O., Miyake, T., Georges, A., and Biermann, S. (2009). Dynamical mean-field theory within an augmented plane-wave framework: Assessing electronic correlations in the iron pnictide LaFeAsO. *Phys. Rev. B*, 80:085101.

[Alameda et al., 1981] Alameda, J. M., Givord, D., Lemaire, R., and Lu, Q. (1981). Co energy and magnetization anisotropies in RCo5 intermetallics between 4.2 k and 300 k. *Journal of Applied Physics*, 52(3):2079–2081.

[Alameda, J. M. et al., 1982] Alameda, J. M., Givord, D., Lemaire, R., Lu, Q., Palmer, S. B., and Tasset, F. (1982). Reduced 4f-moment of the Nd ground state in NdCo5. *J. Phys. Colloques*, 43:C7–133–C7–139.

[Allen, 1985] Allen, J. (1985). Valence fluctuations in narrow band oxides. *Journal of Magnetism and Magnetic Materials*, 47-48:168 – 174.

[Amadon, 2012] Amadon, B. (2012). A self-consistent DFT + DMFT scheme in the projector augmented wave method: applications to cerium, Ce2O3and Pu2O3 with the hubbard I solver and comparison to DFT +U. *Journal of Physics: Condensed Matter*, 24(7):075604.

[Amadon et al., 2008] Amadon, B., Lechermann, F., Georges, A., Jollet, F., Wehling, T. O., and Lichtenstein, A. I. (2008). Plane-wave based electronic structure calculations for correlated materials using dynamical mean-field theory and projected local orbitals. *Phys. Rev. B*, 77:205112.

[Andersen, 1975] Andersen, O. K. (1975). Linear methods in band theory. *Phys. Rev. B*, 12:3060–3083.

[Andersen and Saha-Dasgupta, 2000] Andersen, O. K. and Saha-Dasgupta, T. (2000). Muffin-tin orbitals of arbitrary order. *Phys. Rev. B*, 62:R16219–R16222.

[Anderson, 1961] Anderson, P. W. (1961). Localized magnetic states in metals. *Phys. Rev.*, 124:41–53.

[Andreev et al., 1986] Andreev, A. V., Deryagin, A. V., Kudrevatykh, N., Mushnikov, N. V., V., Re'imer, A., S, V., and Terent'ev (1986). Magnetic properties of Y2Fe14B and Nd2Fe14B and their hydrides. *Sov. Phys. JETP*, 63.

[Anisimov et al., 1997a] Anisimov, V. I., Aryasetiawan, F., and Lichtenstein, A. I. (1997a). First-principles calculations of the electronic structure and spectra of strongly correlated systems: the LDA+U method. *Journal of Physics: Condensed Matter*, 9(4):767–808.

[Anisimov et al., 2005] Anisimov, V. I., Kondakov, D. E., Kozhevnikov, A. V., Nekrasov, I. A., Pchelkina, Z. V., Allen, J. W., Mo, S.-K., Kim, H.-D., Metcalf, P., Suga, S., Sekiyama, A., Keller, G., Leonov, I., Ren, X., and Vollhardt, D. (2005). Full orbital calculation scheme for materials with strongly correlated electrons. *Phys. Rev. B*, 71:125119.

[Anisimov et al., 1997b] Anisimov, V. I., Poteryaev, A. I., Korotin, M. A., Anokhin, A. O., and Kotliar, G. (1997b). First-principles calculations of the electronic structure and spectra of strongly correlated systems: dynamical mean-field theory. *Journal of Physics: Condensed Matter*, 9(35):7359–7367.

[Anisimov et al., 1993] Anisimov, V. I., Solovyev, I. V., Korotin, M. A., Czyżyk, M. T., and Sawatzky, G. A. (1993). Density-functional theory and NiO photoemission spectra. *Phys. Rev. B*, 48:16929–16934.

[Anisimov et al., 1991] Anisimov, V. I., Zaanen, J., and Andersen, O. K. (1991). Band theory and mott insulators: Hubbard u instead of stoner i. *Phys. Rev. B*, 44:943–954.

[Aryasetiawan et al., 2004] Aryasetiawan, F., Imada, M., Georges, A., Kotliar, G., Biermann, S., and Lichtenstein, A. I. (2004). Frequency-dependent local interactions and low-energy effective models from electronic structure calculations. *Phys. Rev. B*, 70:195104.

[Aryasetiawan et al., 2006] Aryasetiawan, F., Karlsson, K., Jepsen, O., and Schönberger, U. (2006). Calculations of hubbard U from first-principles. *Phys. Rev. B*, 74:125106.

[Ballhausen, 1962] Ballhausen, C. J. (1962). *An introduction to ligand field theory.* McGraw Hill, New York.

[Bartolomé et al., 2000] Bartolomé, F., Tonnerre, J. M., Jaouen, N., Raoux, D., Chaboy, J., García, L. M., Maruyama, H., and Steinmann, R. (2000). Strong noncollinearity between

nonequivalent Nd magnetic moments in Nd2Fe14B at low temperature. *Journal of Applied Physics*, 87(9):4762–4764.

[Bauernfeind et al., 2017] Bauernfeind, D., Zingl, M., Triebl, R., Aichhorn, M., and Evertz, H. G. (2017). Fork tensor-product states: Efficient multiorbital real-time DMFT solver. *Phys. Rev. X*, 7:031013.

[Becke, 1993a] Becke, A. D. (1993a). Density-functional thermochemistry. III. the role of exact exchange. *The Journal of Chemical Physics*, 98(7):5648–5652.

[Becke, 1993b] Becke, A. D. (1993b). A new mixing of Hartree–Fock and local density-functional theories. *The Journal of Chemical Physics*, 98(2):1372–1377.

[Becke and Johnson, 2006] Becke, A. D. and Johnson, E. R. (2006). A simple effective potential for exchange. *The Journal of Chemical Physics*, 124(22):221101.

[Becke and Roussel, 1989] Becke, A. D. and Roussel, M. R. (1989). Exchange holes in inhomogeneous systems: A coordinate-space model. *Phys. Rev. A*, 39:3761–3767.

[Belorizky et al., 1987] Belorizky, E., Fremy, M. A., Gavigan, J. P., Givord, D., and Li, H. S. (1987). Evidence in rare-earth (R)–transition metal (M) intermetallics for a systematic dependence of R-M exchange interactions on the nature of the R atom. *Journal of Applied Physics*, 61(8):3971–3973.

[Belozerov and Anisimov, 2014] Belozerov, A. S. and Anisimov, V. I. (2014). Coulomb interaction parameters in bcc iron: an LDA+DMFT study. *Journal of Physics: Condensed Matter*, 26(37):375601.

[Bethe, 1929] Bethe, H. (1929). Termaufspaltung in kristallen. *Annalen der Physik*, 395(2):133–208.

[Bhandary et al., 2016] Bhandary, S., Assmann, E., Aichhorn, M., and Held, K. (2016). Charge self-consistency in density functional theory combined with dynamical mean field theory: k-space reoccupation and orbital order. *Phys. Rev. B*, 94:155131.

[Biermann, 2014] Biermann, S. (2014). *Dynamical Mean Field Theory-Based Electronic Structure Calculations for Correlated Materials*, pages 303–345. Springer Berlin Heidelberg, Berlin, Heidelberg.

[Biermann et al., 2003] Biermann, S., Aryasetiawan, F., and Georges, A. (2003). First-principles approach to the electronic structure of strongly correlated systems: Combining the GW approximation and dynamical mean-field theory. *Phys. Rev. Lett.*, 90:086402.

[Biermann et al., 2005] Biermann, S., Poteryaev, A., Lichtenstein, A. I., and Georges, A. (2005). Dynamical singlets and correlation-assisted Peierls transition in VO_2. *Phys. Rev. Lett.*, 94:026404.

[Blaha et al., 2018] Blaha, P., Schwarz, K., Madsen, G. K. H., Kvasnicka, D., Luitz, J., Laskowski, R., Tran, F., and Marks, L. D. (2018). *WIEN2k, An Augmented Plane Wave + Local Orbitals Program for Calculating Crystal Properties*. Karlheinz Schwarz, Techn. Universität Wien, Austria, ISBN 3-9501031-1-2.

[Blaha et al., 2020] Blaha, P., Schwarz, K., Tran, F., Laskowski, R., Madsen, G. K. H., and Marks, L. D. (2020). WIEN2k: An APW+lo program for calculating the properties of solids. *The Journal of Chemical Physics*, 152(7):074101.

[Bolzoni et al., 1987] Bolzoni, F., Gavigan, J., Givord, D., Li, H., Moze, O., and Pareti, L. (1987). 3d magnetism in R2Fe14B compounds. *Journal of Magnetism and Magnetic Materials*, 66(1):158–162.

[Boucherle, J. X. et al., 1982] Boucherle, J. X., Givord, D., and Schweizer, J. (1982). Measurements of magnetization densities in rare-earth compounds. *J. Phys. Colloques*, 43:C7–199–C7–214.

[Boust et al., 2022a] Boust, J., Aubert, A., Fayyazi, B., Skokov, K. P., Skourski, Y., Gutfleisch, O., and Pourovskii, L. V. (2022a). Ce and Dy substitutions in $Nd_2Fe_{14}B$: Site-specific magnetic anisotropy from first principles. *Phys. Rev. Materials*, 6:084410.

[Boust et al., 2022b] Boust, J., Galler, A., Biermann, S., and Pourovskii, L. V. (2022b). Combining semilocal exchange with dynamical mean-field theory: Electronic structure and optical response of rare-earth sesquioxides. *Phys. Rev. B*, 105:085133.

[Brooks et al., 1997] Brooks, M. S. S., Eriksson, O., Wills, J. M., and Johansson, B. (1997). Density functional theory of crystal field quasiparticle excitations and the ab initio calculation of spin hamiltonian parameters. *Phys. Rev. Lett.*, 79:2546–2549.

[Bulla, 2006] Bulla, R. (2006). Dynamical mean-field theory: from quantum impurity physics to lattice problems. *Philosophical Magazine*, 86(13-14):1877–1889.

[Bulla et al., 2008] Bulla, R., Costi, T. A., and Pruschke, T. (2008). Numerical renormalization group method for quantum impurity systems. *Rev. Mod. Phys.*, 80:395–450.

[Cadogan et al., 1988] Cadogan, J. M., Gavigan, J. P., Givord, D., and Li, H. S. (1988). A new approach to the analysis of magnetisation measurements in rare-earth/transition-metal compounds: application to Nd2Fe14B. *Journal of Physics F: Metal Physics*, 18(4):779–787.

[Caffarel and Krauth, 1994] Caffarel, M. and Krauth, W. (1994). Exact diagonalization approach to correlated fermions in infinite dimensions: Mott transition and superconductivity. *Phys. Rev. Lett.*, 72:1545–1548.

[Carnall et al., 1989] Carnall, W. T., Goodman, G. L., Rajnak, K., and Rana, R. S. (1989). A systematic analysis of the spectra of the lanthanides doped into single crystal LaF3. *The Journal of Chemical Physics*, 90(7):3443–3457.

[Casula et al., 2012] Casula, M., Rubtsov, A., and Biermann, S. (2012). Dynamical screening effects in correlated materials: Plasmon satellites and spectral weight transfers from a Green's function ansatz to extended dynamical mean field theory. *Phys. Rev. B*, 85:035115.

[Ceperley and Alder, 1980] Ceperley, D. M. and Alder, B. J. (1980). Ground state of the electron gas by a stochastic method. *Phys. Rev. Lett.*, 45:566–569.

[Chiu et al., 2012] Chiu, F.-C., Mondal, S., and Pan, T.-M. (2012). *Structural and Electrical Characteristics of Alternative High-k Dielectrics for CMOS Applications*, chapter 5, pages 111–184. John Wiley & Sons, Ltd.

[Chouhan et al., 2018] Chouhan, R. K., Pathak, A. K., Paudyal, D., and Pecharsky, V. (2018). High performance magnetic material with Ce and La: an alternative to Nd-Fe-B magnet. *arXiv:1806.01990*.

[Cococcioni and de Gironcoli, 2005] Cococcioni, M. and de Gironcoli, S. (2005). Linear response approach to the calculation of the effective interaction parameters in the LDA + U method. *Phys. Rev. B*, 71:035105.

[Coey, 2020] Coey, J. (2020). Perspective and prospects for rare earth permanent magnets. *Engineering*, 6(2):119–131.

[Coey, 1996] Coey, J. M. D. (1996). *Rare-Earth Iron Permanent Magnets*. Clarendon Press, Oxford.

[Coey, 2011] Coey, J. M. D. (2011). Hard magnetic materials: A perspective. *IEEE Transactions on Magnetics*, 47(12):4671–4681.

[Colin et al., 2016] Colin, C. V., Ito, M., Yano, M., Dempsey, N. M., Suard, E., and Givord, D. (2016). Solid-solution stability and preferential site-occupancy in (R-R')2Fe14B compounds. *Applied Physics Letters*, 108(24):242415.

[Coqblin and Schrieffer, 1969] Coqblin, B. and Schrieffer, J. R. (1969). Exchange interaction in alloys with cerium impurities. *Phys. Rev.*, 185:847–853.

[Cottenier, 2013] Cottenier, S. (2002-2013). *Density Functional Theory and the Family of (L) APW-Methods: A Step-by-Step Introduction*. (2nd edition), ISBN 978-90-807215-1-7.

[Czyżyk and Sawatzky, 1994] Czyżyk, M. T. and Sawatzky, G. A. (1994). Local-density functional and on-site correlations: The electronic structure of La_2CuO_4 and $LaCuO_3$. *Phys. Rev. B*, 49:14211–14228.

[Daalderop et al., 1992] Daalderop, G., Kelly, P., and Schuurmans, M. (1992). Magnetocrystalline anisotropy of RECo5 compounds. *Journal of Magnetism and Magnetic Materials*, 104-107:737–738.

[Dai et al., 2005] Dai, X., Haule, K., and Kotliar, G. (2005). Strong-coupling solver for the quantum impurity model. *Phys. Rev. B*, 72:045111.

[Delange et al., 2016] Delange, P., Ayral, T., Simak, S. I., Ferrero, M., Parcollet, O., Biermann, S., and Pourovskii, L. (2016). Large effects of subtle electronic correlations on the energetics of vacancies in α-Fe. *Phys. Rev. B*, 94:100102.

[Delange et al., 2017] Delange, P., Biermann, S., Miyake, T., and Pourovskii, L. (2017). Crystal-field splittings in rare-earth-based hard magnets: An ab initio approach. *Phys. Rev. B*, 96:155132.

[Demourgues et al., 2001a] Demourgues, A., Tressaud, A., Laronze, H., Gravereau, P., and Macaudière, P. (2001a). Preparation and structural properties of new series of mixed-anion compounds: rare earth fluorosulfides. *Journal of Fluorine Chemistry*, 107(2):215–221.

[Demourgues et al., 2001b] Demourgues, A., Tressaud, A., Laronze, H., and Macaudière, P. (2001b). Rare earth fluorosulfides LnSF and Ln2AF4S2 as new colour pigments. *Journal of Alloys and Compounds*, 323-324:223–230. Proceedings of the 4th International Conference on f-Elements.

[Dirac, 1929] Dirac, P. A. M. (1929). Quantum mechanics of many-electron systems. *Proceedings of the Royal Society of London. Series A, Containing Papers of a Mathematical and Physical Character*, 123(792):714–733.

[Diviš et al., 2005] Diviš, M., Rusz, J., Michor, H., Hilscher, G., Blaha, P., and Schwarz, K. (2005). Magnetic properties of NdNi2B2C from first principles calculations. *Journal of Alloys and Compounds*, 403(1):29–33.

[El-Kelany et al., 2018] El-Kelany, K. E., Ravoux, C., Desmarais, J. K., Cortona, P., Pan, Y., Tse, J. S., and Erba, A. (2018). Spin localization, magnetic ordering, and electronic properties of strongly correlated Ln_2O_3 sesquioxides (Ln=La, Ce, Pr, Nd). *Phys. Rev. B*, 97:245118.

[Ermolenko, 1976] Ermolenko, A. (1976). Magnetocrystalline anisotropy of rare earth intermetallics. *IEEE Transactions on Magnetics*, 12(6):992–996.

[Ermolenko, 1979] Ermolenko, A. (1979). Exchange interactions and magnetocrystalline anisotropy of rare earth - cobalt compounds with CaCu5-type structure. *IEEE Transactions on Magnetics*, 15(6):1765–1770.

[Ermolenko, 1980a] Ermolenko, A. S. (1980a). *Phys. Met. Metall.*, 50(5):53.

[Ermolenko, 1980b] Ermolenko, A. S. (1980b). Exchange interactions and magnetocrystalline anisotcopy of rare-earth—cobalt compounds with CaCu5-type structure. *physica status solidi (a)*, 59(1):331–339.

[Ermolenko, 1983] Ermolenko, A. S. (1983). *Phys. Met. Metall.*, 55(3):74.

[Ermolenko and Rozenfeld, 1980] Ermolenko, A. S. and Rozenfeld, Y. V. (1980). *Phys. Met. Metall.*, 48(3):44.

[Ermolenko and Rozhda, 1982] Ermolenko, A. S. and Rozhda, A. F. (1982). *Phys. Met. Metall.*, 54(4):64.

[Ermolenko and Rozhda, 1983] Ermolenko, A. S. and Rozhda, A. F. (1983). *Phys. Met. Metall.*, 55(2):53.

[Fan and Tong, 2019] Fan, P. and Tong, N.-H. (2019). Controllable precision of the projective truncation approximation for Green's functions. *Chinese Physics B*, 28(4):047102.

[Fan et al., 2018] Fan, P., Yang, K., Ma, K.-H., and Tong, N.-H. (2018). Projective truncation approximation for equations of motion of two-time Green's functions. *Phys. Rev. B*, 97:165140.

[Fei et al., 2021a] Fei, J., Yeh, C.-N., and Gull, E. (2021a). Nevanlinna analytical continuation. *Phys. Rev. Lett.*, 126:056402.

[Fei et al., 2021b] Fei, J., Yeh, C.-N., Zgid, D., and Gull, E. (2021b). Analytical continuation of matrix-valued functions: Carathéodory formalism. *Phys. Rev. B*, 104:165111.

[Frietsch et al., 2015] Frietsch, B., Bowlan, J., Carley, R., Teichmann, M., Wienholdt, S., Hinzke, D., Nowak, U., Carva, K., Oppeneer, P. M., and Weinelt, M. (2015). Disparate ultrafast dynamics of itinerant and localized magnetic moments in gadolinium metal. *Nat. Commun.*, 6:8262.

[Gaiduk and Staroverov, 2009] Gaiduk, A. P. and Staroverov, V. N. (2009). How to tell when a model Kohn–Sham potential is not a functional derivative. *The Journal of Chemical Physics*, 131(4):044107.

[Galler et al., 2021a] Galler, A., Boust, J., Demourgues, A., Biermann, S., and Pourovskii, L. V. (2021a). Correlated electronic structure and optical response of rare-earth based semiconductors. *Phys. Rev. B*, 103:L241105.

[Galler et al., 2021b] Galler, A., Ener, S., Maccari, F., Dirba, I., Skokov, K. P., Gutfleisch, O., Biermann, S., and Pourovskii, L. V. (2021b). Intrinsically weak magnetic anisotropy of cerium in potential hard-magnetic intermetallics. *npj Quantum Materials*, 6:2.

[Galler and Pourovskii, 2022] Galler, A. and Pourovskii, L. V. (2022). Electronic structure of rare-earth mononitrides: quasiatomic excitations and semiconducting bands. *New Journal of Physics*, 24(4):043039.

[García et al., 2000a] García, L. M., Chaboy, J., Bartolomé, F., and Goedkoop, J. B. (2000a). Orbital magnetic moment instability at the spin reorientation transition of $Nd_2Fe_{14}B$. *Phys. Rev. Lett.*, 85:429–432.

[García et al., 2000b] García, L. M., Chaboy, J., Bartolomé, F., and Goedkoop, J. B. (2000b). Soft x-ray magnetic circular dichroism investigation of the spin reorientation transition in Nd2Fe14B. *Journal of Applied Physics*, 87(9):6567–6569.

[Gasgnier, 1989] Gasgnier, M. (1989). Rare earth compounds (oxides, sulfides, silicides, boron,...) as thin films and thin crystals physico-chemical properties and applications. *physica status solidi (a)*, 114(1):11–71.

[Georges, 2004] Georges, A. (2004). Strongly correlated electron materials: Dynamical mean-field theory and electronic structure. *AIP Conference Proceedings*, 715(1):3–74.

[Georges and Kotliar, 1992] Georges, A. and Kotliar, G. (1992). Hubbard model in infinite dimensions. *Phys. Rev. B*, 45:6479–6483.

[Georges et al., 1996] Georges, A., Kotliar, G., Krauth, W., and Rozenberg, M. J. (1996). Dynamical mean-field theory of strongly correlated fermion systems and the limit of infinite dimensions. *Rev. Mod. Phys.*, 68:13–125.

[Georges et al., 2013] Georges, A., Medici, L. d., and Mravlje, J. (2013). Strong correlations from Hund's coupling. *Annual Review of Condensed Matter Physics*, 4(1):137–178.

[Gillen et al., 2013] Gillen, R., Clark, S. J., and Robertson, J. (2013). Nature of the electronic band gap in lanthanide oxides. *Phys. Rev. B*, 87:125116.

[Goh et al., 2017] Goh, K. H., Haseeb, A., and Wong, Y. H. (2017). Lanthanide rare earth oxide thin film as an alternative gate oxide. *Materials Science in Semiconductor Processing*, 68:302–315.

[Golubkov et al., 1995] Golubkov, A., Prokof'ev, A., and Shelykh, A. (1995). Optical characteristics of Ce2O3 single crystals. *Physics of the Solid State*, 37:1028–1029.

[Gomez Eslava et al., 2021] Gomez Eslava, G., Fayyazi, B., Skokov, K., Skourski, Y., Gorbunov, D., Gutfleisch, O., Dempsey, N. M., and Givord, D. (2021). A two-sublattice model for extracting rare-earth anisotropy constants from measurements on (Nd,Ce)2(Fe,Co)14B single crystals. *Journal of Magnetism and Magnetic Materials*, 520:167470. Magnetic materials and their applications: in Memory of Dominique Givord.

[Granville et al., 2006] Granville, S., Ruck, B. J., Budde, F., Koo, A., Pringle, D. J., Kuchler, F., Preston, A. R. H., Housden, D. H., Lund, N., Bittar, A., Williams, G. V. M., and Trodahl, H. J. (2006). Semiconducting ground state of GdN thin films. *Phys. Rev. B*, 73:235335.

[Griffith, 1971] Griffith, J. S. (1971). *The Theory of Transition-Metal Ions*. Cambridge University Press, Cambridge.

[Gritsenko et al., 1995] Gritsenko, O., van Leeuwen, R., van Lenthe, E., and Baerends, E. J. (1995). Self-consistent approximation to the Kohn-Sham exchange potential. *Phys. Rev. A*, 51:1944–1954.

[Gull et al., 2011] Gull, E., Millis, A. J., Lichtenstein, A. I., Rubtsov, A. N., Troyer, M., and Werner, P. (2011). Continuous-time monte carlo methods for quantum impurity models. *Rev. Mod. Phys.*, 83:349–404.

[Gull et al., 2010] Gull, E., Reichman, D. R., and Millis, A. J. (2010). Bold-line diagrammatic monte carlo method: General formulation and application to expansion around the noncrossing approximation. *Phys. Rev. B*, 82:075109.

[Gull et al., 2008] Gull, E., Werner, P., Parcollet, O., and Troyer, M. (2008). Continuous-time auxiliary-field Monte Carlo for quantum impurity models. *EPL (Europhysics Letters)*, 82(5):57003.

[Gunnarsson et al., 1989] Gunnarsson, O., Andersen, O. K., Jepsen, O., and Zaanen, J. (1989). Density-functional calculation of the parameters in the Anderson model: Application to Mn in CdTe. *Phys. Rev. B*, 39:1708–1722.

[Gutfleisch et al., 2011] Gutfleisch, O., Willard, M. A., Brück, E., Chen, C. H., Sankar, S. G., and Liu, J. P. (2011). Magnetic materials and devices for the 21st century: Stronger, lighter, and more energy efficient. *Advanced Materials*, 23(7):821–842.

[Hastings, 1970] Hastings, W. K. (1970). Monte Carlo sampling methods using Markov chains and their applications. *Biometrika*, 57(1):97–109.

[Haule, 2015] Haule, K. (2015). Exact double counting in combining the dynamical mean field theory and the density functional theory. *Phys. Rev. Lett.*, 115:196403.

[Haule and Kotliar, 2009] Haule, K. and Kotliar, G. (2009). Coherence–incoherence crossover in the normal state of iron oxypnictides and importance of hund's rule coupling. *New Journal of Physics*, 11(2):025021.

[Haule et al., 2010] Haule, K., Yee, C.-H., and Kim, K. (2010). Dynamical mean-field theory within the full-potential methods: Electronic structure of $CeIrIn_5$, $CeCoIn_5$, and $CeRhIn_5$. *Phys. Rev. B*, 81:195107.

[Haverkort et al., 2012] Haverkort, M. W., Zwierzycki, M., and Andersen, O. K. (2012). Multiplet ligand-field theory using Wannier orbitals. *Phys. Rev. B*, 85:165113.

[Hay et al., 2006] Hay, P. J., Martin, R. L., Uddin, J., and Scuseria, G. E. (2006). Theoretical study of CeO_2 and Ce_2O_3 using a screened hybrid density functional. *The Journal of Chemical Physics*, 125(3):034712.

[Hedin, 1965] Hedin, L. (1965). New method for calculating the one-particle Green's function with application to the electron-gas problem. *Phys. Rev.*, 139:A796–A823.

[Herbst, 1991] Herbst, J. F. (1991). $R_2Fe_{14}B$ materials: Intrinsic properties and technological aspects. *Rev. Mod. Phys.*, 63:819–898.

[Hewson, 1993] Hewson, A. C. (1993). *The Kondo Problem to Heavy Fermions*. Cambridge Studies in Magnetism. Cambridge University Press.

[Himmetoglu et al., 2014] Himmetoglu, B., Floris, A., de Gironcoli, S., and Cococcioni, M. (2014). Hubbard-corrected dft energy functionals: The LDA+U description of correlated systems. *International Journal of Quantum Chemistry*, 114(1):14–49.

[Hirosawa et al., 1986] Hirosawa, S., Matsuura, Y., Yamamoto, H., Fujimura, S., Sagawa, M., and Yamauchi, H. (1986). Magnetization and magnetic anisotropy of R2Fe14B measured on single crystals. *Journal of Applied Physics*, 59(3):873–879.

[Hohenberg and Kohn, 1964] Hohenberg, P. and Kohn, W. (1964). Inhomogeneous electron gas. *Phys. Rev.*, 136:B864–B871.

[Huang and Lu, 2016] Huang, L. and Lu, H. (2016). Combined semilocal exchange potential with dynamical mean-field theory. *arXiv:1609.02482*.

[Hubbard, 1963] Hubbard, J. (1963). Electron correlations in narrow energy bands. *Proceedings of the Royal Society of London. Series A. Mathematical and Physical Sciences*, 276(1365):238–257.

[Hubbard, 1964] Hubbard, J. (1964). Electron correlations in narrow energy bands III. an improved solution. *Proceedings of the Royal Society of London. Series A. Mathematical and Physical Sciences*, 281(1386):401–419.

[Hummler and Fähnle, 1996] Hummler, K. and Fähnle, M. (1996). Full-potential linear-muffin-tin-orbital calculations of the magnetic properties of rare-earth–transition-metal intermetallics. I. description of the formalism and application to the series RCo_5 (R=rare-earth atom). *Phys. Rev. B*, 53:3272–3289.

[Ito et al., 2016] Ito, M., Yano, M., Dempsey, N. M., and Givord, D. (2016). Calculations of the magnetic properties of R2M14B intermetallic compounds (R=rare earth, M=Fe, Co). *Journal of Magnetism and Magnetic Materials*, 400:379–383. Proceedings of the 20th International Conference on Magnetism (Barcelona) 5-10 July 2015.

[Jacob et al., 2008] Jacob, D., Haule, K., and Kotliar, G. (2008). Combining the hybrid functional method with dynamical mean-field theory. *EPL*, 84(5):57009.

[Jarrell and Gubernatis, 1996] Jarrell, M. and Gubernatis, J. (1996). Bayesian inference and the analytic continuation of imaginary-time quantum Monte Carlo data. *Physics Reports*, 269(3):133–195.

[Jeschke and Kotliar, 2005] Jeschke, H. O. and Kotliar, G. (2005). Decoupling method for dynamical mean-field theory calculations. *Phys. Rev. B*, 71:085103.

[Jia-Ning et al., 2010] Jia-Ning, Z., Qing-Mei, L., Zhong, F., and Xi, D. (2010). Fast impurity solver for dynamical mean field theory based on second order perturbation around the atomic limit. *Chinese Physics B*, 19(8):087104.

[Jiang, 2013] Jiang, H. (2013). Band gaps from the Tran-Blaha modified Becke-Johnson approach: A systematic investigation. *The Journal of Chemical Physics*, 138(13):134115.

[Jiang, 2018] Jiang, H. (2018). Revisiting the *GW* approach to *d*- and *f*-electron oxides. *Phys. Rev. B*, 97:245132.

[Jiang et al., 2009] Jiang, H., Gomez-Abal, R. I., Rinke, P., and Scheffler, M. (2009). Localized and itinerant states in lanthanide oxides united by *GW* @ LDA + U. *Phys. Rev. Lett.*, 102:126403.

[Jiang et al., 2012] Jiang, H., Rinke, P., and Scheffler, M. (2012). Electronic properties of lanthanide oxides from the *GW* perspective. *Phys. Rev. B*, 86:125115.

[Jones, 2015] Jones, R. O. (2015). Density functional theory: Its origins, rise to prominence, and future. *Rev. Mod. Phys.*, 87:897–923.

[Jones and Gunnarsson, 1989] Jones, R. O. and Gunnarsson, O. (1989). The density functional formalism, its applications and prospects. *Rev. Mod. Phys.*, 61:689–746.

[Karolak et al., 2010] Karolak, M., Ulm, G., Wehling, T., Mazurenko, V., Poteryaev, A., and Lichtenstein, A. (2010). Double counting in LDA+DMFT—The example of NiO. *Journal of Electron Spectroscopy and Related Phenomena*, 181(1):11–15. Proceedings of International Workshop on Strong Correlations and Angle-Resolved Photoemission Spectroscopy 2009.

[Kimura et al., 2000] Kimura, S.-i., Arai, F., and Ikezawa, M. (2000). Optical study on electronic structure of rare-earth sesquioxides. *Journal of the Physical Society of Japan*, 69(10):3451–3457.

[Koelling and Harmon, 1977] Koelling, D. D. and Harmon, B. N. (1977). A technique for relativistic spin-polarised calculations. *Journal of Physics C: Solid State Physics*, 10(16):3107–3114.

[Kohn and Sham, 1965] Kohn, W. and Sham, L. J. (1965). Self-consistent equations including exchange and correlation effects. *Phys. Rev.*, 140:A1133–A1138.

[Koller et al., 2011] Koller, D., Tran, F., and Blaha, P. (2011). Merits and limits of the modified Becke-Johnson exchange potential. *Phys. Rev. B*, 83:195134.

[Kolodiazhnyi et al., 2018] Kolodiazhnyi, T., Sakurai, H., Avdeev, M., Charoonsuk, T., Lamonova, K. V., Pashkevich, Y. G., and Kennedy, B. J. (2018). Giant magnetocapacitance in cerium sesquioxide. *Phys. Rev. B*, 98:054423.

[Kolorenč, 2016] Kolorenč, J. (2016). Metal-oxygen hybridization and core-level spectra in actinide and rare-earth oxides. *MRS Advances*, 1(44):3007–3012.

[Kolorenč et al., 2015] Kolorenč, J. c. v., Shick, A. B., and Lichtenstein, A. I. (2015). Electronic structure and core-level spectra of light actinide dioxides in the dynamical mean-field theory. *Phys. Rev. B*, 92:085125.

[Kostyuchenko et al., 2020] Kostyuchenko, N., Tereshina, I., Gorbunov, D., Tereshina-Chitrova, E., Rogacki, K., Andreev, A., Doerr, M., Politova, G., and Zvezdin, A. (2020). High-field magnetization study of (Nd,Dy)2Fe14B: Intrinsic properties and promising compositions. *Intermetallics*, 124:106840.

[Kotliar et al., 2006] Kotliar, G., Savrasov, S. Y., Haule, K., Oudovenko, V. S., Parcollet, O., and Marianetti, C. A. (2006). Electronic structure calculations with dynamical mean-field theory. *Rev. Mod. Phys.*, 78:865–951.

[Kotliar and Vollhardt, 2004] Kotliar, G. and Vollhardt, D. (2004). Strongly correlated materials: Insights from dynamical mean-field theory. *Physics Today*, 57(3):53–59.

[Kraberger et al., 2017] Kraberger, G. J., Triebl, R., Zingl, M., and Aichhorn, M. (2017). Maximum entropy formalism for the analytic continuation of matrix-valued Green's functions. *Phys. Rev. B*, 96:155128.

[Kutepov, 2020] Kutepov, A. (2020). Self-consistent GW method: O(N) algorithm for polarizability and self energy. *Computer Physics Communications*, 257:107502.

[Kuz'min and Tishin, 2007] Kuz'min, M. and Tishin, A. (2007). Theory of crystal-field effects in 3d-4f intermetallic compounds. In Buschow, K., editor, *Handbook of Magnetic Materials, Vol. 17*, pages 149 – 233. Elsevier.

[Kuz'min, 1995] Kuz'min, M. D. (1995). Single-ion magnetic anisotropy of rare-earth–transition-metal compounds and its description by means of analytical expressions. *Phys. Rev. B*, 51:8904–8916.

[Kuz'min, 2005] Kuz'min, M. D. (2005). Shape of temperature dependence of spontaneous magnetization of ferromagnets: Quantitative analysis. *Phys. Rev. Lett.*, 94.

[Kuz'min et al., 2010] Kuz'min, M. D., Givord, D., and Skumryev, V. (2010). Why the iron magnetization in Gd2Fe14B and the spontaneous magnetization of Y2Fe14B depend on temperature differently. *Journal of Applied Physics*, 107(11):113924.

[Lacroix, 1981] Lacroix, C. (1981). Density of states for the Anderson model. *Journal of Physics F: Metal Physics*, 11(11):2389–2397.

[Lang et al., 1981] Lang, J. K., Baer, Y., and Cox, P. A. (1981). Study of the 4f and valence band density of states in rare-earth metals. II. experiment and results. *Journal of Physics F: Metal Physics*, 11(1):121–138.

[Lebègue et al., 2006] Lebègue, S., Svane, A., Katsnelson, M. I., Lichtenstein, A. I., and Eriksson, O. (2006). Multiplet effects in the electronic structure of heavy rare-earth metals. *Journal of Physics: Condensed Matter*, 18(27):6329–6335.

[Lechermann et al., 2006] Lechermann, F., Georges, A., Poteryaev, A., Biermann, S., Posternak, M., Yamasaki, A., and Andersen, O. K. (2006). Dynamical mean-field theory using Wannier functions: A flexible route to electronic structure calculations of strongly correlated materials. *Phys. Rev. B*, 74:125120.

[Lejus et al., 1976] Lejus, A., Bernier, J., and Collongues, R. (1976). Elaboration et proprietes magnetiques de monocristaux d'oxyde de praseodyme Pr_2O_3. *Journal of Solid State Chemistry*, 16:349–353.

[Leonov et al., 2011] Leonov, I., Poteryaev, A. I., Anisimov, V. I., and Vollhardt, D. (2011). Electronic correlations at the $\alpha-\gamma$ structural phase transition in paramagnetic iron. *Phys. Rev. Lett.*, 106:106405.

[Leonov et al., 2016] Leonov, I., Pourovskii, L., Georges, A., and Abrikosov, I. A. (2016). Magnetic collapse and the behavior of transition metal oxides at high pressure. *Phys. Rev. B*, 94:155135.

[Leskelä et al., 2006] Leskelä, M., Kukli, K., and Ritala, M. (2006). Rare-earth oxide thin films for gate dielectrics in microelectronics. *Journal of Alloys and Compounds*, 418(1):27–34.

[Li et al., 1988] Li, H., Gavigan, J., Cadogan, J., Givord, D., and Coey, J. (1988). A study of exchange and crystalline electric field interactions in Nd2Co14B: Comparison with Nd2Fe14B. *Journal of Magnetism and Magnetic Materials*, 72(3):L241–L246.

[Lichtenstein and Katsnelson, 1998] Lichtenstein, A. I. and Katsnelson, M. I. (1998). Ab initio calculations of quasiparticle band structure in correlated systems: LDA++ approach. *Phys. Rev. B*, 57:6884–6895.

[Lichtenstein et al., 2001] Lichtenstein, A. I., Katsnelson, M. I., and Kotliar, G. (2001). Finite-temperature magnetism of transition metals: An ab initio dynamical mean-field theory. *Phys. Rev. Lett.*, 87:067205.

[Liechtenstein et al., 1995] Liechtenstein, A. I., Anisimov, V. I., and Zaanen, J. (1995). Density-functional theory and strong interactions: Orbital ordering in Mott-Hubbard insulators. *Phys. Rev. B*, 52:R5467–R5470.

[Lin et al., 2020] Lin, Z., Zha, L., Wang, F., Liu, Z., Wu, R., Yang, J., Xue, M., Yang, W., Tian, G., Ma, X., Qiao, L., Franz, A., An, Q., Liu, W., Wang, C., and Yang, J. (2020). Effect of ce substitution on the structural and magnetic properties of nd2fe14b. *Acta Materialia*, 200:502–509.

[Liu et al., 2020] Liu, C., Yao, Y. X., Wang, C.-Z., Ho, K.-M., and Antropov, V. P. (2020). Calculations of anisotropic magnetic properties using spin-orbit energy variations. *Phys. Rev. B*, 102:205119.

[Locht et al., 2016] Locht, I. L. M., Kvashnin, Y. O., Rodrigues, D. C. M., Pereiro, M., Bergman, A., Bergqvist, L., Lichtenstein, A. I., Katsnelson, M. I., Delin, A., Klautau, A. B., Johansson, B., Di Marco, I., and Eriksson, O. (2016). Standard model of the rare earths analyzed from the Hubbard I approximation. *Phys. Rev. B*, 94:085137.

[Loschen et al., 2007] Loschen, C., Carrasco, J., Neyman, K. M., and Illas, F. (2007). First-principles LDA + U and GGA + U study of cerium oxides: Dependence on the effective u parameter. *Phys. Rev. B*, 75:035115.

[Ma and Tong, 2019] Ma, K.-H. and Tong, N.-H. (2019). Improved strong-coupling perturbation theory of the symmetric Anderson impurity model. *Modern Physics Letters B*, 33(27):1950332.

[Martins, 2010] Martins, C. (2010). Interplay of Spin-Orbit Coupling and Electronic Coulomb Interactions in Strontium Iridate Sr2IrO4.

[Marzari and Vanderbilt, 1997] Marzari, N. and Vanderbilt, D. (1997). Maximally localized generalized Wannier functions for composite energy bands. *Phys. Rev. B*, 56:12847–12865.

[Metropolis et al., 1953] Metropolis, N., Rosenbluth, A. W., Rosenbluth, M. N., Teller, A. H., and Teller, E. (1953). Equation of state calculations by fast computing machines. *The Journal of Chemical Physics*, 21(6):1087–1092.

[Metzner and Vollhardt, 1989] Metzner, W. and Vollhardt, D. (1989). Correlated lattice fermions in $d = \infty$ dimensions. *Phys. Rev. Lett.*, 62:324–327.

[Miyake et al., 2009] Miyake, T., Aryasetiawan, F., and Imada, M. (2009). Ab initio procedure for constructing effective models of correlated materials with entangled band structure. *Phys. Rev. B*, 80:155134.

[Miyake et al.,] Miyake, T., Nakamura, K., Arita, R., and Imada, M. comparison of ab initio low-energy models for lafepo, lafeaso, bafe2as2, lifeas, fese, and fete: Electron correlation and covalency.

[Momma and Izumi, 2011] Momma, K. and Izumi, F. (2011). Vesta 3 for three-dimensional visualization of crystal, volumetric and morphology data. *Journal of Applied Crystallography*, 44:1272–1276.

[Mravlje et al., 2011] Mravlje, J., Aichhorn, M., Miyake, T., Haule, K., Kotliar, G., and Georges, A. (2011). Coherence-incoherence crossover and the mass-renormalization puzzles in sr_2ruo_4. *Phys. Rev. Lett.*, 106:096401.

[Mulak and Gajek, 2000] Mulak, J. and Gajek, Z. (2000). *The Effective Crystal Field Potential*. Elsevier Science Ltd, Oxford.

[Mullins et al., 1998] Mullins, D., Overbury, S., and Huntley, D. (1998). Electron spectroscopy of single crystal and polycrystalline cerium oxide surfaces. *Surface Science*, 409(2):307 – 319.

[Newman and Ng, 2000] Newman, D. J. and Ng, B., editors (2000). *Crystal Field Handbook*. Cambridge University Press, Cambridge.

[Nguyen et al., 2018] Nguyen, M. C., Yao, Y., Wang, C.-Z., Ho, K.-M., and Antropov, V. P. (2018). Magnetocrystalline anisotropy in cobalt based magnets: a choice of correlation parameters and the relativistic effects. *Journal of Physics: Condensed Matter*, 30(19):195801.

[Nikitin et al., 2010] Nikitin, S. A., Skokov, K. P., Koshkid'ko, Y. S., Pastushenkov, Y. G., and Ivanova, T. I. (2010). Giant Rotating Magnetocaloric Effect in the Region of Spin-Reorientation Transition in the $NdCo_5$ Single Crystal. *Phys. Rev. Lett.*, 105:137205.

[Novák and Kuriplach, 1994] Novák, P. and Kuriplach, J. (1994). Calculation of crystal-field parameters in the RNi_5 (R=rare earth) system. *Phys. Rev. B*, 50:2085–2089.

[Novák, 1996] Novák, P. (1996). Calculated crystal field parameters in rco5 and rni5 systems. *physica status solidi (b)*, 198(2):729–740.

[Nowik et al., 1990] Nowik, I., Muraleedharan, K., Wortmann, G., Perscheid, B., Kaindl, G., and Koon, N. (1990). Spin reorientation transition in Nd2Fe14B studied by 145Nd-Mössbauer spectroscopy. *Solid State Communications*, 76(8):967–970.

[Onodera et al., 1987] Onodera, H., Yamauchi, H., Yamada, M., Yamamoto, H., Sagawa, M., and Hirosawa, S. (1987). Mössbauer study of the intermetallic compound Nd2Fe14B. II. Temperature dependence and spin reorientation. *Journal of Magnetism and Magnetic Materials*, 68(1):15–27.

[Padé, 1892] Padé, H. (1892). Sur la représentation approchée d'une fonction par des fractions rationnelles. *Annales scientifiques de l'École Normale Supérieure*, 9:3–93.

[Päiväsaari et al., 2005] Päiväsaari, J., Putkonen, M., and Niinistö, L. (2005). A comparative study on lanthanide oxide thin films grown by atomic layer deposition. *Thin Solid Films*, 472(1):275–281.

[Parcollet et al., 2015] Parcollet, O., Ferrero, M., Ayral, T., Hafermann, H., Krivenko, I., Messio, L., and Seth, P. (2015). TRIQS: A toolbox for research on interacting quantum systems. *Computer Physics Communications*, 196:398–415.

[Pashov et al., 2020] Pashov, D., Acharya, S., Lambrecht, W. R., Jackson, J., Belashchenko, K. D., Chantis, A., Jamet, F., and van Schilfgaarde, M. (2020). Questaal: A package of electronic structure methods based on the linear muffin-tin orbital technique. *Computer Physics Communications*, 249:107065.

[Patrick and Staunton, 2019] Patrick, C. E. and Staunton, J. B. (2019). Temperature-dependent magnetocrystalline anisotropy of rare earth/transition metal permanent magnets from first principles: The light $RCo_5 (R = \mathrm{Y}, \mathrm{La\text{-}Gd})$ intermetallics. *Phys. Rev. Materials*, 3:101401.

[Pauwels, 2003] Pauwels, D. (2003). *Structural features of rare-earth-based mixed anions compounds; UV-visible absorption properties.* PhD, Universite Bordeaux I, France.

[Pauwels et al., 2002] Pauwels, D., Demourgues, A., Laronze, H., Gravereau, P., Guillen, F., Isnard, O., and Tressaud, A. (2002). Structural features of new rare earth-based mixed anions (O, S, F) compounds: relationships between optical absorption and rare earth environment. *Solid State Sciences*, 4(11):1471–1479. No special N. BARTLETT.

[Pavarini, 2014] Pavarini, E. (2014). electronic structure calculations with lda+dmft. pages 321–341. Springer International Publishing.

[Pavarini et al., 2004] Pavarini, E., Biermann, S., Poteryaev, A., Lichtenstein, A. I., Georges, A., and Andersen, O. K. (2004). Mott transition and suppression of orbital fluctuations in orthorhombic $3d^1$ perovskites. *Phys. Rev. Lett.*, 92:176403.

[Perdew et al., 1996] Perdew, J. P., Burke, K., and Ernzerhof, M. (1996). Generalized gradient approximation made simple. *Phys. Rev. Lett.*, 77:3865–3868.

[Perdew and Levy, 1983] Perdew, J. P. and Levy, M. (1983). Physical Content of the Exact Kohn-Sham Orbital Energies: Band Gaps and Derivative Discontinuities. *Phys. Rev. Lett.*, 51:1884–1887.

[Petit et al., 2005] Petit, L., Svane, A., Szotek, Z., and Temmerman, W. M. (2005). First-principles study of rare-earth oxides. *Phys. Rev. B*, 72:205118.

[Pivetta et al., 2020] Pivetta, M., Patthey, F., Di Marco, I., Subramonian, A., Eriksson, O., Rusponi, S., and Brune, H. (2020). Measuring the intra-atomic exchange energy in rare-earth adatoms. *Phys. Rev. X*, 10:031054.

[Pourovskii et al., 2007] Pourovskii, L. V., Amadon, B., Biermann, S., and Georges, A. (2007). Self-consistency over the charge density in dynamical mean-field theory: A linear muffin-tin implementation and some physical implications. *Phys. Rev. B*, 76:235101.

[Pourovskii et al., 2020] Pourovskii, L. V., Boust, J., Ballou, R., Eslava, G. G., and Givord, D. (2020). Higher-order crystal field and rare-earth magnetism in rare-earth–Co_5 intermetallics. *Phys. Rev. B*, 101:214433.

[Pourovskii et al., 2009] Pourovskii, L. V., Delaney, K. T., Van de Walle, C. G., Spaldin, N. A., and Georges, A. (2009). Role of atomic multiplets in the electronic structure of rare-earth semiconductors and semimetals. *Phys. Rev. Lett.*, 102:096401.

[Pourovskii et al., 2005] Pourovskii, L. V., Katsnelson, M. I., and Lichtenstein, A. I. (2005). Correlation effects in electronic structure of actinide monochalcogenides. *Phys. Rev. B*, 72:115106.

[Pourovskii et al., 2014] Pourovskii, L. V., Mravlje, J., Ferrero, M., Parcollet, O., and Abrikosov, I. A. (2014). Impact of electronic correlations on the equation of state and transport in ϵ-Fe. *Phys. Rev. B*, 90:155120.

[Prokof'ev and Svistunov, 2007] Prokof'ev, N. and Svistunov, B. (2007). Bold Diagrammatic Monte Carlo Technique: When the Sign Problem Is Welcome. *Phys. Rev. Lett.*, 99:250201.

[Prokofiev et al., 1996] Prokofiev, A., Shelykh, A., and Melekh, B. (1996). Periodicity in the band gap variation of Ln2X3 (X = O, S, Se) in the lanthanide series. *Journal of Alloys and Compounds*, 242(1):41 – 44.

[Radwański, 1986] Radwański, R. (1986). The rare earth contribution to the magnetocrystalline anisotropy in RCo5 intermetallics. *Journal of Magnetism and Magnetic Materials*, 62(1):120–126.

[Rajagopal and Callaway, 1973] Rajagopal, A. K. and Callaway, J. (1973). Inhomogeneous electron gas. *Phys. Rev. B*, 7:1912–1919.

[Rubtsov et al., 2005] Rubtsov, A. N., Savkin, V. V., and Lichtenstein, A. I. (2005). Continuous-time quantum Monte Carlo method for fermions. *Phys. Rev. B*, 72:035122.

[Saito et al., 2017] Saito, K., Doi, S., Abe, T., and Ono, K. (2017). Quantitative evaluation of site preference in Dy-substituted Nd2Fe14B. *Journal of Alloys and Compounds*, 721:476–481.

[Sala et al., 2018] Sala, G., Stone, M. B., Rai, B. K., May, A. F., Dela Cruz, C. R., Suriya Arachchige, H., Ehlers, G., Fanelli, V. R., Garlea, V. O., Lumsden, M. D., Mandrus, D., and Christianson, A. D. (2018). Physical properties of the trigonal binary compound nd_2o_3. *Phys. Rev. Materials*, 2:114407.

[Sandvik, 1998] Sandvik, A. W. (1998). Stochastic method for analytic continuation of quantum Monte Carlo data. *Phys. Rev. B*, 57:10287–10290.

[Sato et al., 2021] Sato, H., Kubo, Y., Yoshioka, T., Tsuchiura, H., Mizuno, Y., Koike, K., Takahashi, K., and Kato, H. (2021). Reduction of Nd moments and local magnetic anisotropy in Nd2Fe14B single crystals. *AIP Advances*, 11(2):025224.

[Savrasov and Kotliar, 2004] Savrasov, S. Y. and Kotliar, G. (2004). Spectral density functionals for electronic structure calculations. *Phys. Rev. B*, 69:245101.

[Savrasov et al., 2001] Savrasov, S. Y., Kotliar, G., and Abrahams, E. (2001). Correlated electrons in δ-plutonium within a dynamical mean-field picture. *Nature*, 410(6830):793–795.

[Schollwöck, 2011] Schollwöck, U. (2011). The density-matrix renormalization group in the age of matrix product states. *Annals of Physics*, 326(1):96–192. January 2011 Special Issue.

[Seth et al., 2016] Seth, P., Krivenko, I., Ferrero, M., and Parcollet, O. (2016). TRIQS/CTHYB: A continuous-time quantum Monte Carlo hybridisation expansion solver for quantum impurity problems. *Computer Physics Communications*, 200:274 – 284.

[Sham and Schlüter, 1983] Sham, L. J. and Schlüter, M. (1983). Density-functional theory of the energy gap. *Phys. Rev. Lett.*, 51:1888–1891.

[Sharp and Horton, 1953] Sharp, R. T. and Horton, G. K. (1953). A variational approach to the unipotential many-electron problem. *Phys. Rev.*, 90:317–317.

[Shick et al., 2009] Shick, A. B., Kolorenč, J., Lichtenstein, A. I., and Havela, L. (2009). Electronic structure and spectral properties of am, cm, and bk: Charge-density self-consistent LDA + HIA calculations in the fp-lapw basis. *Phys. Rev. B*, 80:085106.

[Shim et al.,] Shim, J. H., Haule, K., and Kotliar, G. modeling the localized-to-itinerant electronic transition in the heavy fermion system ceirin$_5$.

[Shim et al., 2007] Shim, J. H., Haule, K., and Kotliar, G. (2007). Fluctuating valence in a correlated solid and the anomalous properties of δ-plutonium. *Nature*, 446(7135):513–516.

[Singh et al., 2006] Singh, N., Saini, S. M., Nautiyal, T., and Auluck, S. (2006). Electronic structure and optical properties of rare earth sesquioxides (R2O3, R=La, Pr, and Nd). *Journal of Applied Physics*, 100(8):083525.

[Skokov and Gutfleisch, 2018] Skokov, K. and Gutfleisch, O. (2018). Heavy rare earth free, free rare earth and rare earth free magnets - vision and reality. *Scripta Materialia*, 154:289–294.

[Skomski, 2016] Skomski, R. (2016). *Permanent Magnets: History, Current Research, and Outlook*, pages 359–395. Springer International Publishing, Cham.

[Skomski and Coey, 2016] Skomski, R. and Coey, J. (2016). Magnetic anisotropy — how much is enough for a permanent magnet? *Scripta Materialia*, 112:3–8.

[Skorodumova et al., 2001] Skorodumova, N. V., Ahuja, R., Simak, S. I., Abrikosov, I. A., Johansson, B., and Lundqvist, B. I. (2001). Electronic, bonding, and optical properties of CeO_2 and Ce_2O_3 from first principles. *Phys. Rev. B*, 64:115108.

[Slater, 1951] Slater, J. C. (1951). A Simplification of the Hartree-Fock Method. *Phys. Rev.*, 81:385–390.

[Slater, 1960] Slater, J. C. (1960). *Quantum theory of atomic structure*. McGraw-Hill.

[Solovyev et al., 1994] Solovyev, I. V., Dederichs, P. H., and Anisimov, V. I. (1994). Corrected atomic limit in the local-density approximation and the electronic structure of d impurities in Rb. *Phys. Rev. B*, 50:16861–16871.

[Solovyev et al., 1998] Solovyev, I. V., Liechtenstein, A. I., and Terakura, K. (1998). Is Hund's Second Rule Responsible for the Orbital Magnetism in Solids? *Phys. Rev. Lett.*, 80:5758–5761.

[Stasyuk and Hera, 2005] Stasyuk, I. V. and Hera, O. B. (2005). Mott transition in the asymmetric Hubbard model at half-filling within dynamical mean-field theory. *The European Physical Journal B - Condensed Matter and Complex Systems*, 48:339–348.

[Steinbeck et al., 1994] Steinbeck, L., Richter, M., Eschrig, H., and Nitzsche, U. (1994). Calculated crystal-field parameters for rare-earth impurities in noble metals. *Phys. Rev. B*, 49:16289–16292.

[Stevens, 1952] Stevens, K. W. H. (1952). Matrix elements and operator equivalents connected with the magnetic properties of rare earth ions. *Proceedings of the Physical Society. Section A*, 65(3):209–215.

[Stoner and Wohlfarth, 1948] Stoner, E. C. and Wohlfarth, E. P. (1948). A mechanism of magnetic hysteresis in heterogeneous alloys. *Philosophical Transactions of the Royal Society of London. Series A, Mathematical and Physical Sciences*, 240(826):599–642.

[Strnat and Strnat, 1991] Strnat, K. J. and Strnat, R. M. (1991). Rare earth-cobalt permanent magnets. *Journal of Magnetism and Magnetic Materials*, 100(1):38 – 56.

[Sucksmith and Thompson, 1954] Sucksmith, W. and Thompson, J. E. (1954). The magnetic anisotropy of cobalt. *Proceedings of the Royal Society of London. Series A. Mathematical and Physical Sciences*, 225(1162):362–375.

[Talman and Shadwick, 1976] Talman, J. D. and Shadwick, W. F. (1976). Optimized effective atomic central potential. *Phys. Rev. A*, 14:36–40.

[Tatsumoto, E. et al., 1971] Tatsumoto, E., Okamoto, T., Fujii, H., and Inoue, C. (1971). Saturation magnetic moment and crystalline anisotropy of single crystals of light rare earth cobalt compounds RCo5. *J. Phys. Colloques*, 32:C1–550–C1–551.

[Thunström et al., 2012] Thunström, P., Di Marco, I., and Eriksson, O. (2012). Electronic entanglement in late transition metal oxides. *Phys. Rev. Lett.*, 109:186401.

[Tie-song et al., 1991] Tie-song, Z., Han-min, J., Guang-hua, G., Xiu-feng, H., and Hong, C. (1991). Magnetic properties of R ions in RCo_5 compounds (R=Pr, Nd, Sm, Gd, Tb, Dy, Ho, and Er). *Phys. Rev. B*, 43:8593–8598.

[Tomczak, 2007] Tomczak, J. M. (2007). *Propriétés spectrales et optiques des Matériaux corrélés*. Theses, Ecole Polytechnique X.

[Tomczak et al., 2013] Tomczak, J. M., Pourovskii, L. V., Vaugier, L., Georges, A., and Biermann, S. (2013). Rare-earth vs. heavy metal pigments and their colors from first principles. *Proceedings of the National Academy of Sciences*, 110(3):904–907.

[Tong, 2015] Tong, N.-H. (2015). Equation-of-motion series expansion of double-time Green's functions. *Phys. Rev. B*, 92:165126.

[Tran and Blaha, 2009] Tran, F. and Blaha, P. (2009). Accurate band gaps of semiconductors and insulators with a semilocal exchange-correlation potential. *Phys. Rev. Lett.*, 102:226401.

[Tran et al., 2007] Tran, F., Blaha, P., and Schwarz, K. (2007). Band gap calculations with Becke–Johnson exchange potential. *Journal of Physics: Condensed Matter*, 19(19):196208.

[Trovarelli, 1999] Trovarelli, A. (1999). Structural and Oxygen Storage/Release Properties of CeO2-Based Solid Solutions. *Comments on Inorganic Chemistry*, 20(4-6):263–284.

[Tserkovnikov, 1981] Tserkovnikov, Y. A. (1981). A method of solving infinite systems of equations for two-time thermal Green's functions. *Theoretical and Mathematical Physics*, 49:993–1002.

[Tsuchiura et al., 2018] Tsuchiura, H., Yoshioka, T., and Novák, P. (2018). Bridging atomistic magnetism and coercivity in Nd-Fe-B magnets. *Scripta Materialia*, 154:248–252.

[Van Vleck, 1932] Van Vleck, J. H. (1932). Theory of the variations in paramagnetic anisotropy among different salts of the iron group. *Phys. Rev.*, 41:208–215.

[Vaugier, 2011] Vaugier, L. (2011). *Electronic Structure of Correlated Materials From First Principles: Hubbard interaction and Hund's exchange*. PhD thesis, Ecole Polytechnique X.

[von Barth and Hedin, 1972] von Barth, U. and Hedin, L. (1972). A local exchange-correlation potential for the spin polarized case. i. *Journal of Physics C: Solid State Physics*, 5(13):1629–1642.

[Wang et al., 2019] Wang, K., Zhang, M., Liu, J., Luo, H., and Sun, J. (2019). Crystal structure, spin reorientation, and rotating magnetocaloric properties of NdCo5-xSix compounds. *Journal of Applied Physics*, 125(24):243901.

[Werner et al., 2006] Werner, P., Comanac, A., de' Medici, L., Troyer, M., and Millis, A. J. (2006). Continuous-time solver for quantum impurity models. *Phys. Rev. Lett.*, 97:076405.

[White, 1992] White, S. R. (1992). Density matrix formulation for quantum renormalization groups. *Phys. Rev. Lett.*, 69:2863–2866.

[Wilson, 1975] Wilson, K. G. (1975). The renormalization group: Critical phenomena and the Kondo problem. *Rev. Mod. Phys.*, 47:773–840.

[Wolfers et al., 2001] Wolfers, P., Bacmann, M., and Fruchart, D. (2001). Single crystal neutron diffraction investigations of the crystal and magnetic structures of R2Fe14B (R=Y, Nd, Ho, Er). *Journal of Alloys and Compounds*, 317-318:39–43. The 13th International Conference on Solid Compounds of Transition Elements.

[Wybourne, 1965] Wybourne, B. G. (1965). *Spectroscopic properties of rare earths*. Interscience Publishers, New York.

[Yamada et al., 1988] Yamada, M., Kato, H., Yamamoto, H., and Nakagawa, Y. (1988). *Phys. Rev. B*, 38:620–633.

[Zener, 1954] Zener, C. (1954). Classical theory of the temperature dependence of magnetic anisotropy energy. *Phys. Rev.*, 96:1335–1337.

[Zhang et al., 1994] Zhang, F., Gignoux, D., Schmitt, D., Franse, J., and Kayzel, F. (1994). High field induced first order magnetization process in NdCo5 single crystal. *Journal of Magnetism and Magnetic Materials*, 136(3):245–250.

[Zhong and Ching, 1989a] Zhong, X.-F. and Ching, W. Y. (1989a). First-principles calculation of crystal-field parameters in $Nd_2Fe_{14}B$. *Phys. Rev. B*, 39:12018–12026.

[Zhong and Ching, 1989b] Zhong, X.-F. and Ching, W. Y. (1989b). Theoretical construction of the magnetic Hamiltonian and zero-temperature anisotropic energy in $Nd_2Fe_{14}B$. *Phys. Rev. B*, 40:5292–5295.

[Zölfl et al., 2001] Zölfl, M. B., Nekrasov, I. A., Pruschke, T., Anisimov, V. I., and Keller, J. (2001). Spectral and Magnetic Properties of α- and γ-Ce from Dynamical Mean-Field Theory and Local Density Approximation. *Phys. Rev. Lett.*, 87:276403.

[Zölfl et al., 2000] Zölfl, M. B., Pruschke, T., Keller, J., Poteryaev, A. I., Nekrasov, I. A., and Anisimov, V. I. (2000). Combining density-functional and dynamical-mean-field theory for $La_{1-x}Sr_xTiO_3$. *Phys. Rev. B*, 61:12810–12815.

ECOLE DOCTORALE

Titre: Propriétés magnétiques et optiques de composés de terres rares corrélés à partir des premiers principes

Mots clés: composés de terres rares, calculs *ab initio*, théorie du champ moyen dynamique, structure électronique corrélée, anisotropie magnétique, *gap* optique

Résumé: Dans les matériaux dits "fortement corrélés", la forte interaction de Coulomb qui corrèle le mouvement des électrons à l'échelle atomique peut donner lieu à des propriétés exceptionnelles à l'échelle macroscopique. Les matériaux étudiés dans cette thèse contiennent des atomes de terres rares (comme le néodyme) qui présentent généralement ces effets de fortes corrélations.
Du fait de leurs propriétés remarquables, les composés de terres rares ont de nombreuses applications technologiques; ils sont par exemple utilisés comme aimants très performants dans les moteurs électriques. La demande en terres rares est donc en plein essor; mais les miner s'avère difficile, coûteux et polluant. Optimiser les propriétés et la composition des matériaux à base de terres rares est ainsi intéressant pour des raisons à la fois technologiques, économiques et écologiques.
Du point de vue de la physique théorique, décrire ces matériaux constitue un véritable défi, précisément de par leur nature fortement corrélée. Dans cette thèse, nous développons des approches théoriques pour étudier les propriétés magnétiques et optiques de composés de terres rares, notamment l'aimant au néodyme employé dans l'industrie. Ces méthodes théoriques sont dites "depuis les premiers principes" car elles reposent sur les lois fondamentales gouvernant la physique à l'échelle atomique.

Title: Magnetic and optical properties of correlated rare-earth compounds from first principles

Keywords: rare-earth compounds, *ab initio* calculations, dynamical mean-field theory, correlated electronic structure, magnetic anisotropy, optical gap

Abstract: In so-called "strongly correlated" materials, the strong Coulomb interaction which correlates the movement of electrons at the atomic scale can give rise to outstanding properties at the macroscopic scale. The materials studied in this thesis contain rare-earth elements (like neodymium) which usually exhibit these strong correlation effects.
Due to their remarkable properties, rare-earth compounds have numerous technological applications; they are for instance used as high-performance magnets in electric motors. The demand for rare earths is therefore increasing; on the other hand, mining them is difficult, expensive and polluting. Hence, optimizing the properties and composition of rare-earth-based materials can be of great technological, economical and environmental interest.
From the point of view of theoretical physics, describing these materials constitutes a real challenge, precisely due to their strongly correlated nature. In this thesis, we develop theoretical approaches to study the magnetic and optical properties of rare-earth compounds, notably the industrially relevant neodymium magnet. These theoretical methods are said to be from "first principles" as they are based on the fundamental laws governing the physics at the atomic level.

Institut Polytechnique de Paris
91120 Palaiseau, France